# Data-Centric Structural Health Monitoring

# Data-Centric Engineering

Edited by
Mohammad Noori, Fuh-Gwo Yuan
and Ehsan Noroozinejad Farsangi

# Data-Centric Structural Health Monitoring

## Mechanical, Aerospace and Complex Infrastructure Systems

Edited by
Mohammad Noori, Fuh-Gwo Yuan
and Ehsan Noroozinejad Farsangi

DE GRUYTER

**Editors**
**Prof. Mohammad Noori**
Mechanical Engineering Department
California Polytechnic State University
1 Grand Avenue
San Luis Obispo, CA 93407
USA
mnoori@calpoly.edu

**Prof. Fuh-Gwo Yuan**
Department of Mechanical and Aerospace Engineering
North Carolina State University
Raleigh, NC 27695
USA
yuan@ncsu.edu

**Dr. Ehsan Noroozinejad Farsangi**
Smart Structures Research Group
University of British Columbia
Vancouver 2329 West Mall
BC Canada V6T 1Z4
ehsan.noroozinejad@ubc.ca

ISBN 978-3-11-079127-3
e-ISBN (PDF) 978-3-11-079142-6
e-ISBN (EPUB) 978-3-11-079151-8
ISSN 2751-983X

**Library of Congress Control Number: 2023938224**

**Bibliographic information published by the Deutsche Nationalbibliothek**
The Deutsche Nationalbibliothek lists this publication in the Deutsche Nationalbibliografie; detailed bibliographic data are available on the internet at http://dnb.dnb.de.

Cover image: monsitj/iStock/Getty Images Plus
Typesetting: Integra Software Services Pvt. Ltd.
Printing and binding: CPI books GmbH, Leck

www.degruyter.com

# Preface

This book is a collection of contributions by active researchers, in the field of Data-Centric Engineering, on important topics in this rapidly evolving field and is an attempt to shed light on the use of data-centric approaches in structural health monitoring (SHM). SHM has continued to gain immense importance in recent years due to the need for timely and accurate diagnosis of potential structural failures. With the increasing complexity of structures and the advent of advanced sensing and data collection technologies, the field of SHM has witnessed a paradigm shift towards data-driven approaches, which rely on data-centric methodologies for data collection, processing, and analysis. The present book aims to present a comprehensive overview of these approaches, their advantages and limitations, and their potential applications in the field of SHM. It covers a wide range of topics, from basic concepts and principles to advanced techniques, and presents case studies and real-world applications to illustrate the relevance and effectiveness of these methods.

One of the key benefits of data-centric SHM is that it allows for continuous monitoring of a structure, providing real-time insights into its health and performance. This can help to identify potential issues before they become critical, allowing for timely maintenance and repairs. Additionally, data-centric SHM can provide a more comprehensive view of a structure's health, compared to traditional inspection methods, which may only focus on certain areas or components.

This edited volume on data-centric structural health monitoring is published as part of a new book series, titled *Data-Centric Engineering*, which has just been established by De Gruyter. The editors of this book are the founding editors of the new series. This volume represents an effort to provide a comprehensive overview of the latest advances and techniques in this rapidly evolving field. By exploring the benefits and limitations of data-driven methodologies and presenting real-world applications, we hope to contribute to the ongoing discussion on the role of data-centric approaches in SHM. We believe that this book will be a valuable resource for researchers, practitioners, and students who are interested in the field of SHM and data-driven approaches. We thank all the contributors for their insightful contributions, and we hope that this book will inspire further research and innovation in this exciting area of study. As the editors of the Data-Centric Engineering series, we also invite and encourage scholars from all branches of engineering and sciences, who are active in this multi-disciplinary field, to contact us if they are interested in publishing edited volumes relevant to this theme in their fields of expertise.

Editors
March 2023

https://doi.org/10.1515/9783110791426-202

# Contents

# Editors’ short biography

**Prof. Mohammad Noori** is Professor of Mechanical Engineering at Cal Poly, San Luis Obispo, a Fellow and Life Member of the American Society of Mechanical Engineering, and a recipient of the Japan Society for Promotion of Science Fellowship. He also holds a visiting professorship position at the University of Leeds, UK. His work in non-linear random vibrations, especially hysteretic systems, seismic isolation, and the application of artificial intelligence methods for structural health monitoring is widely cited. He has authored over 300 refereed papers, including over 150 journal articles, has published 15 scientific books, 31 book chapters in archival volumes, has edited 15 technical books, and has been the Guest Editor of 15 journal volumes and proceedings. Prof. Noori was a co-founder of the National Institute of Aerospace, established through a $379 million 15-year NASA contract in partnership with NASA Langley Research Center. He has also received over $14 million in support of his research from NSF, ONR, National Sea Grant, and industry. He has supervised 24 post-doctoral, 26 PhD, and 53 MS projects. He has given over 100 keynotes and invited lectures. He is the founding executive editor of a scientific journal, serves on the editorial board, or as the associate editor, of over 15 other journals, and has been a member of the scientific committee of numerous conferences. He directed the Sensors Program at the National Science Foundation in 2014 and served as the scientific advisor for several organizations and technical firms. He was the dean of engineering at Cal Poly, and served as a Chaired professor and department head at NC State University and WPI and as the Chair of the national committee of mechanical engineering department heads. Noori has developed a unique online course, “How to Write an Effective Research Paper,” offered by Udemy.com, taken by over 9,000 students worldwide. Noori is an elected member of Sigma Xi, Pi Tau Sigma, Chi-Epsilon, and Sigma Mu Epsilon honorary research societies. In 1996 Noori was invited by President Clinton’s Special Commission on Critical Infrastructure Protection and presented a testimony as a national expert on that topic. Noori is the Founding Editor of Resilience and Sustainability in Civil, Mechanical, Aerospace, and Manufacturing Engineering Systems Series of CRC Press/Taylor and Francis.

**Prof. Fuh-Gwo Yuan** has been with Department of Mechanical and Aerospace Engineering, North Carolina State University since 1989. He is now a Full Professor. Since 2011, he serves as a Samuel P. Langley Professor at National Institute of Aerospace (NIA), Hampton, Virginia. He received his BS from Department of Engineering Science, National Cheng Kung University, Taiwan; MS and PhD from Department of Theoretical and Applied Mechanics, University of Illinois at Urbana-Champaign; and worked at Boeing Co., Air Force Research Laboratory, and NASA Langley Research Center. He is a Fellow of SPIE and American Society of Mechanical Engineering. His recent research includes structural health monitoring/management (SHM), non-destructive inspection (NDI), machine learning, multi-functional materials, nano/meso scale sensors, advanced computing tools with smart sensors, damage prognosis, and energy harvesting. His research areas cover smart materials applications, wireless sensor design, and energy harvesting. He has long-term interest in wavefield imaging for surface hidden damage by employing imaging algorithms in advanced structural materials. Recently, he has focused on non-contact full-field damage imaging using digital cameras together with physics-informed machine learning methods.

**Dr. Ehsan Noroozinejad Farsangi** currently holds multiple prestigious positions within the academic community, serving as both a Senior Researcher at UBC Smart Structures in Canada and a Tenured Faculty Member at the Graduate University of Advanced Technology in Iran. Additionally, he serves as an Adjunct Associate Professor at Southeast University in China, demonstrating his broad global reach and expertise. As the director of the Resilient Structures Research Group, which boasts a large team of esteemed international researchers, Dr. Noroozinejad has made significant contributions to the field of structural engineering. Furthermore, Dr. Noroozinejad’s extensive involvement in academic publishing is

https://doi.org/10.1515/9783110791426-204

impressive. He is the Founder and Chief Editor of the *International Journal of Earthquake and Impact Engineering*, as well as serving as an Associate Editor for the ASCE *Practice Periodical on Structural Design and Construction*, the IET *Journal of Engineering*, and the *Frontiers in Built Environment: Earthquake Engineering Section*. He also holds positions as the Editor of the *Journal of Reliability Engineering and Resilience* and the Engineering Editor of ASCE *Natural Hazards Review*. With over 120 high-impact journal papers in indexed journals and 6 books published with esteemed publishers in his area of expertise, Dr. Noroozinejad has established himself as a prolific and influential academic. His research interests span a wide range of topics, including smart structures, resilience-based design, reliability analysis, artificial intelligence, construction robotics, intelligent infrastructure, and digital twins in construction. His exceptional contributions to the field have been recognized with numerous national and international awards, including the prestigious Associate Editor Award in 2022 from the American Society of Civil Engineers (ASCE) in recognition of his consistent and exemplary service to enhance ASCE’s publication activities.

Julijana Bojadjieva*, Aleksandra Bogdanovic, Kemal Edip,
Vlatko Sheshov, Zoran Rakicevic, Ehsan Noroozinejad Farsangi,
Dejan Ivanovski, Antonio Shoklarovski, Irena Gjorgjeska,
Toni Kitanovski, Dejan Filipovski, Igor Markovski, Filip Manojlovski,
Angela Popovska, Nikola Naumovski

# 1 Seismic site investigation and structural amplification based on geotechnical and structural health monitoring

**Abstract:** The Ohrid region being one of the most beautiful regions in North Macedonia is also earthquake-prone and a couple of strong earthquakes in the past have caused great disasters. The strongest recorded earthquake was reported in February 1911, with

---

***Corresponding author: Julijana Bojadjieva**, Ss. Cyril and Methodius University in Skopje, Institute of Earthquake Engineering and Engineering Seismology-IZIIS, North Macedonia, e-mail: jule@iziis.ukim.edu.mk
Aleksandra Bogdanovic, Ss. Cyril and Methodius University in Skopje, Institute of Earthquake Engineering and Engineering Seismology-IZIIS, North Macedonia, e-mail: saska@iziis.ukim.edu.mk
**Kemal Edip**, Ss. Cyril and Methodius University in Skopje, Institute of Earthquake Engineering and Engineering Seismology-IZIIS, North Macedonia, e-mail: kemal@iziis.ukim.edu.mk
**Vlatko Sheshov**, Ss. Cyril and Methodius University in Skopje, Institute of Earthquake Engineering and Engineering Seismology-IZIIS, North Macedonia, e-mail: vlatko@iziis.ukim.edu.mk
**Zoran Rakicevic**, Ss. Cyril and Methodius University in Skopje, Institute of Earthquake Engineering and Engineering Seismology-IZIIS, North Macedonia, e-mail: zoran_r@iziis.ukim.edu.mk
**Ehsan Noroozinejad Farsangi**, The University of British Columbia, Vancouver, Canada, e-mail: ehsan.noroozinejad@ubc.ca
**Dejan Ivanovski**, Ss. Cyril and Methodius University in Skopje, Institute of Earthquake Engineering and Engineering Seismology-IZIIS, North Macedonia, e-mail: ivanovski@iziis.ukim.edu.mk
**Antonio Shoklarovski**, Ss. Cyril and Methodius University in Skopje, Institute of Earthquake Engineering and Engineering Seismology-IZIIS, North Macedonia, e-mail: antonio@iziis.ukim.edu.mk
**Irena Gjorgjeska**, Ss. Cyril and Methodius University in Skopje, Institute of Earthquake Engineering and Engineering Seismology-IZIIS, North Macedonia, e-mail: gj_irena@iziis.ukim.edu.mk
**Toni Kitanovski**, Ss. Cyril and Methodius University in Skopje, Institute of Earthquake Engineering and Engineering Seismology-IZIIS, North Macedonia, e-mail: tonik@iziis.ukim.edu.mk
**Dejan Filipovski**, Ss. Cyril and Methodius University in Skopje, Institute of Earthquake Engineering and Engineering Seismology-IZIIS, North Macedonia, e-mail: dejan@iziis.ukim.edu.mk
**Igor Markovski**, Ss. Cyril and Methodius University in Skopje, Institute of Earthquake Engineering and Engineering Seismology-IZIIS, North Macedonia, e-mail: igorm@iziis.ukim.edu.mk
**Filip Manojlovski**, Ss. Cyril and Methodius University in Skopje, Institute of Earthquake Engineering and Engineering Seismology-IZIIS, North Macedonia, e-mail: filipmanojlovski@iziis.ukim.edu.mk
**Angela Popovska**, Ss. Cyril and Methodius University in Skopje, Institute of Earthquake Engineering and Engineering Seismology-IZIIS, North Macedonia, e-mail: angela@iziis.ukim.edu.mk
**Nikola Naumovski**, Ss. Cyril and Methodius University in Skopje, Institute of Earthquake Engineering and Engineering Seismology-IZIIS, North Macedonia, e-mail: nikolan@iziis.ukim.edu.mk

https://doi.org/10.1515/9783110791426-001

a magnitude of 6.7 at a depth of 15 km [1]. In view of the high seismicity of the Ohrid region, almost all buildings are exposed to risk of a potential earthquake event. The demand for detailed inspections has been initiated in the 80s of the previous century, which has been a pioneering event in the Balkan regions. One of the sites is the Location Tower, which has been reestablished recently and enables real-time monitoring and recording of data. The Location Tower consists of a surface and three downhole instruments up to 125 meters down the bedrock; it is a nine-story building with two instruments installed on the 6th and 9th stories and four instruments installed at the foundation level. Several small to moderate earthquakes have been recorded during the period 2021–2022. Selected results and comparisons of equivalent analysis are presented in this work using real recorded acceleration data from the analyzed site. Based on a number of geophysical and geotechnical investigations, the soil profile of the location is obtained and evaluated both in situ and by laboratory tests. The obtained results present a promising starting point for further complex site response analysis considering both linearity and nonlinearity of the material models, which can be validated by stronger earthquakes in future.

## 1.1 Introduction

During an earthquake, ground motions subjected to local site conditions can be influenced significantly resulting in changes in the ground accelerations. Usually, large earthquakes can be followed by smaller aftershocks, which also influence the structural behavior but are not considered in the design codes. The site effects are mostly seen in the presence of sediments that have large effects on the amplitude of the seismic wave characteristics. The properties of soil deposits change in relation to the applied strain from earthquake forces, in which the shear modulus is reduced while the damping coefficient increases, thus making the behavior of soil deposit nonlinear. The change in the magnitude of input earthquake signal through the soil medium is usually annexed with site amplification factor. The evaluation of site amplification normally has two levels of earthquake ground motions mainly set to determine whether the seismic resistance is at a rational level, from the viewpoint of public safety. The selection of earthquakes to be used in the analysis of local site effects is also important due to the effects of the earthquakes on the overall attenuation of seismic force.

The destruction of structures and ground motions recorded in Mexico City since the 1985 Michoacan earthquake and in the San Francisco Bay Area from the 1989 Loma Prieta earthquake had promoted the need to study site effects. In addition, the effects of local ground conditions are of particular importance in seismic microzonation, seismic design of major facilities, and seismic safety evaluation of existing structures and implementation of preventive measures to reduce the seismic risk of existing facilities and urban areas, which are exposed to destructive ground motions.

During the seismic event, the time interval between the main events can be small in order to establish a complete structural evaluation. Here, the structural health monitoring plays an important role in predicting the behavior of the structure as a whole and its special elements, subject to earthquake ground motions. Important characteristics of earthquake ground motions are its intensity, duration, and frequency contents, which are subject to local site conditions [2]. Local soil and geological site conditions can cause changes in amplitudes, spectral content, and duration of strong earthquake ground motions, which result in damage of structures on the surface. Although different models might be adopted for definition of geological site conditions, the upper top layers have the greatest role in determining the ground motions. The general approach for representing the site conditions has been modified from linear wave motion including the transfer functions [3] to those associated with earthquake source, spreading path, site effects, and amplification based on topology of the soil medium. As given in the work of Stanko [4], one-dimensional equivalent linear site response analysis tools are commonly used to estimate the site-specific ground response in which recorded or simulated earthquake time histories are used. In the work of Di Fiore [5], the topographic irregularities are shown as important factors for seismic amplification in assessment of seismic site effects. The existing empirical methods and new techniques for seismic microzoning, based on experience from damage of the structures in the past earthquakes and consideration of local site conditions determined from the studies of microtremors and small earthquakes, are hardly reliable methods for evaluation of the seismic design parameters. Verification is ultimately needed for the possibility of extrapolation of small records to predict local soil behavior and site effects in the case of strong earthquake motions, as well as to verify laboratory techniques for elaboration of dynamic soil properties under high strain levels. This triggers the purpose for obtaining seismic records from different locations and levels of excitation sources in order to validate the available empirical analysis methods. In the past decades, the site amplification effects have obtained the attention of scientists in order to determine the process of wave propagation through soil and layered medium situated on rigid rocks. The effects of attenuation of stress waves are considered to be important because of the fact that the soft deposits fortify the ground's motions.

The analysis of the local site effects has its roots back in 80s when a three-dimensional seismic network was established in the Ohrid Lake basin [6] with the support of USGS (United States Geological Survey). These analyses also considered the sedimentary basins of the Ohrid Lake, which can significantly amplify the earthquake ground motion. Similar analyses have been done in Mexico City during the Michoacan earthquake, 1985 and in the South Bay of San Francisco during the Loma Prieta Event, 1989 [7]. Ground motion simulations and their amplifications in soil media even for simplified source implementations such as plane waves have shown significant basin effects.

In this work, the focus of the analysis was to observe the modification of strong ground motions and dynamic response of structural systems combining a three-dimensional seismic network in the Ohrid Lake basin. As given in the work of Dimitriu [8], considerable efforts have been made at the Euro-Seistest strong motion array at Volvi, near Thessaloniki, Greece where a data set covered a wide range of magnitudes. The analyzed case of 3D strong motion array consists of three free field sites with one surface and three downhole instruments each, 125 meters down the bedrock; a nine-story building site with two instruments installed on the building, four instruments installed at the foundation level and one outcropping rock site with one instrument (Location Tower). The extensive recent activities allow real- time recording and health monitoring processes to be enabled at the location. In this work, the main focus is on the site response analysis of the soil profile at the Location Tower in comparison to real acceleration records from different depths at the location.

## 1.2 Site location, soil profile, and structural characteristics

### 1.2.1 Description of the site location

The chosen location represents a commercial building within the city of Ohrid, the so-called "Tower location." Ohrid region represents an active seismic region with large earthquakes, which have nearly covered the seismic zone in the past decades, often with magnitudes greater than six ($M > 6$). In the distant past, there are confirmations of multiple earthquakes, like in 1906, Ohrid $M_L = 6.00$ and in 1911, Ohrid, $M_L = 6.7$. In the recent past, as in 2016, an earthquake with magnitude of around 5 according to the European MSC scale was felt. The epicenter of the earthquake was 12 km northeast of the city and caused considerable damage to older structures, more importantly to ones from cultural heritage. This proved the gap between scientific investigations and engineering practice. In multiple previous studies performed by UKIM-IZIIS [6] for the city of Ohrid, it has been proved that geological conditions in combination with certain intensity of seismic exposure could rise to some geotechnically associated hazards. This is especially important in the regions with significant engineering structures, where these hazards can have an unfavorable effect leading to total damage of structures.

From the latest seismic hazard map of North Macedonia [11], which is prepared according to the Eurocodes (PGA) guidelines, the city of Ohrid is placed in a zone of moderate to high seismicity, with PGA of 0.3 g at bedrock, in the case of a return period of 475 years. The city is settled along the Ohrid lake watershed area, which is characterized by provoking geotechnical conditions:

1. Surface quaternary and deep pliocene sediments.
2. Surface quaternary sediments consisting of fine gravel and sand as well as organic clays and sand down to depth of 20 m.
3. Heterogeneous nature characterized by unfavorable physical-mechanical characteristics. The underground water level is commonly high.

### 1.2.2 Soil profile

The geotechnical characteristics of the site were defined from data from previous investigations as well as data from additionally performed geophysical and geotechnical studies and georadar measurements. Combinations of different methods, seismic refraction, MASW, and HVSR were used to determine the results and from then describe a seismic section to a depth of 150 m. The local discontinuity and deformation in the terrain were defined using the same investigations. This defined section was used to construct analytical models where five lithological media were characterized from the different physically-mechanical characteristics.

The following lithological media are distinguished:

- A surface layer of dusty, sandy, and clayey with seismic velocity values of Vs = 150–200 m/s
- Subsurface layer of clay, dust, and sand with seismic velocity values of Vs = 200–400 m/s
- More compact quaternary sediments with seismic velocity values in the range of Vs = 400–600 m/s
- Pliocene sediments with seismic velocity values in the range of Vs = 650–800 m/s
- Terrain bedrock and Paleozoic shales with seismic velocity values of Vs > 1,000 m/s

From the analysis of data of the newly performed CPT (cone penetration tests), SPT (standard penetration tests), and from the aspects of the lithological composition of the terrain, strength, and deformability characteristics, it can be concluded that the soil in the investigated location is characterized by variable geomechanical characteristics. The lithological structure consists of alternating occurrence of silty clays with fine gravel and clayey silt that are moderately plastic, both with variable thickness of layers. The penetration resistance of silty parts ranging within the limits of qc = (0.5–1.2) MPa was obtained and the corrected number of SPT blows is N60 = 4, whereas those of the sandy and fine gravel parts are in the limits of qc = (6.0–10.0) MPa with N60 = 14. From the extensive soil investigation, the Vs soil profile is presented in Figure 1.1.

### 1.2.3 Structural characteristics

The building is residential, where the ground floor is intended for business while the floors above are designed for housing premises. It has an approximately square shape, with dimensions 24.0 × 24.4 m (Figure 1.2) and has eleven levels: ground floor, mezzanine, first floor, second floor, third floor, fourth floor, fifth floor, sixth floor, seventh floor, eighth floor, and attic. The ground floor has a height of $H = 3.84$ m, the mezzanine is with a height of $H = 2.60$ m, while the other floors have an equal height of $H = 2.88$ m. The structure is a mixed reinforced concrete structural system with square and rectangular columns, which start from the ground floor with larger cross-

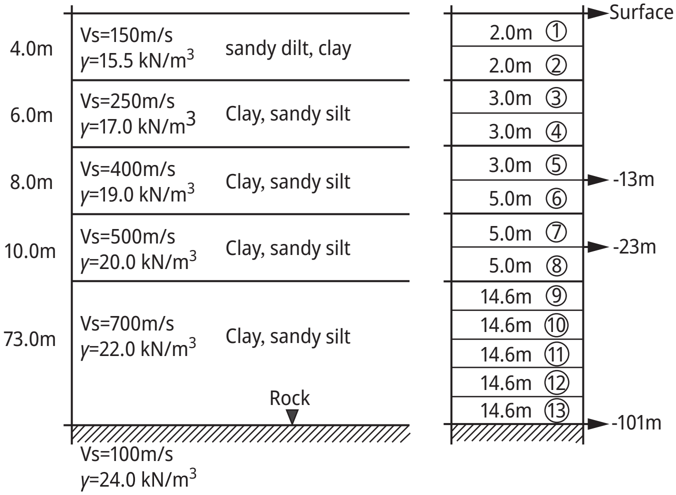

**Figure 1.1:** Shear wave velocity Vs (m/s) profile for analysis of the local site effects.

sections, gradually decreasing to the higher floors. Pile foundation is used through single foundations connected to each other by foundation beams in both orthogonal directions.

For obtaining the dynamic characteristics, ambient vibration method was used as given in Figure 1.3.

The results from the transformed records from all tests are shown in Figure 1.4, which displays the mode shapes for the corresponding natural frequencies of vibration. In Table 1.1, the natural frequencies and the damping in the corresponding modes are given.

Table 1.1 contains information on the dominant frequencies of the structure obtained from a mathematical model, while Table 1.2 shows the values of natural frequencies measured in 1985 as given in the work of Petrovski [6]. When compared, Tables 1.1 and 1.2 show that there is no significant change of frequency and hence no significant change in stiffness of the structure. A slight decrease of frequency, that is, 8% in $y$-direction and 6% in $x$-direction is observed.

In defining the mathematical model, SAP2000 software was used for the analysis and analytical modelling of the tested structure. Modelling of the structural elements was done in accordance with the existing (available) formwork plans and reinforcement details. The columns and the beams were modelled as “frame” elements, whereas the walls and the slabs were modelled as “shell” elements. The linear structural elements were divided into finite elements by use of the “auto frame mesh – intermediate joints” function, whereas the 2D elements were divided into finite elements of 50 cm by use of the “automatic area mesh” function. The structure is fixed to the base, by which its motion is prevented in all directions.

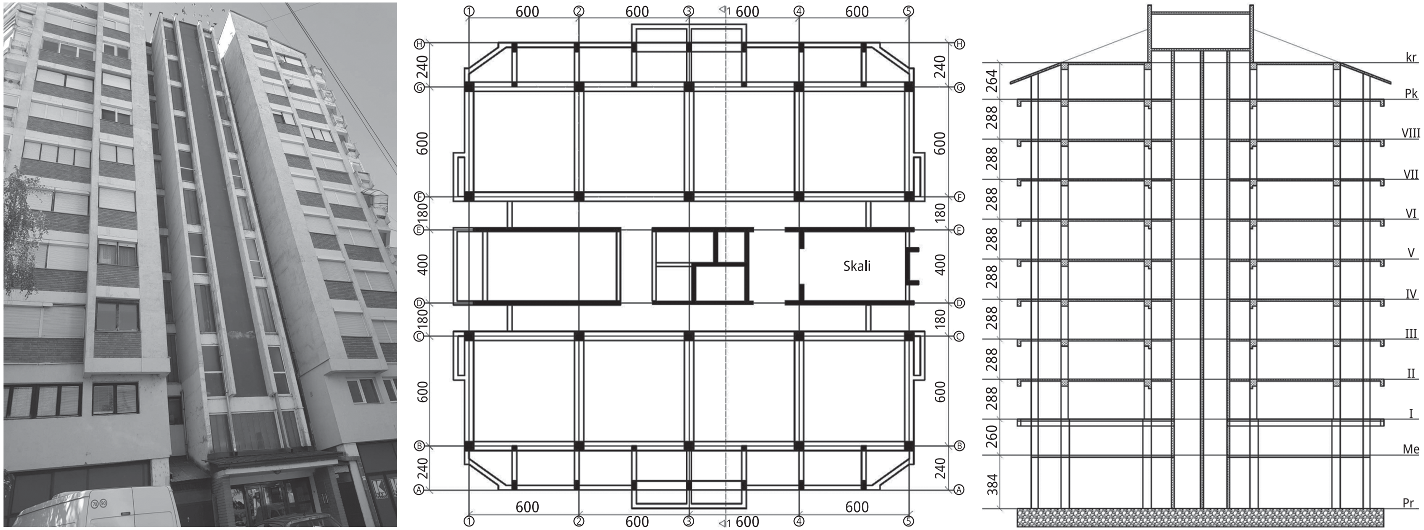

Figure 1.2: Building structure – tower; base and cross-section.

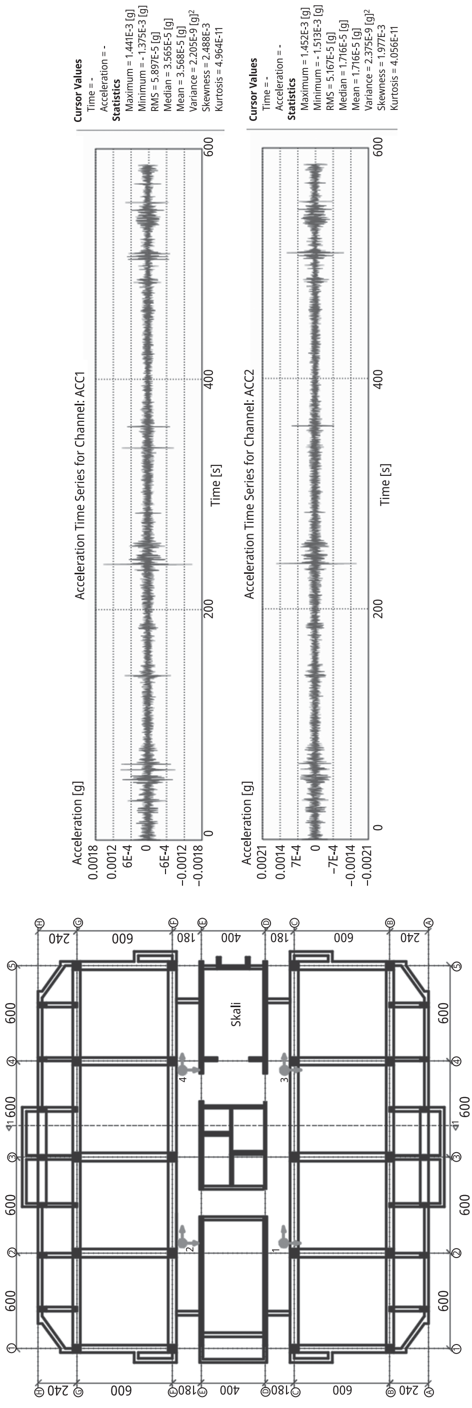

**Figure 1.3:** Records of time histories of acceleration (right) taken by accelerometers 1 and 2 during the first test, attic level (left).

**Table 1.1:** Values of natural frequencies.

| Frequency (Hz) | Damping (%) | Complexity (%) | Description |
|---|---:|---:|---|
| 1.59 | 2.98 | 0.76 | First mode of vibration in transverse direction *X* |
| 1.80 | 0.00 | 16.20 | Torsion |
| 1.93 | 2.48 | 0.28 | First mode of vibration in longitudinal direction *Y* |
| 5.01 | 2.93 | 3.76 | Second mode of vibration in transverse direction *X* |
| 8.45 | 0.00 | 23.65 | Second mode of vibration in longitudinal direction *Y* |

**Table 1.2:** Values of natural frequencies, measurements done 1985.

| Direction | Frequencies (Hz) | | | | Damping (%) |
|---|---|---|---|---|---:|
| | **f1** | **f2** | **f3** | **f4** | **f1** |
| P1 | 2.08 | 2.72 | 3.52 | 6.56 | 3.90 |
| P2 | 1.76 | 2.64 | | 6.56 | 3.70 |
| Torsion | 2.00 | 2.32 | | 6.64 | 3.60 |

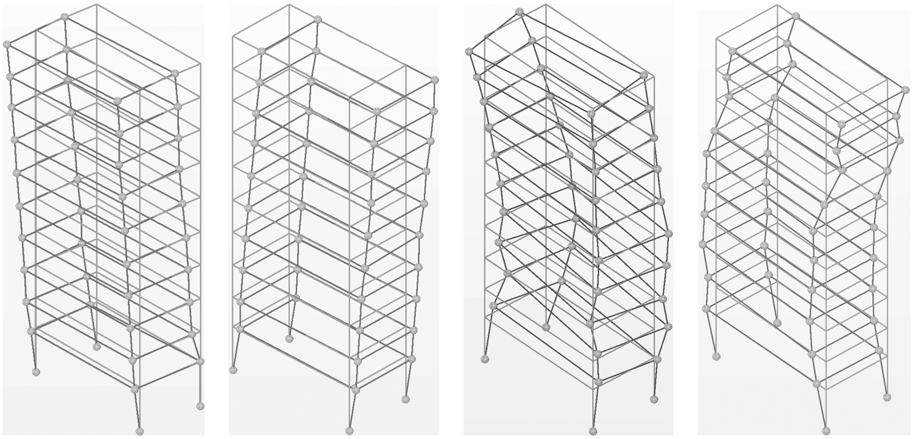

First mode of vibration in transverse direction X (f=1.59Hz)

First mode of vibration in longitudinal direction Y  (f=1.93Hz)

Second mode of vibration in transverse direction X (f=5.01Hz)

Second mode of vibration in longitudinal direction Y(f=1.59Hz)

**Figure 1.4:** Mode shapes for the corresponding natural frequencies of vibration.

There is a difference in the frequency in the *Y*-direction obtained from the analytical model, which is expected, since the loads used for the analytical model correspond to those in the structural project. Taking into account that the building has been exposed to undergoing changes in the course of its serviceability period for which there is no document and that soil-structure interaction is also not taken into

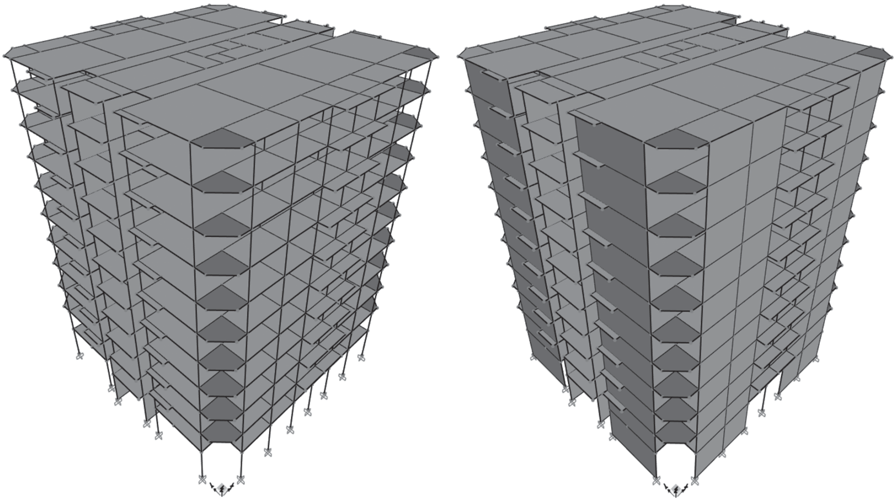

**Figure 1.5:** Analytical model from SAP2000.

**Table 1.3:** Dynamic characteristics of the “fitted” model (SAP2000 output).

| **Output case** | **Step type** | **Step num** | **Period** | **Frequency** | **Circ freq** | **Eigen value** |
|---|---|---|---|---|---|---|
| **Text** | **Text** | **Unitless** | **Sec** | **Cyc/s** | **rad/s** | **$rad^2/s^2$** |
| MODAL | Mode | 1 | 0.62 | 1.590 | 9.99 | 99.85 |
| MODAL | Mode | 2 | 0.55 | 1.814 | 11.40 | 129.99 |
| MODAL | Mode | 3 | 0.43 | 2.315 | 14.55 | 211.72 |

**Table 1.4:** Comparison of dynamic characteristics.

| | ***Y*-direction** | ***X*-direction** |
|---|---|---|
| Measurement 1985 | 2.08 | 1.76 |
| Measurement 2021 | 1.90 | 1.59 |
| SAP2000 | 2.31 | 1.59 |

account in the model, it has been defined that the analytical model shows the behavior of the structure in real conditions well, that is, there is good correlation between the experimental and the analytical results see Figure (1.5) and Table (1.3 and 1.4).

## 1.3 Seismic instrumentation

### 1.3.1 Instrumentation at the site

The Location Tower from the 3D strong motion array consists of one surface and three downhole instruments each, 125 meters down the bedrock; a nine-story building with two instruments installed in the building, on the 6th and 9th stories, and four instruments installed at the foundation level. The number and the depth of the instruments at the locations are presented in Figure 1.6.

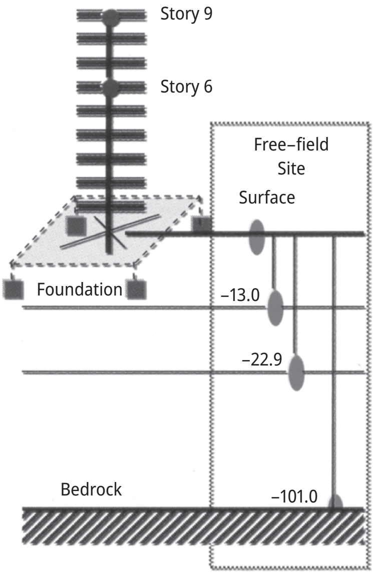

| Instrumentation | Location – 1-Tower in situ laboratory |
|---|---|
| Site type | Instrumented building |
| Instruments on the building structure | 2 (6th and 9th story) |
| Instruments at the level of the foundation structure | 4 |
| Instruments on soil surface | 1 |
| Instruments in soil profile | 2 (13.0 m, 22.9 m) |
| Instruments at bedrock | 1 (101 m) |
| Total number of instruments | 10 |

**Figure 1.6:** Instruments setup and depth at the Location Tower.

### 1.3.2 Obtained records from small to moderate earthquakes

During planning and installation of the Ohrid Lake Seismic Network in the late 70s, the entire network was composed of the most advanced instruments produced by Kinemetrics Inc., Pasadena, California. However, the analogue recording system could not be maintained in the last decade and there was no possibility of recording real time earthquake events. The time period 2020–2021 was the beginning of extensive revitalization of the network [9]. Replacement of the recording system by an analogue-digital conversion device, which enables real-time recording of earthquake events and thus structural and health monitoring at the Location Tower was realized. Since March 2021, several small to moderate earthquake events have proven the functionality of the installed instruments and have provided important data for further investigation at the location. Selected recorded earthquakes are analyzed in this paper, which are given in Table 1.5. The presented registrations are used in simple 1-dimensional linear equivalent site response analysis and are presented in the next chapter. It is worth noting that three directions are recorded with three channels, and for the analysis, one horizontal acceleration per earthquake was used.

**Table 1.5:** Selected registered earthquakes with the monitoring system at the Location Tower.

| | **Date of registered earthquakes** | **Richter Magnitude** | **Epicenter** |
|---|---|---|---|
| EQ1 | 09 January 23:38 Pm (UTC) 2022 | **4.0** | **Bitola, Macedonia, 8 km southeast of Bistrica, Macedonia*** |
| EQ2 | 11 January 17:01 Pm (UTC) 2022 | **3.5** | **Florina, West Macedonia, Greece*** |
| EQ3 | 11 January 17:44 Pm (UTC) 2022 | **4.5** | **Florina, West Macedonia, Greece*** |
| EQ4 | 12 January 03:01 Am (UTC) 2022 | **3.6** | **Florina, West Macedonia, Greece*** |
| EQ5 | 22 April 21:07 (UTC) 2022 | **5.7** | **42 km SE of Mostar, Bosnia and Herzegovina** |
| EQ6 | 15 January 21:37 (UTC) 2023 | **4.8** | **4 km NE of Tirana, Albania** |

*These quakes were likely an aftershock of the 5.3 quake West Macedonia, Greece, Jan 9, 2022 11:43 pm (GMT + 2).

## 1.4 Seismic site amplification analysis

The soil conditions can significantly influence the amplitude and the frequency of the bedrock motion from earthquakes. Depending on the characteristics of the local geotechnical conditions and the characteristics of excitation at the level of the seismic bedrock, these effects can be greater or lesser, making the soil profile advantageous or disadvantageous for the structures to be built on the site.

The effect of the local soil conditions is expressed through variation of the amplitude–frequency characteristics of ground motion upon the surface in respect to the corresponding excitation at the level of the seismic bedrock.

In this work, the analyses are performed by application of the method of vertical propagation of shear seismic waves through a linear viscoelastic system based on the solution of the Kanai wave equation. The procedure of definition of the nonlinear effects in soil resulting from seismic effects includes an approach that uses the equivalent linear characteristics of soil, developed by Seed and Idriss. The analyses were performed by using the SHAKE2000 software [10]. The calculation model, which is presented in Figure 1.1, is analyzed using the selected acceleration records given in Table 1.5 using the methodology as given in the work of other authors [11–15].

The effect of the local medium was evaluated based on the analysis of the dynamic response of the mathematical model. This analysis enabled definition of the peak accelerations along the depth of the model as well as the response spectra of the models for the surface level. With the analyses of the local soil effects, the mean periods of natural vibration of 0.63–0.65 s were obtained for the real recorded acceleration level (without scaling) corresponding to low level of deformations. Figure 1.7 and Table 1.6 show the variation of peak accelerations along the depth of the models obtained by convolution of selected accelerograms, for real recorded input acceleration of $a_{\max}$ between 0.0027 and 0.0069 g.

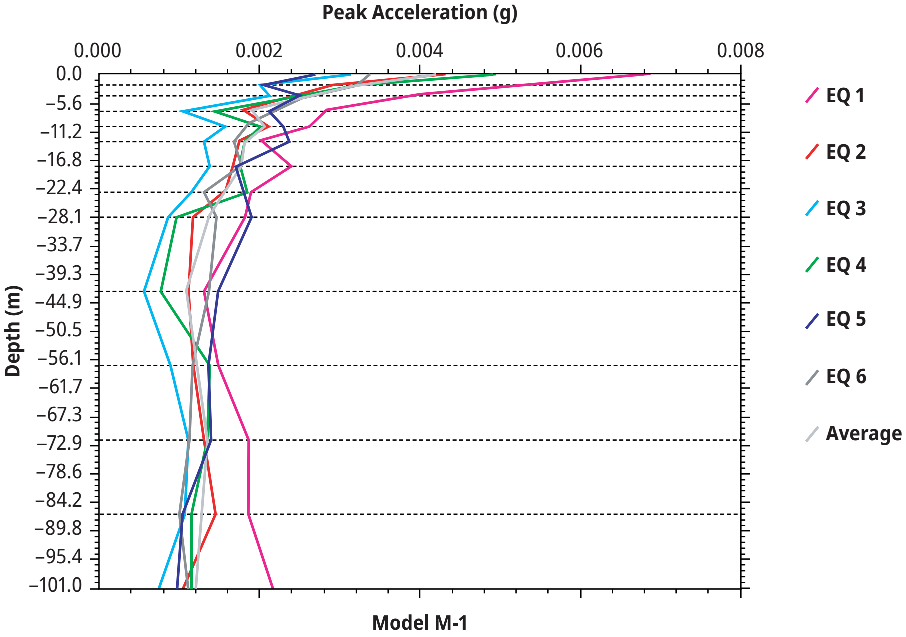

**Figure 1.7:** Peak accelerations along depth for real recorded acceleration response of the soil column.

Figure 1.8 shows the spectra for each of the selected time histories of acceleration, for damping of $D = 5\%$, for both levels of bedrock −101 m (left) and the surface level 0.0 m (right), along with the mean value from all the analyses. From the obtained spectra, it is clear that the dominant amplitudes occur in the period range of 0.4–1.0 s. The diagrams show that the surface layers considerably amplify the earthquake effect, which is the result of the low strength characteristics of the soil in these layers.

**Table 1.6:** Calculated peak accelerations along depth, periods of the soil column, and dynamic amplification factor $(DAF)_{mean}$.

| **Depth** | **Maximum acceleration** | | | | | | |
|---|---|---|---|---|---|---|---|
| | **EQ 1: Florina 11.01.2022 (M4.0)** | **EQ 2: Bitola 09.01.2022 (M4.0)** | **EQ 3: Florina 12.01.2022 (M3.6)** | **EQ 4: Florina 11.01.2022 (M3.5)** | **EQ 5: B&H 22.04.2022 (M5.7)** | **EQ 6: Albania 15.01.2023 (M4.8)** | **Average acc. $a_{max}$ (g)** |
| 0 | 0.0069 | 0.0043 | 0.0033 | 0.0050 | 0.0027 | 0.0034 | 0.0043 |
| −4.0 | 0.0040 | 0.0027 | 0.0021 | 0.0023 | 0.0025 | 0.0026 | 0.0027 |
| −10.0 | 0.00264 | 0.0021 | 0.0016 | 0.0020 | 0.0023 | 0.0019 | 0.0021 |
| −13.0 | 0.0020 | 0.0018 | 0.0013 | 0.0018 | 0.0024 | 0.0017 | 0.0018 |
| −18.0 | 0.0024 | 0.0017 | 0.0014 | 0.0017 | 0.0017 | 0.0017 | 0.0018 |
| −23.0 | 0.0019 | 0.0016 | 0.0011 | 0.0018 | 0.0018 | 0.0013 | 0.0016 |
| −57.20 | 0.0015 | 0.0012 | 0.0014 | 0.0013 | 0.0013 | 0.0019 | 0.0014 |
| −101.0 | 0.0024 | 0.0017 | 0.0015 | 0.0019 | 0.0018 | 0.0016 | 0.0018 |
| DAF (0/−101) | 2.88 | 2.53 | 2.20 | 2.63 | 1.50 | 2.13 | 2.31 |
| DA (−4/−101) | 1.67 | 1.59 | 1.40 | 1.21 | 1.39 | 1.63 | 1.48 |
| Period (s) | 0.66 | 0.64 | 0.63 | 0.64 | 0.66 | 0.65 | Average period: 0.65 s |

Figures 1.9 and 1.10 represent the average computed acceleration time history on the left and the real recorded acceleration time history from instruments on the right for the level of 101.0 m and the surface level 0.0 m for EQ1. The graphs are compatible, and it can be concluded that the modelled soil profile represents the real amplification characteristics of the location. Figures 1.11 and 1.12 represent the average computed acceleration time history on the left and the real recorded acceleration time history from instruments on the right for the level of 101.0 m and the surface level 0.0 m for the earthquake records.

Calculated acceleration records at the same depths where recorded acceleration records were available were compared and results presented in Table 1.7. The obtained dynamic amplification factor is presented in Table 1.8.

The differences between the values show that the newly installed instruments are operating correctly. Moreover, the numerical analysis from SHAKE software is in good correlation with the values, showing that the design of the mathematical model is successful.

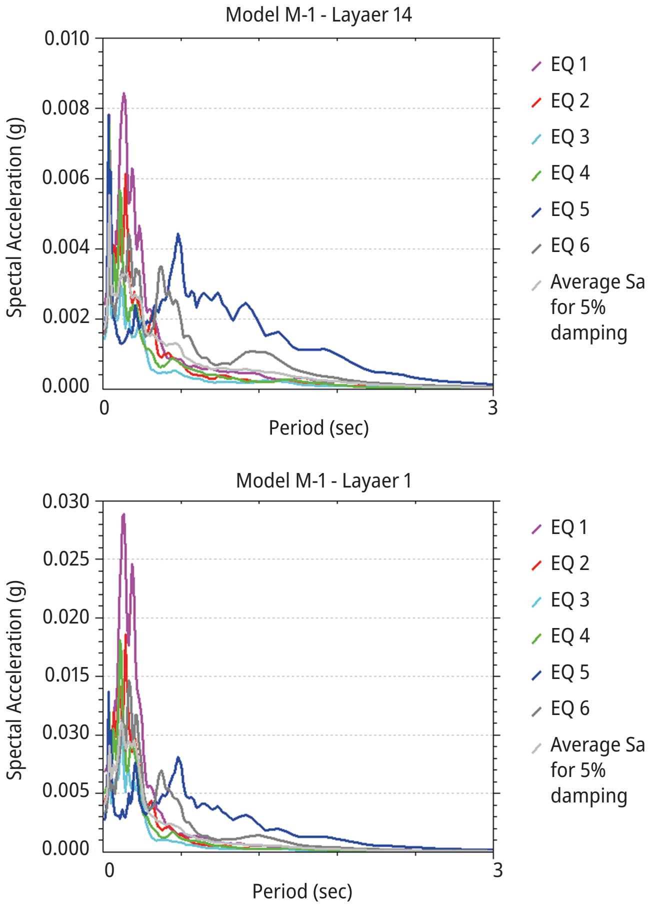

**Figure 1.8:** Spectral acceleration for 5% damping at level −101.0 m (above) and at surface 0.0 m (below).

## 1.5 Seismic structural amplification analysis

For numerical analysis in SAP2000, as an input, accelerations time histories from the recorded accelerations for selected recent earthquakes on the ground floor (0th foundation) are used. Peak ground accelerations (PGA) for the chosen earthquakes are given in Table 1.9.

As can be seen from Figures 1.13 to 1.18 the numerically obtained acceleration time histories and the real recorded acceleration time histories from instrument at the 9th story are in good accordance. From the obtained measurements, it can be seen that the values are similar and thus the accuracy of the model can be confirmed. The slight difference is due to the simulations of soil medium, which is not included in the numerical modelling but is present in the in situ conditions.

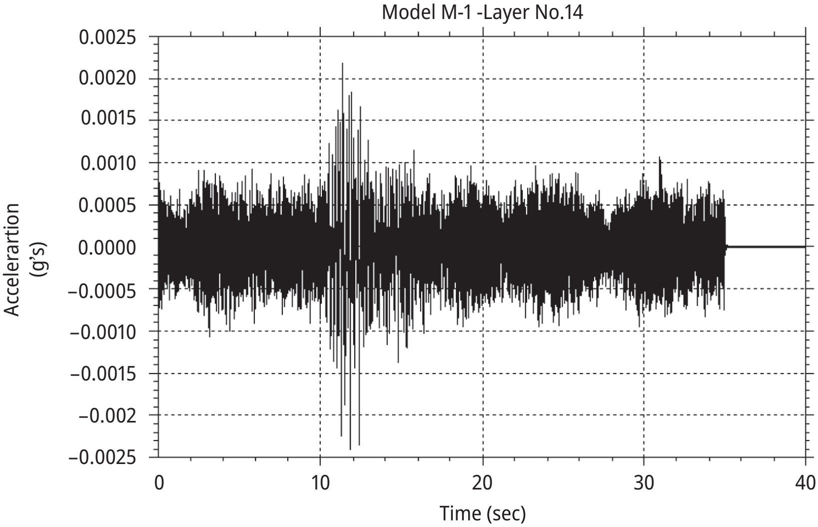

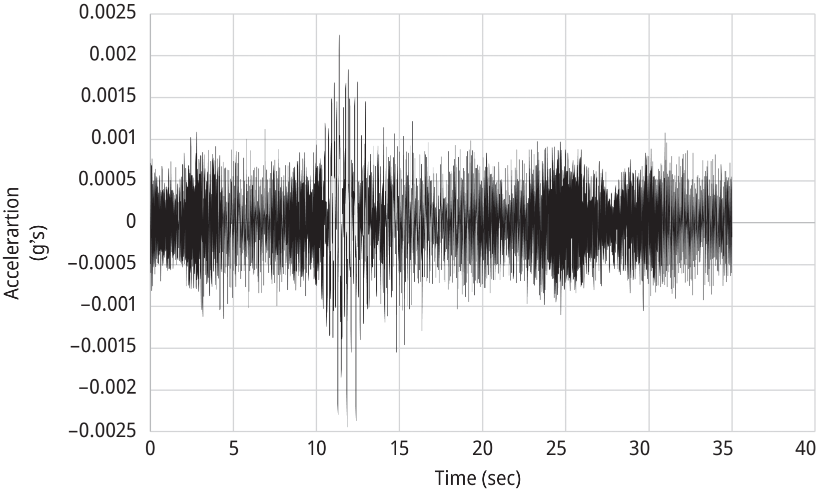

**Figure 1.9:** Computed acceleration time history (above) and the recorded acceleration time history (below) for the depth of −101.0 m – EQ1.

The tables present the values of PGAs of the numerically obtained and measured different earthquakes respectively. The difference in the percentage is given in Table 1.12 and it can be seen that it is different depending on the earthquake records, 37% for the EQ1, 26% for EQ2, 33% for EQ3, and so on. It must be mentioned that the difference is notable because of the soil-structure interaction present in the real structure but not present during the numerical modeling.

When comparing the DAF between the foundation level and the 9th floor it can be said that the amplitude of the amplification is observed clearly as given in

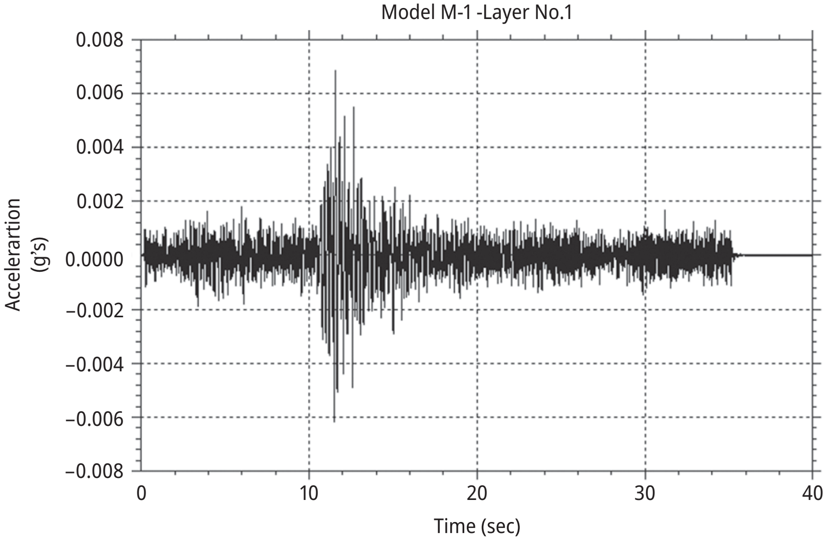

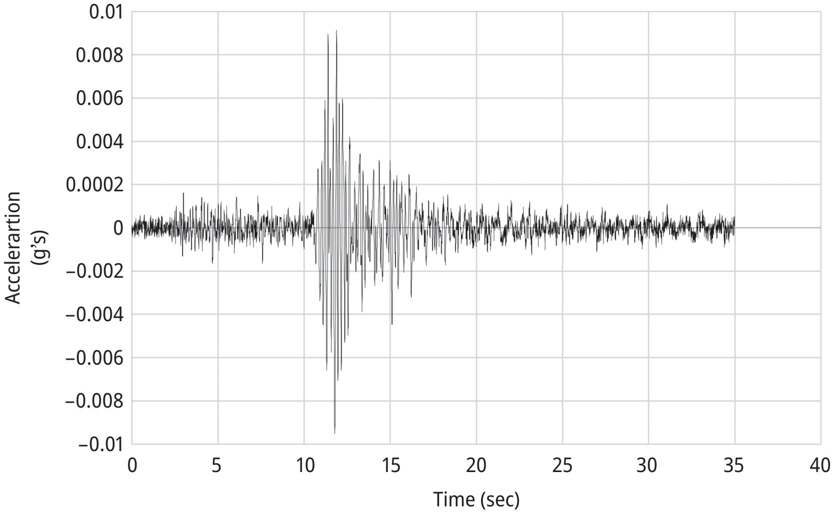

**Figure 1.10:** Computed acceleration time history (above) and the recorded acceleration time history (below) for the surface 0.0 m – EQ1.

Table 1.13. The DAF for the recorded time histories is in the range of 1.4 to 3.8, while for the numerical model the DAF varies between 2.1 to 2.9. This is mainly because of the fact that the numerical model needs improvement in the simulation of soil medium, which will be presented in the next papers from the same group of authors.

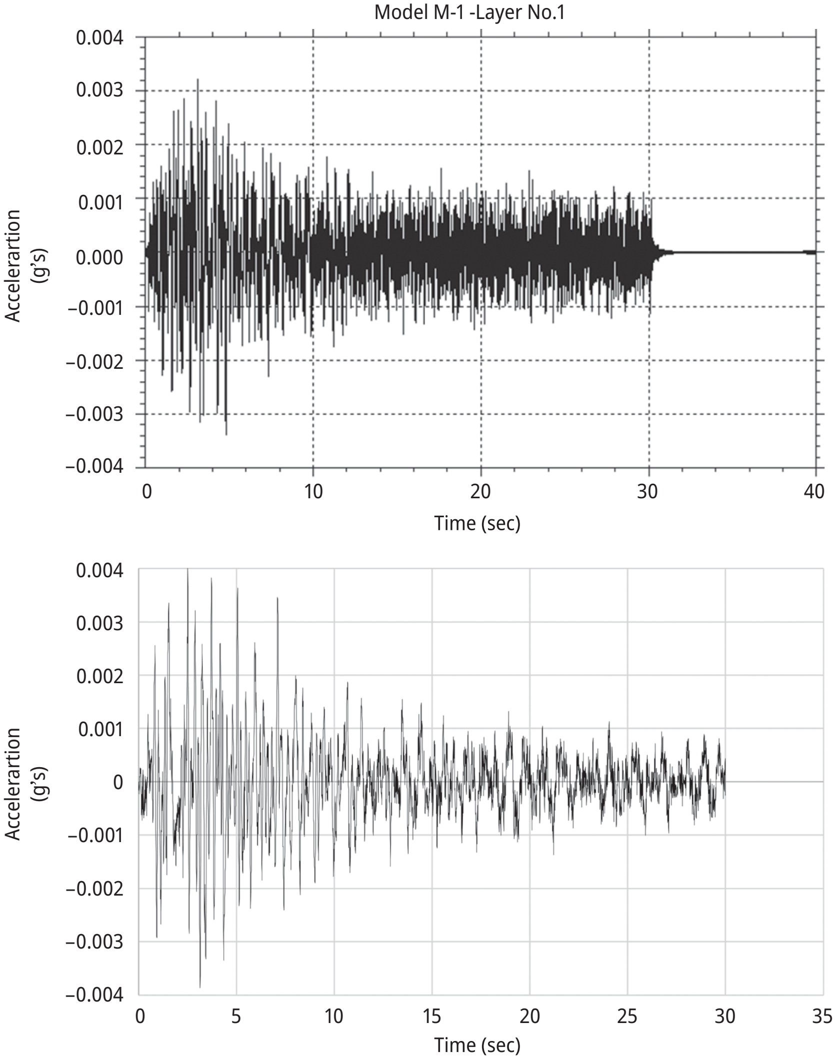

**Figure 1.11:** Computed acceleration time history (above) and the recorded acceleration time history (below) for the surface 0.0 m – (EQ 6).

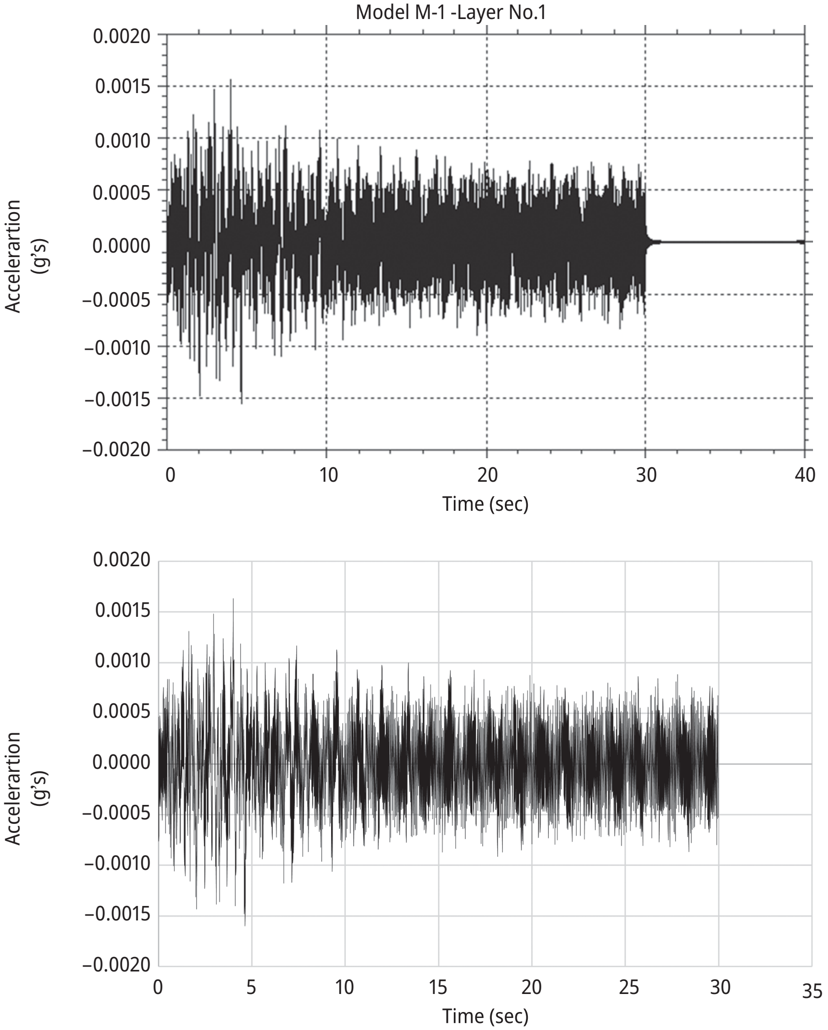

**Figure 1.12:** Computed acceleration time history (above) and the recorded acceleration time history (below) for the depth of −101.0 m – (EQ 6).

**Table 1.7:** Difference in percentage of the recorded acceleration versus the calculated for each depth.

| Depth | Recorded acceleration (g) | | | | | | | |
|---|---|---|---|---|---|---|---|---|
| | **EQ 1: Florina 11.01.2022 (M4.0)** | **EQ 2: Bitola 09.01.2022 (M4.0)** | **EQ 3: Florina 12.01.2022 (M3.6)** | **EQ 4: Florina 11.01.2022 (M3.5)** | **EQ 5: B&H 22.04.2022 (M5.7)** | **EQ 6: Albania 15.01.2023 (M4.8)** | **Average acc. $a_{max}$ (g)** | **Difference with calculation (%)** |
| 0 | **0.0095** | **0.0055** | **0.0024** | **0.0035** | **0.0036** | **0.0040** | **0.0048** | **11.6** |
| −13.0 | **0.0021** | **0.0021** | **0.0012** | **0.0022** | **0.0030** | **0.0030** | **0.0023** | **27.7** |
| −23.0 | **0.0039** | **0.0016** | **0.0011** | **0.0015** | **0.0027** | **0.0016** | **0.0021** | **31.3** |
| −101.0 | **0.0024** | **0.0017** | **0.0015** | **0.0019** | **0.0018** | **0.0016** | **0.0018** | **/** |

**Table 1.8:** Dynamic amplification factor for each depth in respect to the seismic bedrock, calculated versus recorded.

| Depth (m) | DAF (calculated) | DAF (recorded acc.) |
|---|---:|---:|
| 0.0 | **2.31** | **2.52** |
| − 13.0 | **1.02** | **1.27** |
| − 22.9 | **0.87** | **1.10** |
| − 101.0 | **1** | **1** |

**Table 1.9:** Input peak ground acceleration (PGA).

| Story | Input acceleration (PGA) [g] | | | | | |
|---|---:|---:|---:|---:|---:|---:|
| | **EQ 1: Florina 11.01.2022 (M4.0)** | **EQ 2: Bitola 09.01.2022 (M4.0)** | **EQ 3: Florina 12.01.2022 (M3.6)** | **EQ 4: Florina 11.01.2022 (M3.5)** | **EQ 5: B&H 22.04.2022 (M5.7)** | **EQ 6: Tirana 15.01.2023 (M4.8)** |
| 0th (foundation) | 0.0394 | 0.0278 | 0.0219 | 0.0311 | 0.0426 | 0.068 |

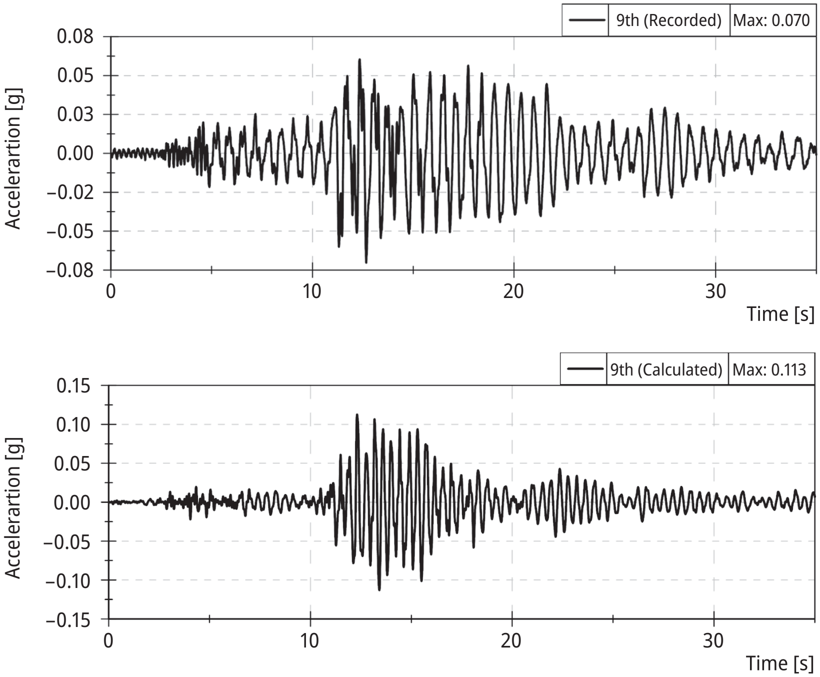

**Figure 1.13:** Recorded acceleration time history (above) and analytically obtained acceleration time history (below) for the 9th story – EQ1.

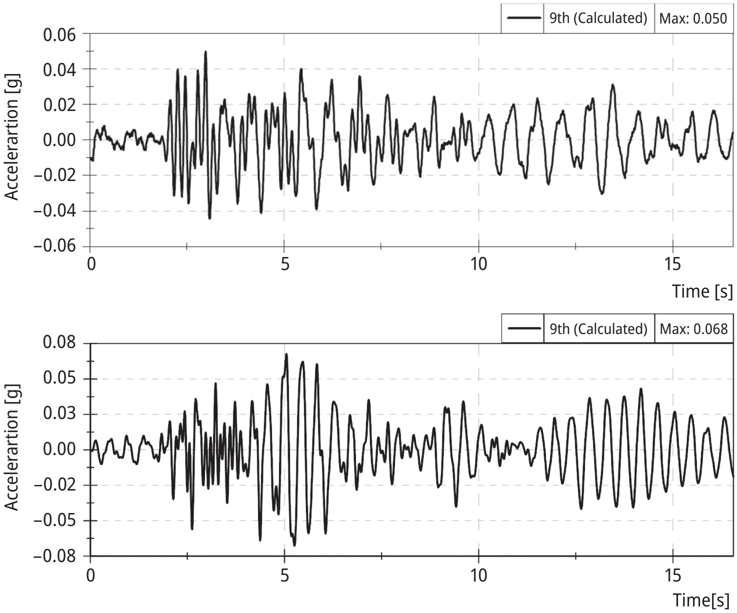

**Figure 1.14:** Recorded acceleration time history (above) and analytically obtained acceleration time history (below) for the 9th story – EQ2.

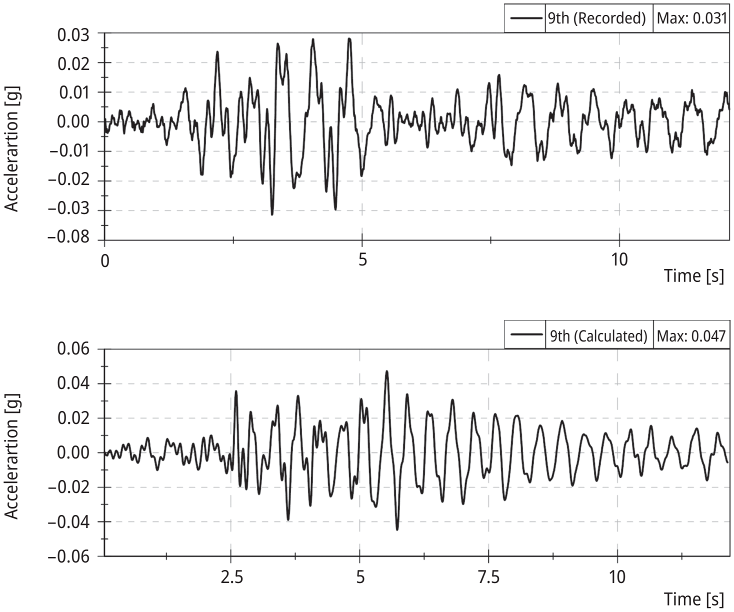

**Figure 1.15:** Recorded acceleration time history (above) and analytically obtained acceleration time history (below) for the 9th story – EQ3.

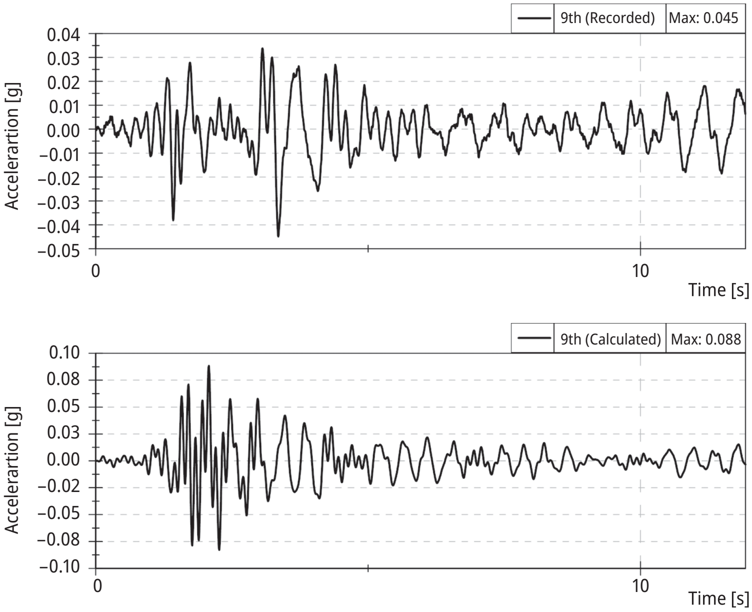

**Figure 1.16:** Recorded acceleration time history (above) and analytically obtained acceleration time history (below) for the 9th story – EQ4.

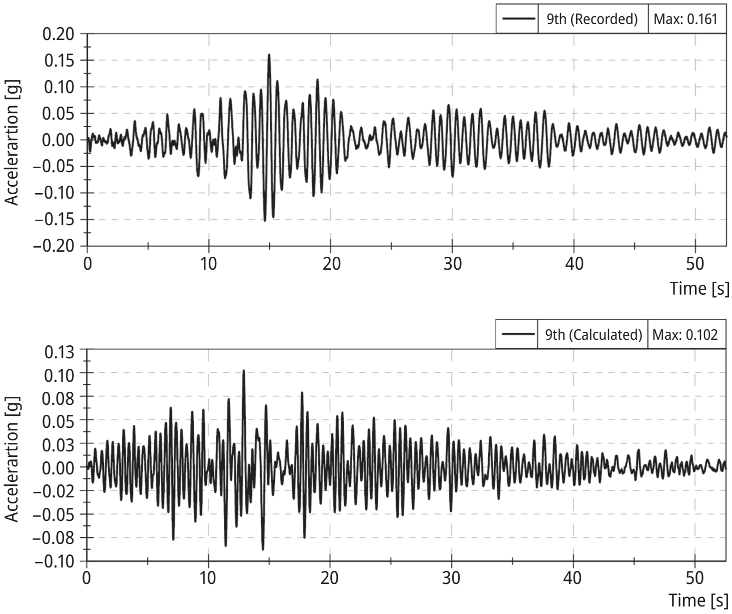

**Figure 1.17:** Recorded acceleration time history (above) and analytically obtained acceleration time history (below) for the 9th story – EQ5.

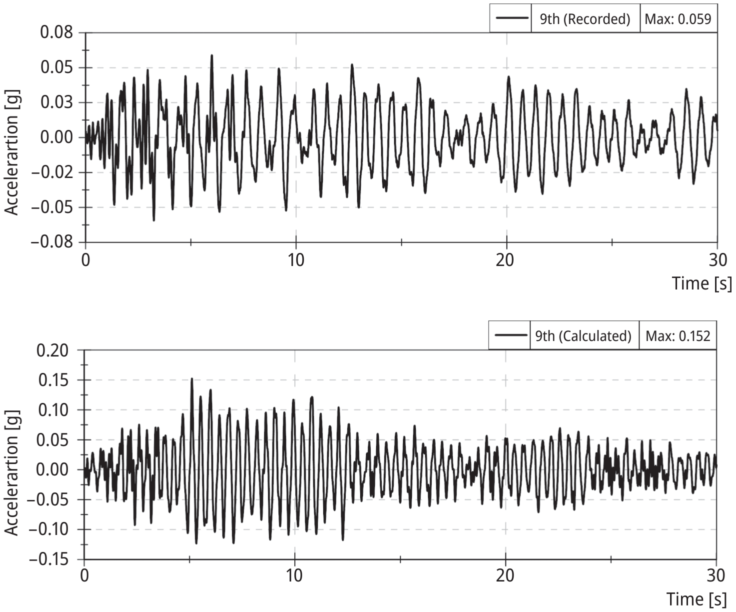

**Figure 1.18:** Recorded acceleration time history (above) and analytically obtained acceleration time history (below) for the 9th story – EQ6.

**Table 1.10:** Numerically obtained peak ground accelerations (PGA).

| Story | Numerically obtained PGA (g)-SAP2000 | | | | | |
|---|---|---|---|---|---|---|
| | **EQ 1: Florina 11.01.2022 (M4.0)** | **EQ 2: Bitola 09.01.2022 (M4.0)** | **EQ 3: Florina 12.01.2022 (M3.6)** | **EQ 4: Florina 11.01.2022 (M3.5)** | **EQ 5: B&H 22.04.2022 (M5.7)** | **EQ 6: Tirana 15.01.2023 (M4.8)** |
| 0th (foundation) | 0.0394 | 0.0278 | 0.0219 | 0.0311 | 0.0426 | 0.068 |
| 9th | 0.113 | 0.068 | 0.047 | 0.088 | 0.102 | 0.152 |

**Table 1.11:** Recorded peak ground accelerations (PGA).

| Story | Recorded acceleration (PGA) (g) | | | | | |
|---|---|---|---|---|---|---|
| | **EQ 1: Florina 11.01.2022 (M4.0)** | **EQ 2: Bitola 09.01.2022 (M4.0)** | **EQ 3: Florina 12.01.2022 (M3.6)** | **EQ 4: Florina 11.01.2022 (M3.5)** | **EQ 5: B&H 22.04.2022 (M5.7)** | **EQ 6: Tirana 15.01.2023 (M4.8)** |
| 0th (foundation) | 0.0394 | 0.0278 | 0.0219 | 0.0311 | 0.0426 | 0.068 |
| 9th | 0.0703 | 0.0498 | 0.0314 | 0.045 | 0.1607 | 0.059 |

**Table 1.12:** Difference in the percentage of the recorded PGA versus the numerically obtained PGA for the 9th story.

| Story | Difference in recorded versus numerically obtained PGA (%) | | | | | |
|---|---|---|---|---|---|---|
| | EQ 1: Florina 11.01.2022 (M4.0) | EQ 2: Bitola 09.01.2022 (M4.0) | EQ 3: Florina 12.01.2022 (M3.6) | EQ 4: Florina 11.01.2022 (M3.5) | EQ 5: B&H 22.04.2022 (M5.7) | EQ 6: Tirana 15.01.2023 (M4.8) |
| 9th | 37.8 | 26.8 | 33.2 | 48.9 | 57.5 | 61.2 |

**Table 1.13:** Dynamic amplification factor (DAF) for the 9th story in respect to the foundation level, calculated versus recorded.

| Story | EQ 1: Florina 11.01.2022 (M4.0) | EQ 2: Bitola 09.01.2022 (M4.0) | EQ 3: Florina 12.01.2022 (M3.6) | EQ 4: Florina 11.01.2022 (M3.5) | EQ 5: B&H 22.04.2022 (M5.7) | EQ 6: Tirana 15.01.2023 (M4.8) |
|---|---|---|---|---|---|---|
| DAF (calculated) | 2.9 | 2.4 | 2.1 | 2.8 | 2.4 | 2.2 |
| DAF (recorded) | 1.8 | 1.8 | 1.4 | 1.4 | 3.8 | 0.9 |

## 1.6 Comparison of site and structural dynamic amplification factor (DAF) with previous studies

The values of DAF were also compared to DAF values given in Petrovski et al. (1995) [1] from the seismic source zones in Albania, Greece, and Macedonia recorded during 1992 (Table 1.5). Four moderate earthquakes with magnitudes in the range of 3.8–4.9 have been recorded on the three dimensional instruments array with the maximum acceleration amplitudes from 0.0010 g to 0.00637 g. The time histories and response spectra for the building site (L2) are given in Figures 1.4–1.6 for the deep downhole B I at the depth of 101 m. in the bedrock with maximum PGA = 0.00121 g, foundation level F4 with PGA = 0.00322 g, and 9th floor PGA = 0.00627 g, all for N-S (transverse) component. DAF at this site for relatively low excitation is in the soil media DAF = 2.66 with respect to the bedrock and 1.95 for the building with respect to the foundation level (Table 1.14).

**Table 1.14:** Peak ground acceleration (PGA) values and DAF from the August 13, 1992 Resen earthquake as given in [6].

| Depth | PGA (g) | DAF |
|---|---|---|
| 9th floor (building structure) | **0.00627** | **1.95 (in respect to the foundation of the building)** |
| Foundation level (0.0 m) | **0.00322** | **2.66 (in respect to the bedrock)** |
| Bedrock (−101 m) | **0.00121** | **1** |

## 1.7 Discussion, conclusions, and further work

Obtained results are a good starting point for further sophisticated analysis including nonlinear site response analysis at the location, which can be verified with stronger recorded earthquakes in future. At the analyzed site, sets of input motions were selected to represent different frequency contents in order to improve the influence of the numerical calculations.

In comparing the DAF between the foundation level and the structure in the 9th floor, it can be said that the amplitude of the amplification for the recorded time histories is in the range of 1.4–3.8, while for the numerical model the DAF varies between 2.1 and 2.9. This is mainly because the numerical model developed for the simulation does not include soil-structure interaction SSI modelling.

The diagrams show that the surface layers considerably amplify the earthquake effect, which is the result of the low strength characteristics of the soil in these layers. The dynamic amplification factor being a nondeterministic quantity is related to the fundamental frequency of the soil layers, thus gaining in importance in the site response analysis. The values of the dynamic amplification factors from the analyzed recorded accelerations match well with the ones obtained and analyzed from previous small to moderate earthquakes at the site from 1992.

Still, to get a more accurate insight, one of the next recommended research steps is to analyze the local soil conditions using a higher number of acceleration records from the site with different magnitudes, compare the obtained acceleration records with acceleration records from nearby seismic stations, and make detailed modelling of the dynamic soil properties (shear modulus and damping) obtained from laboratory experiments on soil samples of the location.

# References

[1] D. Dojcinovski, M. Stojmanovska, M. Garevski, W. Guoxin, B. Dimiskovska, I. Gjorgjeska, and N. Kuljic. Old town core of Ohrid-Seismic parameters for repair and strengthening of structures. 16th World Conference on Earthquake Engineering, 16WCEE 2017, Santiago Chile, January 9th to 13th 2017.

[2] E. M. Rathje, N. A. Abrahamson, and J. D. Bray. Simplified frequency content estimates of earthquake ground motions. *Journal of Geotechnical and Geoenvironmental Engineering*, 124(2):150–159, 1998.

[3] M. D. Trifunac. Site conditions and earthquake ground motion – A review. *Soil Dynamics and Earthquake Engineering*, 90:88–100, 2016.

[4] D. Stanko, et al. Evaluation of the site amplification factors estimated by equivalent linear site response analysis using time series and random vibration theory based approaches. *Soil Dynamics and Earthquake Engineering*, 117:16–29, 2019.

[5] V. Di Fiore. Seismic site amplification induced by topographic irregularity: Results of a numerical analysis on 2D synthetic models. *Engineering Geology*, 114(3–4):109–115, 2010.

[6] J. Petrovski, et al. Characteristics of earthquake ground motions obtained on the Ohrid Lake three dimensional strong motion array in the Republic of Macedonia. In Duma, editor, 10th European Conference on Earthquake Engineering, © 1995 Balkema, Rotterdam, 1995, ISBN 90 5410 528 3.

[7] K. B. Olsen. Site amplification in the Los Angeles basin from three-dimensional modeling of ground motion. *Bulletin of the Seismological Society of America*, 90(6B):S77–S94, 2000.

[8] P. P. Dimitriu, Ch. A. Papaioannou, and N. P. Theodulidis. EURO-SEISTEST strong-motion array near Thessaloniki, Northern Greece: A study of site effects. *Bulletin of the Seismological Society of America*, 88(3):862–873, 1998.

[9] E. N. Farsangi, M. Noori, T. Y. Yang, P. B. Lourenço, P. Gardoni, I. Takewaki, E. Chatzi, and S. Li. *Automation in Construction toward Resilience: Robotics, Smart Materials & Intelligent Systems*. Taylor & Francis (CRC Press), 2023. ISBN 9781032350868.

[10] G. A. Ordonez. SHAKE2000: A computer program for the 1D analysis of geotechnical earthquake engineering problems. Geomotions, LLC, USA, 2000.

[11] Bojadjieva, et al. IZIIS In situ geo laboratory. Proceedings of 1st Croatian Conference on Earthquake Engineering, 1CroCEE Zagreb, Croatia – March 22nd to 24nd, 2021.

[12] J. Bojadjieva, V. Sheshov, K. Edip, J. Chaneva, T. Kitanovski, and D. Ivanovski. GIS Based Assessment of Liquefaction Potential for Selected Earthquake Scenario”. Earthquake Geotechnical Engineering for Protection and Development of Environment and Constructions. Proceedings of the 7th International Conference on Earthquake Geotechnical Engineering, 7th ICEGE, Rome, Italy, 17–20th, June, 2019.

[13] Z. Milutinovic, R. Shalic, and D. Tomic. Seismic Hazard Map (PGA) for Macedonia, based on MKC EN 1998-1:2004 – Eurocode 8, Institute of Earthquake Engineering and Engineering Seismology, Ss. Cyril and Methodius University, Skopje IZIIS Report 2016–26, 2016.

[14] J. Bojadjieva, V. Sheshov, K. Edip, A. Bogdanovic, I. Gjorgjeska, T. Kitanovski, and D. Ivanovski. In situ geotechnical laboratory in urban environment. ICONHIC 2022, Athens, Greece, 2022.

[15] Three-dimensional Network of Instruments for Investigation of the Effect of Local Soil Conditions and Behavior of Structures under the Effect of Earthquakes, Volume IX, IZIIS Report, 85–154, 1985.

Meisam Gordan, Daniel McCrum, Abdollah Malekjafarian,
Ramin Ghiasi

# 2 Impact of industry 4.0 technologies on structural health monitoring

**Abstract:** Structural health monitoring (SHM) and non-destructive test (NDT) methods are significant tools in ensuring structural safety, reliability, integrity, and minimal structural maintenance. Industry 4.0 technologies, for example, Internet of things (IoT), Blockchain, Unmanned Aerial Vehicles (UAVs), and Data Mining have recently received significant interest in SHM due to their ability to improve the SHM systems in terms of performance, automation, cost-effectiveness, and safety, for example. In recent years, traditional SHM approaches have been rapidly upgraded to IoT-based, Internet of Drone (IoD)-based, and data mining-based SHM. This is due to the fact that conventional methods are limited by their high cost and non-real-time SHM. Moreover, the implementation of blockchain-based SHM as an emerging decentralized database technology has been identified for improving the security of data collection. Additionally, Wireless Sensor Networks (WSNs) are widely used in the aforementioned Industry 4.0 technologies. Therefore, IoT, blockchain, IoD, and data mining have been applied to enhance SHM strategies. In this regard, this chapter presents the most recent advanced emerging technologies employed in SHM. To this end, a brief background of these technologies is discussed in this chapter. Then, the development of these advances and current applications in SHM are presented with the aim of showing the benefits and efficiency of these technologies.

## 2.1 Introduction

In general, “damage” is a deficiency in the performance of a structure, caused by external loads, human errors, or environmental conditions [1]. Damage detection techniques can be classified in two categories due to their detection abilities; namely local-based and global-based techniques [2]. Structural health monitoring (SHM) systems have been used to guarantee the safe functioning of structures in order to make satisfactory decisions on structural maintenance, repair, and retrofitting [3–10]. The main steps in SHM implementation are briefly summarized and illustrated in Figure 2.1. A

---

**Acknowledgment:** The authors would like to express their sincere gratitude and appreciation to University College, Dublin for providing the resources and supporting this research. (Grant number: 101021668)

---

**Meisam Gordan, Daniel McCrum, Abdollah Malekjafarian, Ramin Ghiasi,** School of Civil Engineering, University College Dublin, Belfield, D04 V1W8 Dublin, Ireland

https://doi.org/10.1515/9783110791426-002

brief history of SHM is shown in Figure 2.2. As can be observed from Figure 2.2, the first health monitoring approach was conducted in 1937 on the Golden Gate Bridge in San Francisco [11]. Since this first application of SHM, there has been growing global demand for reliable structural health information to minimize maintenance costs and increase human safety [12]. This is due to the fact that the health of structures needs to be monitored to predict damage, retrofit, and prevent collapse as the failure of structures is to be avoided (see Figure 2.3).

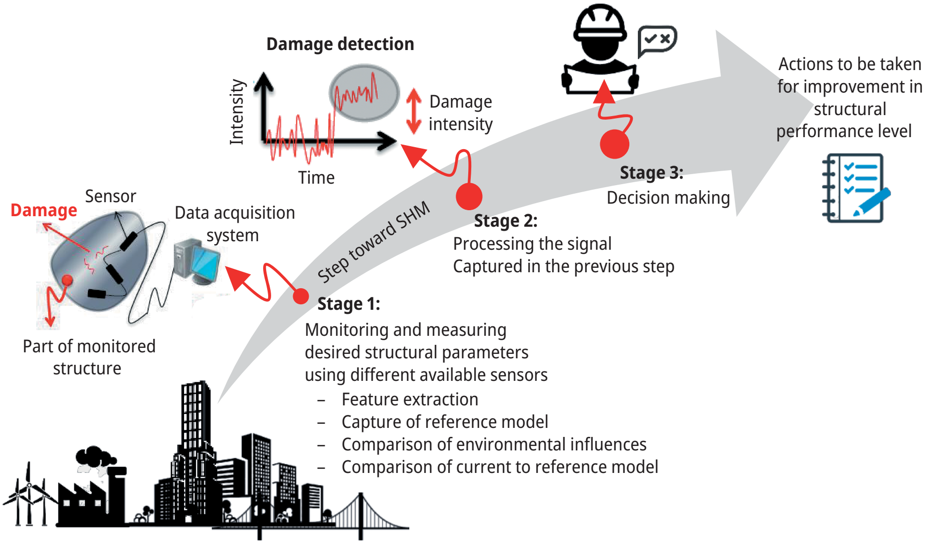

**Figure 2.1:** Schematic operation of SHM systems in civil engineering applications (adapted from [13]).

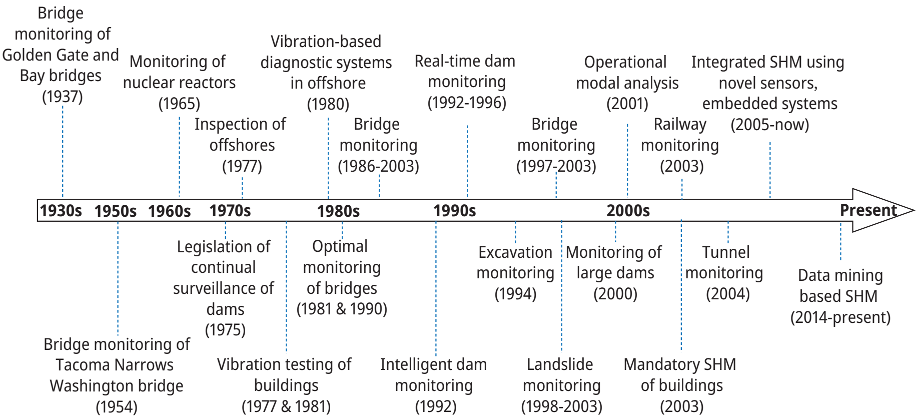

**Figure 2.2:** An overview of SHM evolution over the years.

(a) Tacoma Narrows bridge in Washington, collapsed in **1940**, wind [14]

(b) Silver bridge in Ohio, collapsed in **1967**, corrosion [15]

(c) Ronan Point building, London, collapsed in **1968**, gas explosion [16]

(d) Skyline Plaza in the USA, collapsed in **1973**, framework removal [17]

(e) Mianus River bridge in Greenwich, collapsed in **1983**, corrosion and poor maintenance [18]

f) Hanshin Expressway bridge in Kobe, Japan, collapsed in **1995**, earthquake [19]

(g) Khobar tower in Saudi Arabia, collapsed in **1996**, bombing [20]

(h) The World Trade Center in USA, collapsed in **2001**, terrorist attack [16]

(i) I-35W bridge in Minneapolis, USA, collapsed in **2007**, design flaw [21]

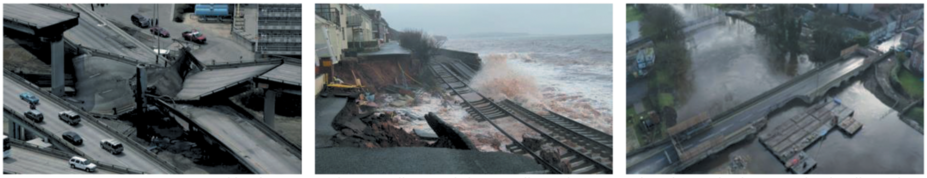

(j) I-580 Connector Ramp –Oakland, California, collapsed in **2007**, fire [18]

(k) Sea wall at Dawlish, UK, collapsed in **2014**, storm [22]

(l) Tadcaster bridge in England, collapsed in **2015**, river scour [23,24]

(m) Plasco tower in Iran, collapsed in **2017**, fire [25]

(n) Morandi bridge in Italy, collapsed in **2018**, poor construction [26]

(o) Nan Fang'ao bridge in Taiwan, collapsed in **2019**, corrosion [27]

(p) Bridge collapse in Bad Neuenahr-Ahrweiler, Germany, **2021**, flood [28]

(q) Metropolis building in Iran, collapsed in **2022**, poor construction and overloading [29,30]

(r) Building collapse in Kahramanmaras, Turkey, **2023**, earthquake [31]

**Figure 2.3:** Sample of some structures subjected to collapse [14–31].

Civil engineering structures may be subjected to different loads such as seismic, wind, wave, traffic, blast, or random impact loads during their service life. Therefore, it is necessary to assess their vulnerability and evaluate if it is necessary to retrofit and enhance their structural capacity. Hence, structural rehabilitation and retrofits of structures have to be conducted [32]. In order to inform any retrofitting strategy or detection of any structural damage, tracking the response of the structure continuously over time is required but presents a major technical challenge as data sensing is the core of most of the current SHM systems (see Figure 2.4) [33, 34]. However, conventional SHM techniques such as visual inspection [35], acoustic emission (AE) [36], chain drag [37], impact echo (IE) [38], radiography [39], X-ray [40], impulse response (IR) [41], and ultrasonic methods [42], which are local SHM approaches, are challenged by low-cost and a lack of real-time event monitoring [43, 44]. Additionally, most of the aforementioned approaches are labour-intensive and time-consuming. Moreover, their implementation is limited to the availability of the structural damage location [45, 46], that is, need to detect damage locally by inspection. However, typically in most cases, the location of damage is unknown. Therefore, these techniques do not have adequate capacity to assess the health condition of structures, particularly for large structures and visually unobservable damages. Consequently, IoT, blockchain, IoD, and data mining are required to be integrated with SHM mainly due to following reasons:

- To overcome the aforementioned drawbacks relating to large structures and visually unobservable damages
- To enhance the application of remotely monitoring complicated structural systems anytime, anywhere
- To implement a reliable, constant, and efficient low-cost SHM system

Due to the rapid growth of sensing technologies, that is, wireless communication and radio-frequency identification [47], IoT is an emerging technology for monitoring systems. In this regard, IoT has received significant attention in SHM due to its flexibility in monitoring various structures, that is, buildings and bridges, especially in smart cities [48]. Therefore, IoT has provided a promising choice for SHM in recent years. For example, Wireless Sensor Network (WSN), as the basic layer of IoT, has recently been employed in SHM schemes due to its intelligent sensing and computing ability [49–51]. Besides, according to [10], drones can generate high-quality images for SHM systems, especially in difficult-to-access areas. Blockchain technology is another emerging trend. The implementation of blockchain-based IoT solutions could solve several issues, that is, the high maintenance cost of centralized approaches [52]. Data mining algorithms, that is, machine learning, artificial intelligence, and statistical techniques have also been used to extract information on the structural health condition by obtaining relationships between data in the form of patterns [53, 54]. Therefore, data mining has provided numerous solutions to SHM problems due to its powerful computational ability by means of classification-, prediction-, and optimization-based methods such as neural networks, fuzzy, support vector machine (SVM), principal component analysis (PCA), Bayesian, genetic algorithm (GA), particle swarm optimization (PSO), and ant colony optimization (ACO) [55]. For example, Knowledge Discovery in Databases (KDD), which is a data mining approach, has been applied in SHM [56] (see Figure 2.5). To explain Figure 2.5, an SHM system should be as specific as feasible to define the impact of the structural damage. Therefore, the development of SHM can be categorized into three parts, that is, damage detection, damage diagnosis, and damage prognosis. On the other hand, damage diagnosis can be also classified into detailed information representing the damage in terms of damage severity, damage type, and damage location. As a result, a hierarchical SHM scheme can be decomposed into five levels, as depicted in Figure 2.5.

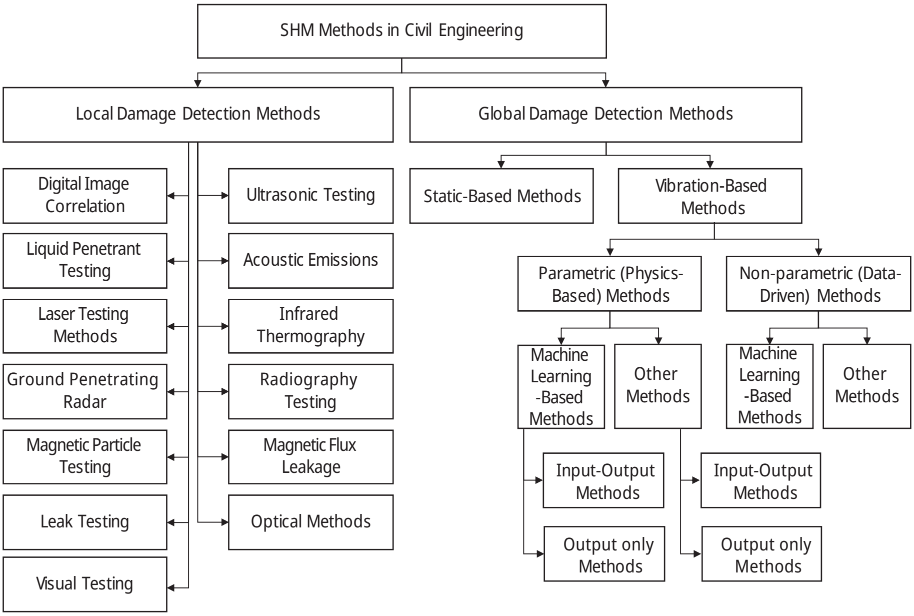

**Figure 2.4:** Classification of SHM methods [57].

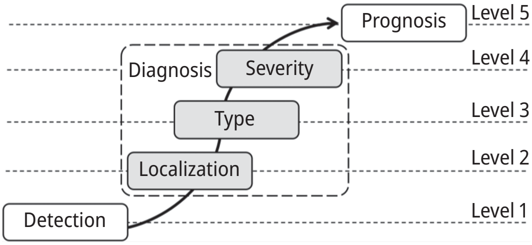

**Figure 2.5:** KDD-based SHM methodology [56].

The main focus of this chapter is to present an overview of SHM implementation based on the integration of advanced Industry 4.0 technologies. Therefore, this chapter is organized as follows. Section 2 highlights the outlook of Industry 4.0 technologies since 2020. Then, the concept and background of IoT, blockchain, UAVs, and data mining are described in Section 3. Section 4 summarizes the observations, challenges, and future directions of these technologies. Then, the concluding remarks are given in Section 5.

## 2.2 The 2020s outlook of industry 4.0 platforms

In Industry 4.0, the term “industry” refers to the creation of products, services, and facilities within an economy. In the twenty-first century, our world is experiencing the fourth step of industrialization, popularly known as the Fourth Industrial Revolution, “Industry 4.0”, or “IR4.0” (see Table 2.1) [58–62]. Industry 4.0 refers to the smart and connected devices (i.e. hosts or networks) that have been designed to interact with the physical world using machine-to-machine communication and human-machine cooperation. IoT, Internet of Services (IoS), Cyber-Physical Systems (CPS), cloud/fog/edge computing, data mining, robotics, and blockchain are fundamental pillars of Industry 4.0, which promote smart tasks and diagnostics in research and analytics to industries and organizations. Hence, the IR4.0 technologies are handling complicated undertakings at a faster rate compared to human performance in the 2020s.

Several reports have indicated the importance of Industry 4.0 technological platforms. The International Data Corporation (IDC) predicted that close to 28 billion connected hosts were used by 2012 [63]. It is now expected that around 55.9 billion hosts will be connectable by 2025, showing significant growth [64]. In addition, according to VisionMobile outlook, the number of IoT developers will increase from 300,000 in 2014 to more than 4.5 million by the 2020s [65].

## 2.3 Industry 4.0 technologies in SHM

### 2.3.1 Internet of things (IoT)

Before going into the details of “Internet of things” relating to SHM, it is important to highlight this term, which consists of “Internet” and “Things.” Internet refers to the global interconnected computer networks, while any object, which is capable of sensing and collecting data, can be considered as a “Thing.” Therefore, IoT is an evolutionary technology comprising billions of physical devices around the world containing embedded sophisticated chips, sensors, and actuators, which are able to connect, collect, share, interact, and exchange any type of data. Hence, in IoT, environmental

**Table 2.1:** Global industrial revolution and their contribution.

| **Industrialization steps** | **Key contributions** |
|---|---|
| Fourth Industrial Revolution (IR 4.0) | – Internet of things (IoT)<br>– Smart factories/Smart Manufacturing/Robotics<br>– Circular economy/Product – Lifecycle – Management (PLM)<br>– Data mining/Big data analytics<br>– Smart sensors/Remote sensing/Wireless sensor network<br>– Cloud computing/Cognitive computing/Mobile computing<br>– Cybersecurity/Blockchain<br>– Digital twin/Smart tasks and diagnostics/Smartification<br>– Virtual reality/Augmented reality/Building Information Modelling<br>– Unmanned Aerial Vehicles (UAVs)/Internet of Drone/Smart cities<br>– Smart environment/Sustainable development/Renewable energy |
| Third Industrial Revolution (IR 3.0) | – Production Automation/Computer and Automation<br>– Information and Technology/Telecommunication<br>– Linear economy<br>– Leveraging Electrical Mechanization<br>– First programmable logic controller (PLC)<br>– Industrial Robotics/Electronic and nuclear industries<br>– Business Computers/Supercomputers/Business software<br>– Internet/World Wide Web |
| Second Industrial Revolution (IR 2.0) | – Electrical Energy/Steam power and petroleum<br>– Skyscrapers<br>– Large scale iron and steel production<br>– Telephones and telegraphs, typewriter, phonograph, motion pictures<br>– Widespread use of machinery in manufacturing<br>– Automobile, airplanes, diesel engines, bicycles, railroads<br>– Chemical, rubber, paper mills, fertilizers<br>– Applied Science<br>– New forms of business organizations |
| First Industrial Revolution (IR 1.0) | – Mechanical Production<br>– New Energy Resources/Water and Steam Power<br>– New raw materials/Iron, coal, textile, steam industries<br>– New machines/Spinning Jenny and the Power loom<br>– Factory system, division of labour, specialization<br>– The locomotive<br>– Expansion of world trade |

sensing with data transmission can be combined with processing by means of wireless communication systems to enhance the quality of life [66]. For example, Figure 2.6 illustrates the idea of IoT, which has changed the means of human living by contacting anybody, anytime, and anywhere.

IoT systems can support real-time applications using low-cost sensors. Therefore, they have gained significant interest for various applications such as smart cities, smart buildings, healthcare, smart grids, industrial manufacturing, and transportation without any intervention of human-human interaction [67–71] (see Figure 2.7). In other words, IoT is changing the physical world with traditional societies and industries into one huge database system that can support real-time applications. In the context of SHM, Figure 2.8 presents the role of internet in damage detection of buildings [72].

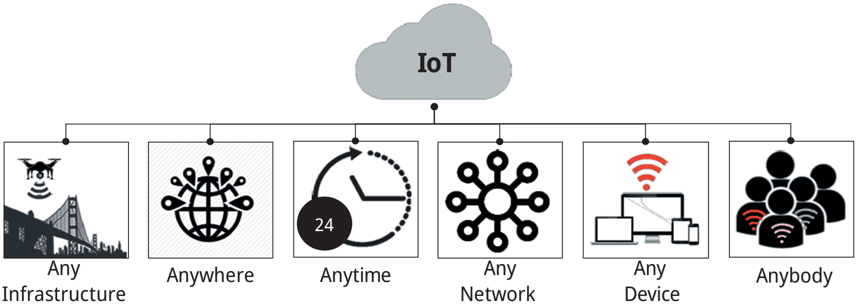

**Figure 2.6:** Concept of the IoT system.

In recent years, conventional SHM has been upgraded to IoT-based SHM. Traditional approaches to SHM are being challenged by IoT-based SHM, which is real-time and low-cost SHM. Applications of IoT in SHM have been reported recently by several researchers to show their capability of identifying structural damage. For example, a real-time health assessment was carried out by Qu et al. [73] in order to improve the effectiveness of prognostic and health management (PHM) systems through obtained data from massive sensors (see Figure 2.9). As can be seen from Figure 2.9, the proposed framework, which was applied to study the online PHM, comprises three levels, that is, strategic, tactical, and operational levels.

As mentioned previously in Section 1, WSN is one of the most important technologies recently applied to SHM. One study by Asay [65] presented the development of IoT-based WSN in SHM. The authors of this study visualized an intelligent and reliable monitoring system, as shown in Figure 2.10. In another work by Wang et al. [74], a cloud-based SHM methodology using IoT was introduced to reduce the processing of big data as well as improve the monitoring system in smart cities. It was shown that various infrastructures, for example, bridges and buildings could be monitored individually under one cloud using attached IoT sensors (see Figure 2.11). A big data reduction scheme was also proposed in [74] to identify the structural damage of smart cities (see Figure 2.12). The signal acquisition stage of this research was conducted using particular requirements, for example, application-specific conditions. In addition, a frequency content analysis was carried out in this study with the aim of sensor

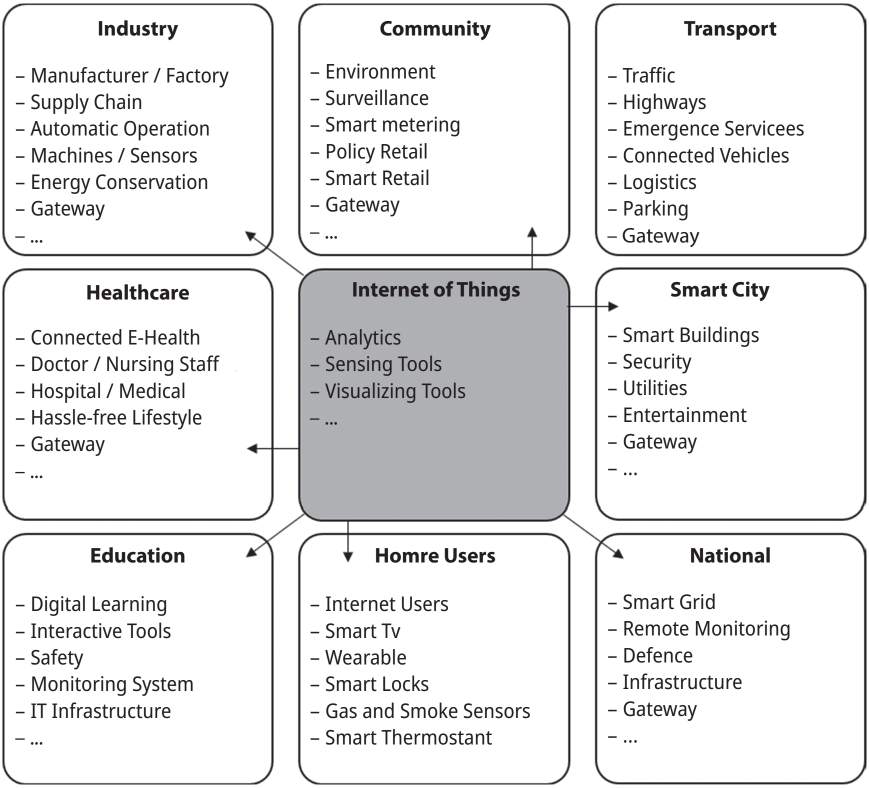

**Figure 2.7:** Integration of IoT applications.

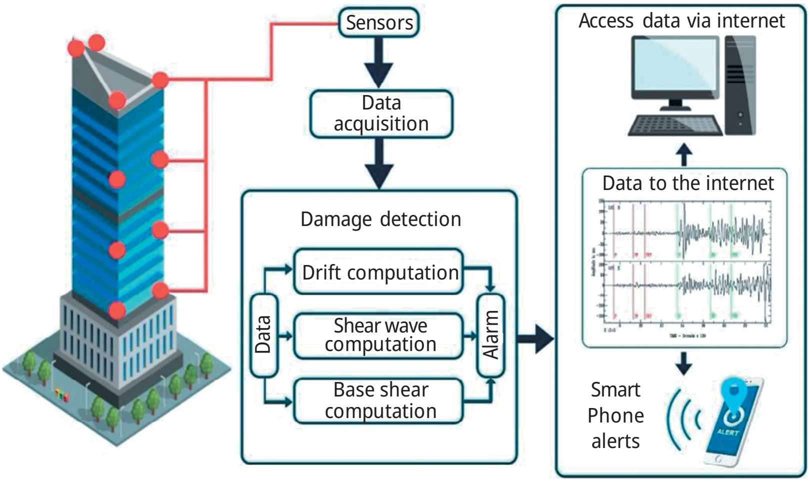

**Figure 2.8:** The operating principle of SHM in buildings using IoT [72].

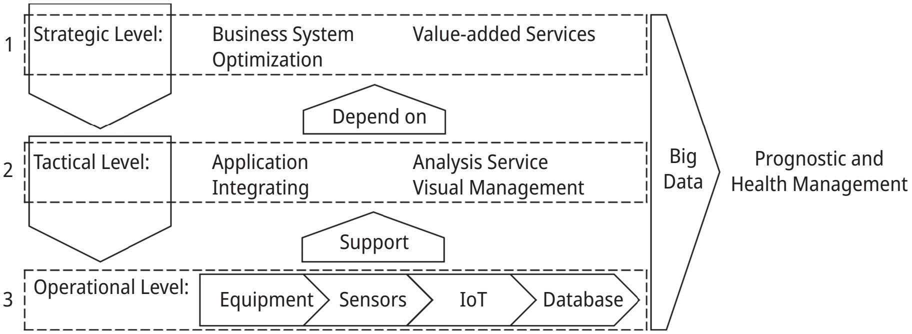

**Figure 2.9:** Integrative prognostics and health management framework based on IoT [73].

signal sensitivity detection. It was concluded that among sensitive and insensitive signals, only sensitive sets had to be transferred to the base station.

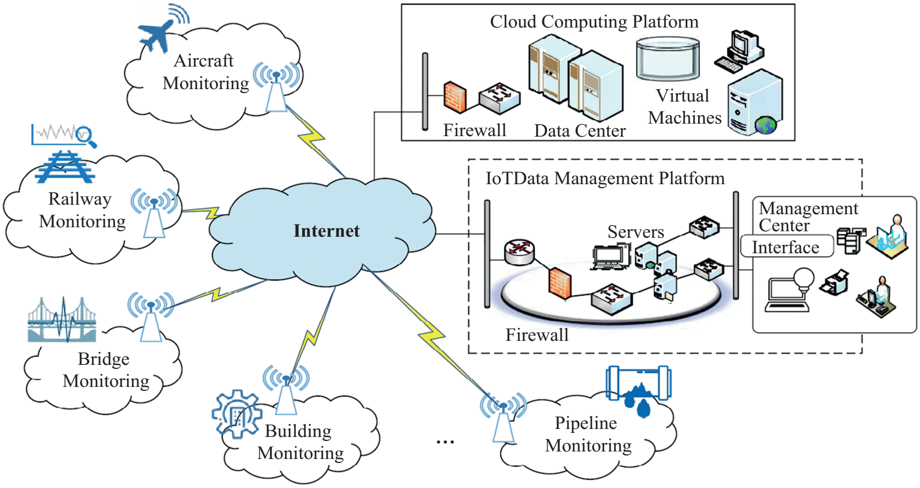

**Figure 2.10:** Overview of the SHM-based IoT workflow adapted from [75].

Wang et al. [76] proposed an IoT-based integrated information system for SHM comprising three layers namely a sensor data collection network, a data processing network, and an SHM service network. Likewise, the architecture of an IoT-SHM system has also been illustrated by Scuro et al. [77] including its library of components, that is, (i) smart sensors, (ii) gateway, (iii) remote control and service room, and (iv) open platform communications server (see Figure 2.13).

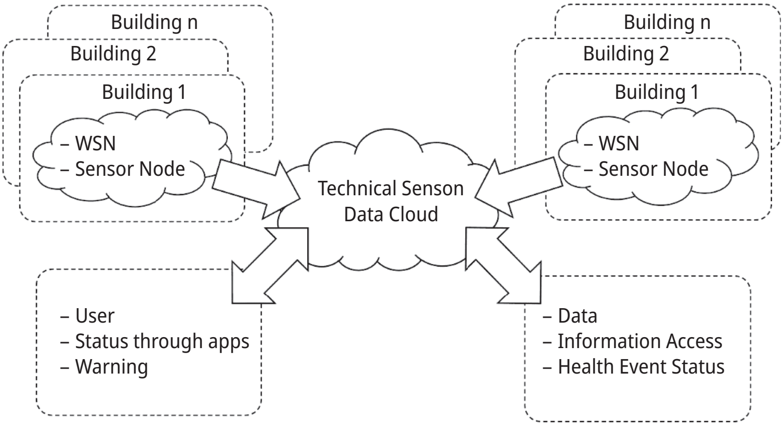

**Figure 2.11:** Combination of WSN data recorded from different infrastructures using sensor data cloud [74].

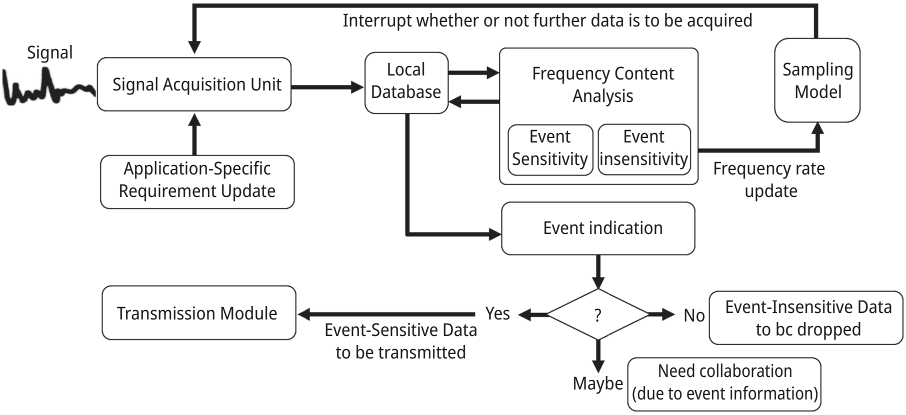

**Figure 2.12:** Flowchart of the proposed data reduction procedure by [74].

## 2.3.2 Blockchain

Blockchain is an emerging decentralized database technology proposed in 2008 [78]. A schematic form of a blockchain is detailed in Figure 2.14, where the blockchain is denoted as a sequence of blocks appended to each other in chronological order. Generally, blockchain can be viewed in three categories, that is, public, private, and consortium blockchain [79]. Any file with data such as transactions or any record can be controlled by this technology [80]. As a result, it has gained significant interest [81]. The novel data structure of blockchain is capable of efficiently setting rules to update the information. Thus, blockchain is gaining attention from a large variety of applications, as shown in

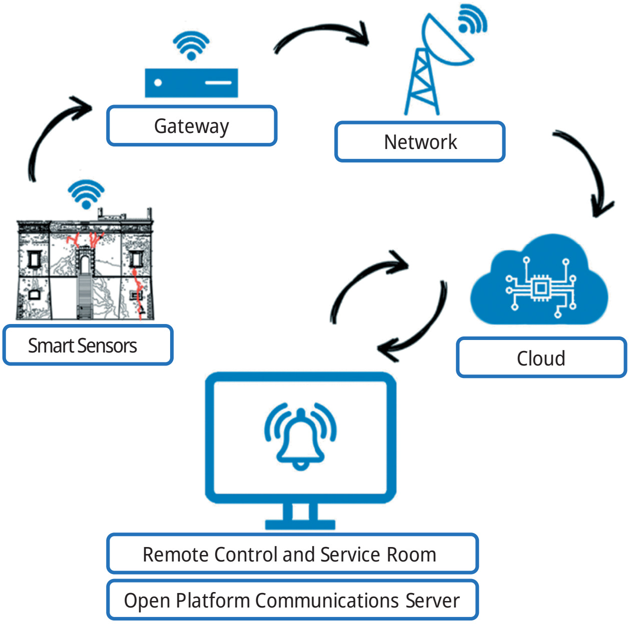

**Figure 2.13:** Architecture of an IoT-based SHM system [77].

Figure 2.15. This could be explained by the fact that it has significant features such as anonymity, decentralization, immutability, and security. Therefore, it can be applied in IoT systems and the outcome is robust and highly reliable, with a major cost reduction [68, 82–84].

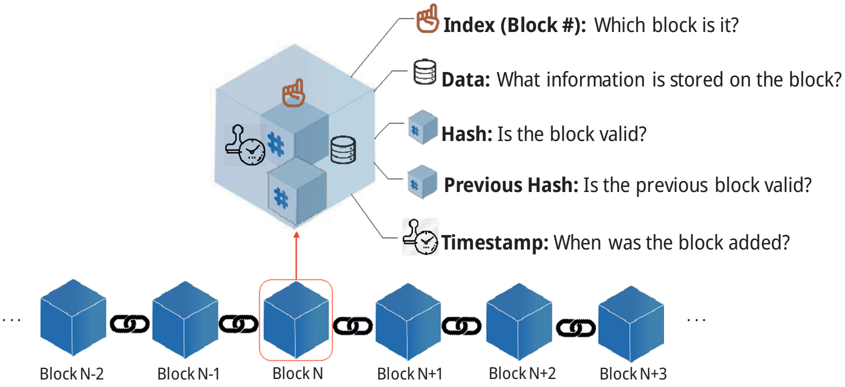

**Figure 2.14:** Structure of a blockchain, adapted from [85].

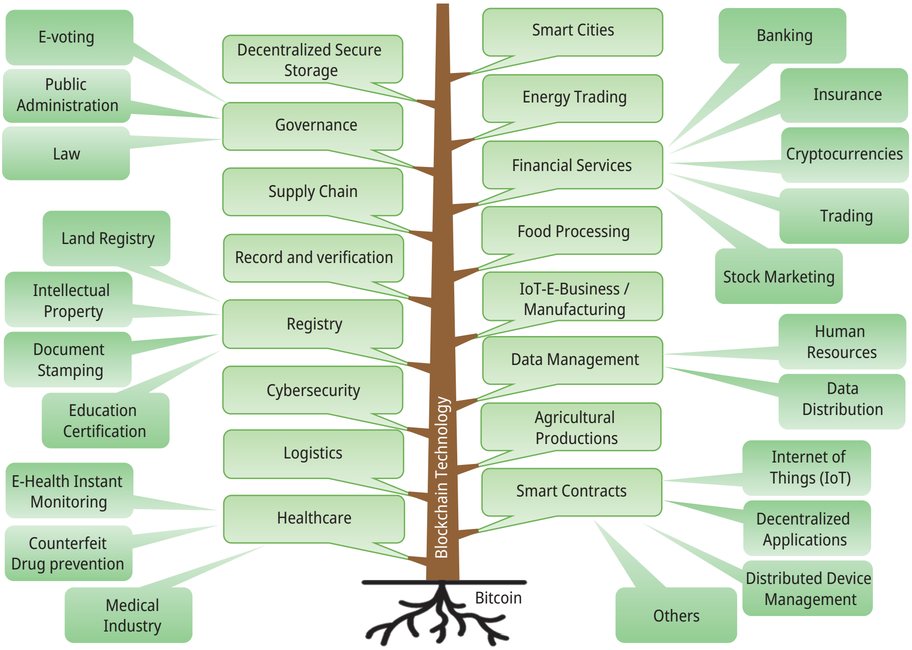

**Figure 2.15:** Blockchain application tree, adapted from [86–88].

A blockchain-IoT-based distributed network was proposed by Jo et al. [89] with the aim of improving the security of data collection in SHM (see Figure 2.16). In addition, an autonomous decision-making approach using blockchain-based smart contracts in SHM was also introduced in this work. The authors verified the performance and feasibility of the proposed method using SHM data from an underground coal mine. As can be seen from Figure 2.16, the blockchain network was divided into core and edge sub-networks and all data could be stored on a distributed ledger. Two types of storage were presented in the proposed model, that is, raw data and structural damage storage. The edge nodes had a low capacity for storage. In contrast, the core participants included a better ability to create new blocks and verify proof-of-work. In addition, hash functions were also implemented in the core network to guarantee the reliability of data. It was concluded that the proposed fully decentralized model could provide more reliable results with high interoperability in comparison to simple [90], WSN [91], IoT [92], and IoT-cloud [48] SHM systems.

One of the most significant benefits of blockchain is that it can manage decentralized databases without failure. By taking advantage of this feature, Gordan et al. [87] proposed a new way to compute in situ wireless sensors data for real-time monitoring of smart structures, which is needed to address the limitations of SHM systems (see Figure 2.17). According to their findings, before starting the SHM procedure, a reliability evaluation of the recorded data using blockchain needs to be carried out in advance to

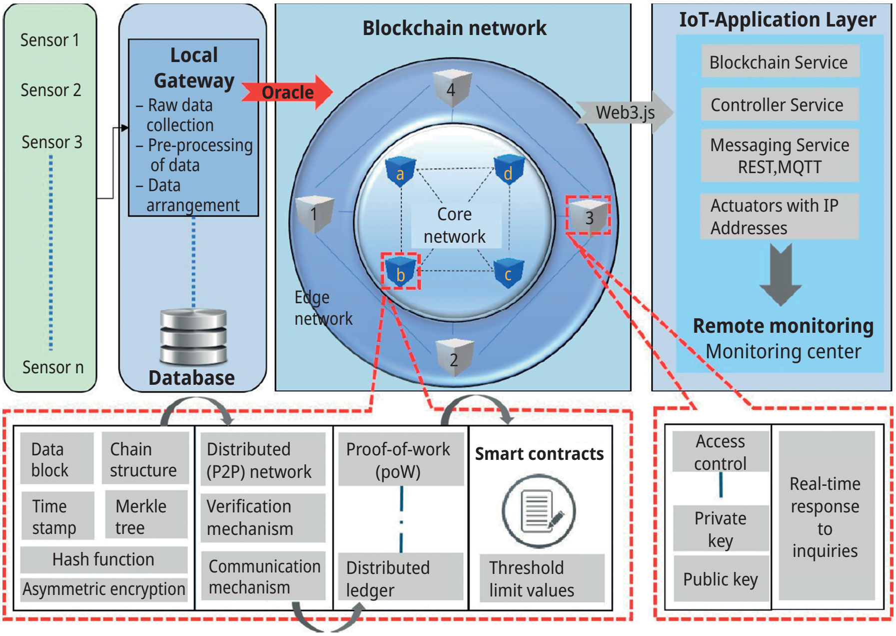

**Figure 2.16:** Architecture of a proposed blockchain-IoT network for SHM [89].

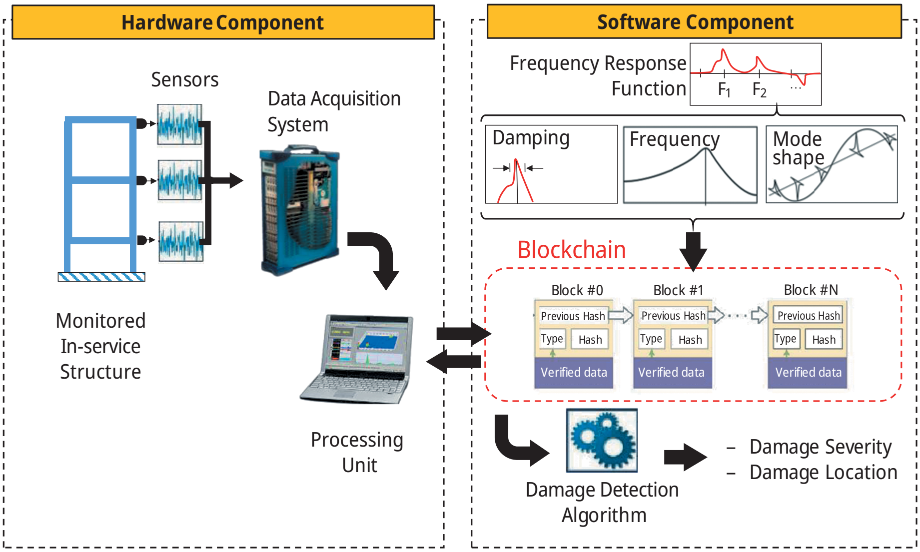

**Figure 2.17:** Schematic illustration of the proposed conceptual framework [87].

verify the authenticity of sensors. As mentioned earlier, blockchain is a series of blocks chained to each other in a sequential manner using cryptographic hash functions, which can set rules on how a database is updated. The only recorded sensor data considered valid are the ones acknowledged by this technology. Therefore, any sensor data entry from a SHM application should be evaluated by blockchain to increase the reliability of the structural damage identification system. To this end, any recorded sensor data cannot be added to the input SHM database without agreement from blockchain.

### 2.3.3 Unmanned aerial vehicles (UAVs)

Remote sensing technology has been used for extracting structural damage detection using non-contact measurement devices [93–100]. This is because the obtained responses from non-contact measurement tools are quicker and at a lower cost in comparison to conventional SHM systems. In addition, they have much wider fields of view. Therefore, the application of remote sensing in recording the SHM databases has been recently reported for structural damage assessment [101]. Figure 2.18 illustrates the remote sensing-based non-contact technologies in three levels, that is, spaceborne, airborne, and ground-based levels. At the ground-based level, the IoD is considered as one of the large-scale heterogeneous networks. The IoD networking resources and capabilities, as a vital need, is required to be developed for conducting the expected services and applications. This communication architecture is able to support complex task management and coordination [102]. Additionally, UAVs are being developed for SHM applications due to their high mobility and direct communication range [103] (see Figure 2.19). In addition, these self-

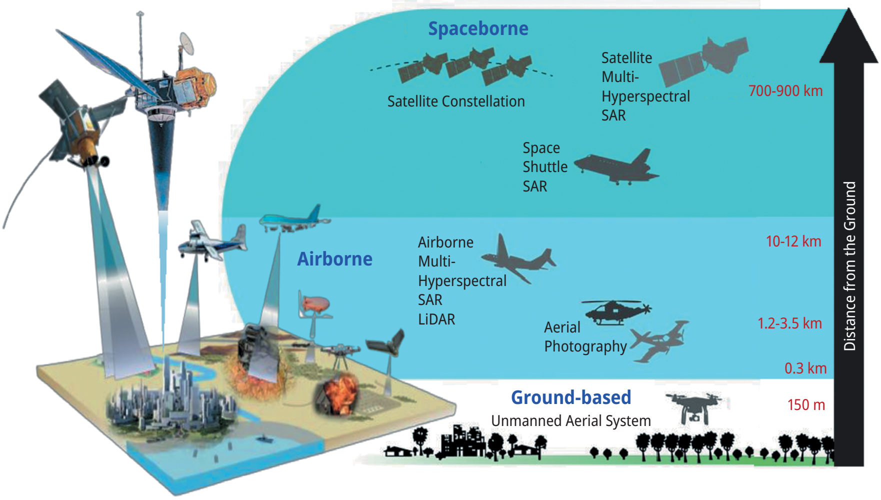

**Figure 2.18:** Non-contact measurement platforms [108].

sufficient devices are relatively low-cost and widespread [104]. Consequently, several services of UAV applications have been developed, for example, navigation, delivery, rescue, disaster management, military, and intelligent transportation [105–107].

(a) Fixed-wing UAVs

(b) Rotary-wing UAVs, and unmanned helicopters

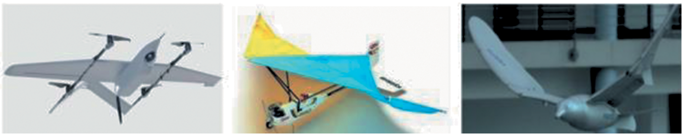

(c) Hybrid UAVs, umbrella-UAVs, and bionic-UAVs

**Figure 2.19:** Several types of drones/UAVs [109].

Carroll et al. [110] developed a customized drone for sensor deployment as well as SHM of a lab-scale bridge (see Figure 2.20). A laser speckle imaging system (LSIS) was also proposed in [111]. The developed approach was used for remote strain sensing as well as non-contact NDT purposes. This research could demonstrate the potential application of LSIS as an effective non-contact measurement system. According to [112], the utilization of remote sensing technologies for SHM can also be an alternate solution for bridge monitoring and maintenance, for example, Morandi Bridge in Italy

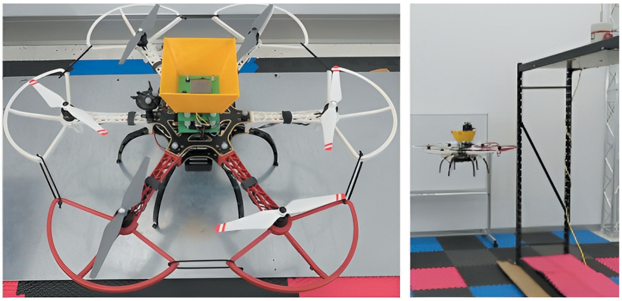

(a) (b)

**Figure 2.20:** (a) Overview of the custom drone and (b) sensor deployment and retrieval experiment on the test apparatus performed by Carroll et al. [110].

[113]. The advantage of integrating the bridge data with remote sensing is to make a comprehensive and strong data collection procedure. Others have used a drone equipped with a Digital Image Correlation (DIC) camera system for dynamic SHM of a railroad tie, as shown in Figure 2.21 [114]. It was concluded that the autonomous system successfully performed a remote structural evaluation.

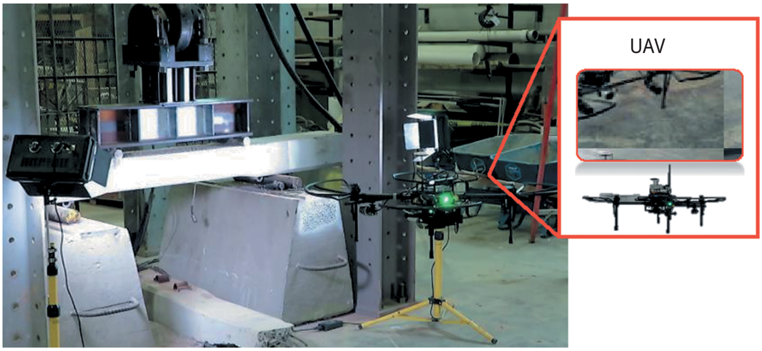

**Figure 2.21:** Overview of experimental setup using UAV for dynamic SHM of a railroad tie [114].

A drone-based mobile sensing platform was implemented by Herrmann et al. [115] to identify the modal frequencies of a wind turbine (see Figure 2.22). In this research, an optical displacement sensor was used for vibration analysis. The applied sensing platform measured the relative displacement between the structure and the drone, which indicated resilient behaviour under wind excitations. The authors of this paper claimed that the absolute movement of the structure could be estimated based on the measured relative distance. They also mentioned that the recorded time domain data was a suitable input for various operational modal analysis algorithms.

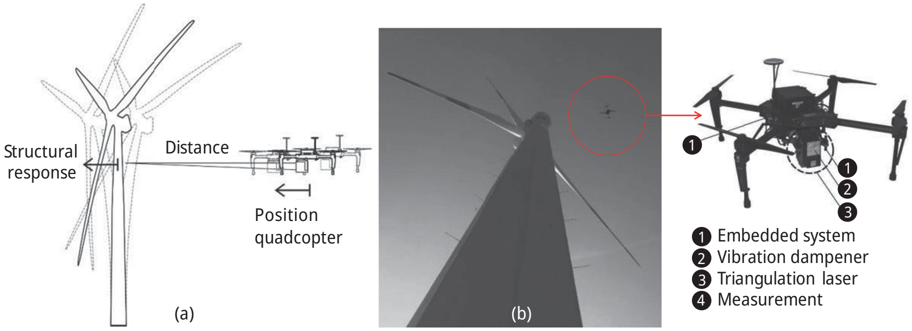

**Figure 2.22:** Vibration measurement of a wind turbine using drone: (a) schematic view and (b) actual measurement [115].

### 2.3.4 Data mining

Data mining is a powerful computing tool used to obtain knowledge from raw data. Data mining is the analysis of datasets to find out the valued data in the form of patterns in order to extract relationships, novel correlations, and trends of data using various functions (see Figure 2.23). In particular, data mining is useful for complex and time-consuming problems (e.g. prediction, classification, visualization, and summarization) that cannot be solved with traditional techniques [102, 116, 117]. In this context, prediction is one of the most important functions not only in data mining but also in SHM [118, 119].

One of the main functions of IoT is to remotely collect the recorded sensor data and transfer it into valued knowledge, which can be utilized for pattern recognition and decision-making purposes. Three types of data mining techniques, statistical, machine learning, and artificial intelligence techniques need to be applied in order to obtain valued knowledge from sensed data (see Figure 2.24) [120]. It should be noted that each of these techniques has several methods. For instance, statistical methods

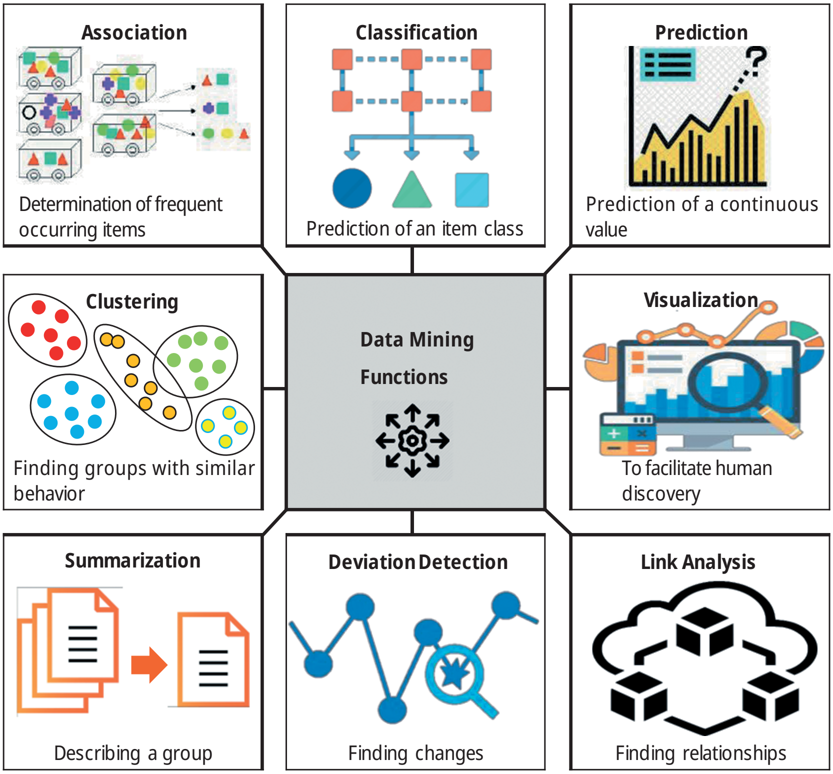

**Figure 2.23:** Data mining functions.

include regression analysis, clustering analysis, and decision tree, and machine learning methods include SVM, PCA, and case-based reasoning. The third category is artificial intelligence, for example, fuzzy logic, genetic algorithm, artificial neural network, and particle swarm algorithm. In recent years, these algorithms have also been used for damage detection of different structures (See Table 2.2 and Figure 2.25).

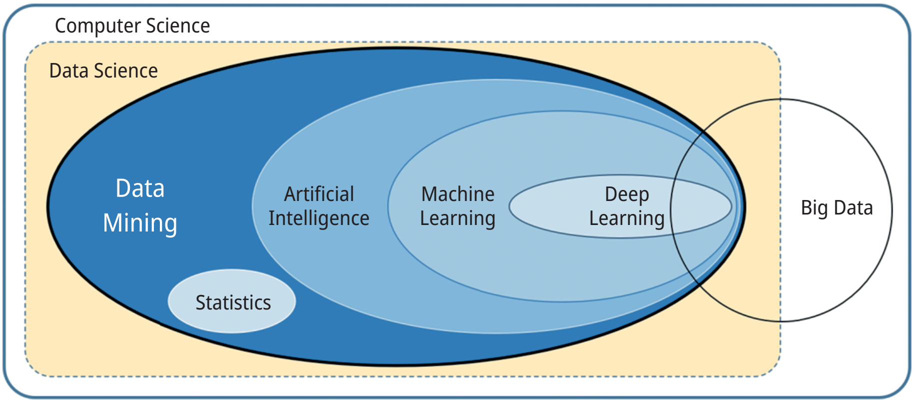

**Figure 2.24:** The relationships between computer science-based techniques [120].

**Table 2.2:** Data mining techniques [117].

| Data mining technique | Category | Learning type |
|---|---|---|
| Support vector machine | Machine learning | Supervised |
| Decision tree | Statistical | Supervised |
| Clustering | Statistical | Unsupervised |
| Principal component analysis | Machine learning | Unsupervised |
| Regression | Statistical | Supervised |
| Fuzzy | Artificial intelligence | Supervised/unsupervised |
| Metaheuristics (see Figure 2.25) | Artificial intelligence | _ |
| Classification | Statistical | Supervised |
| Artificial neural network | Artificial intelligence | Supervised/unsupervised |
| Bayesian | Machine learning | Supervised |

There is a variety of research focusing on the application of data mining in SHM. For instance, a data mining-based damage identification method was performed by Gordan et al. [122] for bridge structures using a hybrid artificial neural network-based imperial competitive algorithm (ANN-ICA). The applicability of the proposed approach was developed to detect the hidden patterns in vibration data using Cross Industry Standard Process for Data Mining (CRISP-DM) tool, as shown in Figure 2.26. It was concluded that the proposed data mining-based damage detection methodology could successfully identify and quantify damage.

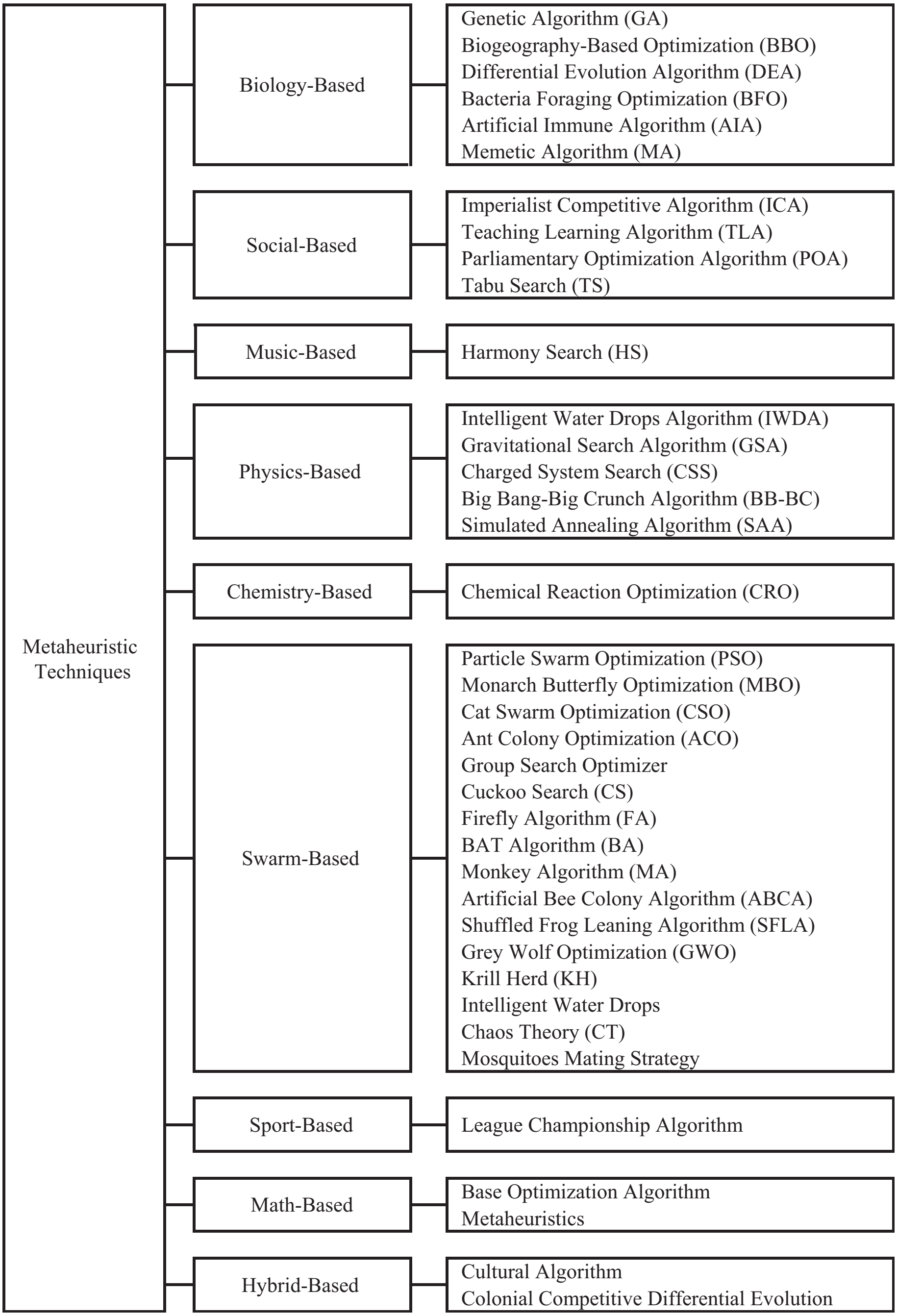

**Figure 2.25:** Overview of metaheuristic techniques [121].

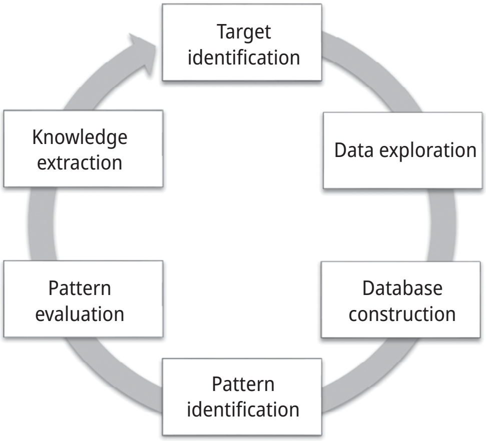

**Figure 2.26:** Generalized framework of CRISP-DM for structural damage identification [122].

As mentioned previously, classical SHM methods such as visual inspections have various limitations, for example, time-consuming procedure, based on human judgement, costly process, and ineffective for large and complex structural systems. To overcome these difficulties, a data mining-based SHM approach was developed by Gordan et al. [123]. This research investigates the applicability of data mining for damage identification of civil engineering structures. For implementation of the proposed methodology, modal parameters obtained from a series of experimental modal analysis of a slab-on-girder bridge structure were used as an input database for data mining. The laboratory work was carried out through various damage scenarios in order to generate the database (see Figure 2.27). The applicability of machine learning, artificial intelligence, and statistical methods was examined using Support Vector Machine (SVM), Artificial Neural Network (ANN), and Classification and Regression Tree (CART) to predict the structural behaviour and damage severity (see Figure 2.28). The performance of the methods was compared to obtain the most accurate method. It was concluded that the artificial intelligence method had the highest accuracy. Likewise, in the second stage, the performance of machine learning technique was better than the statistical method.

Tan et al. [124] applied the combination of a back propagation neural network and modal strain energy in order to quantify and locate damage in a number of steel beams. The authors showed that the results could verify the applicability of the proposed approach. A comprehensive review on structural damage detection in conjunction with data mining was reported by Gordan [125]. In [126], various data mining techniques, which are applicable to SHM, have been thoroughly reviewed. A comparison of data mining applications in SHM and the most used data mining methods with the highest application rates were also discussed in this study. The authors presented the capabilities and drawbacks of several algorithms such as ANN, fuzzy logic, regression, SVM, decision tree, Bayesian analysis, clustering and PCA, GA, PSO, and ACO (see Table 2.3).

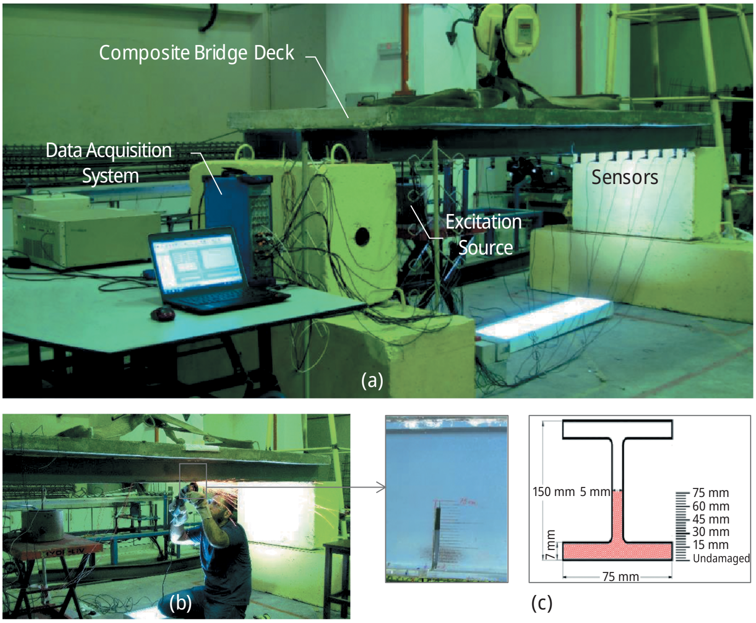

**Figure 2.27:** Experimental modal analysis: (a) test setup, (b) implementation of damage scenarios, and (c) damage depth of beams along with the imposed damage state performed [120].

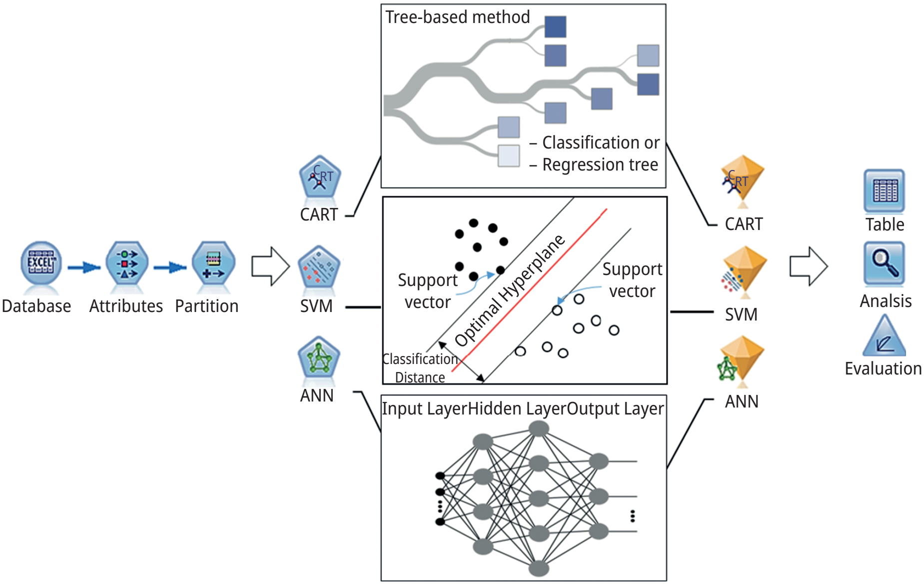

**Figure 2.28:** Flowchart of the modelling procedure [123].

Table 2.3: Abilities and drawbacks of major existing DM techniques [126].

| Technique | Category | Abilities | Drawbacks |
|---|---|---|---|
| ANN | Artificial Intelligence | (1) Accurate<br>(2) Robust to outliers<br>(3) Capable of using with other techniques<br>(4) High flexibility<br>(5) High autonomy<br>(6) High scalability<br>(7) High accessibility<br>(8) High learning capability | (1) Time-consuming training<br>(2) High computational complexity<br>(3) Low interpretability<br>(4) Medium optimization capacity<br>(5) Difficult to use<br>(6) Possible overfitting<br>(7) Uncertainty in assigning weights to connections among layers |
| Fuzzy | Artificial Intelligence | (1) Applicable for uncertain and nonlinear systems<br>(2) Parallel implementation ability<br>(3) High interpretability | (1) Costly trial and error process for membership function<br>(2) Variable shapes determination requires trial and error<br>(3) Low learning capability<br>(4) Inadequate in some decision challenges |
| PCA | Statistical Analysis | (1) High variable transformation power<br>(2) Capable of quick calculation<br>(3) Minimization of data dependency<br>(4) Able to handle sparse/ asynchronous data<br>(5) Able to retain the information of the projection data in the linear projection | (1) Changing of coordinates may cause information loss<br>(2) Large projection distance for poorly fitted data |
| GA | Artificial Intelligence | (1) Accurate<br>(2) Capable of using with other techniques<br>(3) High autonomy<br>(4) High interpretability<br>(5) High optimization capacity | (1) Time-consuming iterations<br>(2) Medium flexibility<br>(3) High computational complexity<br>(4) Medium scalability<br>(5) Low accessibility<br>(6) Lack of memory<br>(7) Disable to keep all solutions using different populations |
| Clustering | Statistical Analysis | (1) Easy to use<br>(2) Capable of using with other techniques | (1) Low accuracy<br>(2) Lack of optimal number of clusters |

**Table 2.3** (continued)

| Technique | Category | Abilities | Drawbacks |
|---|---|---|---|
| SVM | Machine Learning | (1) Can be used without local minimization<br>(2) Capable of quick sample classification<br>(3) Can be used without dimension error<br>(4) Applicable for nonlinear problems | (1) Dependent on potential kernels in nonlinear problems<br>(2) Computational inefficiency |
| Regression | Statistical Analysis | (1) Easy to use<br>(2) High accessibility | (1) Low flexibility<br>(2) Incapable of solving nonlinear problems<br>(3) Low autonomy |
| PSO | Artificial Intelligence | 1) Able to retain the previous knowledge<br>2) Existence of memory | Time-consuming |
| Bayesian | Machine Learning | (1) Capable of using with other techniques | (1) Impose restriction on the dependency structure uncovered among its nodes |
| Decision tree | Statistical Analysis | (1) Handles missing values well<br>(2) Robust to outliers | (1) High variance of tree structure<br>(2) Low flexibility<br>(3) Low autonomy |
| ACO | Artificial Intelligence | (1) Incremental solution structure<br>(2) Capable of using problem-based heuristics | (1) Inappropriate for continuous optimization problems. |

## 2.4 Discussion

### 2.4.1 Observations

With the development in the scope of applications of computing tools in recent decades, much research and development has focused on precise systematic solutions for big data problems. Subsequently, data-driven strategies have been employed to obtain useful patterns from Industry 4.0 sensed data. Industry 4.0 technologies such as IoT, blockchain, and UAVs are becoming highly precise and reliable when performing high-complexity tasks. Additionally, these technologies are part of our daily lives. For example, blockchain technology has recently attracted significant attention from practitioners and academics in various fields such as business [127], energy [128], manufacturing [129], smart cities [130], smart grids [131], finance [132], healthcare [133], transportation [134], and also SHM [135]. Hence, computer-based technologies and their applications are becoming ubiquitous in our daily life, especially in different fields of civil engineering. For instance, traditional SHM has been upgraded to IoT-based SHM due to the advantages of using the automation, intelligence, and specialization of new IoT technologies.

### 2.4.2 Challenges and future directions in SHM

Data-driven SHM diagnostics are based on the interpretation of measured data directly, without recourse to physics-based SHM approaches. In general, data-driven methods require large-scale databases to achieve accurate results. However, in real-world civil engineering applications, big data collection is seldom available, as the process of generating high-quality large data is complicated and time-consuming. On the other hand, physics-based approaches rely on the physical laws governing the structural behaviour, which can minimize overfitting issues, present constraints to the predicted results, and moderate the need of big data collection. Therefore, future work is envisaged to concern the application of emerging technologies (e.g. digital twin, virtual reality, and augmented reality) to guarantee more reliable data-driven-based and physics-based SHM approaches, a point highlighted by other researchers too [136, 137].

## 2.5 Conclusions

In-service civil engineering structures will damage during their lifetime due to ageing or different loads such as fatigue, seismic, wind, wave, traffic, blast, or random impact loads during their service life. The propagation of damage can lead to out-of-service conditions. Therefore, traditional structural health monitoring (SHM) has been rapidly upgraded to IR4.0-based SHM. In this context, the impact of IR4.0 applications on SHM was presented in this book chapter. To this end, IoT, blockchain, UAV, and data mining have been reviewed, accordingly.

One of the main advantages of IoT is that it can support real-time applications. In this regard, WSNs, as the basic layer of IoT, have successfully been used for SHM systems. Hence, the conventional physics-based SHM has been enhanced to IoT-based SHM using IoD-based monitor systems, comprising UAVs and/or remote sensing. Such applications of IoT in SHM have been highlighted in this chapter to show the capability of this evolutionary technology for structural damage identification in civil engineering systems. Blockchain is also an emerging decentralized database technology, which could increase the reliability of databases. On the other hand, data mining, which is one of the main components of KDD, has been employed in order to obtain useful patterns from sensed data. Consequently, data mining-based damage identification systems have been shown to be capable of being applied in SHM. For this reason, the latest research focusing on the application of data mining in SHM was also addressed in this chapter. In relation to future work, it is envisaged that emerging technologies (e.g. digital twin, virtual reality, and augmented reality) will be applied to SHM to guarantee more reliable data-driven-based and physics-based SHM approaches.

# References

[1] P. M. Pawar, and R. Ganguli. Structural health monitoring using genetic fuzzy systems. 2011. https://doi.org/10.1017/CBO9781107415324.004.

[2] S. Saadat, M. N. Noori, G. D. Buckner, T. Furukawa, and Y. Suzuki. Structural health monitoring and damage detection using an intelligent parameter varying (IPV) technique. *International Journal of Non-Linear Mechanics*, 39:1687–1697, 2004. https://doi.org/10.1016/j.ijnonlinmec.2004.03.001.

[3] J. P. Amezquita-Sanchez, and H. Adeli. Nonlinear measurements for feature extraction in structural health monitoring. *Scientia Iranica*, 26:3051–3059, 2019. https://doi.org/10.24200/sci.2019.21669.

[4] G. F. Sirca and H. Adeli. Infrared thermography for detecting defects in concrete structures. *Journal of Civil Engineering and Management*, 24:508–515, 2018. https://doi.org/10.3846/jcem.2018.6186.

[5] J. P. Amezquita-Sanchez, M. Valtierra-Rodriguez, and H. Adeli. Wireless smart sensors for monitoring the health condition of civil infrastructure. *Scientia Iranica*, 25:2913–2925, 2018. https://doi.org/10.24200/sci.2018.21136.

[6] J. P. Amezquita-Sanchez, H. S. Park, and H. Adeli. A novel methodology for modal parameters identification of large smart structures using MUSIC, empirical wavelet transform, and Hilbert transform. *Engineering Structures*, 147:148–159, 2017. https://doi.org/10.1016/j.engstruct.2017.05.054.

[7] Z. Li, H. S. Park, and H. Adeli. New method for modal identification of super high-rise building structures using discretized synchrosqueezed wavelet and Hilbert transforms. *Structural Design of Tall and Special Buildings*, 26:e1312, 2017. https://doi.org/10.1002/tal.1312.

[8] C. A. Perez-Ramirez, J. P. Amezquita-Sanchez, H. Adeli, M. Valtierra-Rodriguez, D. Camarena-Martinez, and R. J. Romero-Troncoso. New methodology for modal parameters identification of smart civil structures using ambient vibrations and synchrosqueezed wavelet transform. *Engineering Applications of Artificial Intelligence*, 48:1–12, 2016. https://doi.org/10.1016/j.engappai.2015.10.005.

[9] J. P. Amezquita-Sanchez and H. Adeli. A new music-empirical wavelet transform methodology for time-frequency analysis of noisy nonlinear and non-stationary signals. *Digital Signal Processing: A Review Journal*, 45:55–68, 2015. https://doi.org/10.1016/j.dsp.2015.06.013.

[10] K. Ghaedi, M. Gordan, Z. Ismail, H. Hashim, and M. Talebkhah. A literature review on the development of remote sensing in damage detection of civil structures. *Journal of Engineering Research and Reports*, 20:39–56, 2021. https://doi.org/10.9734/JERR/2021/v20i1017388.

[11] J. M. W. Brownjohn. Structural health monitoring of civil infrastructure. *Philosophical Transactions: Mathematical, Physical and Engineering Sciences*, 365:589–622, 2007. https://doi.org/10.1098/rsta.2006.1925.

[12] M. Gordan, H. A. Razak, Z. Ismail, and K. Ghaedi. Recent developments in damage identification of structures using data mining. *Latin American Journal of Solids and Structures*, 14:2373–2401.

[13] M. Malekzadeh, M. Gul, I. Kwon, and N. Catbas. An integrated approach for structural health monitoring using an in-house built fiber optic system and non-parametric data analysis. *Smart Structures and Systems*, 14:917–942, 2014. https://doi.org/10.12989/sss.2014.14.5.917.

[14] R. H. Plaut. Snap loads and torsional oscillations of the original Tacoma Narrows Bridge. *Journal of Sound and Vibration*, 309:613–636, 2008. https://doi.org/10.1016/j.jsv.2007.07.057.

[15] A. G. Lichtenstein. The silver bridge collapse recounted. *Journal of Performance of Constructed Facilities*, 7:249–261, 1993.

[16] Ś. Ł. Catenary. Action in precast skeleton structures – Protection against progressive collapse. In *15th International Conference of Postgraduate Students JUNIORSTAV 2013*, 2013.

[17] J. Schellhammer, N. J. Delatte, F. Asce, and P. A. Bosela. Another look at the collapse of Skyline Plaza at Bailey's Crossroads, Virginia. *Journal of Performance of Constructed Facilities*, 27:354–361, 2013. https://doi.org/10.1061/(ASCE)CF.1943-5509.0000333.

[18] M. Gordan, S.-Y. S-R, K. Ghaedi, D. P. Thambiratnam, and Z. Ismail. Introduction to optimized monitoring of bridge infrastructure using soft computing techniques. In *Applied Methods in Design and Construction of Bridges, Highways and Roads-Theory and Practice*, IntechOpen Limited, London, 2022. https://doi.org/dx.doi.org/10.5772/intechopen.104905.

[19] D. Venton. Tectonic tremors could offer insights into the big shakers. *Proceedings of the National Academy of Sciences of the United States of America*, 113:7930–7931, 2016. https://doi.org/10.1073/pnas.1610000113.

[20] B. Abdelwahed. A review on building progressive collapse, survey and discussion. *Case Study in Constuction Materials*, 11:e00264, 2019. https://doi.org/10.1016/j.cscm.2019.e00264.

[21] R. A. Swartz, A. Zimmerman, and J. P. Lynch Structural health monitoring system with the latest information technologies. In *Proceedings 5th Infrastructure Environmental management symptoms*. Yamaguchi, Japan, 2007.

[22] E. J. Palin, A. Quinn, I. S. Oslakovic, and K. Gavin. Implications of climate change for railway infrastructure. *Wiley Interdisciplinary Reviews: Climate Change*, 12:1–41, 2021. https://doi.org/10.1002/wcc.728.

[23] S. Selvakumaran, S. Plank, C. Geiß, C. Rossi, and C. Middleton. Remote monitoring to predict bridge scour failure using interferometric synthetic aperture radar ( InSAR) stacking techniques. *The International Journal of Applied Earth Observation and Geoinformation*, 73:463–470, 2018. https://doi.org/10.1016/j.jag.2018.07.004.

[24] BBC News. Tadcaster footbridge over Wharfe opens to reunite flood-split town 2016. https://www.bbc.com/news/uk-england-york-north-yorkshire-35557412.

[25] T. Yarlagadda, H. Hajiloo, L. Jiang, M. Green, and A. Usmani. Preliminary modelling of plasco tower collapse. *International Journal of High-Rise Buildings*, 7:397–408.

[26] C. Russell. Before and after photos of Genoa Bridge collapse. St Ltd, 2018. https://www.stuff.co.nz/world/europe/106302828/before-and-after-photos-of-genoa-bridge-collapse.

[27] H. R. Fatal. Taiwan bridge collapse is latest example of maintenance failings. New Civil Engineer, 2019. https://www.newcivilengineer.com/latest/fatal-taiwan-bridge-collapse-is-latest-example-of-maintenance-failings-07-10-2019/.

[28] A. Anisha, A. Jacob, R. Davis, and S. Mangalathu. Fragility functions for highway RC bridge under various flood scenarios. *Engineering Structures*, 260:114244, 2022. https://doi.org/10.1016/j.engstruct.2022.114244.

[29] M. A. Marzaleh, and M. Peyravi. Lessons learned from the collapse of the metropole building, Iran, 2022. *Disaster Medicine and Public Health Preparedness*, 2022.

[30] Iran News. Debris removal from the collapsed building of Abadan "Metropolis" continue 2022. https://iranpress.com/content/59104/debris-removal-from-the-collapsed-building-abadan-metropolis-continue.

[31] CBS News. Why did the Turkey earthquake do so much damage? Many buildings collapsed like pancakes, 2023. https://www.cbsnews.com/news/turkey-earthquake-damage-many-buildings-collapsed-like-pancakes/.

[32] M. Gordan. Experimental Investigation of Passive Tuned Mass Damper and Fluid Viscous Damper on A Slender Two Dimension Steel Frame. Master Thesis, University Technology of Malaysia (UTM), Malaysia, 2014.

[33] A. Abdelgawad, and K. Yelamarthi. Internet of things (IoT) platform for structure health monitoring. *Wireless Communications and Mobile Computing*, 2017, 2017. https://doi.org/10.1155/2017/6560797.

[34] H. Fathnejat, B. Ahmadi-nedushan, S. Hosseininejad, M. Noori, A. Wael, and F. Altabey e. A data-driven structural damage identification approach using deep convolutional-attention-recurrent neural architecture under temperature variations. *Engineering Structures*, 276:115311, 2023. https://doi.org/10.1016/j.engstruct.2022.115311.

[35] A. M. Alani, M. Aboutalebi, and G. Kilic. Integrated health assessment strategy using NDT for reinforced concrete bridges. *NDT & E International*, 61:80–94, 2014. https://doi.org/10.1016/j.ndteint.2013.10.001.

[36] A. Nair and C. S. Cai. Acoustic emission monitoring of bridges: Review and case studies. *Engineering Structures*, 32:1704–1714, 2010. https://doi.org/10.1016/j.engstruct.2010.02.020.

[37] S. Yehia, O. Abudayyeh, and A.-Q. I. Zalt A. Ground-penetrating radar, chain drag, and ground truth. *Transportation Research Record*, 05:39–50, 2008. https://doi.org/10.3141/2044-05.

[38] J. Steinbach, and E. Vey. Caisson evaluation by stress wave propagation method. *Journal of the Geotechnical Engineering Division*, 101:361–375.

[39] D. M. Mccann, and M. C. Forde. Review of NDT methods in the assessment of concrete and masonry structures. *NDT&E International*, 34:71–84.

[40] T. Suzuki, H. Ogata, R. Takada, M. Aoki, and M. Ohtsu. Use of acoustic emission and X-ray computed tomography for damage evaluation of freeze-thawed concrete. *Construction and Building Materials*, 24:2347–2352, 2010. https://doi.org/10.1016/j.conbuildmat.2010.05.005.

[41] A. G. Davis. The nondestructive impulse response test in North America: 1985–2001. *NDT&E International*, 36:185–193.

[42] P. Shokouhi, J. Wolf, and H. Wiggenhauser. Detection of delamination in concrete bridge decks by joint amplitude and phase analysis of ultrasonic array measurements. *Journal of Bridge Engineering*, 19:04013005, 2014. https://doi.org/10.1061/(ASCE)BE.1943-5592.0000513.

[43] A. Myers, M. A. Mahmud, A. Abdelgawad, and K. Yelamarthi. Toward integrating structural health monitoring with internet of things (IoT). In *IEEE International Conference on Electrical Engineering and Information & Communication Technology*, 438–441. 2016, 2016-Augus. https://doi.org/10.1109/EIT.2016.7535280.

[44] J. Yu, P. Ziehl, F. Matta, and A. Pollock. Acoustic emission detection of fatigue damage in cruciform welded joints. *Journal of Constructional Steel Research*, 86:85–91, 2013. https://doi.org/10.1016/j.jcsr.2013.03.017.

[45] M. R. Hoseini, X. Wang, and M. J. Zuo. Estimating ultrasonic time of flight using envelope and quasi maximum likelihood method for damage detection and assessment. *Measurement: Journal of the International Measurement Confederation*, 45:2072–2080.

[46] M. U. Hanif, Z. Ibrahim, M. Jameel, K. Ghaedi, and M. Aslam. A new approach to estimate damage in concrete beams using non-linearity. *Construction and Building Materials*, 124:1081–1089.

[47] M. Talebkhah, A. Sali, M. Marjani, M. Gordan, S. J. Hashim, and F. Z. Rokhani. Edge computing: Architecture, applications and future perspectives. In *IICAIET2020 (IEEE International Conference on Artificial Intelligence Engineering and Technology)*, Sabah, Malaysia, 2020. https://doi.org/10.1109/IICAIET49801.2020.9257824.

[48] M. A. Mahmud, K. Bates, T. Wood, A. Abdelgawad, and K. Yelamarthi. A complete internet of things (IoT) platform for structural health monitoring (SHM). In *IEEE World Forum Internet Things WF-IoT 2018 – Procedure;2018-Janua*, 275–279. 2018. https://doi.org/10.1109/WF-IoT.2018.8355094.

[49] J. Y. Xu, G. J. Pottie, and W. J. Kaiser. Enabling large-scale ground-truth acquisition and system evaluation in wireless health. *IEEE Transactions on Biomedical Engineering*, 60:174–178, 2013. https://doi.org/10.1109/TBME.2012.2208111.

[50] A. Belghith, A. Koubaa, and E. Shakshuki. Challenges and trends in wireless ubiquitous computing systems. *Personal and Ubiquitous Computing*, 15:781–782, 2011. https://doi.org/10.1007/s00779-011-0368-2.

[51] X. Xie, J. Guo, H. Zhang, T. Jiang, R. Bie, and Y. Sun. Neural-network based structural health monitoring with wireless sensor networks. In *Nature Computational (ICNC), 2013 Ninth International Conference*, 163–167, IEEE, 2013.

[52] F. Casino, T. K. Dasaklis, and C. Patsakis. A systematic literature review of blockchain-based applications: Current status, classification and open issues. *Telemat Informatics*, 36:55–81, 2019. https://doi.org/10.1016/j.tele.2018.11.006.

[53] Z. Hou, A. Hera, and M. Noori. Wavelet-based techniques for structural health monitoring. *Health Assessment of Engineered Structures: Bridges, Buildings and Other Infrastructures. World Scientific*, 179–202, 2013.

[54] C. A. Edeki. *A Comparative Study of Data Mining and Statistical Learning Techniques for Prediction of Canser Survovability*. Capella University, 2012.

[55] M. Gordan, Z. Ismail, H. A. Razak, and Z. Ibrahim. Vibration-based structural damage identification using data mining. In *4th International Congress on Sound and Vibration*, London, 2017.

[56] Y. Lai, Z. Magd, A. Wahab, N. M. M. Maia, and L. Liu. Data Mining in Structural Dynamic Analysis. 2019. https://doi.org/10.1007/978-981-15-0501-0.

[57] O. Avci, O. Abdeljaber, S. Kiranyaz, M. Hussein, M. Gabbouj, and D. J. Inman. A review of vibration-based damage detection in civil structures: From traditional methods to machine learning and deep learning applications. *Mechanical Systems & Signal Processing*, 147:107077.

[58] A. Nayyar, and A. Kumar. *A Roadmap to Industry 4.0: Smart Production, Sharp Business and Sustainable Development*. Switzerland, 2020.

[59] A. Chauhan, S. K. Jakhar, and C. Chauhan. The interplay of circular economy with industry 4.0 enabled smart city drivers of healthcare waste disposal. *Journal of Cleaner Production*, 279:123854, 2021. https://doi.org/10.1016/j.jclepro.2020.123854.

[60] C. Kuo, J. Z. Shyu, and K. Ding. Industrial revitalization via industry 4.0 – A comparative policy analysis among China, Germany and the USA. *Global Transitions*, 1:3–14, 2019. https://doi.org/10.1016/j.glt.2018.12.001.

[61] L. Y. Oliff H. Towards industry 4.0 utilizing data-mining techniques: A case study on quality improvement. *Procedia CIRP*, 63:167–172, 2017. https://doi.org/10.1016/j.procir.2017.03.311.

[62] K. Douaioui, M. Fri, C. Mabroukki, and E. L. A. Semma. The interaction between industry 4.0 and smart logistics: Concepts and perspectives. In *2018 International Colloquium on Logistics and Supply Chain Management*, 128–132, IEEE, 2018. https://doi.org/10.1109/LOGISTIQUA.2018.8428300.

[63] R. M. Van. *The Organisation of Tomorrow: How AI, Blockchain and Analytics Turn Your Business into a Data Organisation*, 2019.

[64] The International Data Corporation (IDC). How You Contribute to Today’s Growing DataSphere and Its Enterprise Impact 2019. https://blogs.idc.com/2019/11/04/how-you-contribute-to-todays-growing-datasphere-and-its-enterprise-impact/.

[65] M. Asay. The Internet of Things will Need Millions of Developers By 2020. Readwrite 2014. https://readwrite.com/internet-of-things-developers-jobs-opportunity/.

[66] M. Talebkhah, A. Sali, M. Marjani, M. Gordan, S. J. Hashim, and F. Z. Rokhani. IoT and big data applications in smart cities: Recent advances, challenges, and critical issues. *IEEE Access [Internet]*, 9:55465–55484, 2021. https://doi.org/10.1109/ACCESS.2021.3070905.

[67] H. Zhang, J. Guo, X. Xie, R. Bie, and Y. Sun. Environmental Effect Removal Based Structural Health Monitoring in the Internet of Things. 2013 Seventh Int Conf Innov Mob Internet Serv Ubiquitous Comput, 512–517, 2013. https://doi.org/10.1109/IMIS.2013.91.

[68] N. M. Kumar and P. K. Mallick. Blockchain technology for security issues and challenges in IoT. *Procedia Computer Science*, 132:1815–1823, 2018. https://doi.org/10.1016/j.procs.2018.05.140.

[69] D. E. Kouicem, A. Bouabdallah, and H. Lakhlef. Internet of things security: A top-down survey. *Computer Networks*, 141:199–221, 2018. https://doi.org/10.1016/j.comnet.2018.03.012.

[70] J. Shuja, R. W. Ahmad, A. Gani, A. I. Abdalla Ahmed, A. Siddiqa, K. Nisar, et al. Greening emerging IT technologies: Techniques and practices. *Journal of Internet Services and Applications*, 8:1–11, 2017. https://doi.org/10.1186/s13174-017-0060-5.

[71] S. V. Leshchev. The infogenesis and infotectonics of electronic culture: New horizons of information technologies. *Scientific and Technical Information Processing*, 42:135–139, 2015. https://doi.org/10.3103/S014768821503003X.

[72] A. Sivasuriyan, D. S. Vijayan, G. Wojciech, Ł. Wodzy, M. Daria, and E. Koda. Practical implementation of structural health monitoring in multi-story buildings. *Buildings*, 11:1–30.

[73] Y. Qu, X. Ming, S. Qiu, M. Zheng, and Z. Hou. An integrative framework for online prognostic and health management using internet of things and convolutional neural network. *Sensors (Switzerland)*, 19, 2019. https://doi.org/10.3390/s19102338.

[74] T. Wang, M. Z. A. Bhuiyan, G. Wang, M. A. Rahman, J. Wu, and J. Cao. Big data reduction for a smart city's critical infrastructural health monitoring. *IEEE Communications Magazine*, 56:128–133, 2018. https://doi.org/10.1109/MCOM.2018.1700303.

[75] A. C. Tokognon, B. Gao, G. Y. Tian, and Y. Yan. Structural health monitoring framework based on internet of things: A survey. *IEEE Internet of Things Journal*, 4:629–635, 2017. https://doi.org/10.1109/JIOT.2017.2664072.

[76] J. Wang, Y. Fu, and X. Yang. An integrated system for building structural health monitoring and early warning based on an Internet of things approach. *International Journal of Distributed Sensor Networks*, 13, 2017. https://doi.org/10.1177/1550147716689101.

[77] C. Scuro, F. Lamonaca, S. Porzio, G. Milani, and R. S. Olivito. Internet of Things (IoT) for masonry structural health monitoring (SHM): Overview and examples of innovative systems. *Construction and Building Materials*, 290:123092, 2021. https://doi.org/10.1016/j.conbuildmat.2021.123092.

[78] S. Nakamoto. *Bitcoin: A Peer-to-Peer Electronic Cash System*. WwwBitcoinOrg, 9. 2008. https://doi.org/10.1007/s10838-008-9062-00

[79] C. Yang, X. Chen, and Y. Xiang. Blockchain-based publicly verifiable data deletion scheme for cloud storage. *Journal of Network and Computer Applications*, 103:185–193, 2018. https://doi.org/10.1016/j.jnca.2017.11.011.

[80] L. Qiao, S. Dang, B. Shihada, M.-S. Alouini, R. Nowak, and Z. Lv. Can blockchain link the future? Digit Commun Networks 2021. https://doi.org/10.1016/j.dcan.2021.07.004.

[81] C. Ebert, P. Louridas, T. M. Fernández-Caramés, and F.-L. P. Blockchain. Technologies in Practice. *IEEE Software*, 37:17–25, 2020. https://doi.org/10.1109/MS.2020.2986253.

[82] A. Dorri, S. S. Kanhere, and R. Jurdak. MOF-BC: A memory optimized and flexible blockchain for large scale networks. *Future Generation Computer Systems*, 92:357–373, 2019. https://doi.org/10.1016/j.future.2018.10.002.

[83] T. Ž and R. Klinc. Potentials of blockchain technology for construction management. *Procedia Engineer*, 196:638–645, 2017. https://doi.org/10.1016/j.proeng.2017.08.052.

[84] A. Sharif, R. Kumar, J. Ouyang, H. T. Abbas, A. Alomainy, K. Arshad, et al. Making assembly line in supply chain robust and secure using UHF RFID. *Scientific Reports*, 11:1–17, 2021. https://doi.org/10.1038/s41598-021-97598-5.

[85] M. Gordan, P. Y. Siow, A. F. Deifalla, O. Z. Chao, Z. Ismail, and K. S. Yee. Implementation of a secure storage using blockchain for PCA-FRF sensor data of plate-like structures. *IEEE Access [Internet]*, 10:84837–84852, 2022. https://doi.org/10.1109/ACCESS.2022.3197776.

[86] A. Ibrahim, M. Irfan, I. Huang, and R. C. C. Cheung. A survey of breakthrough in blockchain technology: Adoptions, applications, challenges and future research. *Computer Communications*, 169:179–201, 2021. https://doi.org/10.1016/j.comcom.2020.12.028.

[87] M. Gordan, Z. Ismail, F. A. Mohd Rahim, O. Z. Chao, Z. Ibrahim, and H. Hashim et al. Defining A conceptual framework for vibration-based damage detection platforms using blockchain. *Journal of Civil Engineering and Materials Application*, 5:25–33, 2021. https://doi.org/10.22034/JCEMA.2021.266308.1049.

[88] T. Rathee and P. Singh. A systematic literature mapping on secure identity management using blockchain technology. *Journal of King Saud University – Computer and Information Sciences*, 2021. https://doi.org/10.1016/j.jksuci.2021.03.005.

[89] B. W. Jo, R. M. A. Khan, and Y. S. Lee. Hybrid blockchain and internet-of-things network for underground structure health monitoring. *Sensors (Switzerland)*, 18, 2018. https://doi.org/10.3390/s18124268.

[90] Y. Yuan, X. Jiang, and X. Liu. Predictive maintenance of shield tunnels. *Tunnelling and UndergroundSpace Technology*, 38:69–86, 2013. https://doi.org/10.1016/j.tust.2013.05.004.

[91] F. Stajano, N. Hoult, I. Wassell, P. Bennett, C. Middleton, and K. Soga. Smart bridges, smart tunnels: Transforming wireless sensor networks from research prototypes into robust engineering infrastructure. *Ad Hoc Networks*, 8:872–888, 2010. https://doi.org/10.1016/j.adhoc.2010.04.002.

[92] L. Y. Ding, C. Zhou, Q. X. Deng, H. B. Luo, X. W. Ye, and Y. Q. Ni, et al. Real-time safety early warning system for cross passage construction in Yangtze Riverbed metro tunnel based on the internet of things. *Automation in Construction*, 36:25–37, 2013. https://doi.org/10.1016/j.autcon.2013.08.017.

[93] A. Menderes, A. Erener, and G. Sarp. Automatic detection of damaged buildings after earthquake hazard by using remote sensing and information technologies. *Procedia Earth and Planetary Science*, 15:257–262, 2015. https://doi.org/10.1016/j.proeps.2015.08.063.

[94] C. Wu, F. Zhang, J. Xia, Y. Xu, G. Li, and J. Xie et al. Building damage detection using U-Net with attention mechanism from pre- and post-disaster remote sensing datasets. *Remote Sensing*, 13, 2021.

[95] Q. Huang, O. Monserrat, M. Crosetto, B. Crippa, Y. Wang, and J. Jiang et al. Displacement monitoring and health evaluation of two bridges using sentinel-1 SAR images. *Remote Sensing*, 10:1–18, 2018. https://doi.org/10.3390/rs10111714.

[96] S. Ghaffarian, N. Kerle, and T. Filatova. Remote sensing-based proxies for urban disaster risk management and resilience: A review. *Remote Sensing*, 10, 2018. https://doi.org/10.3390/rs10111760.

[97] Q. Zhang, C. Ma, X. Meng, Y. Xie, P. Psimoulis, and L. Wu et al. Galileo augmenting GPS single-frequency single-epoch precise positioning with baseline constrain for bridge dynamic monitoring. *Remote Sensing*, 11, 2019. https://doi.org/10.3390/rs11040438.

[98] X. Meng, D. T. Nguyen, J. S. Owen, Y. Xie, P. Psimoulis, and G. Ye. Application of GeoSHM system in monitoring extreme wind events at the forth road bridge. *Remote Sensing*, 11:1–19, 2019. https://doi.org/10.3390/rs11232799.

[99] M. Sedek, and A. Serwa. Development of new system for detection of bridges construction defects using terrestrial laser remote sensing technology. *Egyptian Journal of Remote Sensing and Space Sciences*, 19:273–283, 2016. https://doi.org/10.1016/j.ejrs.2015.12.005.

[100] Y. Xu, J. M. W. Brownjohn, and F. Huseynov. Accurate deformation monitoring on bridge structures using a cost-effective sensing system combined with a camera and accelerometers: Case study. *Journal of Bridge Engineering*, 24:05018014, 2019. https://doi.org/10.1061/(ASCE)BE.1943-5592.0001330.

[101] L. Dong, and J. Shan. A comprehensive review of earthquake-induced building damage detection with remote sensing techniques. *ISPRS Journal of Photogrammetry and Remote Sensing*, 84:85–99, 2013. https://doi.org/10.1016/j.isprsjprs.2013.06.011.

[102] M. Gordan, Z. Ismail, K. Ghaedi, Z. Ibrahim, H. Hashim, and H. Ghayeb et al. A brief overview and future perspective of unmanned aerial systems for in-service structural health monitoring. *Engineering Advances*, 1:9–15, 2021. https://doi.org/10.26855/ea.2021.06.002.

[103] F. Aftab, A. Khan, and Z. Z. Hybrid self-organized. Clustering scheme for drone based cognitive internet of things. *IEEE Access [Internet]*, 7:56217–56227, 2019. https://doi.org/10.1109/ACCESS.2019.2913912.

[104] K. S. Yakovlev, D. A. Makarov, and E. S. Baskin. Automatic path planning for an unmanned drone with constrained flight dynamics. *Scientific and Technical Information Processing*, 42:347–358, 2015. https://doi.org/10.3103/S0147688215050093.

[105] M. Wazid, A. K. Das, N. Kumar, A. V. Vasilakos, and J. J. P. C. Rodrigues. Design and analysis of secure lightweight remote user authentication and key agreement scheme in internet of drones deployment. *IEEE Internet of Things Journal*, 6:3572–3584, 2019. https://doi.org/10.1109/JIOT.2018.2888821.

[106] G. Grieco, R. Artuso, P. Boccadoro, G. Piro, and L. A. Grieco. An open source and system-level simulator for the internet of drones. In *2019 IEEE 30th International Symposium on Personal, Indoor and Mobile Radio Communications PIMRC Work 2019*, 1–6, 2019. https://doi.org/10.1109/PIMRCW.2019.8880832.

[107] V. V. Arutyunov. On the effectiveness of scientific activities in the priority fields of science, technology, and engineering. *Scientific and Technical Information Processing*, 40:180–184, 2013. https://doi.org/10.3103/S0147688213040023.

[108] A. M. Lechner, G. M. Foody, and D. S. Boyd. Applications in remote sensing to forest ecology and management. *One Earth*, 2:405–412, 2020. https://doi.org/10.1016/j.oneear.2020.05.001.

[109] T. Xiang, G-S. Xia, and L Zhang Mini-UAV-based Remote Sensing: Techniques, Applications and Prospectives. ArXiv Prepr ArXiv, 2018.

[110] S. Carroll, J. Satme, S. Alkharusi, N. Vitzilaios, A. Downey, and D. Rizos. applied sciences drone-based vibration monitoring and assessment of structures. *Applied Sciences (Switzerland) [Internet]*, 11, 2021.

[111] Y. Pang, B. K. Chen, W. Liu, S. Fung, and S. N. Lingamanaik. Development of a non-contact and non-destructive laser speckle imaging system for remote sensing of anisotropic deformation around fastener holes. *NDT & E International*, 111:102219, 2020. https://doi.org/10.1016/j.ndteint.2020.102219.

[112] S. Chen, and Y. Tong. Integrated remote sensing and visualization: Phase two. In *Web-GIS Based Bridg Inf Database*, 4. 2012.

[113] P. Milillo, G. Giardina, D. Perissin, G. Milillo, A. Coletta, and C. Terranova. Pre-collapse space geodetic observations of critical infrastructure: The Morandi Bridge, Genoa, Italy. *Remote Sensing*, 11, 2019. https://doi.org/10.3390/rs11121403.

[114] M. Kalaitzakis, S. R. Kattil, N. Vitzilaios, D. Rizos, and M. Sutton. Dynamic structural health monitoring using a DIC-enabled drone. 2019 Int Conf Unmanned Aircr Syst ICUAS 2019, 321–327, 2019. https://doi.org/10.1109/ICUAS.2019.8798270.

[115] R. Herrmann, A. Moortgat-pick, and S. Marx. Vibration Analysis of Structures using a Drone (UAV) based Mobile Sensing Platform. In *Fifth Conference on Smart Monitoring, Assessment and Rehabilitation of Civil Structures*, 1–8. 2019.

[116] D. W. M. Hofmann, and J. Apostolakis. Crystal structure prediction by data mining. *Journal of Molecular Structure*, 647:17–39.

[117] M. Gordan, Z. Ismail, Z. Ibrahim, and H. Hashim. Data Mining Technology for Structural Control Systems: Concept, Development, and Comparison. Recent Trends Artif. Neural Networks, London: IntechOpen Limited, 2019. https://doi.org/10.5772/intechopen.88651.

[118] M. Saltan, S. Terzi, and E. Ug. Backcalculation of pavement layer moduli and Poisson’s ratio using data mining. *Expert Systems with Applications*, 38:2600–2608.

[119] J. Tinoco, A. Gomes Correia, and P. Cortez. Support vector machines applied to uniaxial compressive strength prediction of jet grouting columns. *Computers and Geotechnics*, 55:132–140.

[120] M. Gordan. Data Mining for Structural Damage Identification Using Hybrid Artificial Neural Network Based Algorithm for Beam and Slab Girder. PhD Thesis, University of Malaya, 2020.

[121] M. Gordan, Z. B. Ismail, H. A. Razak, and K. Ghaedi. Optimization-based evolutionary. Data mining techniques for structural health monitoring. *Journal of Civil Engineering and Construction*, 9:14–23.

[122] M. Gordan, H. A. Razak, Z. Ismail, K. Ghaedi, Z. X. Tan, and H. H. Ghayeb. A hybrid ANN-based imperial competitive algorithm methodology for structural damage identification of slab-on-girder bridge using data mining. *Applied Soft Computing Journal*, 88:106013, 2020. https://doi.org/10.1016/j.asoc.2019.106013.

[123] M. Gordan, Z. Ismail, H. Abdul Razak, K. Ghaedi, Z. Ibrahim, and Z. X. Tan et al. Data mining-based damage identification of a slab-on-girder bridge using inverse analysis. *Measurement*, 151:107175, 2020. https://doi.org/10.1016/j.measurement.2019.107175.

[124] Z. X. Tan, D. P. Thambiratnam, T. H. T. Chan, M. Gordan, and H. Abdul Razak. Damage detection in steel-concrete composite bridge using vibration characteristics and artificial neural network. *Structure and Infrastructure Engineering*, 16:1247–1261, 2020. https://doi.org/10.1080/15732479.2019.1696378.

[125] M. Gordan, H. A. Razak, Z. Ismail, and K. Ghaedi. Recent developments in damage identification of structures using data mining. *Latin American Journal of Solids and Structures*, 14:2373–2401, 2017. https://doi.org/10.1590/1679-78254378.

[126] M. Gordan, S. Sabbagh-yazdi, Z. Ismail, K. Ghaedi, P. Carroll, and D. McCrum et al. State-of-the-art review on advancements of data mining in structural health monitoring. *Measurement*, 193:110939, 2022. https://doi.org/10.1016/j.measurement.2022.110939.

[127] S. Gomathi, M. Soni, G. Dhiman, R. Govindaraj, and P. Kumar. A survey on applications and security issues of blockchain technology in business sectors. *Materials Today: Proceedings*, 2021. https://doi.org/10.1016/j.matpr.2021.02.088.

[128] Q. Wang, and M. Su. Integrating blockchain technology into the energy sector – From theory of blockchain to research and application of energy blockchain. *Computer Science Review*, 37:100275, 2020. https://doi.org/10.1016/j.cosrev.2020.100275.

[129] J. Leng, G. Ruan, P. Jiang, K. Xu, Q. Liu, and X. Zhou et al. Blockchain-empowered sustainable manufacturing and product lifecycle management in industry 4.0: A survey. *Renewable and Sustainable Energy Reviews*, 132:110112, 2020. https://doi.org/10.1016/j.rser.2020.110112.

[130] U. Majeed, L. U. Khan, I. Yaqoob, S. M. A. Kazmi, K. Salah, and C. S. Hong. Blockchain for IoT-based smart cities: Recent advances, requirements, and future challenges. *Journal of Network and Computer Applications*, 181:103007, 2021. https://doi.org/10.1016/j.jnca.2021.103007.

[131] A. Hasankhani, S. M. Hakimi, M. Bisheh-Niasar, M. Shafie-khah, and H. Asadolahi. Blockchain technology in the future smart grids: A comprehensive review and frameworks. *International Journal of Electrical Power & Energy Systems*, 129:106811, 2021. https://doi.org/10.1016/j.ijepes.2021.106811.

[132] M. Kowalski, Z. W. Y. Lee, and T. K. H. Chan. Blockchain technology and trust relationships in trade finance. *Technological Forecasting and Social Change*, 166, 2021. https://doi.org/10.1016/j.techfore.2021.120641.

[133] R. Saranya, and A. Murugan. A systematic review of enabling blockchain in healthcare system: Analysis, current status, challenges and future direction. *Materials Today: Proceedings*, 2021. https://doi.org/10.1016/j.matpr.2021.07.105.

[134] R. Chaudhary, A. Jindal, and G Singh. BEST : Blockchain-based secure energy trading in SDN-enabled intelligent transportation system. *Computer and Security*, 85:288–299, 2019. https://doi.org/10.1016/j.cose.2019.05.006.

[135] J. Xu, H. Liu, and Q. Han. Blockchain technology and smart contract for civil structural health monitoring system. *Computer-Aided Civil and Infrastructure Engineering*, 36:1288–1305, 2021. https://doi.org/10.1111/mice.12666.

[136] J. R. Casas, I. Stipanovic, and R. Chacón. D5.1 SHM Digital Twin Requirements for Residential, Industrial Buildings and Bridges. 2022.

[137] A. Sadhu, J. E. Peplinski, A. Mohammadkhorasani, and F. Moreu. A review of data management and visualization techniques for structural health monitoring using BIM and virtual or augmented reality. *Journal of Structural Engineering*, 149:03122006, 2023. https://doi.org/10.1061/(ASCE)ST.1943-541X.0003498.

Arash Karimi Pour, Ehsan Noroozinejad Farsangi*

# 3 Health monitoring of recycled aggregates-reinforced concrete beams retrofitted by concrete jacket using piezoelectric transducers

**Abstract:** Advanced retrofitting techniques from concrete constructions were sensed and contained using an active-damage interrogation (AI) technique that employs a collection of piezoelectric transducers (PT) mounted to members. By cordially enforcing the element using PT and analyzing the structural answer as detected by the PT, the AI scheme enables the capacity to identify, focus, and assess the amount of the disband. The AI system offers a special way to identify whether the transducer/structural link has deteriorated by using both bounty and stage data from multiple actuator/sensor transfer purposes. This investigation examines the viability of employing the AI technique for health monitoring of reinforced concrete (RC) jacketed beams comprising waste aggregate (WA), and it discusses the benefits and drawbacks of this approach.

## 3.1 Introduction

The primary ingredients used to make concrete materials are cement, gravel, sand, and water, but using cement and aggregates entails costly and environmental impressions [1, 2]. As a result, WA is in the preservation of natural possessions and may be utilized in place of cement and natural particles to create concrete mixtures. The influence of WA on the characteristics of concrete has been the subject of several investigations [3, 4, and 5–8]. The impact of using WA on the mechanical behavior of high-strength concrete was explored by Blessen et al. [9]. Concrete's durability decreased as a result of using WA, while its resistance to abrasion and water engagement enhanced. Ganjian et al. [10] discovered a loss in compressive resistance when WA was incorporated. The impact of WA on the compressive resistance of concrete was examined by Aslani et al. [11]. The obtained data demonstrated that there was little impact on compressive resistance. Additionally, Li et al. [12] and Saberian et al. [4] have examined the impact of WA on the mechanical characteristics of the materials employed

---

***Corresponding Author: Ehsan Noroozinejad Farsangi**, Department of Civil engineering, University of British Columbia (UBC), Vancouver, Canada, e-mail: ehsan.noroozinejad@ubc.ca

**Arash Karimi Pour,** Department of Civil engineering, University of Texas at El Paso (UTEP), Texas, USA, e-mail: akarimipour@miners.utep.edu

https://doi.org/10.1515/9783110791426-003

in the base layer of construction. In 2018, Ramdan et al. explored the mechanical and physical behavior of WA concrete. WA was substituted for natural aggregates in their study to the extent of 10–60%. Both fresh and hardened specimens underwent testing. According to the data, employing WA enhanced compressive resistance by roughly 20%. Additionally, adding WA made concrete easier to work with. Usahanuntha et al. [13] investigated the mechanical characteristics and offered suggestions for using WA in concrete. The consequences showed that WA of various shapes may take the place of both fine and coarse aggregates. Additionally, 20% was the ideal replacement content for WA. Awoyera et al. [14] employed WA as fine and coarse particles in different research to examine the impact on concrete behavior. Three, seven, fourteen, and twenty-eight days of curing were employed to control the compressive and tensile resistances. The findings demonstrated that associated with conservative concrete, the compressive and cracking tensile resistance rose greater with curing age.

WA was employed by Wong et al. [15], who also provided a review of the subject. The study's objectives were to examine mechanical behavior and durability-related characteristics. They came to the conclusion that WA, which may replace up to 20% of particles in concrete and increase its resistance and some durability features, is the most practical use of WA. In their 2015 study, Arora and Singh examined the bending fatigue behavior of an RC beam made entirely of WA. The outcomes were contrasted with those of concrete beams made using natural particles. It has been demonstrated that 100% WA in concrete mixtures led to subpar fatigue consequences. The bending characteristics of beams produced from WA were examined by Azad [16]. WA was employed as recycled particles in their investigation. The specimens' compressive resistance, maximum load capability, load-deflection curve, toughness, and failure mechanisms were established. The findings indicated that up to 15% of WA can be incorporated into concrete. Other researchers assessed how well fibers-reinforced coarse WA concrete flexed. According to the findings, adding fibers significantly enhanced flexural resistance, toughness, and deflection. Adding fibers to WA concrete beams is a proven method of enhancing their flexural features, according to prior studies [6, 17]. Additionally, earlier investigations supported the value of fibers in preventing fracture growth [18, 19]. Besides, by boosting tensile resistance and toughness, fibers aid in preventing brittle fractures.

Beams must occasionally be reinforced either before or after concrete casting. Using components like fibers before producing concrete enhances the bending and shear characteristics of beams. The characteristics of fiber-reinforced concrete beams were premeditated by Kim et al. in [20]. The outcomes indicated that, in addition to recovering management of repeated cracking, the capability and energy degeneracy both greatly enhanced. The impact of fibers on the bending features of RC beams was investigated by Altun and Aktas in [21]. To boost energy absorption and control fracture characteristics, fibers were used as an additional ingredient in concrete. The findings show that fibers incorporation increases the ductility and toughness capability of prismatic RC beams.

On the other hand, there are times when it is important to understand how RC beams behave after failing. It is sometimes necessary to repair a damaged RC beam, and one of the most common ways to accomplish it is by using a concrete jacket. Alternatively, recycling rubber, stone, brick, and concrete debris can contribute to environmental protection. These components can be used in addition to concrete or instead of cement or aggregate. Frequent research has been directed at the repair of RC beams using concrete jacketing under certain load configurations. Concrete jacketing was employed by Chalioris and Pourzitidis [22] to repair the shear-damaged RC beams. Initial four-point bending loads consisted of monotonic loading on three shear-conditioned beams. Then, concrete jacketing was used to fix the broken beams by applying them to the bottom width and both of their vertical sides. The resistance and inclusive characteristics of the jacketed specimens were superior to those of the earlier beams, which indicated that jacketing is a potential restoration technique. Altun [23] examined jacketed RC beams subjected to bending in a different investigation. The bending characteristics of the original and jacketed RC beams were examined to determine the impact of jacketing after they had been loaded to its maximum plastic yield under flexure. The consequences exhibited that the mechanical characteristics of the jacketed RC beams were marginally superior to that of the initial specimens. In a different research, Ruano et al. [24] tested for shear and employed fibers as a retrofitting material for RC beams that had been mended and reinforced using concrete jackets. The findings demonstrated the superior resistance and ductility regaining of the restored beams. The load-bearing capability of the jacketed samples that had not been damaged was greater than that of the tested beams. Monir et al. [25] examined the bending characteristics of jacketed RC beams. It is a challenging task to examine retrofitted RC beams while taking the interfacial slide consequence into account. The slide between the jacket and the beam was ignored in their examination and monolithic behavior. In order to scrutinize retrofitted RC beams while taking into consideration the interfacial slip delivery and the real nonlinear characteristics of concrete and steel bars, a simpler technique was applied. With the aid of this approach, it is possible to evaluate the slip and shear stress circulations and determine the impact of the surface level of roughness.

In the past, strain tracking or acoustic emission monitoring approaches have been the mainstays of structural health monitoring, although both have significant drawbacks [26]. These structural strategies call on ongoing observation of the building being assessed in order to spot any structural problems. As a result, the structural health monitoring scheme is turned off in the event of a power outage. Additionally, the correctness and dependability of the acoustic release monitoring procedure are compromised by the environment's ambient noise. Large data storage is needed for acoustic emission monitoring, which is another significant drawback. To qualify and pinpoint the damage using the strain tracking approach, an expensive finite element strain distribution model must be created. This model will be used to liken the restrained strain delivery athwart the member. Furthermore, neither of these structural health monitoring methods is sensitive enough to identify anything but major structural deterioration, which drastically restricts their usefulness. AI, which uses PT to aggressively stimulate and measure the vibration properties of the member, is one of the most auspicious health monitoring approaches presently being developed [27]. The alteration between this vibration sign and that of an unharmed, normal member is then used to derive a measure for the structure's health. Therefore, these structural health-monitoring methods can be categorized as active-vibration-based methods. In comparison to other constructions, concrete jacketing attached to solid concrete may have diverse vibrational properties. This study aims to evaluate the viability of AI approaches for claims in civil engineering, namely for disband and segregation sensing of composite repairs of concrete beams, as well as to identify and confirm certain significant problems related to it. It displays the test results for RC beams instrumented with an AI technique and strengthened with concrete jackets. The findings show a high degree of application potential for civil engineering constructions. While this is happening, several difficult problems that are essential to the effective application of this technology must be studied more.

## 3.2 AI methodology for health monitoring

PT used in AI is attached to or entrenched inside the member and is used for both actuation and sensing. By actively stimulating the member using PT and analyzing the structural reaction as detected by the PT, the AI scheme offers the capability to identify, locate, and assess the severity of damage to the RC beams. The AI technique offers a special way to identify whether the transducer/structure link has deteriorated by using breadth and stage data from the different actuator/sensor transfer purposes. Over wideband stimulation of the transducers, the AI technique actively inspects the member. The signals from the devices are converted to digital form, and each pair's transfer purpose is calculated. For each actuator/sensor combination, the alteration between the existing PT purpose and the baseline transfer function is regularized statistically by the baseline transfer function's standard deviation.

The sum of standard deviations from the baseline is used to express the PT role deviation for individual combinations. The windowed local averaging function is formerly used to process this statistic, known as the transfer function delta, in order to minimize slight variance brought on by haphazard noise. A single metric for evaluating the scale of alteration of that specific transfer function is provided by the swelling average delta, which is created by integrating the windowed transfer purpose delta for each sensor over the whole seismic frequency spectrum. First-level data is provided by the swelling average delta for individual transfer function and is necessary for locating and quantifying beam damage. The cumulative average delta principles may then be merged to provide a damage indicator metric for the individual actuator, which accounts for all sensor pairings. By locating the actuator with the greatest harm indicator metric or damage index, the damage is subsequently confined to a damage region. It is possible to analyze a range of damage index principles further to pinpoint the damage inside the region.

## 3.3 Experimental database

Various volumetric substitution fractions of natural coarse aggregates with WA, 0%, 50%, and 100%, were incorporated to create 200 mm × 250 mm × 2,000 mm dimensions RC beams. The produced beams were first put through a four-point flexural setup until they failed. The beam was then roughly twisted back to its original shape. Then, sensors were installed on the beam and mended with a 50-mm thick concrete jacket. Figure 3.1 demonstrates the configuration of the RC beams.

Different criteria were used to describe the aggregates. WA was used to substitute natural coarse aggregates at three diverse mass fractions: 0%, 50%, and 100%. Figure 3.2 displays the grading curves of the particles employed in this investigation. Additionally, the features of employed aggregates are listed in Table 3.1.

To create an RC beam, cement was combined with gravel and sand, followed by the addition of water and a high-performance superplasticizer to evenly disperse the elements inside the concrete matrix. Table 3.2 lists the concrete mixtures and the compressive and tensile test results that were achieved. The overall water/cement fraction of all mixtures was held constant at 0.41 due to the similar physical characteristics of natural and waste aggregates. Six 150 mm × 300 mm cylinders were created and verified underneath a hydraulic jack in order to assess the compressive and tensile resistance of samples. The average compressive and tensile resistances of three of the cylinders were used for each blend as per ASTM C293-08 [28], BS EN 12,390-1 (2008).

## 3.4 Disband detection

A test was carried out on beams to measure the AI for bond detection of jacketed repair RC beams, as shown in Figure 3.3. The location of the AI system used in the experimental program is also shown in these figures [29–34]. As can be observed, the AI system consists of an AI dispensation section, a transducer signal production and data system, and one PT placed in the structure being evaluated. A fervor signal source and data acquisition board, which are electrically connected to the actuator/sensor arrangement, are part of the transducer signal group and data-gaining system. A microprocessor is part of the AI dispensation area and is used to run essential computational and numerical dispensation trials.

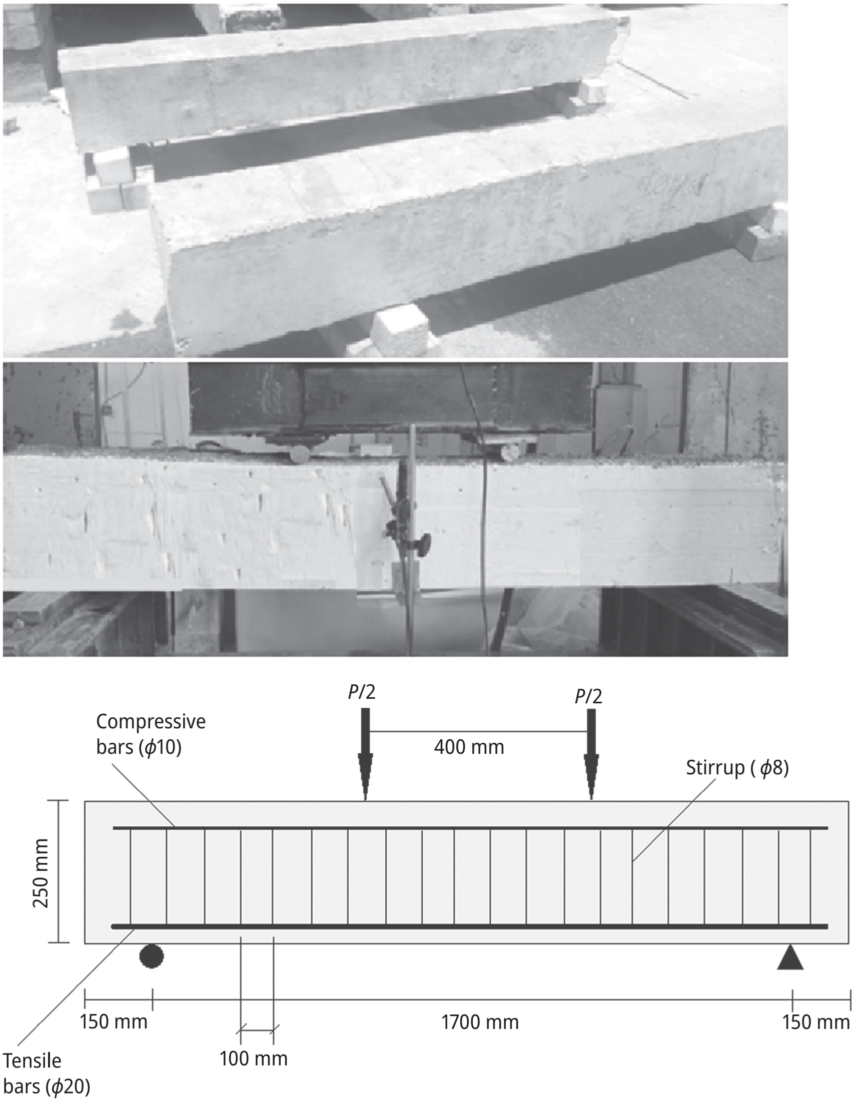

**Figure 3.1:** Arrangement of the bars, the beams' geometry, and other components.

## 3.5 Experimental procedure for debonding detection

The instrumentation's transducer is activated by the AI scheme's operation throughout a frequency range of 0 to 150 kHz via wideband accidental acceleration. The information-gaining scheme digitizes the equivalent signals generated by the sensors in re-

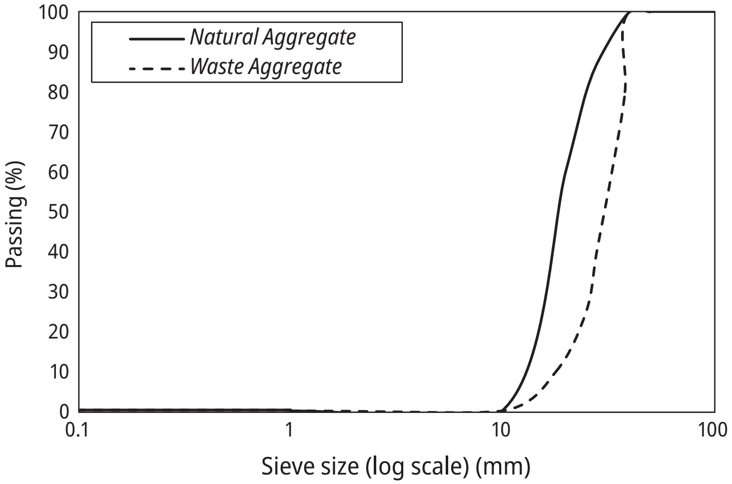

**Figure 3.2:** Used aggregate size distribution.

**Table 3.1:** Physical characteristics of employed aggregates.

| Aggregate sort | Apparent density (g/cm$^3$) | Bulk density (g/cm$^3$) | Water absorption (wt%) | Crushing key (%) | Porosity (%) |
|---|---|---|---|---|---|
| Natural | 2.69 | 2.43 | 1.394 | 29.0 | 3.74 |
| Waste | 2.48 | 2.28 | 1.427 | 39.2 | 3.34 |

**Table 3.2:** Concrete mixtures arrangement and resistances.

| Materials | 0%WA | 50%WA | 100%WA |
|---|---|---|---|
| Water | 170 | 170 | 170 |
| Cement | 415 | 415 | 415 |
| Coarse WA | 0.0 | 425 | 840 |
| Coarse natural aggregates | 850 | 0 | 0 |
| Fine natural aggregates | 940 | 950 | 950 |
| Average tensile stress (MPa) | 3.68 | 3.57 | 4.87 |
| Tensile stress coefficient of variation | 0.19 | 0.12 | 0.11 |
| Average compressive strength (MPa) | 35.2 | 34.3 | 31.8 |
| Compressive strength coefficient of variation | 2.02 | 1.74 | 3.67 |

sponse to this stimulation. The AI dispensation portion next uses the fast Fourier transform to calculate the transfer function (TF) bounty and segment for each sensor in the arrangement. The transfer purpose for individual sensors of the sensor arrangement is then used to calculate the vibration sign of the beams under examination. The test procedure was examined using the experimental setup seen in Figure 3.3 after the jacketing repair had had time to cure.

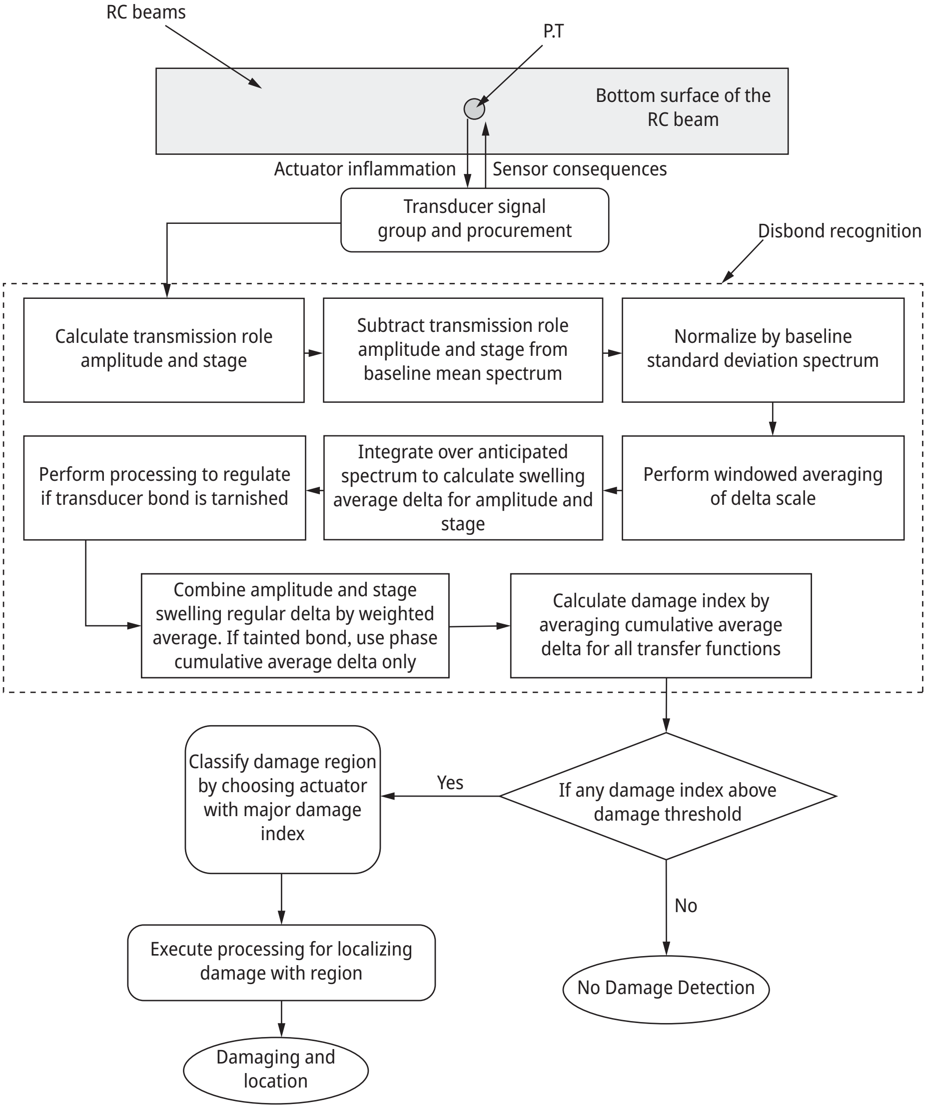

**Figure 3.3:** Calculation procedure for debonding measurement.

### 3.5.1 Segregation documentation

An experiment using jacketed RC beams was carried out using the AI system to show the effectiveness of the AI approach in diagnosing the segregation in strengthened RC beams. Three RC beams having various WA amounts strengthened with concrete jackets were employed, as shown in Figure 3.1. To pinpoint the segregation using the AI system, beams containing a 10 × 25 × 100-mm notch measuring in the bottom of the beam at mid-span were employed to create baseline signals. The segregation procedure was started and accelerated by the notch. In this experimental method, the rate of load until was kept 5 kN/min till the first cracking, and after the occurrence of cracking, the loading rate was reduced to 2 kN/min until the sample completely failed. As observed in Figure 3.4, the bottom surface of the beams was separated into regions I, II, and III in order to locate and recognize the damaged region inside the beam. A total of four PTs were used to instrument each region. Figure 3.4 depicts where the PTs are. Using the AI setup method depicted in Figure 3.3, the AI signals were generated at 10, 60, and 80% of the beam's maximum capacity.

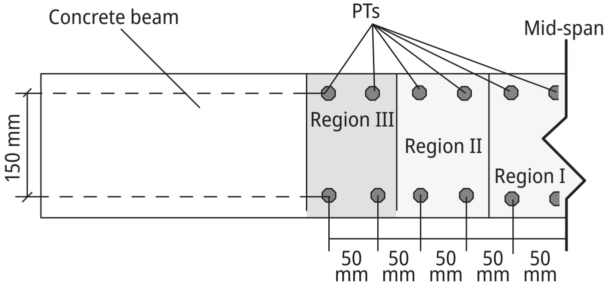

**Figure 3.4:** Arrangements of regions and PTs.

## 3.6 Results and argument

### 3.6.1 Disbond detection

The TF magnitude spectrums of strengthened RC beams are shown in Figure 3.5. The damaged conditions acquired by the PT were obviously different from one another. Peaks in the magnitude spectrum of the TF correspond to local structural characters at advanced frequencies and global structural modes at inferior frequencies. Similar modifications in the structure's vibration sign are brought on fractures and segregation for RC beams having WA.

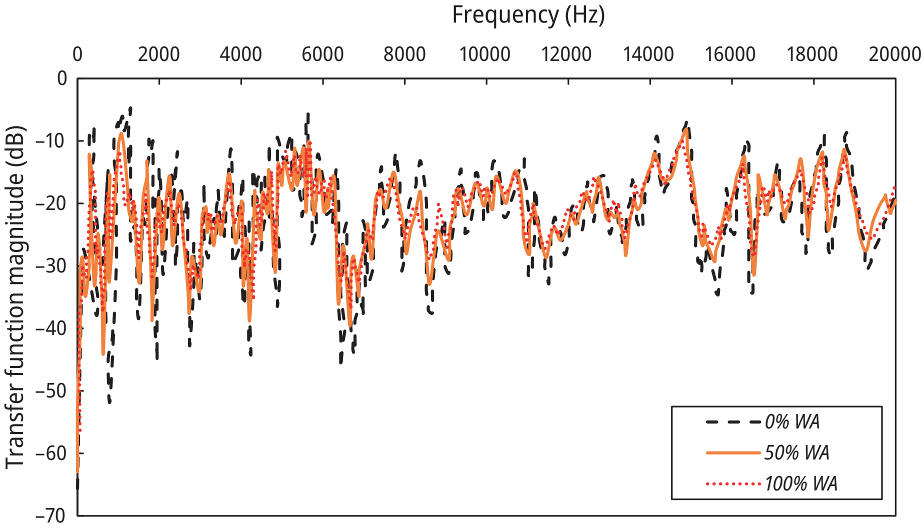

**Figure 3.5:** Magnitude spectra of the transfer functions for strengthened RC beams having WA.

The swelling average delta findings for undamaged and damaged bonds are shown in Figures 3.6 and 3.7. In these figures, the TF amplitude and stage values calculated by the AI scheme for undamaged and damaged bonds were measured. These consequences exhibited that the cumulative average delta values of the damaged beams were greater. Additionally, the WA incorporation leads to raising swelling average delta values. This is because the concrete jacketing fix has come away from the concrete surface. In order to identify the deteriorated bond in the PT, the specific swelling average deltas for stage and amplitude must be calculated. The bond is said to be in good standing if the difference stays below a set cutoff, which is often a tiny portion of the total cumulative average delta that is presumed to be 1. The bond is regarded as deteriorated if the amplitude cumulative average delta surpasses the phase cumulative average delta by an amount larger than the edge. The bond is acceptable for a conventional concrete beam without WA, since the variance among the cumulative average delta amplitude and cumulative average delta phase is 2.48; however, the bond is not good for damaged specimens because the variance among the cumulative average delta amplitude and cumulative average delta stage is 10. These outcomes amply demonstrate the AI system's capability to identify damage and gauge its severity.

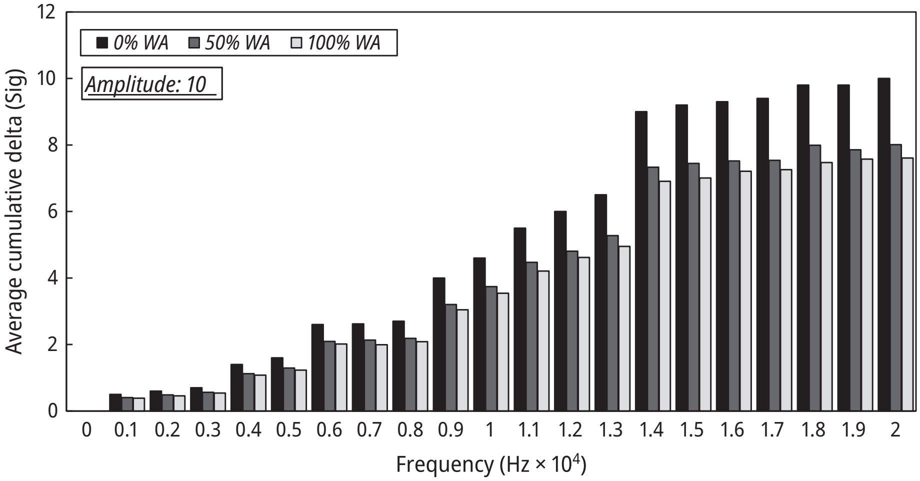

**Figure 3.6:** Cumulative average delta data for undamaged band specimens.

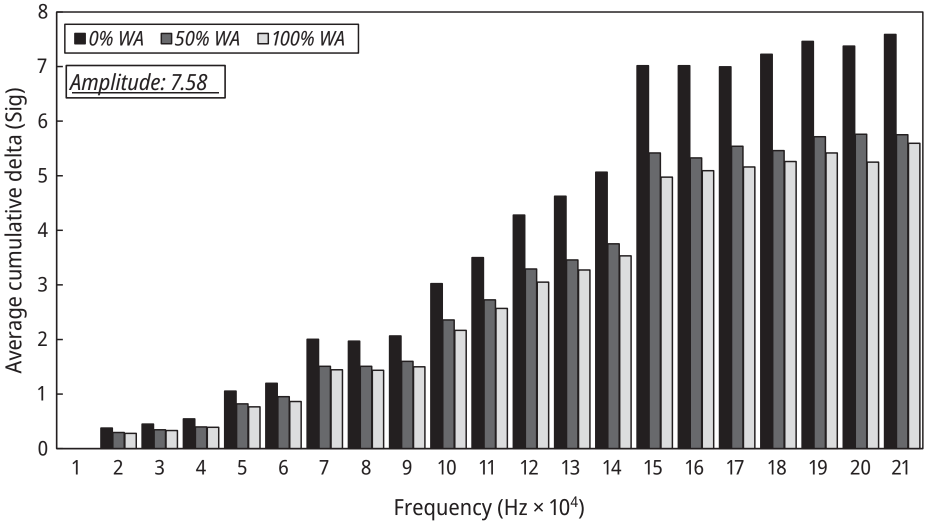

**Figure 3.7:** Cumulative average delta data for damaged band specimens.

### 3.6.2 Segregation detection

The damage index for the individual actuator is calculated as the first phase in determining the damage. Getting a single metric for each actuator entails averaging the cumulative average delta principles for individual TFs using that actuator. The damage region with high segregation was located using the actuator with the peak damage index. The greatest damage index for regions I, II, and III was shown in Figure 3.8 prior to the beam being loaded. The damage indices derived from the AI scheme are inferior because the contact between the concrete jackets and the beam was still intact prior to loading, as shown in Figure 3.8. The damage indices for regions I, II, and III with a 150 kN applied stress are shown in Figure 3.9. As can be observed, region I experiences a little segregation when the performed stress exceeds 150 kN. This was increased further when the WA fraction increased in RC beams. This is due to the fact that interfacial cracking lengthways of the concrete jackets–beam interface started from the lowest surface of the flexural crack when the performed force exceeded the cracking load of the beam, particularly when WA was used. A diagonal crack began at the end of the interfacial fracture and spread across the bending crack when a load of 180 kN was applied. It was discovered that the diagonal crack sped up the interfacial crack's continued extension into region II. This cracking performance supported the damage index in Figure 3.10. Regions I and II, respectively, exhibit considerable and little segregation, as seen in Figure 3.10. Region III's concrete jacket–beam interface, however, is still in good shape. Interfacial fractures spread in region II until 200 mm from the mid-span when the performed load reached 210 kN, which was 80% of the maximum beam capacity. This resulted in big and small segregations in regions II and III, correspondingly, as illustrated in Figure 3.11.

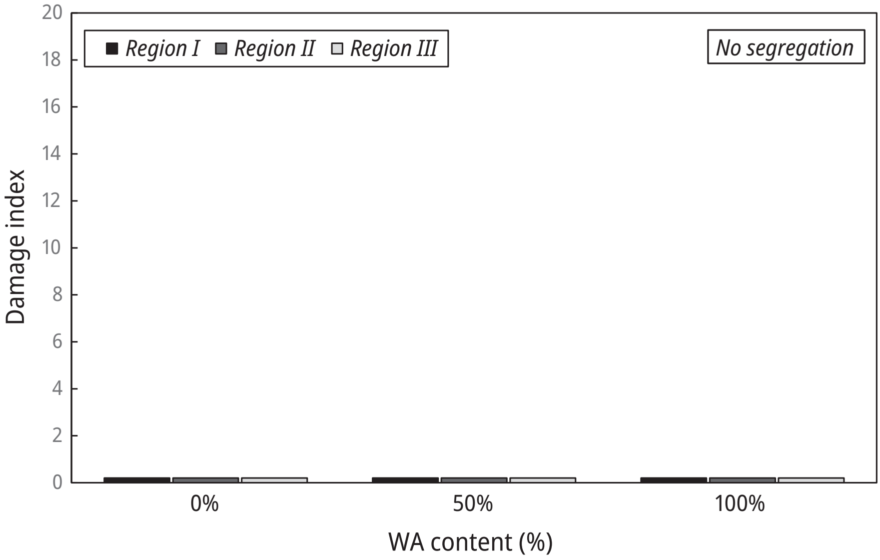

**Figure 3.8:** Damage index for various regions prior to loading.

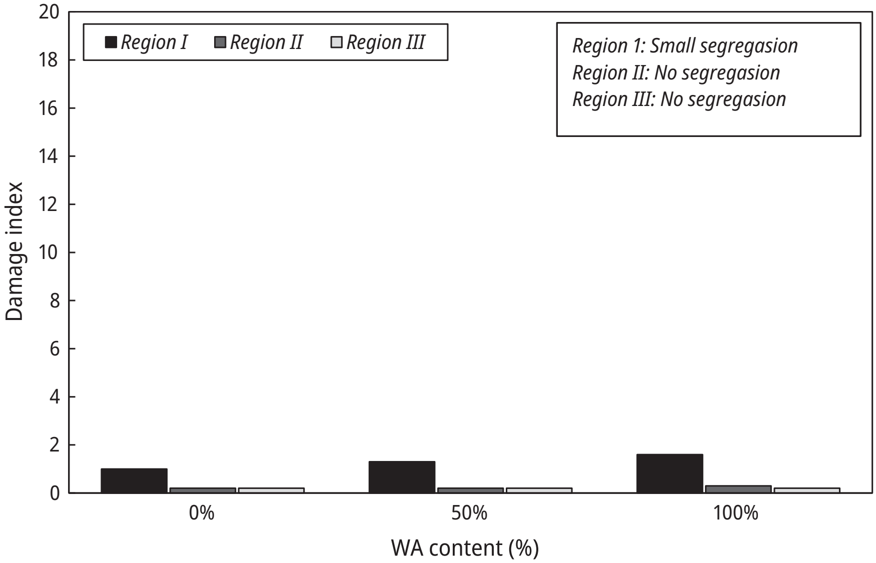

**Figure 3.9:** Damage index for various regions at 150 kN load.

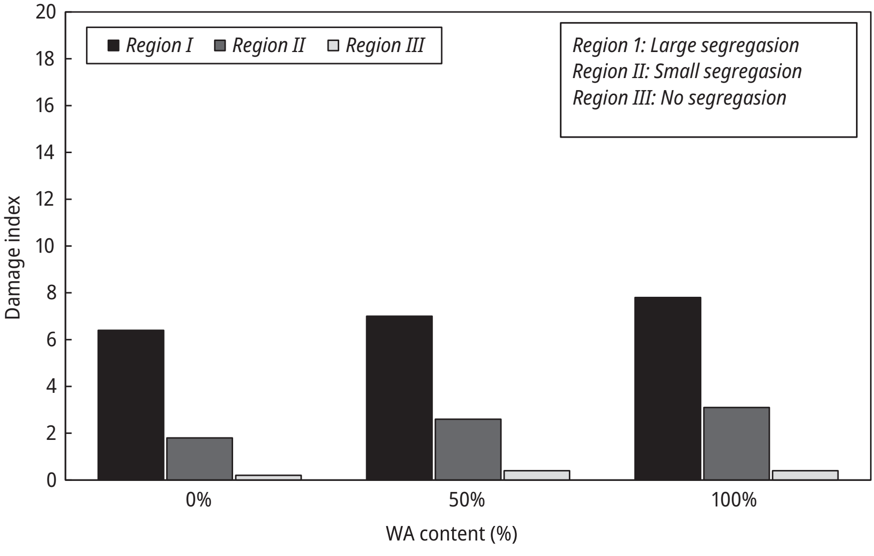

**Figure 3.10:** Damage index for various regions at 180 kN load.

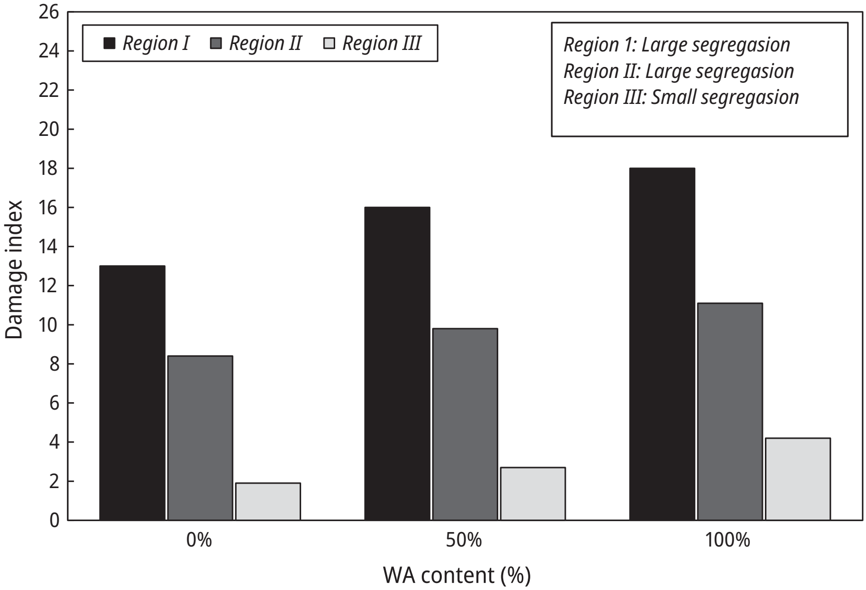

**Figure 3.11:** Damage index for various regions at 210 kN load.

## 3.7 Conclusions

In order to monitor the health of RC beams containing various WA fractions repaired and strengthened using concrete jacketing, the study introduces an AI system that makes use of a variety of PT connected to or embedded inside the beam. The results of the aforementioned studies show that AI can locate disbands and segregation in concrete that has been outwardly reinforced with concrete jackets. Segregations in jacketed RC beams that were being loaded were successfully found. The experimental fracture spread and segregation effects findings supported the damage indices derived from the PT. The damage index was discovered to rise with rising applied load in each region, particularly when WA was employed. This could be associated with the lower resistance of WA in comparison with natural aggregates, which leads to increasing the crack width and propagation. RC beams' damage that was strengthened using concrete jacketing was accurately localized with a 0.24% inaccuracy. The AI approach seems to be a viable way to determine the damage and its severity in RC beams retrofitted with concrete jackets regarding the testing findings. The endurance of PT sensors under dynamic loads and ecological influences is a concern that has to be addressed in additional research and testing before the AI system is employed in field tenders.

# References

[1] A. Karimi Pour, A. Shirkhani, M. S. Kirgiz, and E. Noroozinejad Farsangi. Influence of fiber type on the performance of reinforced concrete beams made of waste aggregates: experimental, numerical and cost analyses. *Practice Periodical on Structural Design and Construction*, 16:42, 2023.

[2] M. Sutcu, O. Gencel, E. Erdogmus, O. Kizinievic, V. Kizinievic, A. Karimi Pour, and P. M. Velasco. Low cost and eco-friendly building materials derived from wastes: Combined effects of bottom ash and water treatment sludge. *Construction and Building Materials*, 324:126669, 2022.

[3] S. Boukour, and M. L. Benmalek. Performance evaluation of a resinous cement mortar modified with crushed clay brick and tire rubber aggregate. *Construction and Building Materials*, 120:473–481, 2016.

[4] M. Saberian, J. Li, and B. Nguyen. Permanent deformation behaviour of pavement base and subbase containing recycle concrete aggregate, coarse and fine crumb rubber. *Construction and Building Materials*, 178:51–58, 2018.

[5] L. J. Hunag, H. Y. Wan, and Y. W. Wu. Properties of the mechanical in controlled low-strength rubber lightweight aggregate concrete (CLSRLC). *Construction and Building Materials*, 112:1054–1058, 2016.

[6] A. Karimi Pour, Z. Mohajeri, and E. Noroozinejad Farsangi. Impact of polypropylene fibers on the mechanical and durability characteristics of rubber tire fine aggregate concrete. *Materials*, 2022.

[7] A. Khitab, M. S. Kırgız, M. L. Nehdi, J. Mirza, A. G. De Sousa Galdino, and A. Karimi Pour. Mechanical, thermal, durability and microstructural behavior of hybrid waste-modified green reactive powder concrete. *Construction and Building Materials*, 344:128184, 2022.

[8] O. Gencel, S. M. Saleem Kazmi, M. J. Munir, G. Kaplan, O. Y. Bayraktar, D. O. Duygu Ozturk Yarar, A. Karimi Pour, and M. R. Ahmad. Influence of bottom ash and polypropylene fibers on the physicomechanical, durability and thermal performance of foam concrete. *An Experimental Investigation, Construction and Building Materials*, 306:124887, 2021.

[9] S. Blessen, R. Thomas, and G. Chandra. Properties of high strength concrete containing scrap tire rubber. *Journal of Cleaner Production*, 113:86–92, 2015.

[10] E. Ganjian, M. Khorami, and A. Maghsoudi. Scrap-tyre-rubber replacement for aggregate and filler in concrete. *Construction and Building Materials*, 23:1828–1836, 2009.

[11] F. Aslani, G. Ma, D. Law, and Y. Wan. Experimental investigation into rubber granules and their effects on the fresh and hardened properties of self-compacting concrete. *Journal of Cleaner Production*, 12.003:2017.

[12] J. Li, M. Saberian, and B. Bao Thach Nguyen. Effect of crumb rubber on the mechanical properties of crushed recycled pavement materials. *Journal of Environmental Management*, 218:291–299, 2018.

[13] N. Usahanuntha, S. Tuprakaya, W. Kongsonga, and S. R. Tuprakay. study of mechanical properties and recommendations for the application of waste Bakelite aggregate concrete. *Case Studies in Construction Materials*, 8:299–314, 2018.

[14] P. O. Awoyera, J. M. Ndambuki, J. O. Akinmusuru, and D. O. Omole. Characterization of ceramic waste aggregate concrete. *Housing and Building National Research Centre HBRC Journal*, 10:1687–4048, 2016.

[15] C. L. Wong, K. H. Mo, S. P. Yap, U. J. Alengaram, and T. C. Ling. Potential use of brick waste as alternate concrete-making materials: A review. *Journal of Cleaner Production*, 6526:31539–7, 2017.

[16] A. M. Azad. Flexural behaviour and analysis of reinforced concrete beams made of recycled PET waste concrete. *Construction and Building Materials*, 155:593–604, 2017.

[17] Y. Guo, J. Zhang, G. Chen, and Z. Xie. Compressive behaviour of concrete structures incorporating recycled concrete aggregates, rubber crumb and reinforced with steel fibre, subjected to elevated temperatures. *Journal of Cleaner Production*, 72:193–203, 2014.

[18] A. Meda, F. Minelli, and G. A. Plizzari. Flexural behaviour of RC beams in fibre reinforced concrete. *Composites, Part B*, 43:2930–2937, 2012.

[19] M. N. Soutsos, T. T. Le, and A. P. Lampropoulos. Flexural performance of fibre reinforced concrete made with steel and synthetic fibres. *Construction and Building Materials*, 36:704–710, 2012.

[20] D. J. Kim, A. E. Naaman, and S. El-Tawil. Comparative flexural behaviour of four fibre reinforced cementitious composites. *Cement and Concrete Composites*, 30:917–928, 2008.

[21] F. Altun, and B. Aktas. Investigation of reinforced concrete beams behaviour of steel fibre added lightweight concrete. *Construction and Building Materials*, 38:575–581, 2013.

[22] C. E. Chalioris and C. N. Pourzitidis. Self-compacting concrete jacketing – tests and analysis. *AASRI Procedia*, 3:624–629, 2012.

[23] F. Altun. An experimental study of the jacketed reinforced-concrete beams under bending. *Construction and Building Materials*, 18:611–618, 2004.

[24] G. Ruano, F. Isla, R. I. Pedraza, D. Sfer, and B. Luccioni. Shear retrofitting of reinforced concrete beams with steel fibre reinforced concrete. *Construction and Building Materials*, 54:646–658, 2014.

[25] A. M. Monir, A. Maged, and A. Youssef. Analysis of reinforced concrete beams strengthened using concrete jackets. *Engineering Structures*, 132:172–187, 2017.

[26] M. Davor and M. Richard. Thermal imaging technique to detect delamination in CFRP plated concrete. *SPI Proceedings*, 3396:22–27, 1998.

[27] P. Lichtenwalner and J. Dunne. Active damage interrogation system for health monitoring. *SPI Proceedings*, 3044:186–194, 1997.

[28] ASTM C293-08. Standard test method for flexural strength of concrete (Using simple beam with centre-point loading). *ASTM International*, 2008.

[29] S. Ramdan, A. Guettala, M. L. Benmalek, and J. B. Aguiar. Physical and mechanical performance of concrete made with waste rubber aggregate, glass powder and silica sand powder. *Journal of Building Engineering*, S2352–7102:30717–307174, 2018.

[30] G. C. Beheraa, T. D. Gunneswara, and C. B. K. Raob. Torsional behaviour of reinforced concrete beams with ferrocement U-jacketing – Experimental study. *Case Studies in Construction Materials*, 4:15–31, 2016.

[31] S. Arora, and S. P. Singh. Analysis of flexural fatigue failure of concrete made with 100% coarse recycled concrete aggregates. *Construction and Building Materials*, 102:782–791, 2016.

[32] J. A. Carneiro, P. R. L. Lima, M. B. Leite, and R. D. Filho. Compressive stress-strain behaviour of steel fibre reinforced-recycled aggregate concrete. *Cement and Concrete Composites*, 46:65–72, 2014.

[33] BS EN 12390-1. Testing hardened concrete: Shape, dimensions and other requirements for specimens and moulds. *British Standards Institution*, 2000.

[34] A. Karimi Pour, A. Shirkhani, M. S. Kirgiz, and E. Noroozinejad Farsangi. Experimental investigation of GFRP-reinforced concrete columns made with waste aggregates under concentric and eccentric loads. *Structural Concrete*, 1–19.

Shun Nakata, Kohei Fujita, Izuru Takewaki*

# 4 Identification of critical response of bilinear-hysteretic SDOF model with tuned inertial mass damper under long-duration ground motion through internal simulation monitoring

**Abstract:** In this paper, the critical (resonant) response of an elastic–plastic single-degree-of-freedom (SDOF) model with a tuned inertial mass damper is derived under a long-duration ground motion. This means a kind of system identification of nonlinear passive control structures through internal monitoring by numerical simulation. Tuned inertial mass dampers exhibit high seismic performance when optimally tuned to the natural period of the structure. However, if the structure shows an elastic–plastic response and the natural period fluctuates from the original one, the damper cannot guarantee its performance. A multi impulse introduced by Kojima and Takewaki [1, 2] is used as a representative of long-duration ground motions. This substitution allows us to evaluate the critical resonant response of the elastic–plastic SDOF model without iterative and time-consuming computation. Finally, the resonance curve of elastic–plastic SDOF models [2, 3] is extended to the nonlinear model with the tuned inertial mass damper, and it is demonstrated that the proposed evaluation method shows a good agreement with the result for the corresponding sinusoidal wave.

## 4.1 Introduction

To investigate the uncertain effect of long-duration and long-period ground motions on the building structural response, the theory on the elastic–plastic response of a damped multi-degree-of-freedom (MDOF) model to the critical multi impulse was developed by Akehashi et al. [4] and Kawai and Takewaki [5] based on the approach by Kojima and Takewaki [6]. In this paper, it is extended to an SDOF elastic–plastic model with a tuned inertial mass damper (TIMD) under the critical multi impulse and the corresponding critical response is derived. This indicates a kind of system identification of nonlinear passive control structures through internal monitoring by numerical simulation.

---

***Corresponding author: Izuru Takewaki,** Department of Architecture and Architectural Engineering, Kyoto University, Kyoto, Japan, https://orcid.org/0000-0002-5673-2409
**Shun Nakata**, Department of Architecture and Architectural Engineering, Kyoto University, Kyoto, Japan
**Kohei Fujita**, Department of Architecture and Architectural Engineering, Kyoto University, Kyoto, Japan, https://orcid.org/0000-0002-4292-6819

https://doi.org/10.1515/9783110791426-004

Kojima and Takewaki [1] proposed a method using multi impulse to approximate long-duration ground motions whose velocity waveforms can be represented by harmonic waves. By replacing the inputs with impulses, it was made possible to find the resonance response characteristics of elastic–plastic structures with low computation load. Subsequently, Kojima abd Takewaki [2] developed a critical excitation method for undamped SDOF systems with bilinear hysteretic properties under multi impulse. Then, Akehashi et al. [4] extended the problem to elastic–plastic SDOF systems with linear viscous damping. Furthermore, Kawai and Takewaki [5] treated a damped MDOF model with bilinear restoring force characteristics and extended the concept of double impulse pushover (DIP) developed by Akehashi and Takewaki [7] for near-fault ground motions to MIP (multi impulse pushover), which is to evaluate the resonant elastic–plastic response under multi impulse as replacement of long-period long duration ground motions.

The design method of tuned mass dampers for elastic–plastic structures can be developed by using the method of equivalent linearization based on the least-squares approximation method proposed by Caughey [8, 9]. Although the resonant response can be directly evaluated for an undamped SDOF system in the Caughey’s method, the accuracy may not be guaranteed in the range where the ratio of post-yield stiffness to elastic stiffness is relatively small as found in actual building structures. Accurate period evaluation is essential for the design of tuned mass dampers and is not suited to the equivalent linearization method. The methods of Caughey [8, 9] and Iwan [3] were developed under the condition of constant acceleration amplitude, but in the current seismic design standards, the input seismic motion level is defined by the maximum velocity amplitude when designing structures. These methods cannot be directly applied to the design of seismically controlled structures such as those treated in this study. In contrast, the multi impulse method proposed by Kojima and Takewaki [1] enables the critical response evaluation using the maximum velocity amplitude as a parameter. Furthermore, Akehashi and Takewaki [7] defined the critical impulse input timing for an MDOF model as “the timing that maximizes the input energy due to the impulse to the structure”. According to this definition, the resonance of the structures in the elastic–plastic range can be computed without performing iterative computations.

## 4.2 Multi impulse representing long-duration ground motion

The multi impulse was introduced to represent the principal part of a long-duration ground motion simulated as a multi-cycle sine wave [1]. The motivation is that, while the combination of free- and forced-vibration components is inevitable in the analysis of the response to the forced input, the multi impulse induces only a free-vibration. This enables us to avoid the solution of the transcendental equation characterizing resonance curves and use a simple energy balance law to derive the maximum response without laborious time-history response analysis. The essential property of a long-duration ground motion is first simulated by multi-cycle sine wave $\ddot{u}_g^{\mathrm{SW}}(t)$ as shown in eq. (4.1) (see Figure 4.1) and then transformed into a double impulse $\ddot{u}_g^{\mathrm{MI}}(t)$ expressed by eq. (4.2) (see Figure 4.2):

$$\ddot{u}_g^{\mathrm{SW}}(t) = A_l \sin \omega_l t \tag{4.1}$$

$$\begin{aligned} \ddot{u}_g^{\mathrm{MI}}(t) &= 0.5V\delta(t) - V\delta(t-t_0) + V\delta(t-2t_0) \\ &\quad - V\delta(t-3t_0) + \cdots + (-1)^{N-1}V\delta(t-(N-1)t_0) \end{aligned} \tag{4.2}$$

where $A_l$, $\omega_l$, $V$, and $t_0$ indicate the acceleration amplitude of the multi-cycle sine wave, circular frequency of the multi-cycle sine wave, the velocity amplitude of the multi impulse, and the time interval of each impulse ($N$: impulse number), respectively. Kojima and Takewaki [1] used a criterion in this transformation, that is, the same maximum Fourier amplitude of these two inputs.

The ratio $a$ of $A_l$ to $V$ in this transformation is introduced by

$$A_l = aV \tag{4.3}$$

The parameter $a$ as a function of $t_0 = \pi/\omega_l$ can be derived as

$$a(t_0) = \frac{A_l}{V} = \frac{\max\limits_{\omega}\left|\sum\limits_{n=0}^{N-1}(-1)^n e_0^{-i\omega n t_0}\right|}{\max\limits_{\omega}\left|\frac{2\pi t_0}{\pi^2-(\omega t_0)^2}\sin 0.5N\omega t_0\right|} \tag{4.4}$$

The maximum velocity $V_p$ of the multi-cycle sine wave can then be expressed by

$$V_l = \frac{A_l}{\omega_l} = \frac{2}{\pi}V \tag{4.5}$$

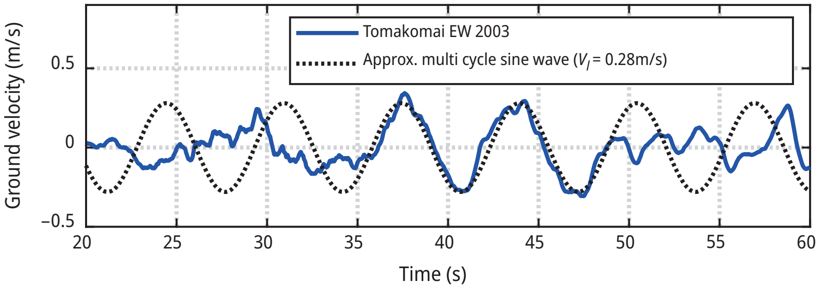

**Figure 4.1:** Transformation of main part of ground motion (Tomakomai EW component during Tokachioki earthquake 2003) by multi impulse.

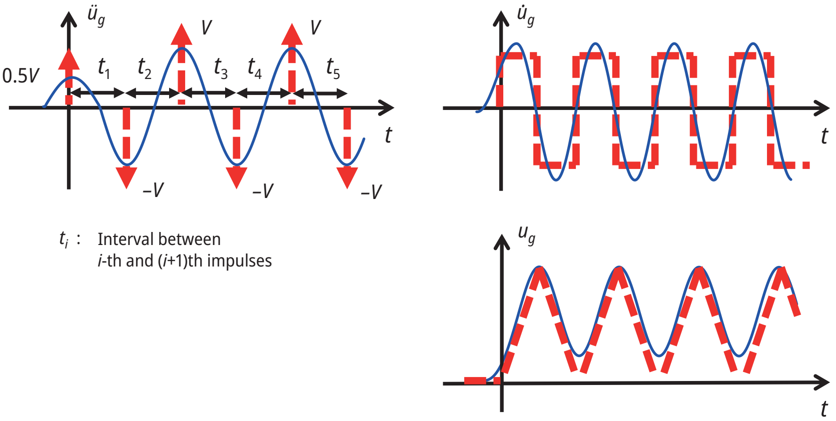

**Figure 4.2:** Long duration earthquake ground motion in terms of sinusoidal waves and corresponding multi impulse [1, 5].

## 4.3 Tuned inertial mass damper

The present TIMD is composed of three elements: an inertial mass element, a viscous element, and a stiffness element of the supporting member. In this study, the inertial mass element and the viscous element are configured in parallel, and these two elements are supported in series by a stiffness element. For the detailed explanation of this damper, see Ikago et al. [10, 11]. Although TIMD has three design variables, when the mass ratio, that is, the ratio of the inertial mass of the damper to the mass of the structure, is given, the other two parameters, that is, the damping coefficient and the stiffness, can be automatically obtained using the fixed-point theory [10, 12–14]. It should also be noted that the inertial mass damper (IMD) is realized with a rotational mechanism [15]. This mechanism has the property of amplifying the apparent mass by several thousand times the actual mass. Aside from the damper configuration treated in this study, quite a few applications of IMD are investigated such as a tuned inerter damper (TID, [16]) and a tuned mass damper inerter (TMDI, [17]).

The equation of motion of the model shown in Figure 4.3 is described as

$$\begin{bmatrix} m & 0 \\ 0 & z \end{bmatrix} \begin{Bmatrix} \ddot{u} \\ \ddot{u}_z \end{Bmatrix} + \begin{bmatrix} c & 0 \\ 0 & c_z \end{bmatrix} \begin{Bmatrix} \dot{u} \\ \dot{u}_z \end{Bmatrix} + \begin{bmatrix} k+k_z & -k_z \\ -k_z & k_z \end{bmatrix} \begin{Bmatrix} u \\ u_z \end{Bmatrix} = -\begin{bmatrix} m & 0 \\ 0 & z \end{bmatrix} \begin{Bmatrix} 1 \\ 0 \end{Bmatrix} \ddot{u}_g \quad (4.6)$$

Here, $m, c, k$ stand for the mass, the damping coefficient, and the stiffness of the structure, respectively. In addition, $z, c_z, k_z$ stand for the inertial mass, the damping coefficient of the damper, and the stiffness of the supporting member, respectively. $u, u_z, \ddot{u}_g$ denote the displacement of the structure relative to ground, the deformation of the damper, and the ground acceleration, respectively. Until the next section, the main structure is treated as a linear elastic structure to derive the Kelvin-Voigt model for TIMD. However, after that, the main structure is dealt with as a bilinear hysteretic model as shown in Figure 4.4.

We define non-dimensional parameters $\mu, \beta, h_z$ as

$$\mu = \frac{z}{m}, \ \beta = \frac{\omega_z}{\omega_1}, \ h_z = \frac{c_z}{2\sqrt{zk_z}} \tag{4.7}$$

Hereafter, the mass ratio $\mu$ is treated as a parameter to determine the seismic performance of the system.

When the mass ratio $\mu$ is given, $\beta, h_z$ are derived as follows [10]:

$$\beta^{\mathrm{FP}} = \frac{1}{\sqrt{1-\mu}} \tag{4.8}$$

$$h_d^{\mathrm{FP}} = \frac{1}{2}\sqrt{\frac{3\mu}{2-\mu}} \tag{4.9}$$

Let $\beta^{\mathrm{FP}}, h_z^{\mathrm{FP}}$ denote the specific values of $\beta, h_z$ derived by the fixed-point theory.

According to eqs. (4.7), (4.8), and (4.9), $z, c_z, k_z$ are obtained by:

$$z = \mu m \tag{4.10}$$

$$k_z = z(\beta \cdot \omega_1)^2 \tag{4.11}$$

$$c_z = 2z \cdot h_z \cdot \beta \cdot \omega_1 \tag{4.12}$$

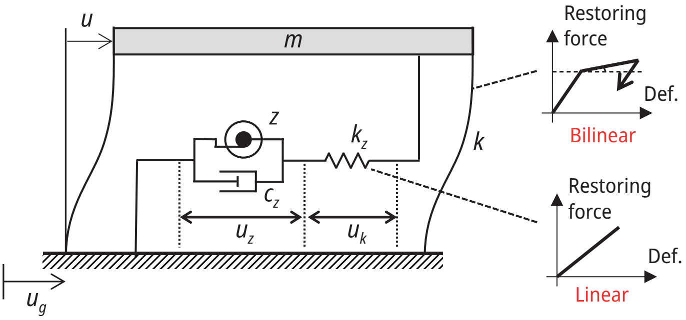

**Figure 4.3:** Bilinear SDOF model with TIMD.

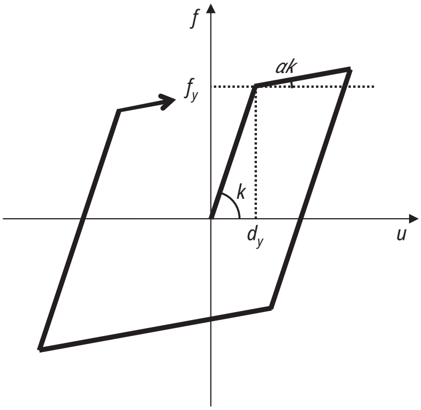

**Figure 4.4:** Bilinear hysteretic restoring force-deformation characteristic.

## 4.4 Transformation of TIMD to Kelvin-Voigt model

As shown in Figure 4.5, the series elements of TIMD are converted to the Kelvin-Voigt model, which is a frequency-dependent parallel element. From the damping force equilibrium and the deformation compatibility conditions of the series elements, the following equation holds:

$$f(t) = k_z(u - u_z) = z\ddot{u}_z + c_z\dot{u}_z \tag{4.13}$$

Fourier transformation of eq. (4.13) yields the following equation:

$$F(\omega) = k_z(U - U_z) = \left(-\omega^2 z + i\omega c_z\right)U_z(\omega) \tag{4.14}$$

Here, $\omega$ denotes the circular excitation frequency and $i = \sqrt{-1}$ is the imaginary unit. Under the condition that eq. (4.14) is equivalent to the damper force in the Kelvin-Voigt model, the relationship between these two models can be expressed in terms of the frequency-dependent viscous coefficient $C_e(\omega)$ and stiffness $K_e(\omega)$ of the Kelvin-Voigt model as:

$$\frac{k_z\left(-z\omega^2 + i\omega c_z\right)}{k_z - z\omega^2 + i\omega c_z}U(\omega) = \left(i\omega C_e(\omega) + K_e(\omega)\right)U(\omega) \tag{4.15}$$

From eq. (4.15), $C_e(\omega)$ and $K_e(\omega)$ can be expressed as

$$K_e(\omega) = \frac{k_z\left[-\omega^2 z\left(k_z - \omega^2 z\right) + \omega^2 {c_z}^2\right]}{\left(k_z - \omega^2 z\right)^2 + \omega^2 {c_z}^2} \tag{4.16}$$

$$C_e(\omega) = \frac{{k_z}^2 c_z}{\left(k_z - \omega^2 z\right)^2 + \omega^2 {c_z}^2} \tag{4.17}$$

The natural circular frequency $\omega_e$ and the damping ratio $h_e$ of the SDOF model reduced to the Kelvin-Voigt model are given by

$$\omega_e(\omega) = \sqrt{\frac{k + k_e(\omega)}{m}} \tag{4.18}$$

$$h_e(\omega) = \frac{C_e(\omega)}{2m\omega_e(\omega)} \tag{4.19}$$

Figure 4.6 shows $\omega_e$, $h_e$, and the first derivative of $h_e$ with respect to $\omega/\omega_1$ when the mass ratio of the damper is set to $\mu = 0.10$. Here, $\omega_1 = \sqrt{k/m}$ denotes the undamped natural circular frequency. From Figure 4.6, it can be found that $\omega_1 = \lim_{\omega/\omega_1 \to 0} \omega_\mathrm{e}(\omega)$ and $c_z/2m\omega_1 = \lim_{\omega/\omega_1 \to 0} h_\mathrm{e}(\omega)$ hold. This means that the system including the damper can be approximately evaluated as an SDOF system with the natural circular frequency $\omega_1$ and the damping ratio $c_z/2m\omega_1$ when $\omega/\omega_1$ approaches to 0. Also, $\partial h_e/\partial\omega = 0$ holds at $\omega = \omega_1$. This means that the input of a sinusoidal wave with the circular frequency $\omega = \omega_1$ maximizes the dissipation energy of the damper. The maximization of the damper dissipation energy is equivalent to the maximization of the input energy to the entire system in an undamped linear elastic structure.

In later sections, the elastic–plastic response of the main structure is considered. When the level of the plastic deformation becomes larger, the equivalent natural frequency and the corresponding frequency of the critical multi impulse tend to become smaller. In this case, the above-mentioned parameters of the equivalent natural circular frequency and the equivalent damping ratio at $\omega/\omega_1 \to 0$ can be used approximately. The validity of this approximation will be investigated in later sections through the time-history response analysis of the elastic–plastic SDOF model with the tuned mass damper.

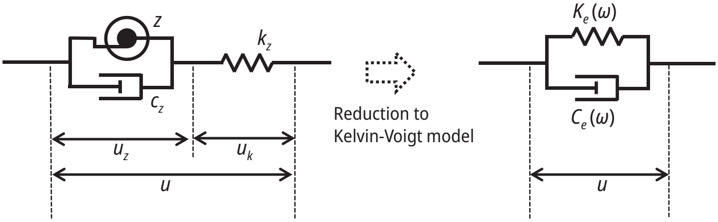

**Figure 4.5:** Transformation of TIMD to Kelvin-Voigt model.

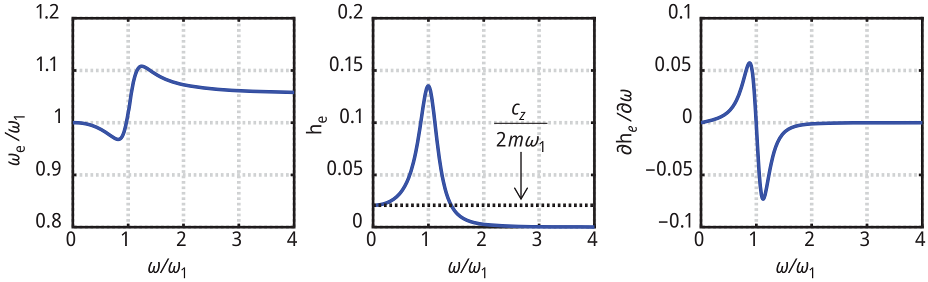

**Figure 4.6:** Evaluation of damper performance in frequency domain using Kelvin-Voigt model.

## 4.5 Critical impulse timing

The critical impulse timing is obtained following the procedure by Kojima and Takewaki [5].

Figure 4.7 presents the normalized critical impulse interval ${t_0}^c/T_1$ with respect to the input velocity level $V/V_y$ for several mass ratios $\mu = 0.025,\ 0.050,\ 0.075,\ 0.10$ and three post-yield stiffness ratios $\alpha = 0.90$, $\tan(\pi/8)$, $\tan(2\pi/180)$. Here $V_y = \omega_1 d_y$ denotes the input velocity level of the impulse at which the undamped elastic–plastic SDOF model just yields after the first impulse. In this paper, we use the structural parameters, that is, the fundamental natural circular frequency $\omega_1 = 2\pi\,\mathrm{rad/s}$ $(T_1 = 1.0\,\mathrm{s})$ and the yield deformation $d_y = 0.04$ m, and $V_y = 0.25\,\mathrm{m/s}$. It can be seen that, the larger the post-yield stiffness ratio $\alpha$ is, the quicker the critical impulse interval ${t_0}^c/T_1$ converges. Also, the larger the mass ratio is, the shorter the critical impulse timing ${t_0}^c/T_1$ in the elastic range becomes. In the range where the post-yield stiffness is close to the elastic stiffness ($\alpha = 1.0$), the critical impulse interval converges more quickly because the damper is well tuned with the structure and provides a large damping ratio. On the other hand, in the range where the post-yield stiffness ratio is close to zero, the critical impulse interval does not converge due to the fact that the damper provides little damping effect. This is because the elastic–plastic behaviour of the structure lengthens the natural period of the structure and the damper may be untuned under such conditions.

Figure 4.8 shows the normalized critical impulse timing ${t_0}^c/T_1$ with respect to post-yield stiffness ratio $\alpha$ for various input levels $V/V_y$ and mass ratios. Also, the approximation of the convergent value is shown in Figure 4.8. The approximate value of ${t_0}^c/T_1$ is derived from $\pi/\left(\omega_\alpha\sqrt{1-h_\alpha^2}\right)$ (half of the damped natural period of the SDOF model with a natural circular frequency $\omega_\alpha = \sqrt{\alpha}\omega_1$ and a damping ratio $h_\alpha = c_z/\left(2m\omega_1\sqrt{\alpha}\right)$) with the post-yield stiffness ratio $\alpha$ as a parameter. Here, the displacement–shear force relationship of the structure is elliptically approximated (Akehashi et al. [4]). From Figure 4.8, ${t_0}^c/T_1$ converges to the approximate value as the input velocity level increases.

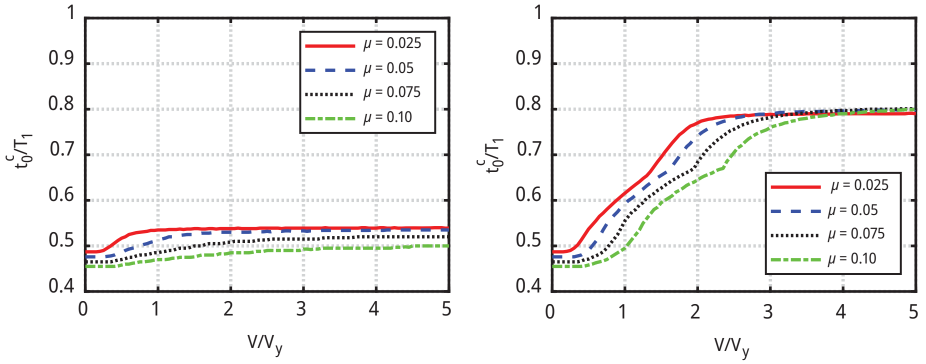

(a) $\alpha = 0.90$ (b) $\alpha = \tan(\pi/8) = 0.414$

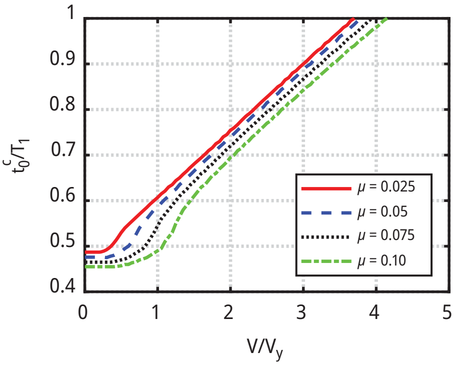

(c) $\alpha = \tan(2\pi/180) = 0.0349$

**Figure 4.7:** Normalized critical impulse timing $t_0{}^c/T_1$ with respect to input level $V/V_y$ for various mass ratios $\mu$.

Figure 4.8(a) shows that the approximate value and the value computed by the time-history response analysis are asymptotically close for all input velocity levels in the range of $\alpha \geq 0.60$. On the other hand, the approximate values do not converge for all input velocity levels except for the input velocity level in $\alpha \leq 0.60$. This is because, as can be seen in Figure 4.7, the smaller the post-yield stiffness ratio is, the worse the convergence of the approximate value with increasing input velocity level becomes.

## 4.6 Maximum deformation and energy response under critical multi impulse

Figure 4.9 illustrates the maximum deformation $u_{\max}/d_y$ to the critical multi impulse and the corresponding sine wave with respect to the input level $V/V_y$ for three post-yield stiffness ratios $\alpha = 0.90$, $\tan(\pi/8)$, $\tan(2\pi/180)$ and several mass ratios

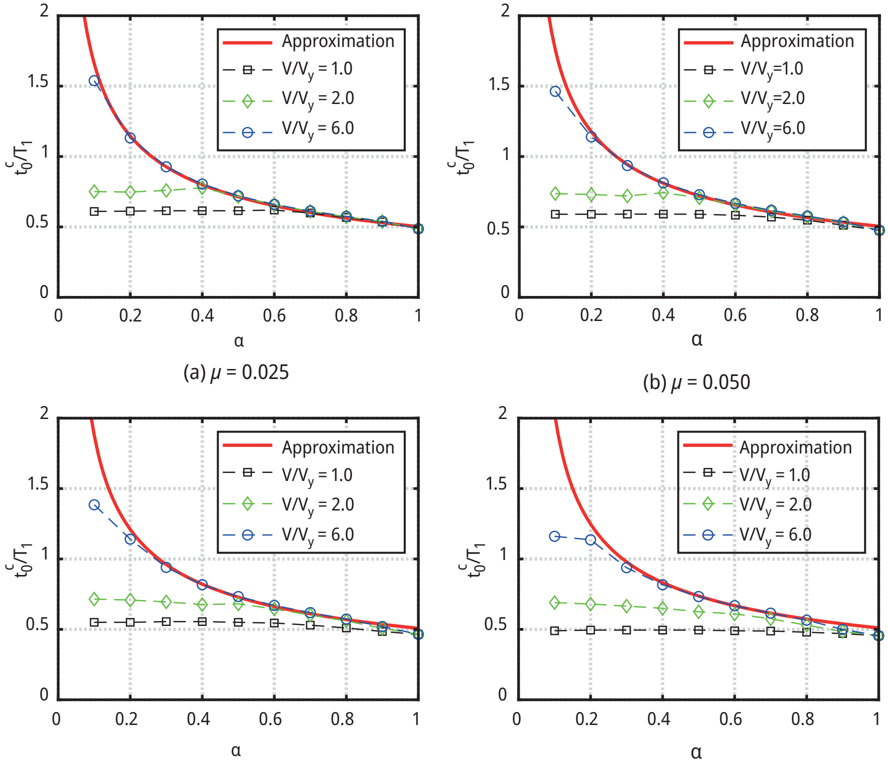

(a) $\mu = 0.025$

(b) $\mu = 0.050$

(c) $\mu = 0.075$

(d) $\mu = 0.10$

**Figure 4.8:** Normalized critical impulse timing $t_0{}^c/T_1$ with respect to post-yield stiffness ratio $\alpha$ for various input levels $V/V_y$.

$\mu = 0.025,\ 0.050,\ 0.075,\ 0.10$. These post-yield stiffness ratios were taken from the past related work [1, 3]. The structural and computational parameters $T_1 = 1.0\text{s}$, $d_y = 0.04\text{m}$, $\Delta t = 5.0 \times 10^{-3} T_1$ are used in the time-history response analysis and the number of impulses used in the time-history response analysis for the convergence of the responses is 50, regardless of the structural parameters. From Figures 4.9(a) and 4.9(b), it can be seen that the responses to the critical multi impulse and the multi-cycle sine wave correspond well for $\alpha = 0.90$, $\tan(\pi/8)$, $\tan(2\pi/180)$, and $\mu = 0.025,\ 0.050,\ 0.075,\ 0.10$, when the maximum values of the Fourier amplitude spectrum are adjusted to be equal. Figures 4.9(b), 4.9(c), and 4.9(d) show that the steady-state responses to the critical multi impulse and the multi-cycle sine wave generally correspond well, although some differences are observed in the case of $\alpha = \tan(\pi/8)$, $\mu = 0.025$ and $\alpha = \tan(2\pi/180)$ compared to the case of $\alpha = 0.90$, $\tan(\pi/8)$. Kojima and Takewaki [1] showed that in order to equalize the maximum deformation of the elastic–plastic response to the critical multi impulse and the multi-cycle sine wave, the Fourier amplitude of the corresponding multi-cycle sine wave must be adjusted to that of the critical multi impulse and then multiplied by a magnification factor of 1.15 in the elastic–perfectly plastic models. In the case of $\alpha = \tan(\pi/8)$, the response increases sharply near $V/V_y = 2.0$. This is due to the difference between the case when the impulse input occurs in the loading process (elastic stiffness range] and the case when it occurs in the unloading process (secondary stiffness range).

Figure 4.10 shows the maximum deformation $u_{\max}/d_y$ of the structure, the maximum deformation $u_{d,\max}/d_y$ of the damper (inertial mass and dashpot), and the maximum deformation $(u - u_d)_{\max}/d_y \left( = u_{k,\max}/d_y \right)$ of the damper supporting member to the critical multi impulse and the corresponding sine wave with respect to the input velocity level for three post-yield stiffness ratios $\alpha = 0.90$, $\tan(\pi/8)$, $\tan(2\pi/180)$ and several mass ratios $\mu = 0.025,\ 0.050,\ 0.075,\ 0.10$. Figure 4.10 indicates that the responses to the critical multi impulse and the multi-cycle sine wave correspond well for both the building and the damper elements, except when the post-yield stiffness ratio and the mass ratio are both in the small range. It can also be found that the deformation of the damper exceeds the displacement of the building. Therefore, it can be said that the amplification of the damper deformation due to tuning occurs even when a large plastic deformation is experienced in the building. Figure 4.10(a) shows that for the case $\alpha = 0.90$, the maximum deformation of the building and damper elements increases almost in proportion to the input velocity level. In the case of $\alpha = \tan(\pi/8)$, the response increases sharply near $V/V_y = 2.0$. This is due to the difference between the case when the impulse input occurs in the loading process (elastic stiffness range) and the case when it occurs in the unloading process (secondary stiffness range). Figure 4.10(c) indicates that in the case of $\alpha = \tan(2\pi/180)$, there exist the maxima and minima with respect to the input velocity level in the deformation of the supporting member. The maxima of the maximum deformation of the support member with respect to the input velocity level $V/V_y$ are caused by the maximization of the damper performance due to tuning when the building is linearly elastic or experiences a sufficiently small plastic deformation. On the other hand, the minima of the maximum deformation of the supporting member with respect to the input velocity level $V/V_y$ are caused by the convergence of the critical impulse interval as shown in Figure 4.7, after the damper performance is maximized.

Figure 4.11 shows the normalized energy responses $E_I/mV^2$, $E_Q/mV^2$, $E_D/mV^2$ to the critical multi impulse and the sine wave with respect to the input velocity level $V/V_y$ for three post-yield stiffness ratios $\alpha = 0.90$, $\tan(\pi/8)$, $\tan(2\pi/180)$ and several mass ratios $\mu = 0.025,\ 0.050,\ 0.075,\ 0.10$. Here, $E_I$, $E_Q$, and $E_D$ stand for the input energy to the structure, the hysteretic dissipation energy of the structure, and the damping energy by the damper, respectively. From Figure 4.11, the energy responses to the critical multi impulse and the multi-cycle sine wave correspond very well under the condition that the maximum values of the Fourier amplitudes of both inputs are chosen to be equal. Figure 4.11(a) indicates that when the post-yield stiffness ratio is set to $\alpha = 0.90$, the energy consumed by the damper accounts for most of the input energy, even when the input velocity level increases. This is because in the range where the post-yield stiffness is close to the elastic stiffness, the natural period during the elas-

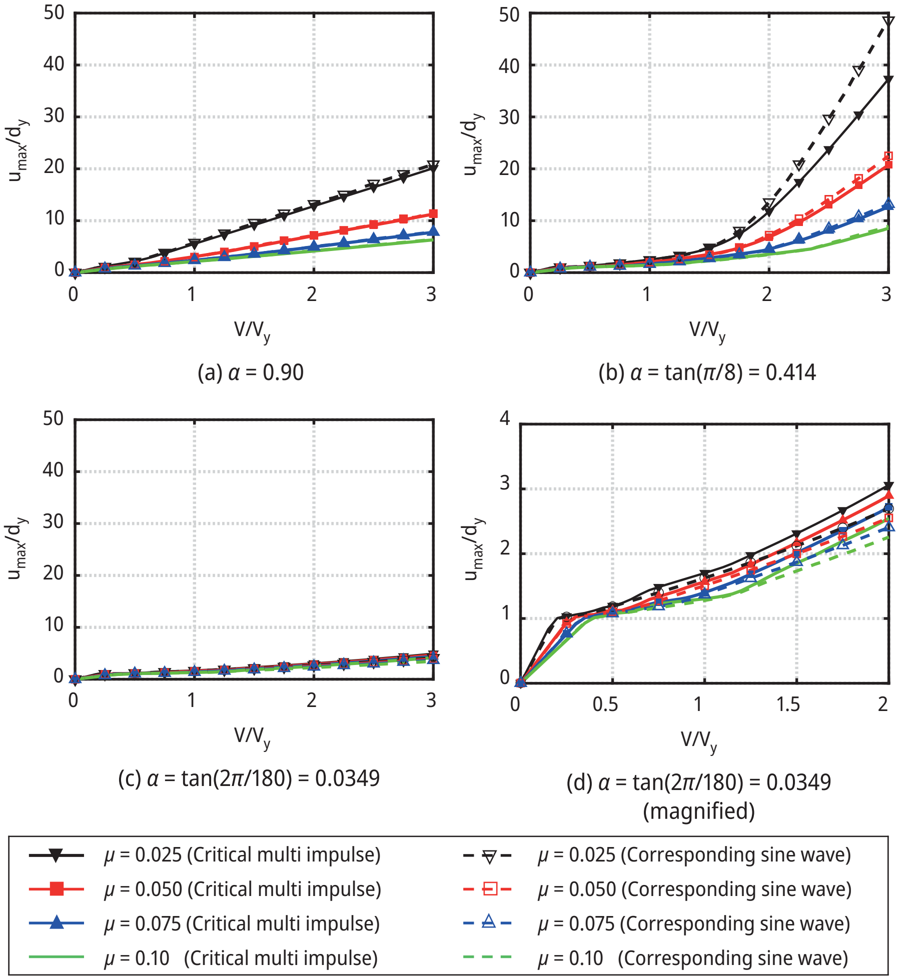

(a) $\alpha = 0.90$

(b) $\alpha = \tan(\pi/8) = 0.414$

(c) $\alpha = \tan(2\pi/180) = 0.0349$

(d) $\alpha = \tan(2\pi/180) = 0.0349$ (magnified)

**Figure 4.9:** Maximum deformation $u_{\max}/d_y$ to critical multi impulse and corresponding sine wave with respect to input level $V/V_y$ for various mass ratios $\mu$.

tic-plastic response tends to be rather stable, and therefore the damper maintains the effect of tuning and consumes energy efficiently. In Figure 4.11(b), the minimum value of $E_I/mV^2$ and $E_D/mV^2$ with respect to the input velocity level is caused by the convergence of the critical impulse interval. Figure 4.11(c) shows that in the case of $\alpha = \tan(2\pi/180)$, the natural period of the structure is relatively long due to the elastic–plastic response and the energy dissipation effect by tuning can hardly be expected. Therefore, the value of $E_I/mV^2$ decreases inversely proportion to the input velocity level. It can also be said that the response of the system can approximately be regarded as that of a linear elastic model with stiffness $ak$.

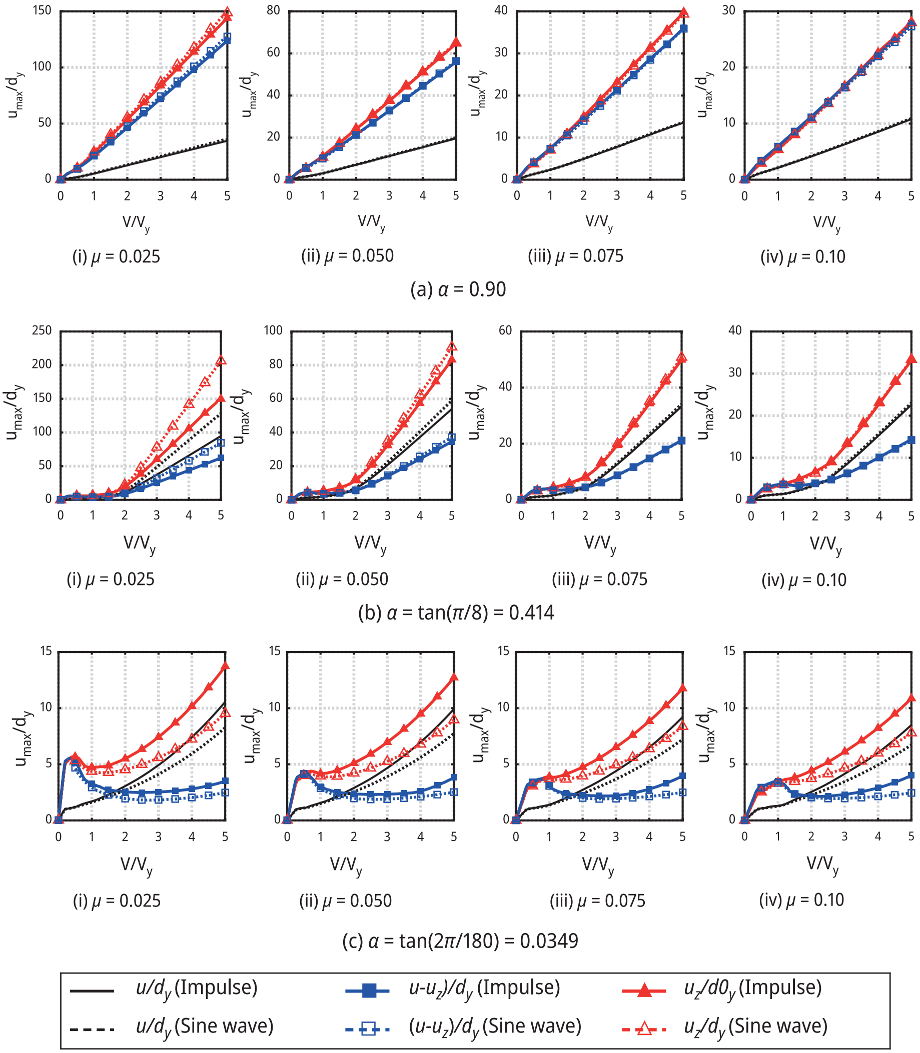

**Figure 4.10:** Maximum deformation $u_{\max}/d_y$ (structure and damper) to critical multi impulse and corresponding sine wave with respect to input level $V/V_y$ for various mass ratios$\mu$.

Figure 4.12 illustrates the Monte Carlo simulation of the normalized input energy for 2,500 mutually independent and uniformly generated random patterns with respect to the post-yield stiffness ratio and the input velocity level in the range $0 \leq \alpha \leq 1$, $0 \leq V/V_y \leq 5$. Here, $N$ denotes the number of impulse inputs. Figure 4.12 shows that $E_I/(mV^2N)$ is constant in the range where the input velocity level is small and the post-yield stiffness ratio is close to 1. This is because the system behaves like a linear elastic system in these ranges, and therefore, the amount of input energy is

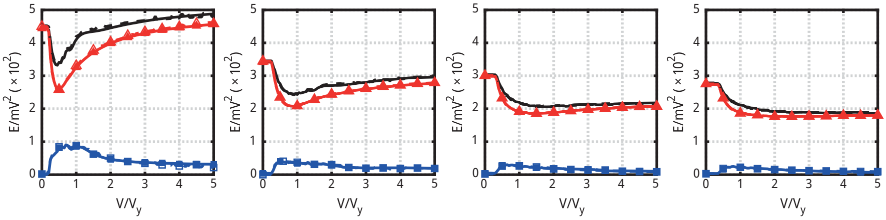

(i) $\mu$ = 0.025 (ii) $\mu$ = 0.050 (iii) $\mu$ = 0.075 (iv) $\mu$ = 0.10

(a) $\alpha$ = 0.90

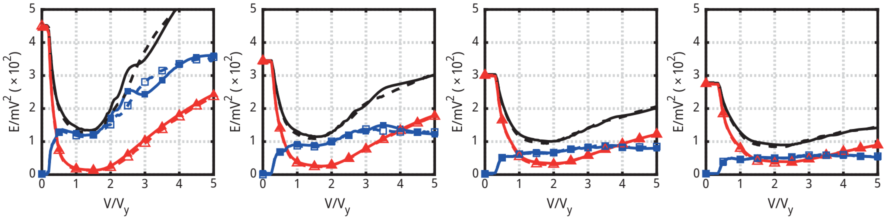

(i) $\mu$ = 0.025 (ii) $\mu$ = 0.050 (iii) $\mu$ = 0.075 (iv) $\mu$ = 0.10

(b) $\alpha$ = tan($\pi$/8) = 0.414

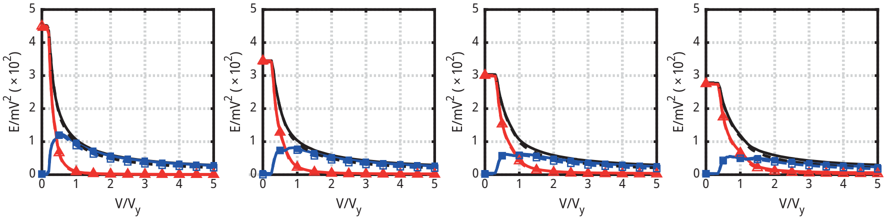

(i) $\mu$ = 0.025 (ii) $\mu$ = 0.050 (iii) $\mu$ = 0.075 (iv) $\mu$ = 0.10

(c) $\alpha$ = tan(2$\pi$/180) = 0.0349

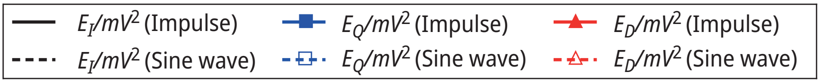

**Figure 4.11:** Normalized energy response $E_I/mV^2$, $E_Q/mV^2$, $E_D/mV^2$ to critical multi impulse and corresponding sine wave with respect to input level $V/V_y$ for various mass ratios $\mu$.

proportional to the square of the input velocity level. In addition, $E_I/(mV^2N)$ decreases temporarily as the input velocity level increases. The reason is that the building's hysteretic energy dissipation becomes dominant due to the elastic–plastic response, and the proportion of energy dissipation by the damper decreases. Furthermore, as the input velocity level increases, $E_I/(mV^2N)$ is enlarged near $\alpha = 0.5$. This is due to the fact that the performance of the tuned damper becomes stable with the increase of the input velocity level as the natural period of the structure converges.

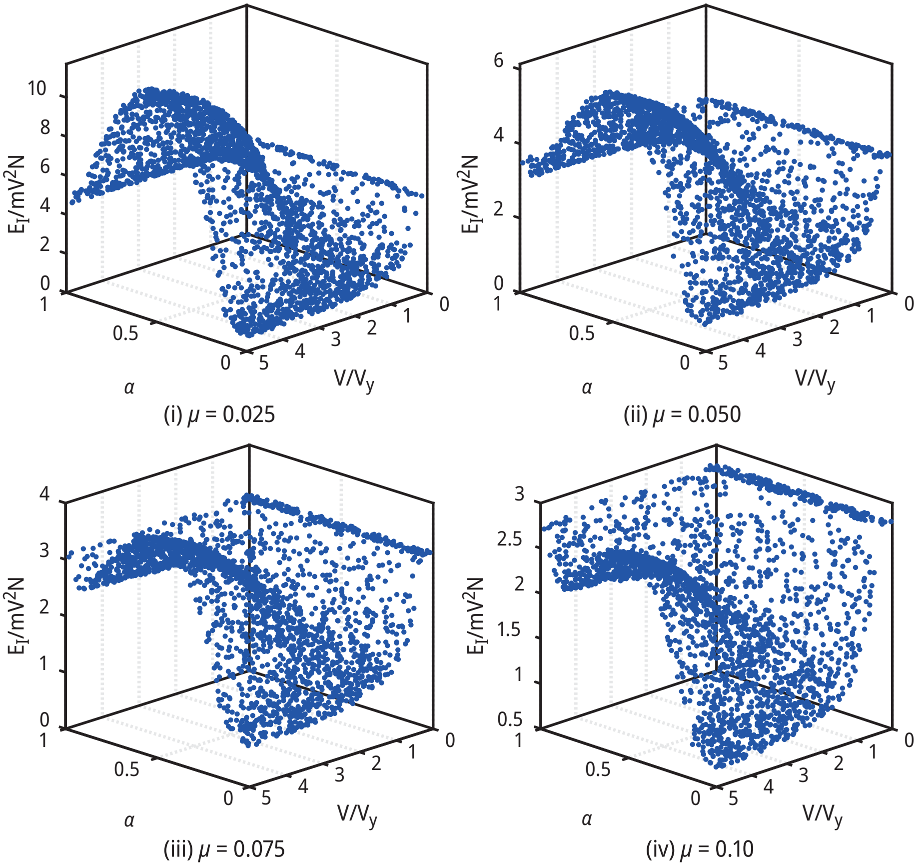

**Figure 4.12:** Monte Carlo simulation for energy response $E_I/(mV^2N)$ to critical multi impulse with respect to input level $V/V_y$ and post-yield stiffness ratio $\alpha$ for various mass ratios $\mu$.

Figure 4.13 shows the maximum deformation $u_{max}/d_y$ of the structure with respect to the impulse interval of the multi impulse for three input velocity levels $V/V_y$, three post-yield stiffness ratios $\alpha = 0.90$, $\tan(\pi/8)$, $\tan(2\pi/180)$, and several mass ratios $\mu = 0.025,\ 0.050,\ 0.075,\ 0.10$. From Figures 4.13(a) and 4.13(b), it can be confirmed that the maximum deformation is almost maximum at $t_0 = {t_0}^c$, that is, at the critical impulse interval. On the other hand, in case of $\alpha = 0.90$, the response is not necessarily maximized at $t_0 = {t_0}^c$. This is because the period maximizing the damper dissipation energy and the period maximizing the building deformation do not correspond when the damper is optimally tuned for the linear elastic structure.

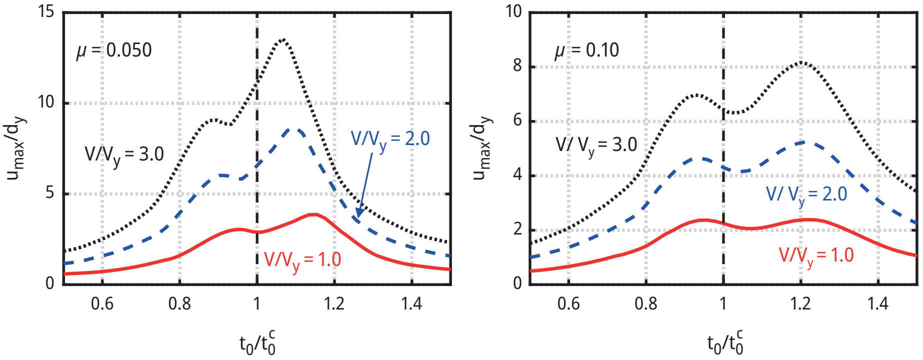

(a) $\alpha = 0.90$

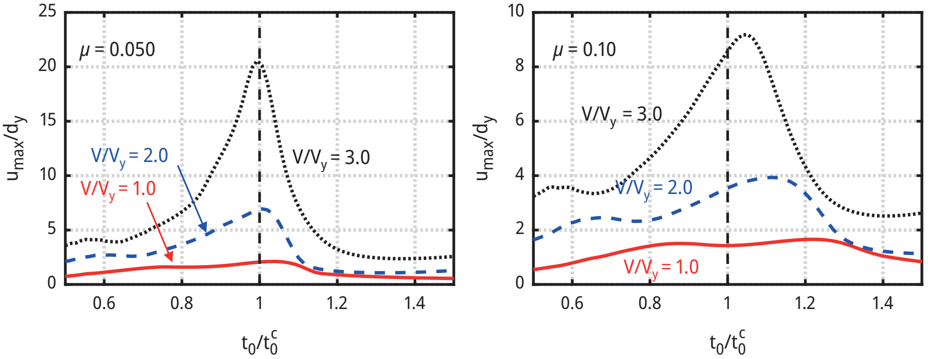

(b) $\alpha = \tan(\pi/8) = 0.414$

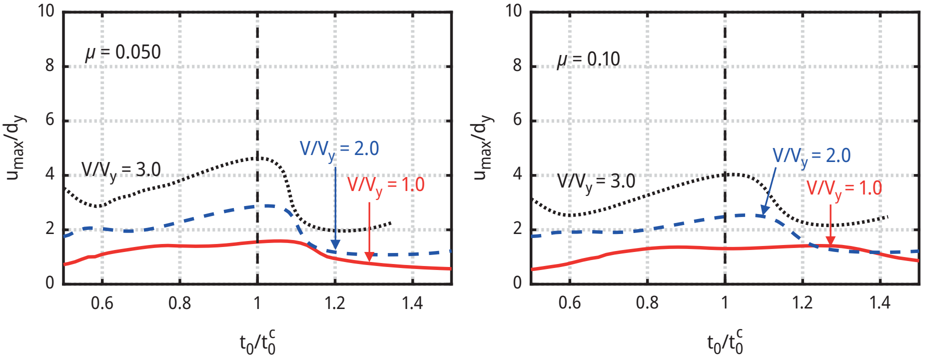

(c) $\alpha = \tan(2\pi/180) = 0.0349$

**Figure 4.13:** Maximum deformation $u_{\max}/d_y$ with respect to timing of multi impulse $t_0/t_0{}^c$ for various input levels.

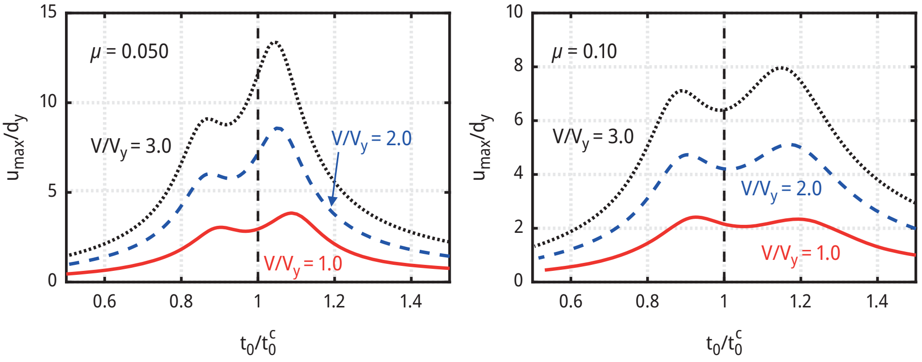

(a) $\alpha = 0.90$

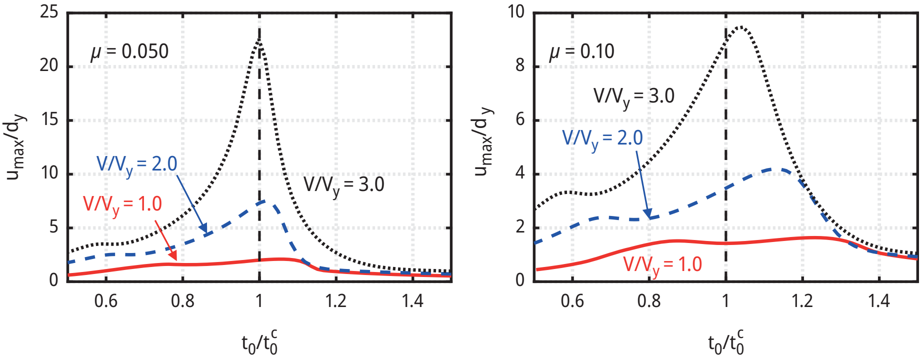

(b) $\alpha = \tan(\pi/8) = 0.414$

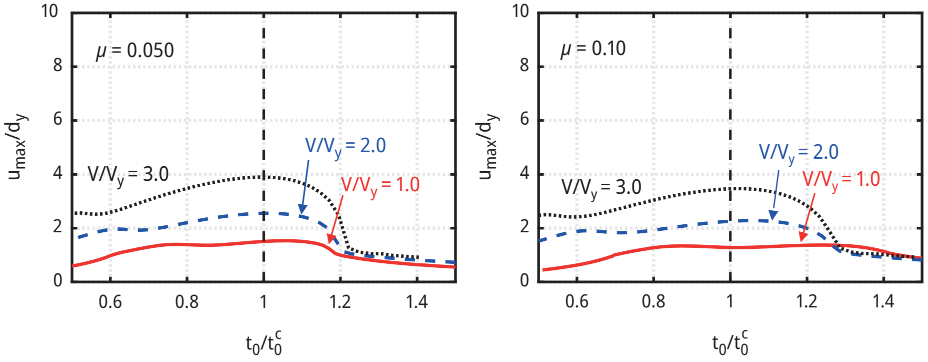

(c) $\alpha = \tan(2\pi/180) = 0.0349$

**Figure 4.14:** Maximum deformation $u_{\max}/d_y$ with respect to period $T_l/T_l^c\,(=t_0/t_0^c)$ of corresponding sine wave for various input levels.

## 4.7 Applicability of critical multi impulse timing to corresponding sine wave

Figure 4.14 shows the maximum deformation $u_{\max}/d_y$ with respect to the period of the corresponding sine wave $T_l/T_l{}^c(=t_0/t_0{}^c)$ for three input velocity levels $V/V_y$, three post-yield stiffness ratios $\alpha=0.90,\ \tan(\pi/8),\ \tan(2\pi/180)$, and several mass ratios $\mu=0.025,\ 0.050,\ 0.075,\ 0.10$. The velocity amplitude of the sine wave is expressed in terms of the input velocity level of the impulse to facilitate the comparison with the multi impulse. The horizontal axis, $T_l/T_l{}^c$, is the period of the sine wave $T_l$ divided by $T_l{}^c(=2t_0{}^c)$. Figures 4.13 and 4.14 demonstrate clearly that the responses of the critical multi impulse and the sine wave correspond precisely, regardless of the impulse interval.

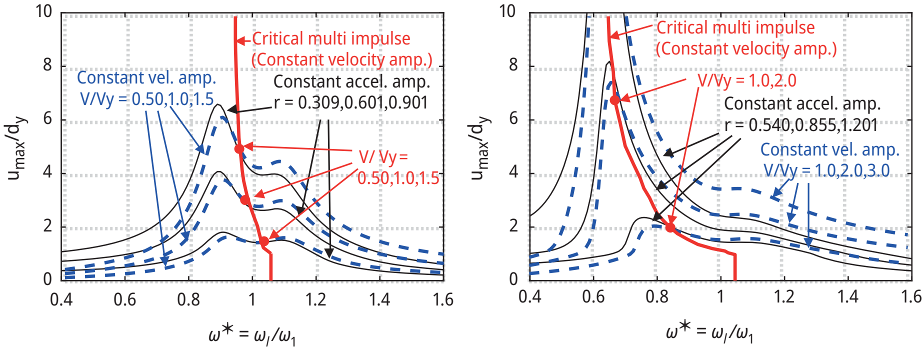

(a) $\alpha$ = 0.90

(b) $\alpha$ = tan($\pi$/8) = 0.414

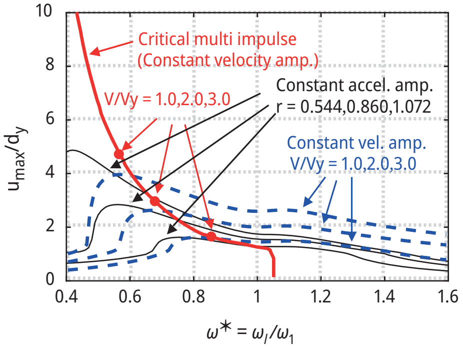

(c) $\alpha$ = tan(2$\pi$/180) = 0.0349

**Figure 4.15:** Comparison of maximum deformation to critical impulse (constant velocity amplitude) and resonance curve for sine wave (constant acceleration amplitude and constant velocity amplitude): mass ratio $\mu$ = 0.050.

Figures 4.15 and 4.16 show a comparison of the maximum deformation (constant velocity amplitude) to the critical multi impulse and the resonance curves (constant acceleration amplitude and constant velocity amplitude) to a sine wave for three post-yield stiffness ratios $\alpha = 0.90$, $\tan(\pi/8)$, $\tan(2\pi/180)$ for two different mass ratios $\mu = 0.050,\ 0.10$, respectively. As mentioned earlier, $t_0 = t_0{}^c$ does not necessarily maximize the deformation in $\alpha = 0.90$. This is also the case in sine wave inputs, and it can be seen that the responses of the critical multi impulse and the corresponding sine wave match well.

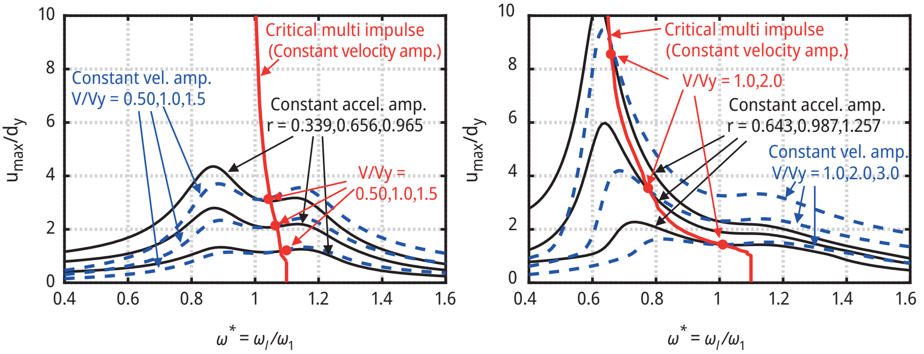

(a) $\alpha = 0.90$

(b) $\alpha = \tan(\pi/8) = 0.414$

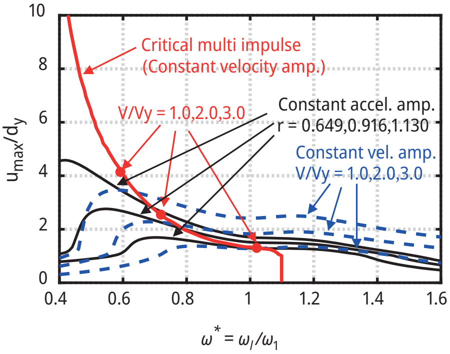

(c) $\alpha = \tan(2\pi/180) = 0.0349$

**Figure 4.16:** Comparison of maximum deformation to critical impulse (constant velocity amplitude) and resonance curve to sine wave (constant acceleration amplitude and constant velocity amplitude): mass ratio $\mu = 0.10$.

## 4.8 Conclusions

The theory on the elastic–plastic response of a damped MDOF model to the critical multi impulse, developed by Akehashi and Takewaki [7] and Kawai and Takewaki [5], was extended to an elastic–plastic SDOF model with a tuned inertial mass damper (TIMD). This indicates a kind of system identification of nonlinear passive control structures through internal monitoring by numerical simulation. The main conclusions can be summarized as follows:

(1) The damper was replaced by a Kelvin-Voigt model and the frequency characteristics were evaluated only in a section for clarifying the damper characteristics. It was shown that it is possible to calculate the input period of the multi impulse maximizing the input energy to the linear elastic models by evaluating the response characteristics in the frequency domain. Furthermore, the Kelvin-Voigt model enables us to evaluate an approximate natural period of the structure in the elastic–plastic range.

(2) The relation between the input velocity level and the critical impulse interval was clarified numerically by the time-history response analysis. It was shown that the critical impulse interval converges more quickly for larger post-yield stiffness ratios. The convergent value of the critical impulse interval can be accurately obtained by elliptically approximating the displacement–shear force relation of the structure.

(3) The relation between the input velocity level and the deformation of the structure and damper elements under the critical multi impulse was investigated. It was shown that, as the input velocity level increases, the supporting member deformation of the damper decreases temporarily but tends to be amplified again when the natural period of the structure converges.

(4) The relationship between the input velocity level and the energy responses were investigated. It was shown that, as the input velocity level increases, the input energy and hysteretic energy temporarily decrease, but tend to increase as the natural period of the structure converges. Furthermore, Monte Carlo simulations were performed to evaluate the response characteristics of the input energy when the input velocity level and the post-yield stiffness ratio were varied simultaneously.

(5) The resonance curves for the sine wave inputs and the elastic–plastic response to the critical multi impulse were compared. It was found that the responses to the critical multi impulse and the sine wave inputs correspond very well. While the resonance curves for the sine wave inputs require a laborious time-history response analysis under the condition of constant acceleration or velocity amplitude, the elastic–plastic resonant response to the multi impulse can be easily calculated with much shorter computation time.

# References

[1] K. Kojima, and I. Takewaki. Critical input and response of elastic-plastic structures under long-duration earthquake ground motions. *Frontiers in Built Environment*, 1:15, 2015b.

[2] K. Kojima, and I. Takewaki. Critical steady-state response of single-degree-of-freedom bilinear hysteretic system under multi impulse as substitute of long-duration ground motion. *Frontiers in Built Environment*, 3:41, 2017.

[3] W. D. Iwan. The Dynamic Response of Bilinear Hysteretic Systems. Ph.D. thesis, California Institute of Technology, Pasadena, 1961.

[4] H. Akehashi, K. Kojima, E. N. Farsangi, and I. Takewaki. Critical response evaluation of damped bilinear hysteretic SDOF model under long duration ground motion simulated by multi impulse motion. *International Journal of Earthquake and Impact Engineering*, 2(4):298–321, 2018.

[5] A. Kawai, and I. Takewaki. Critical response of multi-story damped bilinear hysteretic shear building under multi impulse as representative of long-period, long-duration earthquake ground motions. *Frontiers in Built Environment*, 6:588980, 2020.

[6] K. Kojima, and I. Takewaki. Critical earthquake response of elastic-plastic structures under near-fault ground motions (Part 1: Fling-step input). *Frontiers in Built Environment*, 1:12, 2015a.

[7] H. Akehashi, and I. Takewaki. Optimal viscous damper placement for elastic-plastic MDOF structures under critical double impulse. *Frontiers in Built Environment*, 5:20, 2019.

[8] T. K. Caughey. Sinusoidal excitation of a system with bilinear hysteresis. *Journal of Applied Mechanics*, 27:640–643, 1960a.

[9] T. K. Caughey. Random excitation of a system with bilinear hysteresis. *Journal of Applied Mechanics*, 27:649–652, 1960b.

[10] K. Ikago, K. Saito, and N. Inoue. Seismic control of single-degree-of-freedom structure using tuned viscous mass damper, *Earthquake Engineering & Structural Dynamics*, 41:453–474, 2012.

[11] K. Ikago, Y. Sugimura, and N. Inoue. Modal response characteristics of a multiple-degree-of-freedom structures incorporated with tuned viscous mass dampers. *Journal of Asian Architecture and Building Engineering*, 11(2):375–382, 2012.

[12] J. E. Brock. A note on the damped vibration absorber. *Journal of Applied Mechanics*, 68:A–248, 1946.

[13] J. P. Den Hartog. *Mechanical Vibrations*. 4th ed, Dover, New York, 1985.

[14] K. Liu, and J. Liu. The damped dynamic vibration absorbers. Revisited and new result. *Journal of Sound and Vibration*, 284:1181–1189, 2005.

[15] M. C. Smith. Synthesis of mechanical networks: The Inerter. *IEEE Transactions of Automatic Control*, 47(10):1648–1662, 2002.

[16] I. F. Lazar, S. Neild, and D. Wagg. Using an inerter-based device for structural vibration suppression, *Earthquake Engineering and Structural Dynamics*, 43:1129–1147, 2014.

[17] D. De Domenico and G. Ricciardi. An enhanced base isolation system equipped with optimal tuned mass damper inerter (TMDI). *Earthquake Engineering & Structural Dynamics*, 47:1169–1192, 2018.

Matteo Torzoni*, Luca Rosafalco*, Andrea Manzoni, Stefano Mariani,
Alberto Corigliano

# 5 Damage identification using physics-based datasets: From convolutional to metric-informed damage-sensitive feature extractors

**Abstract:** Two alternative strategies addressing damage identification in structural health monitoring are presented in this contribution. Both strategies rely on reduced data representations – or features – to enable damage identification from vibrational data. To exploit a supervised learning scheme, training datasets are generated through numerical simulations, possibly speeded up through reduced order modelling. The first strategy deals with damage identification as a classification task employing one-dimensional convolutional neural networks. Despite the good performance displayed in the proposed numerical benchmark of an eight-storey building, this approach suffers from the need of defining the possible damage classes a–priori, and from the lack of robustness of the extracted features. Both issues are successfully addressed by a second strategy, which relies on a Siamese architecture to learn a damage-sensitive low-dimensional metric space. In this second case, damage identification can be performed by solving a regression task in the learned metric space. This second approach is assessed against a test case involving a railway bridge, displaying impressive damage localization capabilities.

## 5.1 Introduction

Safety of infrastructures is a key challenge of our society. Material ageing, enhanced service demands, extreme loadings whose frequency is even increased by climate change (e.g. heat waves, floods) threaten the safety of infrastructures. In situ inspec-

---

**Acknowledgment:** M.T. acknowledges the financial support by Politecnico di Milano through the interdisciplinary Ph.D. Grant “Physics-Informed Deep Learning for Structural Health Monitoring”.

---

***Corresponding authors: Matteo Torzoni and Luca Rosafalco**, Dipartimento di Ingegneria Civile ed Ambientale, Politecnico di Milano, piazza, L. da Vinci 32, 20133, Milano e-mail: matteo.torzoni@polimi.it; luca.rosafalco@polimi.it
**Stefano Mariani, Alberto Corigliano,** Dipartimento di Ingegneria Civile ed Ambientale, Politecnico di Milano, piazza, L. da Vinci 32, 20133, Milano
**Andrea Manzoni,** MOX, Dipartimento di Matematica, Politecnico di Milano, piazza, L. da Vinci 32, 20133, Milano

https://doi.org/10.1515/9783110791426-005

tions are costly, possibly risky [12], and necessarily related to the moment they are performed. The development of digital technology and of the internet of things paradigm has recently enabled the use of pervasive sensor systems providing a great amount of data almost in real time. In this work, we describe Data-centric Structural Health Monitoring (SHM) techniques for damage detection and damage localization, as key enablers for automatic and continuous assessment of structural performance [15].

SHM can be envisioned as a pattern recognition problem, in which the onset of damage is assessed by comparing data previously obtained for known structural conditions, usually the undamaged ones in the early stage of structural life cycle, with new incoming measurements. A pattern recognition paradigm for SHM was proposed in [16] to be distinguished into four steps: (i) operational evaluation; (ii) data acquisition; (iii) feature selection and extraction; (iv) statistical modelling for feature discrimination. The last stage consists in setting up a statistical model to perform damage identification (our task of interest) using the features extracted during stage (iii).

A feature is a synthetic representation of the data, (ideally) capable of coding meaningful information for damage identification. For instance, structural frequencies are often exploited as features because they may be sensitive to the ongoing damage [49]. Often, features are related to the structural dynamic response; a model to represent such response can be physics-based, if physical knowledge is exploited for its definition, or otherwise data-based, if relying on data-based relationships only. For example, in [6], the parameters calibrating a Finite Element (FE) model were employed as features. However, in several cases features might not have a clear physical meaning, like, e.g., when they are extracted through crude statistical methods [5]. More in general, features extracted through data-based models may not enjoy a clear interpretability, e.g., in case of parameters and residuals of autoregressive models adopted as damage-sensitive features, see e.g. [50, 13].

Feature selection and extraction, and statistical modelling stage are considered as two separate components in Machine Learning (ML)-based approaches. However, both stages can be simultaneously addressed through a single end-to-end learning process, according to the Deep Learning (DL) paradigm [28]. This approach allows to further automatise the selection and extraction of features, optimized for the task at hand [34, 36], and its convenience for the SHM of large structures becomes clearer in the presence of varying environmental and operational conditions [1, 41]. Indeed, the DL paradigm also enables to automatically blend data coming from different sources, such as temperature and structural acceleration recordings [47, 48].

Among the Neural Network (NN) architectures to enable the DL paradigm within a SHM framework, convolutional ones were proposed in [34, 38] to perform feature extraction from structural vibrations, which are actually Multivariate Time Series (MTS) acquired with pervasive sensor networks. Vibration measurements can be exploited as they may carry relevant information about the mechanical properties of a structure [23, 46], well-suited to allow both local and global structural health assessments [49], even in large scale applications [11]. Nevertheless, features extracted through convolutional NNs usually suffer from lack of explainability [39], and may be not robust to differences between the probability distributions underlying training and incoming data [33, 40], which are unavoidable due to the unavailability of information related to the occurrence of damage. In this work, data related to damage conditions during the service life of the structure are generated through physics-based models [44, 2] within a simulation-based approach to damage identification. Alternatively, adversarial learning was also exploited in [9] to cope with the possible lack of robustness of the extracted features. Following a different approach, in [45] a metric for the feature space was set by means of a Siamese architecture [4] trained with pairwise contrastive learning [19]. This approach has the advantage that the NN is let free to learn a suitable feature metric space, mitigating the lack of explainability and enhancing the robustness of the identification procedure.

The reminder of the chapter is organized as follows. In Section 5.2, the proposed simulation-based damage identification framework is discussed: the composition of the handled physics-based datasets is detailed in Section 5.2.1; modelling aspects, in terms of full-order and reduced-order modelling strategies are shown in Section 5.2.2; two damage identification procedures, exploiting convolutional layers for automatic feature extraction and employing damage–sensitivity into a low-dimensional metric space through a Siamese architecture are then touched in Section 5.2.3. Some details regarding the working principles of convolutional and fully connected layers are also provided for the sake of completeness. Relevant numerical results are then discussed in Section 5.3, with reference to a shear-type building and a railway bridge. Conclusions and future perspectives are finally given in Section 5.4.

## 5.2 Simulation-based damage identification using neural networks

### 5.2.1 Data specification: labeled vibration datasets

The dataset needed to build data-based models performing the damage identification task, is here provided with a number $\mathrm{N_i}$ of MTS $\mathbf{U}_{\mathrm{n_i}}$, with $\mathrm{n_i} = 1, \ldots, \mathrm{N_i}$, recordings of the vibrational response of the structure. Each MTS, also termed instance, collects the measurements $\boldsymbol{u}_{\mathrm{n_i}}^{\mathrm{n_u}} \in \mathbb{R}^{L}$ acquired by $\mathbf{n}_u = 1, \ldots, \mathrm{N_u}$ sensors, thus yielding $\mathbf{U}_{\mathrm{n_i}} = \left[\boldsymbol{u}_{\mathrm{n_i}}^{1}, \ldots, \boldsymbol{u}_{\mathrm{n_i}}^{\mathrm{N_u}}\right] \in \mathbb{R}^{L \times \mathrm{N_u}}$. When a simulation-based approach is employed, vibrations are collected for the $\mathrm{N_u}$ degrees of freedom (dofs) coinciding with the sensor positions and spatial orientations. Accordingly, the number $L$ of measurements depends on the time interval $(0, T)_{,}$ which the recordings refer, and on the sampling rate $\mathscr{f}$.

Each instance is associated to a label that depends on the required task, being thus different for the classification or the regression task. Classification and regression are possible ways of formalizing damage detection and localization, where the latter avoids the a–priori definition of target classes and thus enables a more precise description of the damage location.

Classification involves the prediction of an output class label to categorize a given input. In this case, the output labels to be predicted identify a set of $\mathrm{N_c}$ predefined damage scenarios, each referring to a different damage location. The dataset next used for classification (CL) is defined as:

$$\mathbf{D}_{\mathrm{CL}} = \left\{ \left(\mathbf{U}_{\mathrm{n_i}}, \boldsymbol{b}_{\mathrm{n_i}}\right) \right\}_{\mathrm{n_i}=1}^{\mathrm{N_i}} , \tag{5.1}$$

where $\boldsymbol{b}_{\mathrm{n_i}} = [b^1_{\mathrm{n_i}}, \ldots, b^{\mathrm{N_c}}_{\mathrm{n_i}}]^\top \in \mathbb{B}^{\mathrm{N_c}}$ is a Boolean vector, or one-hot encoding, with entries $b^j_{\mathrm{n_i}}$ equal to 1 if the target class for the $\mathrm{n_i}$–th instance is $j$ and 0 otherwise, with $j \in \{1, \ldots, \mathrm{N_c}\}$. This strategy has been adopted by the authors, e.g., in [34, 37, 48].

Regression involves, instead, the prediction of a target value in a non-discretised setting, which represents the damage condition behind the considered vibrational response. In concrete terms, damage is parametrized through a vector $\mathscr{y} \in \mathbb{R}^{\mathrm{N_{dam}}}$, collecting $\mathrm{N_{dam}}$ input parameters describing the position of damage. Accordingly, the dataset used for regression (RG) is assembled as:

$$\mathbf{D}_{\mathrm{RG}} = \left\{ \left(\mathbf{U}_{\mathrm{n_i}}, \mathscr{y}_{\mathrm{n_i}}\right) \right\}_{\mathrm{n_i}=1}^{\mathrm{N_i}} . \tag{5.2}$$

This strategy has been adopted by the authors in [37, 48].

The definition of $\mathbf{D}_{\mathrm{CL}}$ and $\mathbf{D}_{\mathrm{RG}}$ is independent of the simulation-based approach adopted in this work. Such an approach is crucial to cope with the unavailability of data related to the onset and propagation of damage while monitoring the structure, and allows to synthesize $\mathbf{D}_{\mathrm{CL}}$ and $\mathbf{D}_{\mathrm{RG}}$ through numerical simulations.

### 5.2.2 Parametric numerical models for dataset generation

By modeling the structure as a linear–elastic continuum and introducing a space discretization through a FE method, its dynamic response is described by the following system of second-order ordinary differential equations:

$$\begin{cases} \mathbf{M}_{\mathrm{HF}}\ddot{\mathbf{d}}^{\mathrm{HF}}(t) + \mathbf{K}_{\mathrm{HF}}(\boldsymbol{\mu})\mathbf{d}^{\mathrm{HF}}(t) = \mathbf{f}_{\mathrm{HF}}(t, \boldsymbol{\mu}), \quad t \in (0, T) \\ \mathbf{d}^{\mathrm{HF}}(0) = \mathbf{d}_0^{\mathrm{HF}} \\ \dot{\mathbf{d}}^{\mathrm{HF}}(0) = \dot{\mathbf{d}}_0^{\mathrm{HF}}, \end{cases} \tag{5.3}$$

which is referred to as the High-Fidelity (HF) Full-Order Model (FOM). Here: $t \in (0, T)$ denotes time; $\mathbf{d}^{\mathrm{HF}}(t)$ and $\ddot{\mathbf{d}}^{\mathrm{HF}}(t) \in \mathbb{R}^{\mathscr{M}}$ are the vectors of nodal displacements and accelerations, respectively; $\mathscr{M}$ is the number of dofs; $\mathbf{M}_{\mathrm{HF}} \in \mathbb{R}^{\mathscr{M} \times \mathscr{M}}$ is the mass matrix; $\mathbf{K}_{\mathrm{HF}}(\boldsymbol{\mu}) \in \mathbb{R}^{\mathscr{M} \times \mathscr{M}}$ is the stiffness matrix; $\mathbf{f}_{\mathrm{HF}}(t, \boldsymbol{\mu}) \in \mathbb{R}^{\mathscr{M}}$ is the vector of external forces; $\boldsymbol{\mu} \in \mathbb{R}^{\mathrm{N_{par}}}$ is a vector of $\mathrm{N_{par}}$ parameters ruling the operational, damage and (possibly) environmental conditions; $\mathbf{d}_0^{\mathrm{HF}}$ and $\dot{\mathbf{d}}_0^{\mathrm{HF}}$ are the initial conditions (at $t=0$), respectively, in terms of nodal displacements and velocities. Because of the small relevance in the identification of the properties of continuously excited systems, structural damping is disregarded, see e.g. [10].

The parametrization of damage according to the one-hot encoding $\boldsymbol{b}$ or the regression target $\mathscr{y}$ is also addressed by means of the parameter vector $\boldsymbol{\mu}$. As often assumed in the SHM literature, see e.g. [17, 24], damage is modeled as a local reduction of the material stiffness. In concrete terms, the stiffness matrix is parametrized through a set of parameters collected in $\boldsymbol{\mu}$, which governs the position and the magnitude of the local stiffness reduction. With reference to damage scenarios characterized by a low damage evolution rate, the damage condition is hold fixed during the time interval $(0, T)$, thus allowing for a timescale separation between damage evolution and health assessment.

By adopting a uniform partition of the time interval $(0, T)$, the solution of problem (3) is advanced in time using the implicit Newmark time integration method, to provide $\mathbf{d}_l^{\mathrm{HF}}$, $\dot{\mathbf{d}}_l^{\mathrm{HF}}$ and $\ddot{\mathbf{d}}_l^{\mathrm{HF}}$, for $l=1,\ldots,L$; by choosing an unconditionally stable integration rule, the integration step can be arbitrarily chosen on the basis of the fundamental structural frequencies and of the sensor sampling rate $\mathscr{f}$.

To speed up the generation of synthetic datasets, a low-fidelity (LF) model with reduced computational cost can be derived from the FOM. The LF model considered in this paper is a projection-based reduced-order model (ROM), built by relying on the proper orthogonal decomposition (POD)-Galerkin reduced basis method [31], see also [36, 37, 48].

The solution of problem (3) in terms of nodal displacements is approximated by linearly combining $\mathscr{M}_{\mathrm{LF}} \ll \mathscr{M}$ POD-basis functions $\mathbf{w}_k \in \mathbb{R}^{\mathscr{M}}$, $k=1,\ldots,\mathscr{M}_{\mathrm{LF}}$, as $\hat{\mathbf{d}}^{\mathrm{HF}}(t,\boldsymbol{\mu}) = \mathbf{W}\mathbf{d}^{\mathrm{LF}}(t,\boldsymbol{\mu})$, where $\mathbf{W}=[\mathbf{w}_1,\ldots,\mathbf{w}_{\mathscr{M}_{\mathrm{LF}}}] \in \mathbb{R}^{\mathscr{M}\times\mathscr{M}_{\mathrm{LF}}}$ is the projection matrix and $\mathbf{d}^{\mathrm{LF}}(t,\boldsymbol{\mu}) \in \mathbb{R}^{\mathscr{M}_{\mathrm{LF}}}$ is the vector of unknown POD-coefficients. The corresponding $\mathscr{M}_{\mathrm{LF}}$-dimensional dynamical system to be solved is obtained through a Galerkin projection to enforce the orthogonality between the residuals and the subspace spanned by the first $\mathscr{M}_{LF}$ POD-modes, and reads:

$$\begin{cases} \mathbf{M}_{\mathrm{LF}}\ddot{\mathbf{d}}^{\mathrm{LF}}(t) + \mathbf{K}_{\mathrm{LF}}(\boldsymbol{\mu})\mathbf{d}^{\mathrm{LF}}(t) = \mathbf{f}_{\mathrm{LF}}(t,\boldsymbol{\mu}), \qquad t \in (0,T) \\ \mathbf{d}^{\mathrm{LF}}(0) = \mathbf{W}^{\top}\mathbf{d}_0^{\mathrm{HF}} \\ \dot{\mathbf{d}}^{\mathrm{LF}}(0) = \mathbf{W}^{\top}\dot{\mathbf{d}}_0^{\mathrm{HF}}, \end{cases} \tag{5.4}$$

whose solution is advanced in time using the same strategy employed for the HF model. Here, the reduced arrays play the same role of their HF counterparts, yet with dimension ruled by $\mathscr{M}_{\mathrm{LF}}$ instead $\mathscr{M}$, according to:

$$\mathbf{M}_{\mathrm{LF}} \equiv \mathbf{W}^{\top}\mathbf{M}_{\mathrm{HF}}\mathbf{W}, \quad \mathbf{K}_{\mathrm{LF}}(\boldsymbol{\mu}) \equiv \mathbf{W}^{\top}\mathbf{K}_{\mathrm{HF}}(\boldsymbol{\mu})\mathbf{W}, \quad \mathbf{f}_{\mathrm{LF}}(t,\boldsymbol{\mu}) \equiv \mathbf{W}^{\top}\mathbf{f}_{\mathrm{HF}}(t,\boldsymbol{\mu}). \tag{5.5}$$

An optimal projection matrix $\mathbf{W}$ is obtained by means of POD, exploiting the so-called method of snapshots. To this aim, a matrix $\mathbf{S} = \left[\mathbf{d}_1^{\mathrm{HF}},\ldots,\mathbf{d}_{\mathscr{S}}^{\mathrm{HF}}\right] \in \mathbb{R}^{\mathscr{M}\times\mathscr{S}}$ is assembled from $\mathscr{S}$ solution snapshots computed by integrating problem (3) in time for different values of parameters $\boldsymbol{\mu}$, and then factorized through singular value decomposition as:

$$\mathbf{S} = \mathbf{P}\Sigma\mathbf{Z}^\top, \tag{5.6}$$

where: $\mathbf{P} = [\mathbf{p}_1, \ldots, \mathbf{p}_{\mathscr{M}}] \in \mathbb{R}^{\mathscr{M}\times\mathscr{M}}$ and $\mathbf{Z} = [\mathbf{z}_1, \ldots, \mathbf{z}_{\mathscr{S}}] \in \mathbb{R}^{\mathscr{S}\times\mathscr{S}}$ are two orthogonal matrices, whose columns are the left and right singular vectors of $\mathbf{S}$, respectively; $\Sigma \in \mathbb{R}^{\mathscr{M}\times\mathscr{S}}$ is a pseudo-diagonal matrix collecting the singular values $\sigma_1 \geq \sigma_2 \geq \ldots \geq \sigma_{\mathscr{R}} \geq 0$ of $\mathbf{S}$, $\mathscr{R} = \min(\mathscr{M}, \mathscr{S})$ being the rank of $\mathbf{S}$.

As each singular value quantifies the information content of $\mathbf{S}$ described by the corresponding left singular vector, the order $\mathscr{M}_{\text{LF}}$ of the ROM can be set by prescribing a tolerance $\epsilon$ on the fraction of energy content retained in the LF model, according to:

$$\frac{\sum_{m=1}^{\mathscr{M}_{\text{LF}}} (\sigma_m)^2}{\sum_{m=1}^{\mathscr{R}} (\sigma_m)^2} \geq 1 - \epsilon^2, \tag{5.7}$$

which is a standard energy–content criterion to select the POD-basis functions.

To populate the datasets described in Section 5.2.1 with training instances, the parametric input space described by $\boldsymbol{\mu}$ is assumed to have a prescribed probability distribution and is then sampled via the Latin hypercube rule. The number of samples is equal to the number of instances $\mathrm{N_i}$. Nodal displacements or accelerations in $(0, T)$ are first collected, either as $\mathbf{V} = \left[\hat{\mathbf{d}}_1^{\text{HF}}, \ldots, \hat{\mathbf{d}}_L^{\text{HF}}\right] \in \mathbb{R}^{\mathscr{M}\times L}$ or as $\mathbf{V} = \left[\ddot{\hat{\mathbf{d}}}_1^{\text{HF}}, \ldots, \ddot{\hat{\mathbf{d}}}_L^{\text{HF}}\right] \in \mathbb{R}^{\mathscr{M}\times L}$, depending on the handled measurements, by evaluating problem (4). The relevant vibration recordings $\mathbf{U}$ are then obtained as

$$\mathbf{U} = (\mathbf{T}\mathbf{V})^\top, \tag{5.8}$$

where $\mathbf{T} \in \mathbb{B}^{\mathrm{N_u}\times\mathscr{M}}$ is a Boolean matrix whose $(n, m)$-th entry is equal to 1 only if the $n$-th sensor output coincides with the $m$-th dof.

Due to the formulation of problem (4), each instance $\mathbf{U}_{\mathrm{n_i}}$ of $\mathbf{D}_{\text{CL}}$ and of $\mathbf{D}_{\text{RG}}$ depends on $\boldsymbol{\mu}$, namely $\mathbf{U}_{\mathrm{n_i}} = \mathbf{U}_{\mathrm{n_i}}(\boldsymbol{\mu}_{\mathrm{n_i}})$, and therefore, on the damage parameters. When damage identification is performed by adopting the regression setting, dataset $\mathbf{D}_{\text{RG}}$ is made up by collecting $\mathbf{U}_{\mathrm{n_i}}$ and the corresponding label $\mathscr{Y}_{\mathrm{n_i}}$, which describes the spatial coordinates of the subdomain wherein the stiffness is reduced. On the other hand, if the classification setting is considered, dataset $\mathbf{D}_{\text{CL}}$ is assembled with $\mathbf{U}_{\mathrm{n_i}}$ and the corresponding one-hot encoding $\boldsymbol{b}_{\mathrm{n_i}}$, with the latter having a single nonzero component in correspondence of the entry associated with the target class.

## 5.2.3 Damage identification models

### 5.2.3.1 Details on convolutional and fully connected layers

NNs work by aggregating the computations of basic units, termed neurons, to approximate a target function. For the classification task, the target function models the relation between input vibration recordings and the one-hot encoding $\boldsymbol{b}$ labeling the subdomain in which damage is assumed to be possibly located; for the regression task, it instead models the relation between input vibration recordings and the parameter vector $\mathscr{y}$ ruling the damage location.

In a fully connected layer $\mathcal{F}_1$, each neuron ($\mathcal{N}$) provides an output $\beta$ computed as an affine transformation of its input, ruled by a nonlinear activation function $\mathcal{A} : \mathbb{R} \to \mathbb{R}$ as follows:

$$\beta = \mathcal{A}\left(\boldsymbol{\omega}_{\mathcal{N}}^{\top}\boldsymbol{a} + \mathscr{b}_{\mathcal{N}}\right), \tag{5.9}$$

where $\boldsymbol{a} \in \mathbb{R}^{\mathrm{N}\alpha}$ is the input to the neuron, $\boldsymbol{\omega}_{\mathcal{N}} \in \mathbb{R}^{\mathrm{N}\alpha}$ are the connection weights of the linear mapping and $\mathscr{b}_{\mathcal{N}} \in \mathbb{R}$ is a bias term. The activation function $\mathcal{A}$ is usually chosen as the hyperbolic tangent (tanh) or the rectified linear unit (ReLU). The relation mapped by $\mathcal{N}$ is tuneable through $\boldsymbol{\omega}_{\mathcal{N}}$ and $\mathscr{b}_{\mathcal{N}}$.

Since $\mathcal{F}_1$ simultaneously applies a set of $\mathrm{N_n}$ neurons to its input, the output of $\mathcal{F}_1$ is a vector $\boldsymbol{\beta}^{\mathcal{F}_1} \in \mathbb{R}^{\mathrm{N_n}}$ computed as:

$$\boldsymbol{\beta}^{\mathcal{F}_1} = \mathcal{F}_1\left(\boldsymbol{a}, \Xi_{\mathcal{F}_1}, \boldsymbol{\mathscr{b}}_{\mathcal{F}_1}\right), \tag{5.10}$$

where $\Xi_{\mathcal{F}_1} = \left[\boldsymbol{\omega}_{\mathcal{F}_1}^{1}, \ldots, \boldsymbol{\omega}_{\mathcal{F}_1}^{\mathrm{N_n}}\right] \in \mathbb{R}^{\mathrm{N_n} \times \mathrm{N}\alpha}$ and $\boldsymbol{\mathscr{b}}_{\mathcal{F}_1} = [\mathscr{b}_{\mathcal{F}_1}^{1}, \ldots, \mathscr{b}_{\mathcal{F}_1}^{\mathrm{N_n}}] \in \mathbb{R}^{\mathrm{N_n}}$ respectively, collect the weights and biases of the learnable affine transformations. By applying a second fully connected layer $\mathcal{F}_2$ to $\boldsymbol{\beta}^{\mathcal{F}_1}$, it is possible to compute:

$$\boldsymbol{\beta}^{\mathcal{F}_2} = \mathcal{F}_2\left(\boldsymbol{\beta}^{\mathcal{F}_1}, \Xi_{\mathcal{F}_2}, \boldsymbol{\mathscr{b}}_{\mathcal{F}_2}\right) = \mathcal{F}_2 \circ \mathcal{F}_1\left(\boldsymbol{a}, \left[\Xi_{\mathcal{F}_1}, \Xi_{\mathcal{F}_2}\right], \left[\boldsymbol{\mathscr{b}}_{\mathcal{F}_1}, \boldsymbol{\mathscr{b}}_{\mathcal{F}_2}\right]\right). \tag{5.11}$$

Such an architecture composed of two fully connected layers is said to be a feed forward NN with a single hidden layer. The vector $\boldsymbol{\beta}^{\mathcal{F}_1}$ is an internal representation of the inputs or, in other words, forms a set of features. In this sense, a NN epitomizes the essence of the DL paradigm.

In general, stacking multiple layers allows to perform strong nonlinear transformations of the input, and approximate complex target functions. The relevant weights are then calibrated during a training phase through the optimization of a loss function on the available datasets.

For ease of explanation, a one-dimensional (1d) array $\boldsymbol{a}$ has been considered as input vector for $\mathcal{F}_1$. However, 2d–arrays like the MTS $\mathbf{U}$ can be similarly treated. In that case, the number of weights would highly increase, therefore requiring a greater number of training data. To limit the size of the training datasets $\mathbf{D}_{\mathrm{CL}}$ and $\mathbf{D}_{\mathrm{RG}}$, convolutional layers [32] are often preferred for feature extraction purposes. They reduce the number of tuning weights by exploiting local correlation within their inputs (the convolutional kernel inputs are in close proximity with one another and isolated from distal entities) and translation equivariance (the learned rule can be reused across different localities in the input). In other words, convolutional layers enjoy sparse connectivity and parameter sharing, leading to a great computational efficiency.

When MTS data are treated, 1d convolutional layers are usually employed [26]. Assuming the vibration recordings $\mathbf{U}$ as input of a convolutional layer $\mathcal{C}_1$ featuring a single output filter, the output $\boldsymbol{\beta}^{\mathcal{C}_1}$ is computed as

$$\boldsymbol{\beta}^{\mathcal{C}_1} = \mathcal{C}_1\left(\mathbf{U}, \Xi_{\mathcal{C}_1}, \mathscr{b}_{\mathcal{C}_1}\right) = \mathcal{A}\left(\sum_{\mathrm{n_u}=1}^{\mathrm{N_u}} \boldsymbol{\omega}_{\mathcal{C}_1}^{\mathrm{n_u}} \ast \mathbf{u}^{\mathrm{n_u}} + \mathscr{b}_{\mathcal{C}_1}\right), \tag{5.12}$$

where $\Xi_{\mathcal{C}_1} = \left[\boldsymbol{\omega}_{\mathcal{C}_1}^{1}, \ldots, \boldsymbol{\omega}_{\mathcal{C}_1}^{\mathrm{N_u}}\right] \in \mathbb{R}^{\mathrm{N_h} \times \mathrm{N_u}}$ are the kernel filters of $\mathcal{C}_1$; $\ast : \left(\mathbb{R}^{\mathrm{N_h}} \times \mathbb{R}^{L}\right) \to \mathbb{R}^{L}$ is the discrete convolution operator [21]; $\mathrm{N_h}$ is the kernel dimension, setting the dimension of the local correlation sought by the convolutional layer. For ease of explanation, $\mathcal{C}_1$ has been here designed to output a 1d–array, i.e. a single output channel, but a straightforward extension of eq. (5.12) can be elaborated to output 2d–arrays; see [33] for a complete treatment of how NNs can handle monitoring vibrational data. Like fully connected layers, also convolutional layers can be stacked multiple times to obtain hierarchical high-level representations useful to approximate the target function. If 1d convolutional layers are employed for feature extraction purposes, the obtained NN architecture is defined as a 1d Convolutional Neural Network (CNN).

#### 5.2.3.2 Multivariate time series classification using one-dimensional convolutional neural networks

We address now the multiclass classification task underlying a damage detection and localization problem through a 1d CNN $\mathcal{NN}_{\mathrm{CNN}}$. The set of weights and biases parametrizing $\mathcal{NN}_{\mathrm{CNN}}$ and collectively denoted as $\boldsymbol{\Theta}_{\mathrm{CL}}$ is learned by minimizing a loss function over the training dataset $\mathbf{D}_{\mathrm{CL}}$; for classification tasks, the probabilistic categorical cross-entropy between the predicted and target label classes is adopted, as follows:

$$H(\boldsymbol{\Theta}_{\mathrm{CL}}, \mathbf{D}_{\mathrm{CL}}) = -\frac{1}{\mathrm{N_i}} \sum_{\mathrm{n_i}=1}^{\mathrm{N_i}} \sum_{j=1}^{\mathrm{N_c}} b_{\mathrm{n_i}}^{j} \log\left(\hat{b}_{\mathrm{n_i}}^{j}\right). \tag{5.13}$$

$H(\boldsymbol{\Theta}_{\mathrm{CL}}, \mathbf{D}_{\mathrm{CL}})$ provides a measure of the distance between the discrete probability distribution describing $\boldsymbol{b}$ (collected in $\mathbf{D}_{\mathrm{CL}}$) and its estimated counterpart $\hat{\boldsymbol{b}}$; its minimization is equivalent to maximizing the likelihood of the training dataset on the parameters of the model. The minimization is performed by exploiting the optimization algorithm Adam [27]. Herein, $\hat{\boldsymbol{b}} = \left(\hat{b}^{1}, \ldots, \hat{b}^{\mathrm{N_c}}\right)^{\top} \in \mathbb{R}^{\mathrm{N_c}}$ is a vector collecting the confidence levels $\hat{b}^{j}$ by which the current instance is assigned to the $j$–th damage class. Such a probability distribution of $\hat{\boldsymbol{b}}$ over the $\mathrm{N_c}$ possible classes is provided with a Softmax activation function $\hat{\boldsymbol{b}} = \mathrm{Softmax}(\mathbf{a})$ as follows:

$$\hat{b}^j(\mathbf{a}) = \frac{\exp(a^j)}{\sum_{\iota=1}^{\mathrm{N_c}} \exp(a^\iota)}, \quad j = 1, \ldots, \mathrm{N_c}, \tag{5.14}$$

which converts a vector of real-valued inputs $\mathbf{a} = (a^1, \ldots, a^{\mathrm{N_c}})^\top \in \mathbb{R}^{\mathrm{N_c}}$ into a discrete probability distribution. When the trained model is exploited for prediction purposes, the most likely class is selected as the one that best explains the processed measurements. The NN architecture comprising $\mathcal{NN}_{\mathrm{CNN}}$ and adopted to map the MTS vibration recordings $\mathbf{U}$ onto the probability distribution $\hat{\boldsymbol{b}}$ will be detailed in Sec. 5.3.1.

The performance of $\mathcal{NN}_{\mathrm{CNN}}$ against the considered classification task is assessed in terms of the accuracy indicator $\mathrm{Acc} = \frac{\mathrm{CC}}{\mathrm{AC}}$, which measures the ratio between the number CC of correct classifications to the overall number AC of classifications. The evolution of the classification accuracy, together with the loss score, are monitored during training to evaluate the learning process advancement. To avoid overfitting, part of the instances collected in $\mathbf{D}_{\mathrm{CL}}$ are employed to monitor the $\mathcal{NN}_{\mathrm{CNN}}$ performance during training, without affecting the calibration of weights $\boldsymbol{\Theta}_{\mathrm{CL}}$; those instances are said to be employed for validation purposes. Once $\mathcal{NN}_{\mathrm{CNN}}$ is trained, its performance is tested against a set of $\mathrm{N_i^T}$ instances unseen during training and validation.

#### 5.2.3.3 Encoding damage sensitivity into a low-dimensional metric space through a Siamese architecture

The regression task underlying a damage identification problem is finally addressed through the construction (learning) of an ordered and smooth mapping of the vibration recordings onto a low-dimensional feature space. This is useful to effectively encode the sought damage parameters $\mathscr{y}$, so that they can be easily predicted directly in the low-dimensional space. With reference to the damage localization task, here, the sought damage parameters are the coordinates of the damaged region in a regression-like fashion, see e.g. [46, 45].

The aforementioned mapping is driven by $\mathcal{NN}_{\mathrm{H}}$, with the subscript H standing for “head”, designed to map vibration recordings $\mathbf{U}(\boldsymbol{\mu})$ onto its feature representation $\mathscr{h}(\mathscr{y}) \in \mathbb{R}^{N_{\mathscr{h}}}$ in a low-dimensional space of size $N_{\mathscr{h}}$, as:

$$\mathscr{h}(\mathscr{y}) = \mathcal{NN}_{\mathrm{H}}(\boldsymbol{U}(\mu)), \tag{5.15}$$

where the trainable layers will be better specified in Sec. 5.3.2.

In order to code the damage parameters $\mathscr{y}$ through the low-dimensional representation $\mathscr{h}(\mathscr{y})$, we require that a suitable distance function $\mathcal{E}_{\mathscr{h}} = \mathcal{E}_{\mathscr{h}}(\mathscr{h}_1(\mathscr{y}_1), \mathscr{h}_2(\mathscr{y}_2))$ of any pair of mappings $\mathscr{h}_1(\mathscr{y}_1)$ and $\mathscr{h}_2(\mathscr{y}_2)$ semantically approximates the Euclidean distance $\mathcal{E}_{\mathscr{y}}(\mathscr{y}_1, \mathscr{y}_2) = ||\mathscr{y}_1 - \mathscr{y}_2||_2$ between the associated damage parameters $\mathscr{y}_1$

and $\mathscr{y}_2$. This is achieved through the Siamese architecture [4] sketched in Figure 5.1, which is made of two identical heads $\mathcal{NN}_\mathrm{H}$ sharing the same set of weights. The two NNs are linked by the loss function $\mathcal{L}_{\mathrm{sq-sq}}$, hence, those data points are processed in pairs, yielding two outputs $\mathscr{h}_1(\mathscr{y}_1)$ and $\mathscr{h}_2(\mathscr{y}_2)$. To this aim, the dataset $\mathbf{D}_{\mathrm{RG}}$ is augmented to $\mathbf{D}^{\mathrm{P}}_{\mathrm{RG}}$ through a pairing process; by prescribing a threshold distance $\overline{\mathcal{E}_{\mathscr{y}}}$, $\zeta_+$ positive pairs, characterized by similar damage conditions $\left(\mathcal{E}_{\mathscr{y}} \leq \overline{\mathcal{E}_{\mathscr{y}}}\right)$, and $\zeta_-$ negative pairs, characterized by dissimilar damage conditions $(\mathcal{E}_{\mathscr{y}} > \overline{\mathcal{E}_{\mathscr{y}}})$, are assembled for each data instance, to provide:

$$\mathbf{D}^{\mathrm{P}}_{\mathrm{RG}} = \left\{ \left(\mathbf{U}_1(\boldsymbol{\mu}_1),\, \mathscr{y}_1 \mathbf{U}_2(\boldsymbol{\mu}_2),\, \mathscr{y}_2\right)_{\mathrm{n}^{\mathrm{P}}_{\mathrm{i}}} \right\}_{\mathrm{n}^{\mathrm{P}}_{\mathrm{i}}=1}^{\mathrm{N}^{\mathrm{P}}_{\mathrm{i}}}, \tag{5.16}$$

where $\mathrm{N}^{\mathrm{P}}_{\mathrm{i}} = \mathrm{N}_{\mathrm{i}}(\zeta_+ + \zeta_-)$ is the total number of pairs.

During training, the set of weights $\boldsymbol{\Theta}_\mathrm{H}$ parametrizing $\mathcal{NN}_\mathrm{H}$ is optimized by minimizing the following square–square loss function:

$$\mathcal{L}_{\mathrm{sq-sq}}\left(\boldsymbol{\Theta}_\mathrm{H}, \mathbf{D}^{\mathrm{P}}_{\mathrm{RG}}\right) = \frac{1}{\mathrm{N}^{\mathrm{P}}_{\mathrm{i}}} \sum_{\mathrm{n}^{\mathrm{P}}_{\mathrm{i}}=1}^{\mathrm{N}^{\mathrm{P}}_{\mathrm{i}}} \left\{ (1-\gamma)\frac{1}{2}(\mathcal{E}_{\mathscr{h}})^2 + \gamma\frac{1}{2}\left[\max\left(0, \psi - \mathcal{E}_{\mathscr{h}}\right)\right]^2 \right\}_{\mathrm{n}^{\mathrm{P}}_{\mathrm{i}}}, \tag{5.17}$$

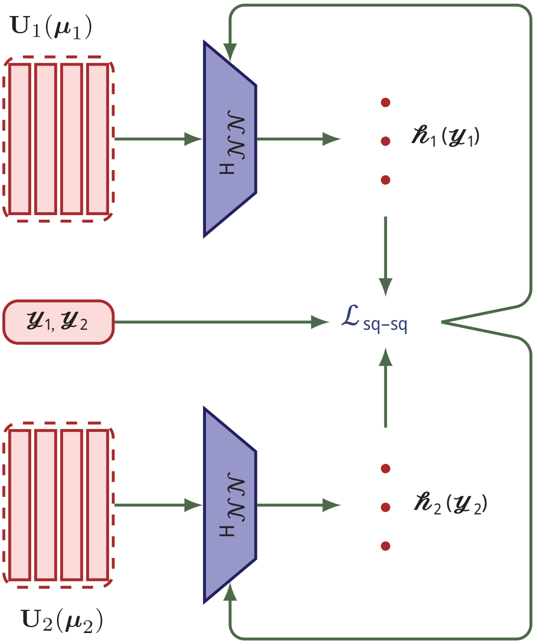

**Figure 5.1:** Scheme of the Siamese architecture. The set of weights parametrizing the mapping $\mathcal{NN}_\mathrm{H}$ is learned by processing paired vibration recordings $\mathbf{U}_1(\boldsymbol{\mu}_1)$ and $\mathbf{U}_2(\boldsymbol{\mu}_2)$, and by minimizing a function of the distance between the relative low-dimensional representations $\mathscr{h}_1(\mathscr{y}_1)$ and $\mathscr{h}_2(\mathscr{y})_2$, and of the corresponding damage parameters $\mathscr{y}_1$ and $\mathscr{y}_2$.

where: $\gamma = \{0, 1\}$, respectively, if $\mathscr{y}_1$ and $\mathscr{y}_2$ identify a positive or a negative pair; $\psi > 0$ is a margin beyond which negative pairs do not contribute to $\mathcal{L}_{\mathrm{sq-sq}}$; the metric adopted for the computation of distances in the low-dimensional space is the Euclidean one, although this can be further generalized. The minimization of $\mathcal{L}_{\mathrm{sq-sq}}$ yields a distance function $\mathcal{E}_{\mathscr{h}}$, such that dissimilar pairs are kept away by at least the margin $\psi$, while similar pairs are pushed to be as close as possible.

Once trained, the Siamese architecture is discarded, and only $\mathcal{NN}_{\mathrm{H}}$ is retained together with $\mathbf{D}_{\mathrm{RG}}$. The damage position for a data instance $\mathbf{U}_{(u)}$ unseen during the training phase is then predicted through a k-nearest neighbours (KNN) regression in the low-dimensional space. To calibrate the KNN regressor, $\mathbf{D}_{\mathrm{RG}}$ is projected onto the low-dimensional space to provide:

$$\mathbf{D}_{\mathscr{h}} = \left\{ \left( \mathscr{h}_{\mathrm{n_i}}, \mathscr{y}_{\mathrm{n_i}} \right) \right\}_{\mathrm{n_i}=1}^{\mathrm{N_i}}, \tag{5.18}$$

so that the low-dimensional encodings of the training data and the relative labels can be stored by the KNN model.

At prediction time, the KNN regressor computes the distances between $\mathscr{h}_{(u)} = \mathcal{NN}_{\mathrm{H}}\left(\mathbf{U}_{(u)}\right)$ and its nearest neighbors among $\mathscr{h}_{\mathrm{n_i}}$, $\mathrm{n_i} = 1, \ldots, \mathrm{N_i}$, to provide an estimate $\widehat{\mathscr{y}}_{(u)}$ of the associated damage parameters as a weighted average of the corresponding labels. The number of neighbors accounted for in such a regression and the associated weighting rule are not set a–priori, but their value is determined through an $N$–fold cross-validation strategy. This approach is expected to reduce the potential influence of outliers within $\mathbf{D}_{\mathscr{h}}$ identifying a model of optimal complexity.

## 5.3 Results

For the considered case studies, the HF and LF numerical models have been implemented in the Matlab environment, using the redbKIT library [30]. The NN architectures have been implemented through the Tensorflow-based Keras API [8]. These architectures as well as the relevant hyperparameters and training options, are selected through a preliminary sensitivity study, aimed at minimizing the loss function of interest while retaining the corresponding generalization capabilities.

### 5.3.1 Damage identification in a shear-type building

We first assess the performance of damage identification as a classification task in the case of the shear building model depicted in Figure 5.2. The structure, originally proposed in [7], is an idealized eight story shear building with constant floor mass

$m = 625$ ton and interstory stiffness $k = 10^6$ kN/m. The vibrational response of the building in the horizontal direction is simulated by employing 1 dof per floor; therefore, given that the model accounts for only $\mathscr{M} = 8$ dofs, a LF model further reducing the number of dofs is not employed in this case.

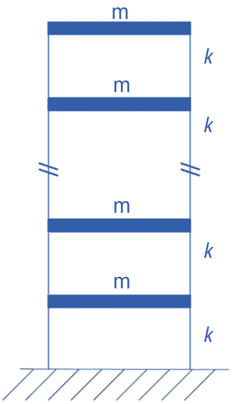

**Figure 5.2:** Shear building model.

To construct $\mathbf{D}_{\mathrm{CL}}$, $\mathrm{N_c} = 9$ possible damage classes are considered: the classes labelled as “1”, “2”, . . . “8” refer to a 25% stiffness reduction associated with the corresponding interstory link, while “0” denotes the undamaged state class. As reported in Table 5.1, only two trends can be highlighted in terms of structural frequencies for the different damage classes: the reduction of each structural frequency induced by a damage in the first interstory connection and the reduction of the first structural frequency induced by each damage class.

Displacements time histories $\mathbf{u}^{\mathrm{nu}}$ are recorded for all the $\mathrm{N_u} = 8$ floors, with sensors numbered from bottom to top. Recordings are provided for a time interval $(0, T = 10\,\mathrm{s})$ with an acquisition frequency $\mathscr{f} = 66$ Hz, in order to avoid aliasing for both the undamaged and the damaged classes.

**Table 5.1:** Shear building. Structural frequencies (in Hz) of the lateral vibrations for the considered damage classes (0 labels the undamaged state class).

| | **Damage class** | | | | | | | | |
|---|---|---|---|---|---|---|---|---|---|
| **Mode** | **0** | **1** | **2** | **3** | **4** | **5** | **6** | **7** | **8** |
| 1 | 1.175 | 1.131 | 1.134 | 1.140 | 1.146 | 1.154 | 1.162 | 1.169 | 1.173 |
| 2 | 3.484 | 3.368 | 3.427 | 3.480 | 3.467 | 3.400 | 3.355 | 3.375 | 3.445 |
| 3 | 5.678 | 5.522 | 5.668 | 5.570 | 5.467 | 5.614 | 5.647 | 5.488 | 5.522 |
| 4 | 7.673 | 7.521 | 7.630 | 7.401 | 7.663 | 7.448 | 7.532 | 7.600 | 7.394 |
| 5 | 9.409 | 9.287 | 9.143 | 9.322 | 9.126 | 9.362 | 9.114 | 9.396 | 9.105 |
| 6 | 10.825 | 10.745 | 10.471 | 10.764 | 10.665 | 10.490 | 10.812 | 10.528 | 10.598 |
| 7 | 11.873 | 11.833 | 11.659 | 11.510 | 11.750 | 11.857 | 11.596 | 11.560 | 11.755 |
| 8 | 12.516 | 12.505 | 12.456 | 12.378 | 12.273 | 12.227 | 12.328 | 12.421 | 12.484 |

Two load cases are considered to show the performance of the approach when the frequency band of the loading is either narrow or broad. The first load case applies at each floor a force featuring a narrow frequency band, possibly exceeding the structural frequencies range. This load case is termed sinusoidal because of the specific type of time variation in accordance with:

$$\mathrm{q}_{\mathrm{n_i}}^{\mathrm{n_u}}(\mathrm{t}) = \sum_{\iota=1}^{2} \frac{\mathrm{n_u}}{8} \eta_{\mathrm{n_i}}^{\iota} \sin\left(2\pi\phi_{\mathrm{n_i}}^{\iota}\mathrm{t}\right), \quad \text{with} \quad \mathrm{n_u} = 1, \ldots, 8, \tag{5.19}$$

which provides a summation over two harmonic components. For the $\mathrm{n_i}$–th instance, each harmonic component features: amplitude $\eta_{\mathrm{n_i}}^{\iota}$ sampled from a normal probability density function with zero mean and standard deviation equal to 1 KN; frequency $\phi_{\mathrm{n_i}}^{\iota}$ computed by taking one of the undamaged vibration frequencies and then multiplying it with a value sampled from a normal probability density function with zero mean and standard deviation equal to $\sqrt{2}$. The spatial variation of the load is inspired by the lateral force method reported in [14], while the sinusoidal time law is somehow due to the fact that any time variations can be decomposed through a Fourier series. Examples of force evolution in time are reported in Figure 5.3.

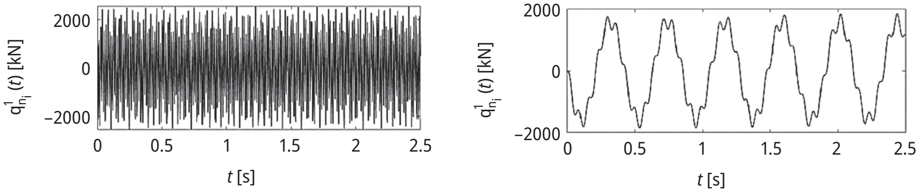

(a) $\eta_{n_i}^1 = -0.446$ kN, $\eta_{n_i}^2 = -1.53$ kN
$\phi_{n_i}^1 = 21.1$ Hz, $\phi_{n_i}^2 = 69.2$ Hz

(b) $\eta_{n_i}^1 = 0.192$ kN, $\eta_{n_i}^2 = 1.22$ kN
$\phi_{n_i}^1 = 14.5$ Hz, $\phi_{n_i}^2 = 2.36$ Hz

**Figure 5.3:** Shear building, sinusoidal load case. Exemplary time evolutions of the load applied to the first floor over the first 2.5 s of the total time window.

The acquired measurements are then mimicked by corrupting the output of numerical simulations with an additive Gaussian noise, so that the resulting signals feature a signal-to-noise ratio equal to 15 dB. A comparison between noise-free (numerical) and noisy signals is provided in Figure 5.4.

The second load case, termed white noise one, is characterized by a force whose time amplitude is sampled from a normal probability density function with zero mean and standard deviation equal to 10 kN. The resulting frequency spectrum is then processed by means of a low-pass filter with roll-off between 5 and 7 Hz. This type of random excitation may be caused by low-energy seismicity from urban or natural sources [22, 3]. A possible realization of this load case is reported in Figure 5.5.

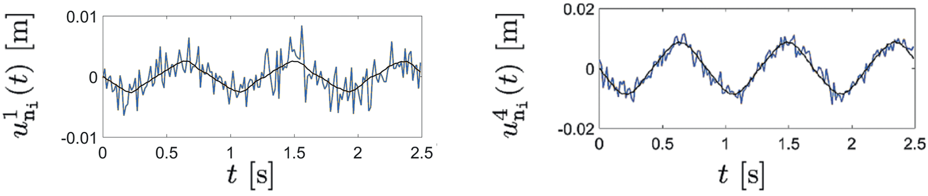

**(a)** 1st floor **(b)** 4th floor

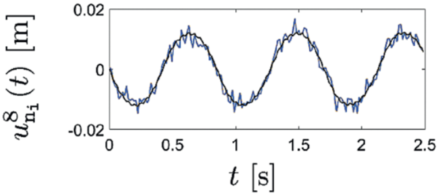

**(c)** 8th floor

**Figure 5.4:** Shear building, sinusoidal load case. Exemplary displacement time-histories $\boldsymbol{u}^1_{n_i}$, $\boldsymbol{u}^4_{n_i}$, $\boldsymbol{u}^8_{n_i}$ corresponding to $\eta^1_{n_i} = -0.446$ kN, $\eta^2_{n_i} = 1.531$ kN, $\phi^1_{n_i} = 21.1$ Hz, and $\phi^2_{n_i} = 69.2$ Hz. The blue lines denote pseudo–experimental displacements, whereas black lines refer to the noise-free output of the numerical model.

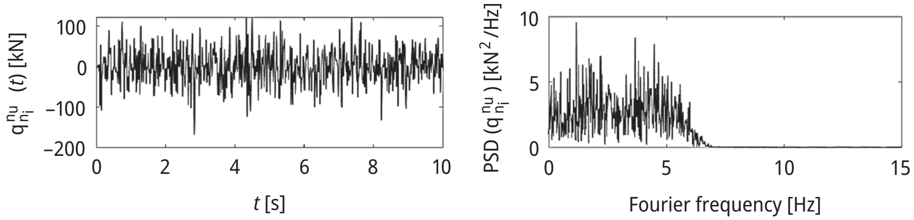

(a) (b)

**Figure 5.5:** Shear building, white noise load case. Exemplary time evolution (left) and power spectral density PSD (right) of the applied forces $q^{n_u}_{n_i}(t)$, with $n_u = 1, \ldots, 8$.

For each load case, $\mathbf{D}_{\mathrm{CL}}$ is assembled with $\mathrm{N_i} = 3500$ numerically simulated instances $\left(\mathbf{U}_{n_i}, \boldsymbol{b}_{n_i}\right)$, where $\boldsymbol{b}_{n_i}$ encodes the damage class for the $\mathtt{n_i}$–th instance. $\mathbf{D}_{\mathrm{CL}}$ is then splitted with a ratio of 80 : 20 for training and validation purposes.

Damage classification is addressed with the 1d $\mathcal{NN}_{\mathrm{CNN}}$ receiving $\mathbf{U}_{n_i}$ as input and returning $\hat{\boldsymbol{b}}_{n_i}$ as output. $\mathcal{NN}_{\mathrm{CNN}}$ is composed of three convolutional units, each one consisting of a convolutional layer, ReLU activation function, and batch normalization [18]. The resulting output is then run through a global average pooling layer [43] and, finally, through a Softmax-activated fully connected layer. The convolutional layers respectively feature 16, 32, 16 filters with a kernel size of 8, 5, 3. The cross-entropy loss function is computed as in eq. (5.13), having determined a confidence level $\hat{\boldsymbol{b}}_{\mathrm{n_i}}$ for each possible damage class, according to eq. (5.14). Adopting a learning rate of $10^{-3}$ and a batch size of 10, the loss function is minimized for a maximum of 1500 epochs. The training is then stopped whenever overfitting is detected from the loss function score attained on the validation instances; this strategy, termed early stopping, avoids $\mathcal{NN}_{\mathrm{CNN}}$ from barely memorizing the input-output pairs contained in $\mathbf{D}_{\mathrm{CL}}$.

The evolution of the loss function $H$ during training is reported in Figure 5.6 for the sinusoidal load case, together with the corresponding evolution of the accuracy indicator Acc. To assess the performance of the classifier, this latter must be compared with the accuracy score resulting from a random guess $(\mathrm{Acc} = 1/\mathrm{N_C})$. The most significant gains in terms of classification accuracy are displayed in the first stages of the training, after which only a limited increase in the generalization capabilities of $\mathcal{NN}_{\mathrm{FCN}}$ is attained.

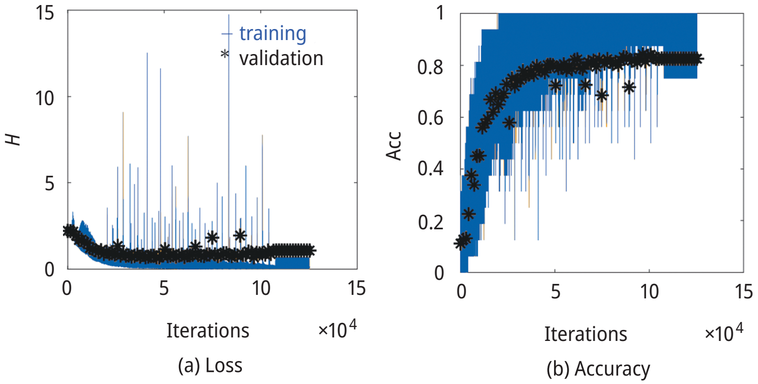

(a) Loss

(b) Accuracy

**Figure 5.6:** Shear building, sinusoidal load case. Evolution of the loss function and of the accuracy indicator of $\mathcal{NN}_{\mathrm{CNN}}$ during training, related to the training (blue) and validation (black) data instances.

Once trained, $\mathcal{NN}_{\mathrm{CNN}}$ is tested against $\mathrm{N_i^T} = 1152$ new instances, providing an overall accuracy of 76.8% for the sinusoidal load case. Most of the misclassifications are related to the damage classes connected to the stiffness reduction at the highest floors, see Table 5.2. This is reasonable, as the response of the upper floors is expected to be more sensitive to damage below; also note the corresponding frequency drift reported in Table 5.1. On the other hand, the damage states at the lowest floors are mostly correctly identified. The undamaged state 0 is reported to be often misclassified as damage classes 7 and 8, for the same reasons discussed above: it is difficult to detect small frequency variations due to a stiffness reduction in the highest interstoreys, especially in the presence of noise.

A better performance is reported for the white noise load case. In particular, the overall classification accuracy attained by $\mathcal{NN}_{\mathrm{CNN}}$ against $\mathrm{N_i^T} = 1152$ newly collected instances reaches 99.3%. This excellent outcome is due to the fact that, for the consid-

**Table 5.2:** Shear building, sinusoidal load case. Accuracy of each damage classification as attained by $\mathcal{NN}_{\text{CNN}}$.

| **Damage class** | | | | | | | | |
|---|---|---|---|---|---|---|---|---|
| 0 | 1 | 2 | 3 | 4 | 5 | 6 | 7 | 8 |
| 78.9% | 99.2% | 96.1% | 88.3% | 85.9% | 82.8% | 75.0% | 63.3% | 61.7% |

ered white noise load case, the first three structural modes are always excited, thus allowing $\mathcal{NN}_{\text{CNN}}$ to correctly catch how the resulting vibrations are affected by each damage class.

The reported performance of $\mathcal{NN}_{\text{CNN}}$ for the two considered load cases is counterbalanced by two aspects. First, the need of an a–priori definition of the possible damage classes to be accounted for: if a damage scenario not considered shows up, $\mathcal{NN}_{\text{CNN}}$ would be unable to correctly classify it. Second, the features extracted with $\mathcal{NN}_{\text{CNN}}$ could be not robust to small deviations between the probability distributions underlying the training data and the incoming data. These issues can be addressed by means of the low-dimensional metric space obtained with the Siamese architecture illustrated in Section 5.2.3.3 and whose application is shown next.

## 5.3.2 Damage identification in a railway bridge

This case study aims to assess the performance of the damage localization strategy proposed in Section 5.2.3.3 against the railway bridge depicted in Figure 5.7. This bridge is an integral concrete portal frame located along the Bothnia line, featuring a span of 15.7 m, a free height of 4.7 m and a width of 5.9 m (edge beams excluded). The thickness of the structural elements is 0.5 m for the deck, 0.7 m for the frame walls, and 0.8 m for the wing walls. The mechanical properties of concrete are: $E = 34$ GPa, $\nu = 0.2$, $\rho = 2500\ \text{kg/m}^3$; for further details, see [37, 45]. The bridge is subjected to the transit of trains composed of two wagons, traveling with a speed $v \in [160, 215]\ \text{km/h}$ and with each axle carrying a mass $\phi \in [16, 22]$ ton.

The bridge is discretized with 17,057 tetrahedral elements, resulting in $\mathcal{M} = 17,292$ dofs. The monitoring system features $\text{N}_\text{u} = 10$ sensors and is deployed as depicted in Figure 5.8 to provide $\mathbf{U}(\boldsymbol{\mu}) = [\mathbf{u}_1, \ldots, \mathbf{u}_{\text{N}_\text{u}}]$. Data are assumed to be collected along the time interval $(0, T = 1.5\ \text{s})$ with frequency $\mathscr{f} = 400$ Hz.

$\mathbf{D}_{\text{RG}}$ is assembled by considering that damage can take place anywhere in the two lateral frame walls and in the deck, within subdomains $\Omega_y$ as depicted in Figure 5.8. The stiffness reduction can occur with a magnitude $\delta \in$ [30%, 40%] constant within $(0, T)$, whose spatial coordinates $\mathscr{y} = (x_\Omega, z_\Omega) \in \mathbb{R}$ are characterized by either $x_\Omega$ or $z_\Omega$ varying in the ranges [–0.115, 16.63] m and [0.25, 6.25] m.

**Figure 5.7:** Hörnefors railway bridge.

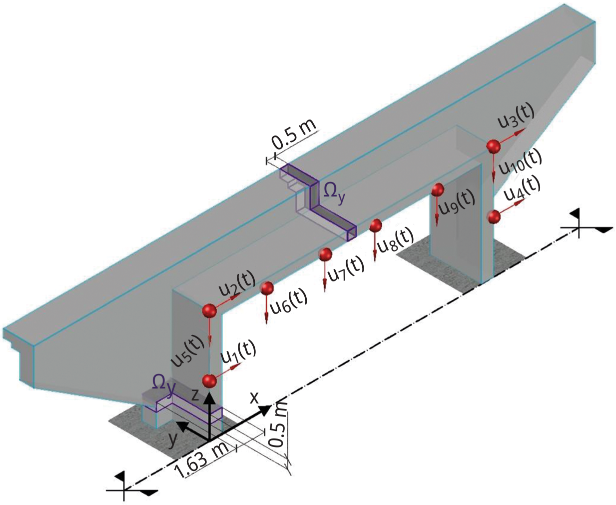

**Figure 5.8:** Railway bridge. Cross-section with details of the synthetic recordings related to displacements $u_1(t)\ldots, u_{10}(t)$ and exemplary damaged regions $\Omega_y$.

The dataset $\mathbf{D}_{\mathrm{RG}}$ is built with $\mathrm{N_i} = 8000$ instances computed with an ROM featuring $\mathscr{M}_{\mathrm{LF}} = 528$ POD–modes in place of the original 17, 292 dofs, and augmented to $\mathbf{D}_{\mathrm{RG}}^{\mathrm{P}}$ with $\zeta_+ = \zeta_- = 10$ pairs after prescribing a threshold distance $\overline{\mathcal{E}_{\mathscr{y}}} = 0.25$ m. The testing dataset consists of $\mathrm{N_i^T} = 800$ instances generated through the FOM. Both the training and testing data are corrupted with an additive Gaussian noise, yielding a signal-to-noise ratio equal to 20.80 dB. An exemplary time history of the vertical displacement at midspan is reported in Figure 5.9, to compare the FOM solution and the noise-corrupted ROM approximation.

The architecture of $\mathcal{NN}_{\mathrm{H}}$ features three 1d convolutional units, each one consisting of a convolutional layer, a nonlinear activation function, batch normalization, a max pooling layer, and a dropout layer [42]. The convolutional layers respectively feature 16, 32, 16 filters with a kernel size of 25, 13, 7. The output features are then flattened and run through a stack of three fully connected layers, respectively featuring 64, 16, 4 neurons, whose output is the low-dimensional representation $\hbar$, with $N_{\hbar} = 4$; further insights on how to choose $N_{\hbar}$ can be found, e.g., in [35, 45]. No activation is applied to the last dense layer, while the tanh activation function is employed elsewhere.

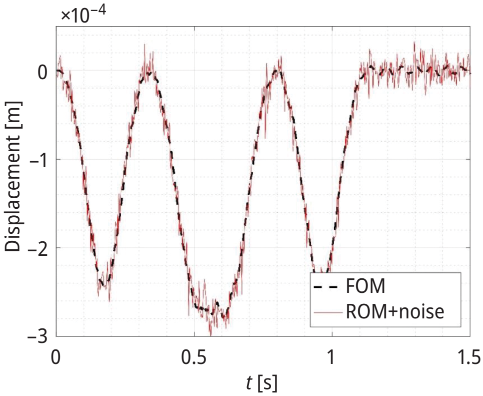

**Figure 5.9:** Railway bridge. Time history of the vertical displacement at midspan ($x_{\Omega} = 8.25$ m, $z_{\Omega} = 6.25$ m, $\delta = 0.35$, $v = 210$ km/h, and $\phi = 20$ ton): comparison between FOM and noise-corrupted ROM approximation.

By splitting $\mathbf{D}^{\mathrm{P}}_{\mathrm{RG}}$ with a ratio 75 : 25 for training and validation purposes and by adopting a batch size of 32, the loss function $\mathcal{L}_{\mathrm{sq-sq}}$ is minimized for a maximum of 100 epochs. The learning rate is initially set to $10^{-4}$, and decreased for 80 epochs by adopting a cosine decay schedule with weight decay 0.05. An early stopping strategy is used to interrupt the learning process.

A compact representation of the low-dimensional embeddings collected in $\mathbf{D}_{\hbar}$ is shown in Figure 5.10, as obtained by applying the metric version of multidimensional scaling. Multidimensional scaling is a nonlinear dimensionality reduction method that seeks a low-dimensional representation of the input data, preserving pairwise distances as much as possible [20]. In these graphs, the color channel refers to the target damage position along the $x$-axis, i.e., $\{x_{\Omega \mathrm{n_i}}\}_{\mathrm{n_i}=1}^{\mathrm{N_i}}$, and along the $z$-axis, i.e., $\{z_{\Omega \mathrm{n_i}}\}_{\mathrm{n_i}=1}^{\mathrm{N_i}}$. Intuitively, these plots show that $\mathcal{NN}_{\mathrm{H}}$ correctly encodes the damage position in the low-dimensional space, with higher accuracy along the $z$-axis as the portion of the manifold describing the variation along the $x$-axis looks more confused and increased in size.

Damage is located by exploiting a KNN regressor accounting for 51 nearest neighbors with inverse distance weights, which provides the maximum folds averaged regression score against a 20-fold cross-validation. The distributions of the prediction error along the $x$ and $z$ directions, in relation to the $\mathrm{N_i^T} = 800$ testing instances, are reported in Figure 5.11; in these charts, the counts refer to the number of instances for which a certain prediction error is reported. The observed values are distributed in a rather narrow range around the origin, showing that the damage position is almost always identified with high accuracy. From a quantitative point of view, damage locations feature a mean absolute error $\mathrm{MAE}_x = 0.453$ m, $\mathrm{MAE}_z = 0.260$ m, respectively along the $x$-axis and $z$-axis. This result confirms what stated about the more confused manifold portion describing the variation of damage position along the $x$-axis. Nevertheless, the overall result is still noteworthy, especially considering the involved dynamic response triggered by the moving load and the limited extension of the considered damage regions: both MAE values are smaller then the width of the damaged regions, which is 0.5 m.

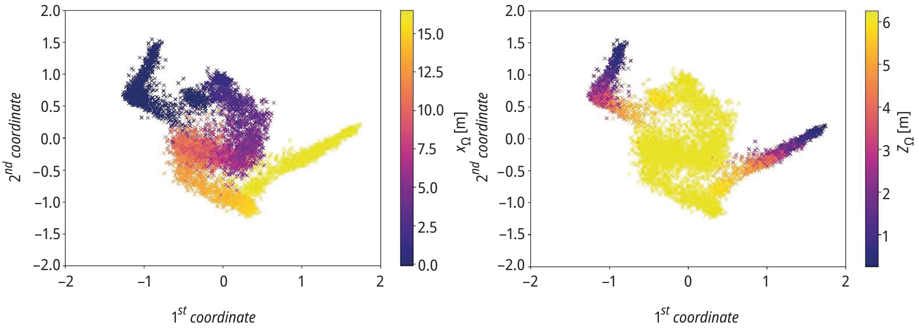

**Figure 5.10:** Railway bridge. Multidimensional scaling of the low-dimensional representation of the training instances provided by $\mathcal{NN}_\mathrm{H}$, to report the correct damage position along the (left) $x$-direction $\{x_{\Omega n_i}\}_{n_i=1}^{N_i}$ and (right) $z$-direction $\{z_{\Omega n_i}\}_{n_i=1}^{N_i}$.

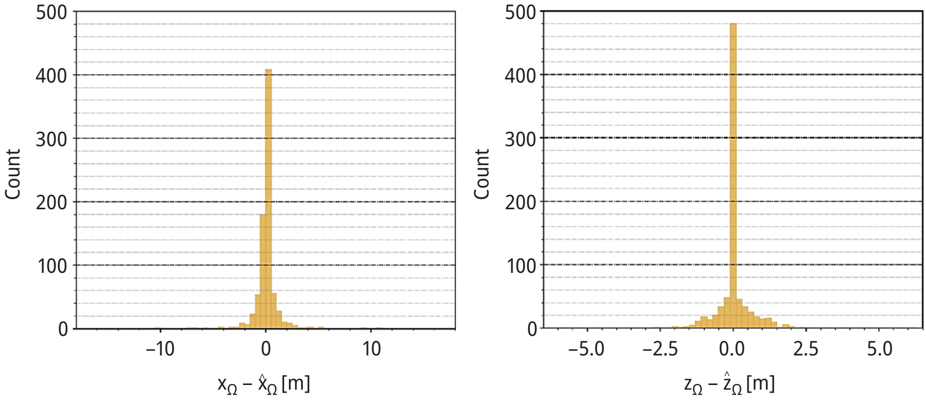

**Figure 5.11:** Railway bridge. Distribution of the prediction error over the testing instances along the (a) $x$-direction and (b) $z$-direction.

## 5.4 Conclusions

In this work, we have proposed a damage identification approach based on the simulation-based paradigm of structural health monitoring. Assuming a slow damage progression, we have considered two alternative strategies relying on learnable feature extractors and enabling damage detection and localization in civil structures: a classification-based one, to categorize multivariate time series using one-dimensional convolutional neural networks; a regression-like one, enjoying a low-dimensional metric feature space resting on contrastive pairwise learning and capable of coding damage–sensitivity.

The proposed framework relies on an offline phase of data generation and training. Within a supervised learning setting, a physics-based numerical model has been adopted to systematically simulate the structural response and generate training data pertaining to specific damage conditions under varying operational conditions. To relieve the relevant computational burden, the data generation phase has been speeded up through a model order reduction strategy for parametrized systems. The results obtained for the considered test cases prove the capability of the approach to allow damage identification under the effect of measurement noise and varying operational conditions.

Future activities will be devoted to integrate the proposed structural health monitoring tools within a sequential decision framework, to enable a digital twin concept for the structural asset to be monitored, see e.g. [25, 29]. This will allow to inform an optimal planning of maintenance, inspection, and management actions.

## References

[1] S. Alampalli. Influence of in-service environment on modal parameters. In *Proceedings – SPIE the International Society for Optical Engineering*. Vol. 1, 111–116. Citeseer, 1998.

[2] C. Bigoni, and J. S. Hesthaven. Simulation-based anomaly detection and damage localization: An application to structural health monitoring. *Computer Methods in Applied Mechanics and Engineering*, 363:112896, 2020.

[3] S. Bonnefoy-Claudet, F. Cotton, and P-Y. Bard. The nature of noise wavefield and its applications for site effects studies: A literature review. *Earth–Science Reviews*, 79(3):205–227, 2006.

[4] J. Bromley, I. Guyon, Y. LeCun, E. Säckinger, and R. Shah. Signature verification using a “Siamese” time delay neural network. *International Journal of Pattern Recognition and Artificial Intelligence*, 7:25, 1993.

[5] T. Buckley, B. Ghosh, and V. Pakrashi. A feature extraction & selection benchmark for structural health monitoring. *Structural Health Monitoring*, 0(0):14759217221111141, 0.

[6] A. Cabboi, C. Gentile, and A. Saisi. From continuous vibration monitoring to FEM-based damage assessment: Application on a stone–masonry tower. *Construction and Building Materials*, 156:252–265, 2017.

[7] R. A. De Callafon, B. Moaveni, J. P. Conte, X. He, and E. Udd. General realization algorithm for modal identification of linear dynamic systems. *Journal of Engineering Mechanics*, 134(9):712–722, 2008.

[8] François Chollet et al. Keras, 2015. https://keras.io.

[9] G. Colombera, L. Rosafalco, M. Torzoni, F. Gatti, S. Mariani, A. Manzoni, and A. Corigliano. A generative adversarial network based autoencoder for structural health monitoring. *Computer Sciences & Mathematics Forum*, 2(1):9, 2022.

[10] A. Corigliano, and S. Mariani. Parameter identification in explicit structural dynamics: Performance of the extended Kalman filter. *Computational Methods in Applied Mechanics and Engineering*, 193(36–38):3807–3835, 2004.

[11] A. D'Alessandro, A. Costanzo, C. Ladina, F. Buongiorno, M. Cattaneo, S. Falcone, C. La Piana, S. Marzorati, S. Scudero, G. Vitale, S. Stramondo, and C. Doglioni. Urban seismic networks, structural health and cultural heritage monitoring: The National Earthquakes Observatory (INGV, Italy) experience. *Frontiers in Built Environment*, 5:127, 2019.

[12] Ariel J. E., D. Kelliher, A. G. L. Borthwick, and G. P. Thomas. Offshore monopile in the southern North Sea: Part I, calibrated input sea state. *Proceedings of the Institution of Civil Engineers – Maritime Engineering*, 170(3+4):122–132, 2017.

[13] A. Entezami, and H. Shariatmadar. An unsupervised learning approach by novel damage indices in structural health monitoring for damage localization and quantification. *Structural Health Monitoring*, 17(2):325–345, 2018.

[14] European commitee for standardization. Eurocode 8: design of structures for earth- quake resistance – part 1: general rules, seismic actions and rules for buildings. 66–74, 2003.

[15] C. Farrar and K. Worden. *Structural Health Monitoring: A Machine Learning Perspective*. Wiley, Hoboken, NJ, 2013.

[16] C. R. Farrar, S. W. Doebling, and D. A. Nix. Vibration-based structural damage identification. *Philosophical Transactions of the Royal Society A: Mathematical, Physical and Engineering Sciences*, 359(1778):131–149, 2001.

[17] A. Fernandez-Navamuel, D. Zamora-Sánchez, A. J. Omella, D. Pardo, D. Garcia- Sanchez, and F. Magalhães. Supervised deep learning with finite element simulations for damage identification in bridges. *Engineering Structures*, 257:114016, 2022.

[18] X. Glorot and Y. Bengio. Understanding the difficulty of training deep feedforward neural networks. In Yee Whye Teh, and Mike Titterington, editors, *Proceedings of the Thirteenth International Conference on Artificial Intelligence and Statistics*, *Volume 9 of Proceedings of Machine Learning Research*, 249–256, Chia Laguna Resort, Sardinia, Italy, 13–15 May 2010. PMLR.

[19] R. Hadsell, S. Chopra, and Y. LeCun. Dimensionality reduction by learning an invariant mapping. In *Proceedings IEEE Computer Society Conference on Computer Vision and Pattern Recognition*, 1735–1742, 2006.

[20] T. Hastie, R. Tibshirani, and J. Friedman. *The Elements of Statistical Learning*. Springer Series in Statistics. Springer New York Inc., 2001.

[21] J. Hu, L. Shen, and G. Sun. Squeeze-and-excitation networks. In *2018 IEEE/CVF Conference on Computer Vision and Pattern Recognition*, *18 June–23 June*, 7132–7141, Salt Lake City, UT, 2018.

[22] S. S. Ivanovic, M. D. Trifunac, and M. I. Todorovska. Ambient vibration tests of structures – a review. *ISET Journal of Earthquake Technology*, 37(4):165–197, 2000.

[23] A. Kamariotis, E. Chatzi, and D. Straub. Value of information from vibration-based structural health monitoring extracted via Bayesian model updating. *Mechanical Systems and Signal Processing*, 166:108465, 2022.

[24] M. G. Kapteyn, D. J. Knezevic, and K. Willcox. Toward predictive digital twins via component-based reduced-order models and interpretable machine learning. In *AIAA Scitech 2020 Forum*, 2020.

[25] M. G. Kapteyn, J. V. R. Pretorius, and K. E. Willcox. A probabilistic graphical model foundation for enabling predictive digital twins at scale. *Nature Computational Science*, 1(5):337–347, 2021.

[26] F. Karim, S. Majumdar, H. Darabi, and S. Harford. Multivariate LSTM–FCNs for time series classification. *Neural Networks*, 116:237–245, 2019.

[27] D. Kingma and J. Ba. Adam: A method for stochastic optimization. In *International Conference on Learning Representations (ICLR)*, *7–9 May*, 1–13, San Diego, CA, 2015.

[28] Y. LeCun, Y. Bengio, and G. Hinton. Deep learning. *Nature*, 521:436–444, 2015.

[29] C. Li, S. Mahadevan, Y. Ling, S. Choze, and L. Wang. Dynamic Bayesian network for aircraft wing health monitoring digital twin. *AIAA Journal*, 55:1–12, 2017.

[30] F. Negri. redbkit, version 2.2, 2016. http://redbkit.github.io/redbKIT.

[31] A. Quarteroni, A. Manzoni, and F. Negri. *Reduced basis methods for partial differential equations: an introduction*. Springer, 2015.

[32] W. Rawat and Z. Wang. Deep convolutional neural networks for image classification: A comprehensive review. *Neural Computation*, 29(9):2352–2449, 2017.

[33] L. Rosafalco. *Blending physics and data in structural health monitoring*. PhD thesis, Politecnico di Milano, 2022. Ph.D.-Thesis defended at Politecnico di Milano, May 30, 2022, http://hdl.handle.net/10589/187737.

[34] L. Rosafalco, A. Manzoni, S. Mariani, and A. Corigliano. Fully convolutional networks for structural health monitoring through multivariate time series classification. *Advanced Modeling and Simulation in Engineering Sciences*, 7:38, 2020.

[35] L. Rosafalco, A. Manzoni, S. Mariani, and A. Corigliano. An autoencoder-based deep learning approach for load identification in structural dynamics. *Sensors*, 21(12), 2021.

[36] L. Rosafalco, A. Manzoni, S. Mariani, and A. Corigliano. Combined model order reduction techniques and artificial neural network for data assimilation and damage detection in structures. In T. Tuovinen, J. Periaux, and P. Neittaanmäki, editors, *Computational Sciences and Artificial Intelligence in Industry: New Digital Technologies for Solving Future Societal and Economical Challenges*, pages 247–259, Cham, 2022. Springer International Publishing.

[37] L. Rosafalco, M. Torzoni, A. Manzoni, S. Mariani, and A. Corigliano. Online structural health monitoring by model order reduction and deep learning algorithms. *Computers & Structures*, 255:106604, 2021.

[38] L. Rosafalco, M. Torzoni, A. Manzoni, S. Mariani, and A. Corigliano. A self-adaptive hybrid model/data-driven approach to SHM based on model order reduction and deep learning. In A. Cury, D. Ribeiro, F. Ubertini, and M. D. Todd, editors, *Structural Health Monitoring Based on Data Science Techniques*, pages 165–184. Springer International Publishing, Cham, 2022.

[39] W. Samek, G. Montavon, A. Vedaldi, L. K. Hansen, and K.-R. Müller, editors. *Explainable AI: Interpreting, Explaining and Visualizing Deep Learning, Volume 11700 of Lecture Notes in Computer Science*. Springer, 2019.

[40] P. Seventekidis, and D. Giagopoulos. Model error effects in supervised damage identification of structures with numerically trained classifiers. *Mechanical Systems and Signal Processing*, 184:109741, 2023.

[41] H. Sohn, K. Worden, and C. R. Farrar. Statistical damage classification under changing environmental and operational conditions. *Journal of Intelligent Material Systems and Structures*, 13(9):561–574, 2002.

[42] N. Srivastava, G. Hinton, A. Krizhevsky, I. Sutskever, and R. Salakhutdinov. Dropout: A simple way to prevent neural networks from overfitting. *Journal of Machine Learning Research*, 15(56):1929–1958, 2014.

[43] C. Szegedy, W. Liu, Y. Jia, P. Sermanet, S. Reed, D. Anguelov, D. Erhan, V. Van-Houcke, and A. Rabinovich. Going deeper with convolutions. In *The IEEE Conference on Computer Vision and Pattern Recognition CVPR*, *26 June–1 July*, pages 1–9, Boston, MA, 2015.

[44] T. Taddei, J. D. Penn, M. Yano, and A. T. Patera. Simulation-based classification; a model-order-reduction approach for structural health monitoring. *Archives of Computational Methods in Engineering*, 25(1):23–45, 2018.
[45] M. Torzoni, A. Manzoni, and S. Mariani. Structural health monitoring of civil structures: A diagnostic framework powered by deep metric learning. *Computers & Structures*, 271:106858, 2022.
[46] M. Torzoni, A. Manzoni, and S. Mariani. A deep neural network, multi-fidelity surrogate model approach for Bayesian model updating in shm. In *European Workshop on Structural Health Monitoring*, 1076–1086. Springer International Publishing, 2023.
[47] M. Torzoni, L. Rosafalco, and A. Manzoni. A combined model-order reduction and deep learning approach for structural health monitoring under varying operational and environmental conditions. *Engineering Proceedings*, 2(1):94, 2020.
[48] M. Torzoni, L. Rosafalco, A. Manzoni, S. Mariani, and A. Corigliano. SHM under varying environmental conditions: An approach based on model order reduction and deep learning. *Computers & Structures*, 266:106790, 2022.
[49] S. W. Doebling, C. Farrar, and M. Prime. A summary review of vibration-based damage identification methods. *The Shock and Vibration Digest*, 30:91–105, 1998.
[50] Y. Wang, S. Khoo, A.-J. Li, and H. Hao. FEM calibrated ARMAX model updating method for time domain damage identification. *Advances in Structural Engineering*, 16(1):51–60, 2013.

A. Kahouadji, S. Tiachacht*, M. Slimani, A. Behtani, B. Benaissa,
T. Khatir, M. Noori

# 6 Structural health monitoring of steel plates using modified modal strain energy indicator and optimization algorithms

**Abstract:** Assessing structural damage in plate structures is a critical issue in various engineering fields such as mechanical and civil engineering. In this paper, an efficient approach based on a modified modal strain energy (MSE) indicator, combined with robust optimization algorithms, is proposed to accurately detect, locate, and quantify structural damage in a square plate structure. A finite element model is built in MATLAB software, and the damage is simulated by element stiffness reduction. This approach precisely identifies single and multiple damages by incorporating frequency response in the MSE method. An optimization problem is then formulated using an objective function based on the modified indicator to determine the extent of the damage. The approach is evaluated using three optimization algorithms: Snake optimization, marine predators algorithm, and moth flame optimizer (MFO). Results show that the approach accurately locates and quantifies damage in all examined cases. The MFO algorithm yields superior outcomes in terms of convergence, CPU time, and accuracy of damage extent.

## 6.1 Introduction

Plate structures are widely used in various engineering applications such as civil, mechanical [1–4], and design engineering [5–9]. These structures are subjected to various external and internal loads that can lead to damage, including cracks, fractures, and other forms of structural damage. Structural damage can significantly affect the performance, safety, and durability of these structures, making their assessment and detection a crucial issue. Therefore, developing efficient and accurate techniques for structural

---

*__Corresponding author: S. Tiachacht__, Laboratory of Mechanics, Structure and Energetics (LMSE), Mouloud Mammeri University of Tizi-Ouzou, B.P.N°17 RP, 15000, Algeria, e-mail: Samir.tiachacht@ummto.dz

**A. Kahouadji, M. Slimani, A. Behtani,** Laboratory of Mechanics, Structure and Energetics (LMSE), Mouloud Mammeri University of Tizi-Ouzou, B.P.N°17 RP 15000, Algeria

**B. Benaissa,** Toyota Technological Institute, Department of Mechanical Systems Engineering, Design Engineering Lab, 468-8511, Aichi, Nagoya, Tempaku Ward, Hisakata, Japan

**T. Khatir,** Department of Technology, University Centre of Naama, P.O.Box 66, 45000 Naama, Algeria

**M. Noori,** Department of Mechanical Engineering, California Polytechnic State University, San Luis Obispo, CA, 93405, USA; School of Civil Engineering, University of Leeds, Leeds, UK

https://doi.org/10.1515/9783110791426-006

health monitoring is of extreme importance. According to existing literature, Rytter [10] proposed a framework consisting of four primary stages for monitoring the health of structural systems. Firstly, the initial stage involves the detection of damage in the structure. Subsequently, the second stage pertains to the localization of the damage within the structure. The third stage involves the assessment of the severity of the detected damage. Lastly, the fourth stage is concerned with predicting the remaining service life of the damaged structure. Numerous research studies have been carried out to develop reliable and efficient vibration-based methods for structural damage assessment, including methods based on identification using frequency contours, mode shape curvature, changes in natural frequencies, modal strain energy, and changes in dynamic flexibility [11].

Tiachacht et al. introduced an altered iteration of the Cornwell Indicator and applied it alongside a genetic algorithm to devise a method that is both stronger and more effective in precisely identifying, locating, and measuring structural damages [12, 13]. Based on the numerical findings, the GA-MCI technique proves to be a precise predictor of the location and intensity of the structural damage under various conditions, surpassing analogous methodologies identified in existing literature [14–16]. In their paper, De Oliveira et al. [17] presented a different method for monitoring the health of structures. Their approach involved the use of a lead zirconate titanate patch as an actuator to stimulate the structure, along with three patches serving as sensors to measure the structural response. Additionally, they employed singular spectrum analysis to calculate statistical metrics, thereby ensuring dependable detection of any damage.

Khatir et al. [18–22] explored the use of metaheuristic algorithms to detect damage in steel plates by utilizing FRF damage indicators. Their inverse analysis revealed that the Wild Horse Optimizer algorithm surpassed both the Harris Hawks Optimization and Arithmetic Optimization Algorithm in terms of convergence speed and CPU time. Behtani et al. [23, 24] studied the modal strain energy (MSE) damaged indicator on both undamaged and damaged CFRP beams for modal analysis. Their results indicate that the use of MSE, based on frequency, is more effective than using mode shape, and that the MSE calculated using the first mode is significantly superior to other modes. Kahouadji et al. [25] introduced a methodology that employs optimization techniques, and utilizes LFCR as a means to identify damage. Student psychology-based optimization algorithm accurately detects damage severity in 20 bar 2D and 28 bar 3D trusses, demonstrating precise damage detection and location with LFCR.

This article presents a novel methodology that effectively identifies and measures harm in plate structures through the application of an updated damage indicator and optimization strategies. Our technique involves modifying the modal strain energy (MSE) method by integrating frequency response to pinpoint the affected components. Additionally, we utilize three optimization algorithms, namely snake optimization (SO), marine predators algorithm (MPA), and moth flame optimizer (MFO) to precisely gauge the extent and severity of the harm. The proposed approach boasts of impressive accuracy in detecting and pinpointing damaged elements, as well as accurately quantifying the degree and severity of damage.

## 6.2 Modal strain energy using the frequency response

The modal strain energy (MSE) indicator is commonly used to detect potential damage in structures by identifying changes in their modal characteristics. The traditional method for MSE relies on eigenvectors, but this can be difficult to obtain and may be affected by noise. An alternative approach is to use the frequency response function, which can be easily obtained from finite element simulations. The MSE of both healthy and damaged structures can be calculated using the following equation:

$$\mathrm{MSE}_{ij}^{u} = \frac{1}{2}\left(\Phi_{i}^{u}\right)^{T} K_j \Phi_i^u, \quad \mathrm{MSE}_{ij}^{d} = \frac{1}{2}\left(\Phi_{i}^{d}\right)^{T} K_j \Phi_i^d \tag{6.1}$$

The undamaged and damaged cases' frequency response is provided by the mode number and the element number denoted as $i$ and $j$, respectively. The stiffness matrix $K_j$, mode shape $\Phi_i$, and superscripts $u$ representing the undamaged structure and $d$ representing the damaged structure are also involved:

$$\begin{cases} \{X(w)\} = \left\{\left(-w^2[M] + [K]^{-1}\right)\right\}\{F(w)\} \\ \{X_d(w)\} = \left\{\left(-w^2[M]_d + [K]_d^{-1}\right)\right\}\{F(w)\} \end{cases} \tag{6.2}$$

Equation (6.2) will be used instead of the eigenvectors in eq. (6.1) as follows:

$$\mathrm{MMSE}_{ij}^{u} = \frac{1}{2}\left(X_{i}^{u}\right)^{T} K_j X_i^u, \quad \mathrm{MMSE}_{ij}^{d} = \frac{1}{2}\left(X_{i}^{d}\right)^{T} K_j X_i^d \tag{6.3}$$

By dividing the discrepancy between the modified modal strain energy of the damaged structure and the unimpaired structure with the modified modal strain energy of the unimpaired structure, the recalibrated MSE Indicator can be computed as depicted below:

$$\mathrm{MMSEI}_{ij} = \frac{\left|\mathrm{MMSE}_{ij}^{d} - \mathrm{MMSE}_{ij}^{u}\right|}{\mathrm{MMSE}_{ij}^{u}} \tag{6.4}$$

## 6.3 Optimization

In this study, we have utilized three distinct optimization algorithms to quantify the damage, with the objective of comparing their efficacy.

### 6.3.1 Snake optimizer (SO)

Snake optimizer (SO), introduced by Hashim and Hussein [26], is an innovative swarm-based algorithm that leverages the mating behavior of snakes to tackle optimization problems. This algorithm emulates the foraging and reproductive actions of snakes, where both the male and female snakes compete to secure the best partner in conditions of ample food and low temperature. In the SO, solutions to optimization problems are depicted as snakes, and their movements are guided by the snake mating behavior. The algorithm strives to attain a balance between exploration and exploitation by utilizing a dynamically adapted search radius. Additionally, the swarm is equally split into male and female groups in the snake optimizer algorithm. At each iteration, the best potential solution is determined by scrutinizing the male and female groups' individual best solutions.

The Snake Optimizer algorithm utilizes a swarm that is divided equally into male and female groups. In each iteration, the algorithm selects the best individual candidate solution by analyzing the male and female groups to determine their individual best solutions.

During the exploitation phase, the Snake Optimizer algorithm employs two conditions to identify the best solutions. The first condition involves comparing the positions of the male and female individuals with the position of the best individual. The second condition compares the quality of the food with a predetermined threshold. If the food quality is lower than the threshold, the snakes will engage in either fighting or mating behavior. When in fighting mode, the male and female agents calculate their fighting abilities based on their positions and the position of the best individual in the opposite group.

### 6.3.2 Marine predators algorithm (MPA)

Faramarzi et al. [27] developed the MPA, which takes inspiration from the foraging behavior of ocean predators. Specifically, the algorithm incorporates the use of Lévy and Brownian movements, as well as an optimal encounter rate policy with their prey. Each potential solution is modeled as a predator, and the algorithm utilizes these strategies to balance both exploration and exploitation during the search process. By adhering to the natural rules that govern foraging and encounter rate in marine ecosystems, the algorithm employs these principles to direct the movement of each "predator" toward a potential optimal solution.

The MPA optimization process has three phases, each with a specific velocity ratio mimicking a predator's step size to catch its prey:

- Phase 1: initial optimization iterations favor exploration, and the optimal strategy for the predator is to remain still at a high-velocity ratio.

- Phase 2: intermediate optimization phase aims to shift from exploration to exploitation, with the optimal strategy for the predator being Brownian at a unit velocity ratio, while the prey moves in Lévy.
- Phase 3: the final optimization phase emphasizes high exploitation capability, with the optimal strategy for the predator being Lévy at a low-velocity ratio.

The algorithm imitates predator and prey life cycles, with assigned periods for each phase, based on their movement rules. Predators use both Lévy and Brownian movements, with no movement in phase one, Brownian in phase two, and Lévy in phase three. The prey use Brownian in phase one and Lévy in phase two.

The algorithm divides the iterations into thirds for each phase, instead of cycling between them. It is inspired by the ocean predator's foraging behavior to optimize solutions effectively.

## 6.3.3 Moth flame optimization (MFO)

The MFO algorithm, proposed by Mirjalili [28], is inspired by the navigation behavior of moths, specifically the transverse orientation. This behavior allows moths to fly straight by maintaining a fixed angle with respect to the moon. However, artificial lights can cause moths to become disoriented and trapped, leading to dangerous situations. The MFO algorithm models this behavior for optimization. The algorithm generates a group of moths that each represents a potential solution to the problem. Moths move toward the best solution found, represented as a flame, with the attraction force pulling them toward it, the repulsion force pushing them away from other moths, and the randomization force adding stochasticity for exploring the search space.

The MFO algorithm consists of three main components:

- Generating an initial population of moths,
- Updating the moths' positions,
- Updating the number of flames.

Moths and flames are both solutions, but in different ways. Moths search the space, while flames are the best positions found by moths. Flames act as markers dropped by moths during their search, and each moth updates the flame if it finds a better solution while searching around it.

MFO uses three functions to reach the global optimum: transverse orientation for searching, balancing moth motion near the flame for exploitation and exploration, and keeping optimal solutions for each repetition. The algorithm updates the number of flames to improve exploitation, and moves moths to different locations to avoid missing promising solutions.

This algorithm, based on moth navigation, optimizes problems by moving toward the best solution represented as a flame. It uses three forces and involves generating an initial moth population, updating their positions, and the number of flames. MFO balances exploration and exploitation to converge to the global optimum using three functions: transverse orientation, optimal solution retention, and flame number updates.

## 6.4 Numerical analysis

In order to evaluate the efficacy of the suggested method for identifying and measuring the extent of harm, a square plate configuration was employed, which featured two types of damage as illustrated in Figure 6.1. The physical characteristics of this configuration have been enumerated in Table 6.1, while Table 6.2 provides further elucidation on the two specific damage scenarios.

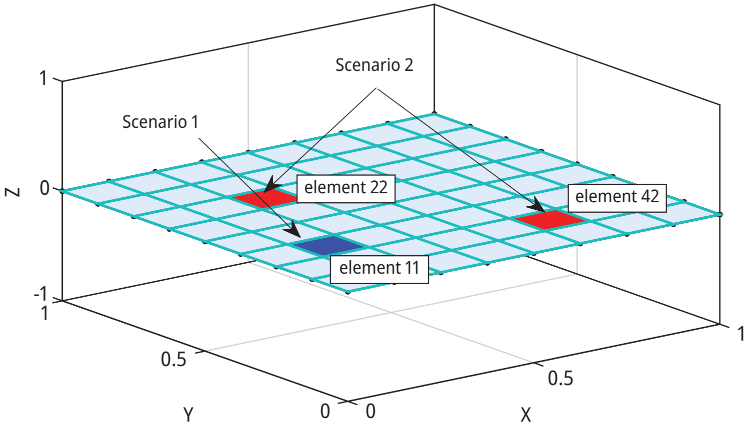

**Figure 6.1:** 8 × 8 mesh for the plate structure.

**Table 6.1:** Material properties of the plate structure.

| Material property | value |
|---|---|
| Modulus of elasticity | 10,920 |
| Thickness-to-side ratio | 0.1 |
| Poisson’s coefficient | 0.3 |

Table 6.3 displays the non-dimensional natural frequencies of both damaged and undamaged cases for the CCCF plate, which are defined in eq. (6.5):

$$\overline{w} = wa\sqrt{\frac{\delta}{G}} \tag{6.5}$$

**Table 6.2:** Damage scenarios for the plate structure.

| Case | Element no. | Reduction in stiffness |
|---|---|---|
| Case 1 | 11 | 25% |
| Case 2 | 22 | 20% |
|  | 42 | 30% |

**Table 6.3:** Healthy and damaged natural frequencies of the plate structure.

| Mode | Healthy |  | Actual FEM | Damaged |  |
|---|---|---|---|---|---|
|  | [29] | [30] |  | Case 1 | Case 2 |
| 1st | 1.0923 | 1.089 | 1.1236 | 1.1233 | 1.1163 |
| 2nd | 1.7566 | 1.758 | 1.7915 | 1.7897 | 1.7649 |
| 3rd | 2.7337 | 2.673 | 2.9476 | 2.9468 | 2.9125 |
| 4th | 3.2591 | 3.216 | 3.4252 | 3.4182 | 3.3371 |
| 5th | 3.3541 | 3.318 | 3.5302 | 3.5244 | 3.4773 |

### 6.4.1 Damage localization based on the modified modal strain energy indicator

The present section describes the implementation of the modified MSE indicator for detecting and locating damaged elements in plate structures under both single and multiple damage scenarios. The MMSE indicator values of damaged elements are higher than those of healthy ones, allowing for a clear distinction between the two states. As illustrated in Figure 6.2, the MMSE-based approach demonstrates a high level of accuracy in identifying damaged elements. The identification of damage in a plate structure is a complex process, and one crucial step in this process is the use of optimization algorithms. By neglecting the healthy elements in the structure, these algorithms can assess the extent and severity of the damage more accurately, thereby reducing the computational time required. The results of this approach are promising, suggesting that it has the potential to become a reliable and effective tool for localizing damage in plate structures.

### 6.4.2 Optimization-based damage quantification

This section evaluates the damage rate after removing healthy elements, using three optimization algorithms: SO, MPA, and MFO. The algorithms use a modified MSE indicator that considers the frequency response of the plate structure.

Figure 6.3 provides an assessment of the damage extent in the first scenario where three optimization algorithms were employed for quantification. The results reveal that all three algorithms effectively measure the damage extent. Nevertheless,

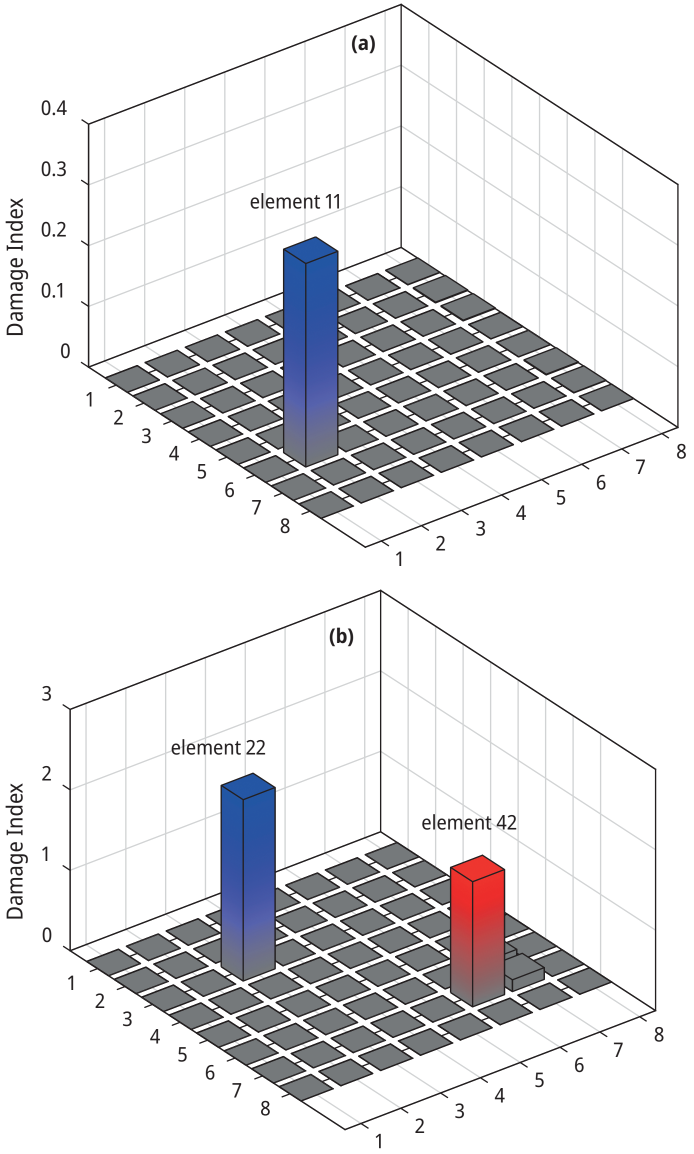

**Figure 6.2:** Damage localization in the plate structure: (a) scenario 1 and (b) scenario 2.

the MFO exhibits superior performance compared to the other two algorithms in terms of convergence speed. This is evidenced by the shorter computation time, displayed in Table 6.4, and a lower value of the objective function.

The findings presented in Figure 6.4 clearly demonstrate that the approach proposed in this study is highly effective in accurately quantifying the degree of damage in a plate structure containing two damaged elements, when all three optimization

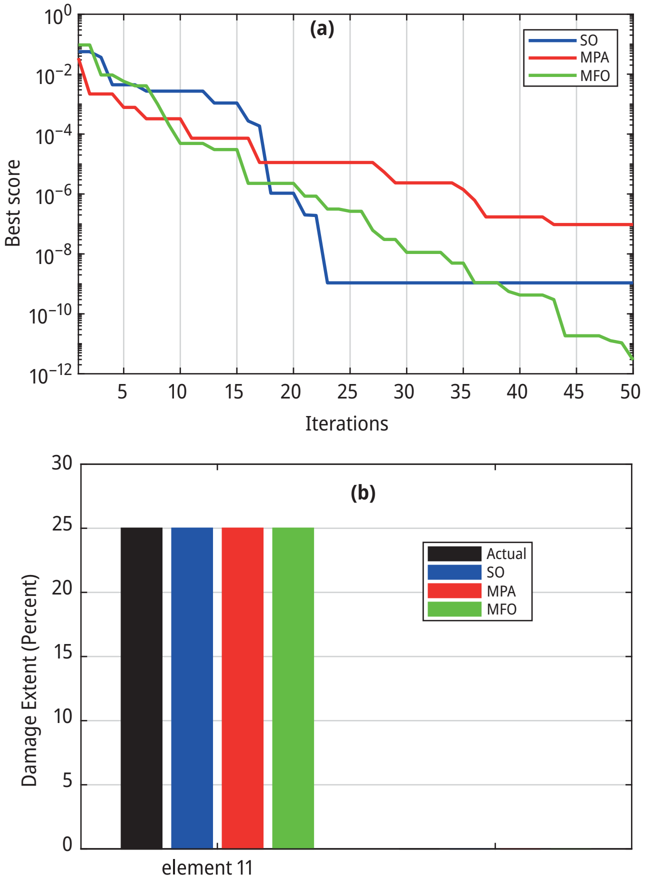

**Figure 6.3:** Case 1 of damage: (a) objective function convergence and (b) damage quantification.

algorithms are utilized. However, upon closer examination of the results, it becomes apparent that the MFO outperforms the other algorithms in terms of both convergence and accuracy when it comes to determining the extent of the damage.

The proficient execution of the proposed approach utilizing multiple optimization algorithms and diverse damage scenarios is a clear testament to its effectiveness in accurately detecting and quantifying damage in plate structures. Table 6.4 further establishes the superiority of MFO over other algorithms in terms of CPU time in both scenarios.

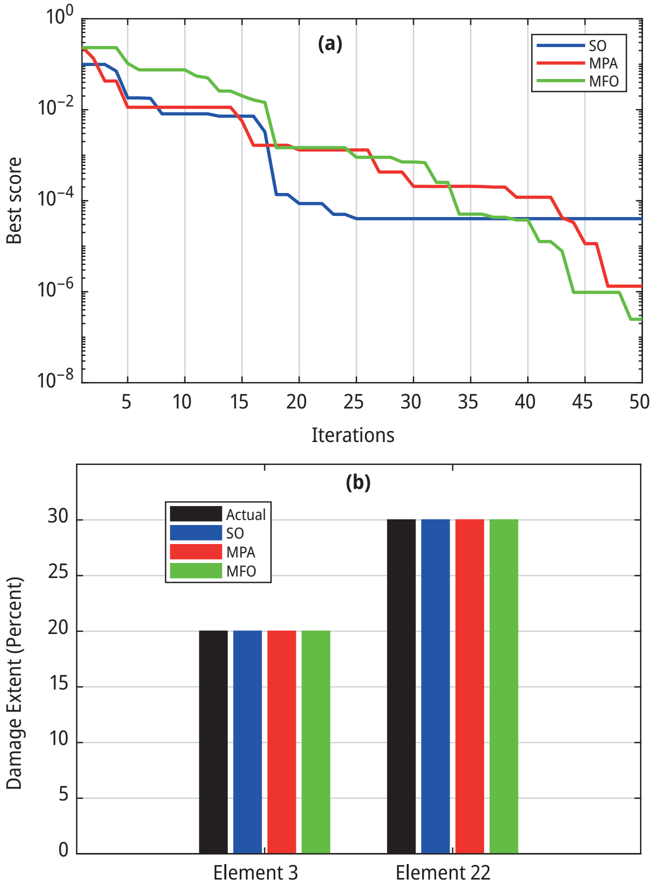

**Figure 6.4:** Case 2 of damage: (a) objective function convergence and (b) damage quantification.

**Table 6.4:** CPU time for all cases.

| – | **Case 1** | **Case 2** |
|---|---|---|
| SO | 2487.00107 | 2484.07459 |
| MPA | 4870.12512 | 4870.62903 |
| MFO | 2436.29274 | 2405.20888 |

## 6.5 Conclusion

This paper proposed a novel approach for detecting and quantifying structural damage in square plate structures, based on the Modified Modal Strain Energy (MSE) indicator, combined with robust optimization algorithms. The proposed approach accurately identified, located, and quantified single and multiple damages in the examined cases. The application of the frequency response in the MSE method, followed by formulating an optimization problem to determine the extent of the damage using an objective function based on the modified indicator, was effective. The three optimization algorithms tested, SO, MPA, and Moth Flame Optimizer (MFO), demonstrated that the MFO algorithm provided superior outcomes with respect to convergence, CPU time, and the accuracy of damage extent. Overall, the proposed approach has potential for use in mechanical and civil engineering fields to accurately assess and monitor structural damage.

# References

[1] B. Benaissa, S. Khatir, M. S. Jouini, and M. K. Riahi. Optimal axial-probe design for foucault-current tomography: A global optimization approach based on linear sampling method. *Energies*, 16:2448, 2023.

[2] H. Haddar, Z. Jiang, and M. K. Riahi. A robust inversion method for quantitative 3D shape reconstruction from coaxial eddy current measurements. *Journal of Scientific Computing*, 70:29–59, 2017.

[3] H. Haddar and M. K. Riahi. Near-field linear sampling method for axisymmetric eddy current tomography. *Inverse Problems*, 37:105002, 2021.

[4] M. K. Riahi. A fast eddy-current non destructive testing finite element solver in steam generator. *Journal of Coupled Systems and Multiscale Dynamics*, 4:60–68, 2016.

[5] M. Al Ali, M. Shimoda, B. Benaissa, and M. Kobayashi, Concurrent multiscale hybrid topology optimization for light weight porous soft robotic hand with high cellular stiffness. In *Proceedings of the International Conference of Steel and Composite for Engineering Structures: ICSCES 2022*, 265–278. 2023.

[6] M. Al Ali and M. Shimoda. Investigation of concurrent multiscale topology optimization for designing lightweight macrostructure with high thermal conductivity. *International Journal of Thermal Sciences*, 179:107653, 2022.

[7] M. A. Ali, and M. Shimoda. Toward multiphysics multiscale concurrent topology optimization for lightweight structures with high heat conductivity and high stiffness using MATLAB. *Structural and Multidisciplinary Optimization*, 65:1–26, 2022.

[8] M. Fujioka, M. Shimoda, and M. Al Ali. Concurrent shape optimization of a multiscale structure for controlling macrostructural stiffness. *Structural and Multidisciplinary Optimization*, 65:211, 2022.

[9] M. Shimoda, M. Umemura, M. Al Ali, and R. Tsukihara. Shape and topology optimization method for fiber placement design of CFRP plate and shell structures. *Composite Structures*, 309:116729, 2023.

[10] A. Rytter. “Vibrational based inspection of civil engineering structures,” 1993.

[11] -J.-J. Sinou. A review of damage detection and health monitoring of mechanical systems from changes in the measurement of linear and non-linear vibrations. *Mechanical Vibrations: Measurement, Effects and Control*, 643–702, 2009.

[12] S. Tiachacht, A. Bouazzouni, S. Khatir, M. Abdel Wahab, A. Behtani, and R. Capozucca. Damage assessment in structures using combination of a modified cornwell indicator and genetic algorithm. *Engineering Structures*, 177:421–430, 2018/12/15/ 2018.

[13] M. Slimani, T. Khatir, S. Tiachacht, D. Boutchicha, and B. Benaissa. Experimental sensitivity analysis of sensor placement based on virtual springs and damage quantification in CFRP composite. *Journal of Materials and Engineering Structures «JMES»*, 9:207–220, 2022.

[14] M. Slimani, S. Tiachacht, A. Behtani, T. Khatir, S. Khatir, and B. Benaissa et al. Improved ANN for damage identification in laminated composite plate. In *Proceedings of the International Conference of Steel and Composite for Engineering Structures: ICSCES 2022*, 186–198. 2023.

[15] N. Amoura, B. Benaissa, M. Al Ali, and S. Khatir. Deep neural network and YUKI algorithm for inner damage characterization based on elastic boundary displacement. In *Proceedings of the International Conference of Steel and Composite for Engineering Structures: ICSCES 2022*, 220–233. 2023.

[16] M. I. Shirazi, S. Khatir, B. Benaissa, S. Mirjalili, and M. A. Wahab. Damage assessment in laminated composite plates using modal strain energy and YUKI-ANN algorithm. *Composite Structures*, 116272, 2022.

[17] M. A. de Oliveira, J. Vieira Filho, V. Lopes, and D. J. Inman. A new approach for structural damage detection exploring the singular spectrum analysis. *Journal of Intelligent Material Systems and Structures*, 28:1160–1174, 2017.

[18] S. Khatir, M. Abdel Wahab, S. Tiachacht, C. Le Thanh, R. Capozucca, and E. Magagnini et al. Damage identification in steel plate using FRF and inverse analysis. *Frattura Ed Integrita Strutturale-Fracture and Structural Integrity*, 58:416–433, 2021.

[19] S. Khatir, S. Tiachacht, B. Benaissa, C. Le Thanh, R. Capozucca, and M. Abdel Wahab. Damage identification in frame structure based on inverse analysis. In *Proceedings of the 2nd International Conference on Structural Damage Modelling and Assessment*, 197–211. 2022.

[20] A. Khatir, R. Capozucca, S. Khatir, E. Magagnini, B. Benaissa, and C. Le Thanh et al. A new hybrid PSO-YUKI for double crack identification in CFRP cantilever beam. *Composite Structures*, 116803, 2023.

[21] W. A. Syafruddin, M. Köppen, and B. Benaissa. Does the Jaya Algorithm really need no parameters? *Indo-Japan Chamber of Commerce & Industry*, 264–268, 2018.

[22] A. Khatir, R. Capozucca, S. Khatir, E. Magagnini, B. Benaissa, and C. Le Thanh et al. A new hybrid PSO-YUKI for double cracks identification in CFRP cantilever beam. *Composite Structures*, 311:116803, 2023.

[23] A. Behtani, S. Tiachacht, T. Khatir, S. Khatir, M. A. Wahab, and B. Benaissa. Residual force method for damage identification in a laminated composite plate with different boundary conditions. *Frattura Ed Integrità Strutturale*, 16:35–48, 2022.

[24] A. Behtani, S. Tiachacht, S. Khatir, M. Slimani, L. Mansouri, and A. Bouazzouni et al. The sensitivity of modal strain energy for damage localization in composite stratified beam structures. In *Proceedings of the 13th International Conference on Damage Assessment of Structures: DAMAS 2019*, *9–10 July 2019*, *Porto, Portugal*, 863–874. 2020.

[25] A. Kahouadji, S. Tiachacht, M. Slimani, A. Behtani, S. Khatir, and B. Benaissa. Vibration-based damage assessment in truss structures using local frequency change ratio indicator combined with metaheuristic optimization algorithms. In *Proceedings of the International Conference of Steel and Composite for Engineering Structures*, 171–185. Cham, 2023.

[26] F. A. Hashim, and A. G. Hussien. Snake optimizer: A novel meta-heuristic optimization algorithm. *Knowledge-Based Systems*, 242:108320, 2022/04/22/ 2022.

[27] A. Faramarzi, M. Heidarinejad, S. Mirjalili, and A. H. Gandomi. Marine predators algorithm: A nature-inspired metaheuristic. *Expert Systems with Applications*, 152:113377, 2020/08/15/ 2020.

[28] S. Mirjalili. Moth-flame optimization algorithm: A novel nature-inspired heuristic paradigm. *Knowledge-Based Systems*, 89:228–249, 2015/11/01/ 2015.

[29] A. J. Ferreira. *MATLAB Codes for Finite Element Analysis*. Springer, 2009.

[30] E. Hinton. *Numerical Methods and Software for Dynamic Analysis of Plates and Shells*. Pineridge Press, 1988.

Shahin Ghazvineh, Gholamreza Nouri, Vahidreza Gharehbaghi,
Seyed Hossein Hosseini Lavasani, Ehsan Noroozinejad Farsangi,
Mohammad Noori

# 7 Vibration-based damage detection using a novel hybrid CNN-SVM approach

**Abstract:** In classic machine learning-based damage detection algorithms, extracting damage-sensitive features from time series is a challenging issue. Also, this paradigm can delay processing procedures and requires preprocessing. Many efforts have been made to overcome this limitation by expanding deep learning (DL) in structural health monitoring (SHM). However, because most of these systems require considerable measurements during the training step, they are unsuitable for real-time applications. To solve the challenges above, we offer a robust approach using two-dimensional convolutional neural networks (CNNs) and support vector machines (SVMs), merging feature extraction and a rapid classifier at the same time. The method employs a shallow CNN network that receives raw acceleration signals. Both noisy and noise-free datasets are used to verify the hybrid CNN-SVM approach. The results showed an increase in robustness, speed efficiency, and accuracy over traditional machine learning approaches. The results proved efficient, making the algorithm reliable even under high noise conditions.

## 7.1 Introduction

Various structural defects occur during a structure's service life, putting the system's integrity and performance at risk. Environmental circumstances, natural risks, or human influences could all cause damage. Such a degradation process generates ex-

---

**Acknowledgment:** We would like to thank Dr. Osama Abdeljaber from Structural Dynamics Team for kindly providing the double damage cases used in this study.

---

**Statements and Declarations:** The authors did not receive support from any organization for the submitted work.

---

**Shahin Ghazvineh**, **Gholamreza Nouri**, **Seyed Hossein Hosseini Lavasani,** Faculty of Civil Engineering, Kharazmi University, Tehran, Iran
**Vahidreza Gharehbaghi,** Department of Civil, Environmental and Architectural Engineering, University of Kansas, USA
**Ehsan Noroozinejad Farsangi,** Department of Civil Engineering, The University of British Columbia (UBC), Vancouver, Canada
**Mohammad Noori,** Department of Mechanical Engineering, California Polytechnic State University, San Luis Obispo, USA; School of Civil Engineering, University of Leeds, Leeds, UK

https://doi.org/10.1515/9783110791426-007

cessive deflections in the components, rebar corrosion, and the onset of cracks, all of which might interrupt the service functionality in the long or short term. In contrast to visual inspection and manual damage detection, which have limitations in implementation, structural health monitoring (SHM) aims to provide an automated, precise, and accurate solution for condition assessment that takes advantage of advanced sensing and computation innovations.

Structural responses, such as deflections, strains, and accelerations, include scalable information on the state of the monitored system, allowing any changes in the system status to be tracked back to the associated responses [1]. Anomalies in the time, frequency, or time-frequency domain are investigated using modal characteristics, frequency response functions (FRFs), and structural matrices. To determine system attributes, model-based and data-driven strategies are used. In contrast to the first methodology, data-driven procedures do not necessitate prior knowledge of the boundary conditions, damage location, and material attributes. As a result, they are more practical in working with large structures, which require considerable effort to find the optimum value of parameters [2].

Sensors collect various responses, including information about the monitored structure in data-driven processes. Displacement, velocity, strain, and acceleration all contain system information. Signal processing methods are the most often used to extract information from recorded signals. Time series and signal transformations like wavelets, Stockwell, and Hilbert–Huang transforms have been used to discover anomalies in responses. Although these methods are efficient for damage detection, feature extraction and selection are made manually, which are time-consuming and error-prone.

On the other hand, machine learning techniques are used for pattern recognition, feature extraction, and data classification. They can also be combined with signal processing techniques to produce an automated feature extractor and feature selector. For example, in these models, time series were mixed with ReliefF and machine learning classifiers to differentiate damage scenarios [3]. To extract features, discrete wavelets were combined with neighborhood component analysis (NCA), while support vector machines (SVMs) and k-nearest neighbors (KNNs) were used to classify damages inside structures [4].

Because the number of neurons is limited, increasing the input data causes the performance of conventional machine learning algorithms to plateau. On the other hand, deep learning (DL) algorithms deal with a larger amount of data, resulting in higher prediction and discrimination accuracy. DL, a subclass of machine learning, has been used in a wide range of applications, including computer vision [5], speech recognition [6], and signal processing [7]. Convolutional Neural Networks (CNNs) are one of the most commonly used deep neural networks; they were initially created to analyze image data; nevertheless, it has recently been shown that CNN has excellent potential for subsequent data analysis, such as natural language processing. CNNs are commonly employed in SHM applications due to recent advances in computation facilities and training using GPUs. As an example, Modarres et al. [8] established a CNN for detecting and recognizing damage and compared the results to four other approaches for noisy and clean images. Shihavuddin et al. [9] developed a CNN architecture for detecting surface flaws on wind turbine blades using images. Avci et al. [10] established a decentralized one-dimensional CNN-based technique to assess the level of structural damage using only two states of the structure as input for the training stage (damaged and undamaged data). Han et al. [11] took advantage of transfer learning by introducing AlexNet and ResNet18 in both 2D and 1D forms for bolt loosening identification purposes.

Although CNNs are used in SHM, the computation cost and robustness in adverse signal conditions are still untouched. Hence, the authors attempt to establish a fast model for damage detection by combining CNN and SVM as a single body in this paper. To evaluate the feasibility of the decentralized technique, the authors used acceleration data from the three nearest accelerometers to each joint to train a two-dimensional hybrid CNN-SVM for each joint in the Qatar University Grandstand Simulator (QUGS) dataset [12, 13]. Notably, the authors have used a similar methodology previously, using a single CNN with limited damage scenarios [14], while this study employs all damage scenarios, including cases in which two joints were damaged simultaneously, under a hybrid CNN-SVM strategy.

The paper outline follows: first, the research technique is thoroughly detailed. The training and testing procedures are then described. Afterward, a brief explanation of the benchmark and the data set is given in the following section. Then, the performance in different signal conditions and the robustness of the CNN-SVM against changing the hyperparameters are evaluated. Last, conclusions and representative works are studied in light of the findings.

## 7.2 Methodology

The research methodology is illustrated in sequential steps in this section. The architecture of two-dimensional CNN as a feature extractor is first demonstrated. The extracted features are then fed to an SVM to classify various damage cases of the benchmark.

### 7.2.1 Network architecture

The authors advocate using a compact hybrid CNN-SVM model rather than a deep architecture to improve computational performance. This technique assigns a different CNN-SVM to each structure component to assess its condition. The proposed methodology is depicted in Figure 7.1.

Each CNN-SVM has an architecture consisting of two convolutional blocks followed by a dropout function before the SVM. Each convolutional block consists of a batch normalization, activation, and pooling layer. Batch normalization is done to the input data prior to the first convolution block to reduce nonuniform distribution. The typical architecture of the proposed network is seen in Figure 7.2. The following sections briefly describe the role of each layer.

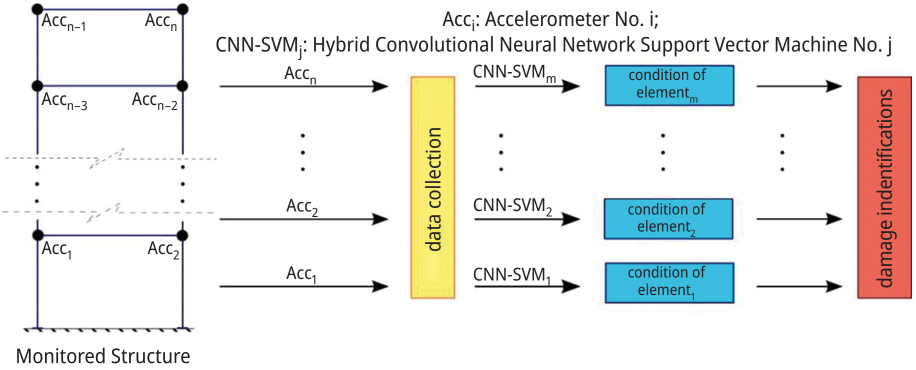

**Figure 7.1:** Evaluation system of the proposed methodology.

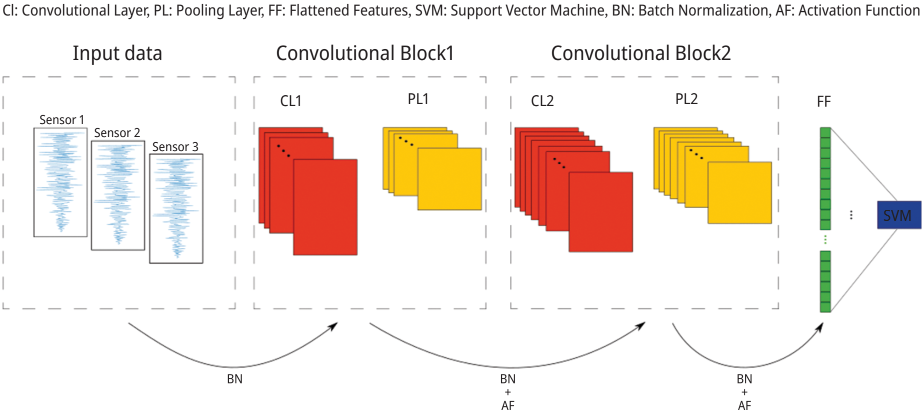

**Figure 7.2:** Architecture of CNN-SVM.

#### 7.2.1.1 Convolutional layer

As the name implies, the convolutional layer is the essence of a CNN, distinguishing it from earlier machine learning systems. In this layer, convolution is a mathematical process used to extract features from the input. In this case, convolution is the sum of a dot product between a slider kernel and the layer's input with a bias. A convolution layer comprises several kernels with learnable weights that convolve the input one by one to generate a new matrix called the feature map, which is then given to the next layer. Kernels should have the same number of channels as the input, regardless of whether their width and length are the same or lesser than the input [15]. Convolution layers with zero paddings keep the feature map from shrinking in size. Figure 7.3 depicts the performance of a two-dimensional convolutional layer with zero padding for improved comprehension.

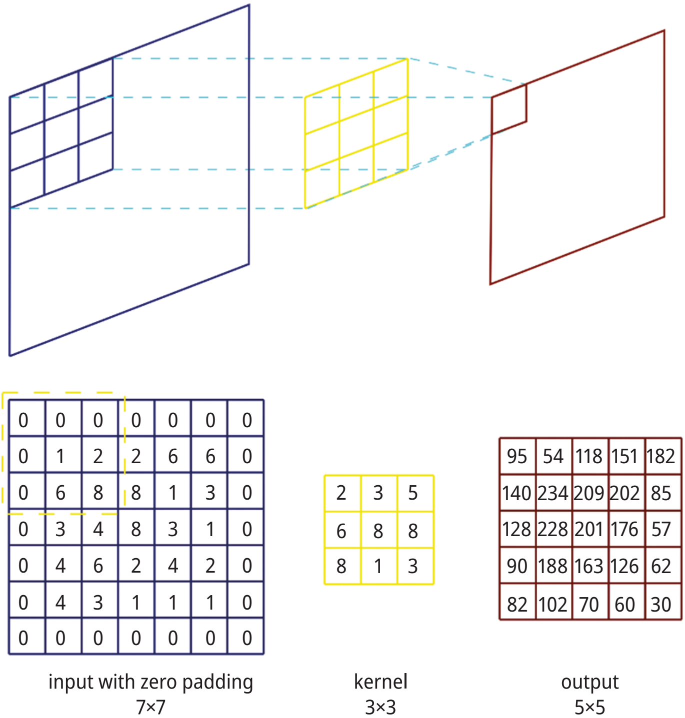

|  |  |  |  |  |  |  |
|---|---|---|---|---|---|---|
| 0 | 0 | 0 | 0 | 0 | 0 | 0 |
| 0 | 1 | 2 | 2 | 6 | 6 | 0 |
| 0 | 6 | 8 | 8 | 1 | 3 | 0 |
| 0 | 3 | 4 | 8 | 3 | 1 | 0 |
| 0 | 4 | 6 | 2 | 4 | 2 | 0 |
| 0 | 4 | 3 | 1 | 1 | 1 | 0 |
| 0 | 0 | 0 | 0 | 0 | 0 | 0 |

input with zero padding
7×7

|  |  |  |
|---|---|---|
| 2 | 3 | 5 |
| 6 | 8 | 8 |
| 8 | 1 | 3 |

kernel
3×3

|  |  |  |  |  |
|---|---|---|---|---|
| 95 | 54 | 118 | 151 | 182 |
| 140 | 234 | 209 | 202 | 85 |
| 128 | 228 | 201 | 176 | 57 |
| 90 | 188 | 163 | 126 | 62 |
| 82 | 102 | 70 | 60 | 30 |

output
5×5

**Figure 7.3:** Example of convolutional operation with zero padding.

### 7.2.1.2 Batch normalization

Since the training procedure is done batch by batch, a nonuniform distribution of each batch can significantly impede convergence. Sergey Ioffe and Christian Szegedy [16] presented a batch normalization method to overcome this problem known as internal covariate shift. Batch normalization (BN) is a powerful technique for parametrizing virtually any type of neural network. It calculates the mean and variance of each input batch and then scales and shifts them to 0 and 1, respectively, using eqs. (7.1)–(7.4). Since BN is performed in a mini-batch, it is computationally efficient, and it also enables the use of higher learning rates:

$$\mu_B = \frac{1}{m}\sum_{i=1}^{m} x_i \tag{7.1}$$

$$\sigma^2{}_B = \frac{1}{m}\sum_{i=1}^{m}(x_i - \mu_B)^2 \tag{7.2}$$

$$\hat{x}_i = \frac{x_i - \mu_B}{\sqrt{(\sigma^2{}_B + \epsilon)}} \tag{7.3}$$

$$y_i = \gamma\hat{x}_i + \beta \tag{7.4}$$

where $\epsilon$ is a small number to prevent division by zero, $x$ is input data, $\hat{x}$ is the standardized form of the input data, and $y$ is the linear transform of $\hat{x}$ with the scaling factor of $\gamma$ and $\beta$ as bias.

### 7.2.1.3 Activation function

One of the most critical components of a neural network is its activation functions. They give the network nonlinearity, making the input more learnable and capable of executing more complex tasks. The rectified linear unit (ReLU) [17, 18] has become the most popular among many activation functions in recent years. It adheres to a straightforward formula, as given in eq. (7.5):

$$y = \max(0, x) \tag{7.5}$$

The first advantage of ReLU over previous algorithms is its capacity to tackle the vanishing gradient problem, which was prevalent in sigmoid [19], and the second advantage over previous algorithms is that it is computationally cheap, making the network faster in training. ReLU is inserted immediately after the BN layer in the proposed design.

### 7.2.1.4 Max pooling

Following the activation function, the final layer of each convolutional block in the CNNs is a pooling layer. It attempts to reduce the size of the feature map by keeping vital information and reducing the amount of data that must be pushed forward to the next layer. In addition to the previously mentioned benefit, pooling makes learning more independent of minor translations of input data.

The two most common types of pooling are max pooling and average pooling. Average pooling moves a window through the feature map and computes the mean of the values in the window, whereas max pooling takes the largest value and disregards the rest. As it is quicker to calculate, we used max pooling in this process. Figure 7.4 shows an example of how max pooling works.

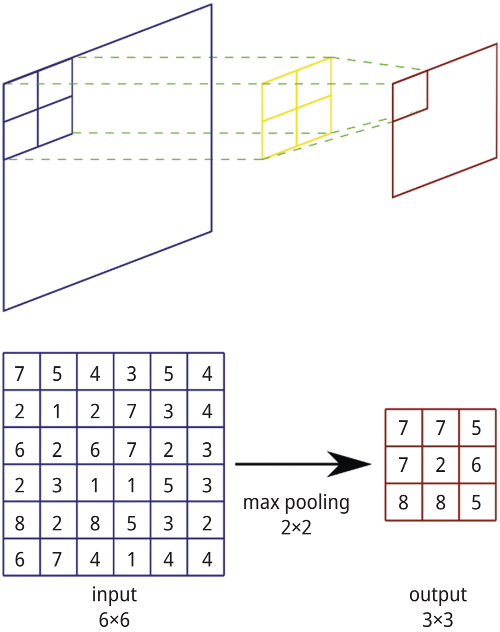

|  |  |  |  |  |  |
|---|---|---|---|---|---|
| 7 | 5 | 4 | 3 | 5 | 4 |
| 2 | 1 | 2 | 7 | 3 | 4 |
| 6 | 2 | 6 | 7 | 2 | 3 |
| 2 | 3 | 1 | 1 | 5 | 3 |
| 8 | 2 | 8 | 5 | 3 | 2 |
| 6 | 7 | 4 | 1 | 4 | 4 |

|  |  |  |
|---|---|---|
| 7 | 7 | 5 |
| 7 | 2 | 6 |
| 8 | 8 | 5 |

**Figure 7.4:** Example of max pooling operation.

### 7.2.1.5 Dropout

For the first time, Srivastava et al. [20] suggested this method as a simple solution to the overfitting problem. Dropout, in a nutshell, causes some units in a neural network to be temporarily disregarded during training by the probability of *p*, requiring the network to learn features rather than memorizing noisy training input data. It also shortens training time by lightening the network. Dropout is used before the SVM to prevent overfitting in the network.

### 7.2.1.6 Classifier

After extracting features by convolutional blocks, they must be classified. In a typical CNN, the classifier is a fully connected (FC) layer that classifies a vector of features. An FC layer in binary classification seeks to build a boundary between the features in order to give the best possible classification results on training data. However, this strategy may result in an overfitting problem. SVMs, on the other hand, aim to maximize the margin between the decision border and the nearest features belonging to each class. This notion improves the network's performance when it comes to managing new data. SVM is replaced as the classifier immediately after the flattening layer in the suggested network architecture.

#### 7.2.1.7 Loss function and optimizer

Hinge loss is utilized as the loss function to calculate the network's prediction error when training all network sections as a single body. The hinge loss, primarily used in SVMs to maximize margin, is defined in eq. (7.6):

$$L(y_s) = \max(0,\ 1 - y_t.y_s) \tag{7.6}$$

where $y_s$ shows the classifier's raw score and $y_t$ stands for the actual class label.

In order to reduce the value of the stated equation during the training phase, the Adam optimizer method [21] with an L2 normalization is used instead of the standard stochastic gradient descent.

### 7.2.2 Training and testing

As previously stated, this method assesses the structure's condition by monitoring each element separately using a different CNN-SVM; in contrast to most prior centralized methods, decentralization aids in detecting several class damages that co-occur in the structure. Raw acceleration signals in both damaged and healthy states are used to train the CNNs. Signal data from three accelerometers are used as input in the suggested approach. Using the signals of two auxiliary accelerometers could reduce the amount of data required for training. Considering a structure with $M$ elements and $N$ accelerometers, $M$ CNN-SVMs must be trained to monitor all elements. Every accelerometer in the network collects a vector of the structure's acceleration responses. Suppose $Z$ features were required to train each CNN using only a single accelerometer signal for each element, NZ features would need to be collected from the accelerometers to train all the CNNs. In this case, adding data from two more existing accelerometers reduces it to almost NZ/3 features. The authors proposed employing data from the element's nearby accelerometers as an auxiliary, with more specific information demonstrated in the following section, combining data from three accelerometers in conjunction with the suggested CNN-SVM improved accuracy.

For element $i$, undamaged and damaged data are as follows:

$$U_i = [\,U_{i1} \quad U_{i2} \quad U_{i3}\,] \tag{7.7}$$

$$D_i = [\,D_{i1} \quad D_{i2} \quad D_{i3}\,] \tag{7.8}$$

where $U_i$ and $D_i$ denote measurement signals for $i$th element in undamaged and damaged states, respectively. The terms $U_{i1}$, $U_{i2}$, and $U_{i3}$ represent the acceleration responses for the healthy condition of the $i$th element recorded by the first, second, and third nearest accelerometers, respectively. The same pattern is established for the damaged condition.

In this approach, the undamaged data set for the $i$th element includes signal responses in the $i$th element's healthy state, while one of the others was likewise damaged. This approach mitigates the effects of other damaged elements on the monitored element's classification performance.

As CNN can only work with fixed input sizes, the next step is to divide the responses into many fixed-length frames with a length of $s_f$ after collecting responses in both damaged and undamaged states of the $i$th element. In this process, damaged frames are labeled 1, and undamaged frames are labeled 0:

$$U_i = \begin{bmatrix} U_{i1,1} & U_{i2,1} & U_{i3,1} \\ U_{i1,2} & U_{i2,2} & U_{i3,2} \\ & \vdots & \\ U_{i1,N_u} & U_{i2,N_u} & U_{i3,N_u} \end{bmatrix} \tag{7.9}$$

$$D_i = \begin{bmatrix} D_{i1,1} & D_{i2,1} & D_{i3,1} \\ D_{i1,2} & D_{i2,2} & D_{i3,2} \\ & \vdots & \\ D_{i1,N_d} & D_{i2,N_d} & D_{i3,N_d} \end{bmatrix} \tag{7.10}$$

where $N_d$ and $N_u$ stand for the number of damaged and undamaged frames, respectively. In eqs. (7.11) and (7.12), the $j$th frame of signals in the undamaged and damaged condition of element $i$ is shown. Each frame has a dimension of $s_f \times 3$:

$$UF_{i,j} = \begin{bmatrix} U_{i1,j} & U_{i2,j} & U_{i3,j} \end{bmatrix} \tag{7.11}$$

$$\mathrm{D}F_{i,j} = \begin{bmatrix} D_{i1,j} & D_{i2,j} & D_{i3,j} \end{bmatrix} \tag{7.12}$$

Assuming that each accelerometer's signal consists of $s_u$ and $s_d$ samples for the undamaged and damaged states of a given element, the total number of frames in the undamaged and damaged cases is determined as follows:

$$N_u = \frac{s_u}{s_f} \tag{7.13}$$

$$N_d = \frac{s_d}{s_f} \tag{7.14}$$

Given that damage in other elements is considered the healthy condition for a single element, the values of $N_u$ and $N_d$ are noticeably different, resulting in an unbalanced data set for training. To overcome this issue, during the framing step, an equal number of rows from each scenario in the undamaged condition was chosen, separated into equal length frames, and shuffled; the first $N_d$ frames are then used as undamaged frames for training.

After supplying the necessary data for each CNN-SVM, they should be trained individually for several epochs using the backpropagation algorithm. Based on validation data, the best performance of each of them will be saved during the training approach. This approach keeps the network from overfitting the training data.

The final step in this method is to put each CNN-SVM through its paces on new data that the networks have never seen before. The following are the steps in the testing procedure:

1. Divide input signals into frames of fixed-length $s_f$.
2. For each element, classify undamaged frames as 0 and damaged frames as 1 by the related network.
3. Calculate the percentage of the damage possibility ($\mathrm{DP}_i$) for the $i$th element by averaging the outputs as follows:

$$\mathrm{DP}_i = \frac{\sum_{j=1}^{n_i} L_{i,j}}{n_i} \times 100 \tag{7.15}$$

where $L_{i,j}$ is the label output of the $j$th frame processed by $\mathrm{CNN}_i$ and $n_i$ is the total number of the input frames classified by $\mathrm{CNN}-\mathrm{SVM}_\mathrm{i}$. $\mathrm{DP}_i$ is expected to be close to 0 for undamaged elements and 100 for damaged elements.

Section 4 provides details about the hyperparameters of the typical CNN-SVM in this paper.

## 7.3 Case study

This paper tests the proposed technique on the Qatar University Grandstand Simulator (QUGS), a new large-scale SHM benchmark problem. This benchmark is considered challenging as detecting joint damages demands computationally expensive models, which may lead to a slower approach [22]. For validation, both noise-free and noisy signals are employed. The algorithm's resistance is further tested by varying batch sizes, signal durations, and sample rates.

The structure of QUGS is depicted in Figure 7.5. A laboratory steel structure with 8 girders and 25 filler beams supported on four columns serves as the benchmark. Thirty accelerometers are installed in this structure's joints. Loosening the bolts at the beam-to-girder joints under white noise shaker excitation at a sampling frequency of 1,024 Hz is used to mimic various damage situations. This method was repeated twice for each case, and the results were presented as two data sets. The data set includes 36 different scenarios, including 30 single damage cases with damage at each joint, five double damage cases, and a completely undamaged case. Each signal comprises 262,144 samples collected over 256 s. Reference [23] provides more information on the benchmark structure. Structural Dynamics Team [24] published the data in 2018 as an SHM benchmark.

The following section discusses applying the proposed method to the mentioned benchmark in various signal conditions.

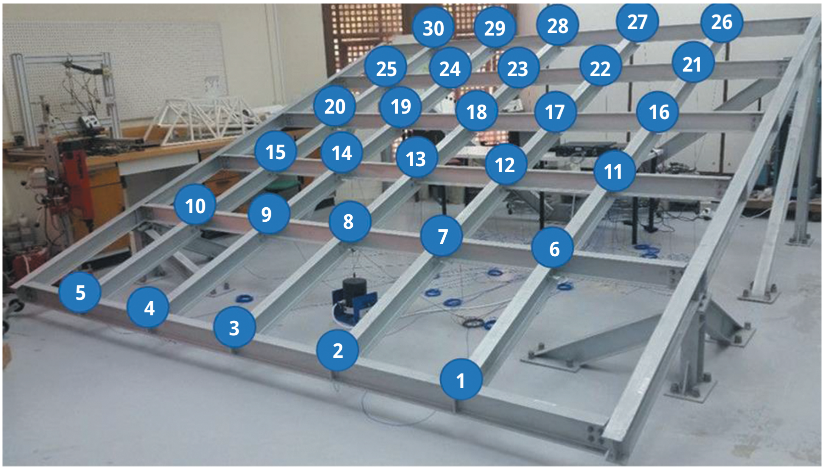

**Figure 7.5:** Qatar University Grandstand simulator structural steel frame [25].

## 7.4 Results and discussions

This section discusses the results of training and evaluating 240 networks. The method's efficiency is examined using various signal conditions. The effect of changing hyperparameters is investigated on noise-free data, as well as evaluating the rapidness of the network.

### 7.4.1 Validation results on noise-free data

The network's hyperparameters are determined by trial and error. Table 7.1 shows the typical CNN-SVM setup used in the method. In this network, the batch size is 8, the signal length is 256, and the learning rate begins at 0.01 and steadily lowers after a series of epoch points. To speed things up, the training uses the PyTorch framework in the Python 3.8 language environment, with an Intel Core i7-4720HQ CPU and an NVIDIA GTX 950 m graphic card.

About 75% of data set A is used to train 30 networks using the technique described in Section 2.2, while 12.5% of data set B is used to validate them. A test data set including 245 frames from each scenario is also used to evaluate the technique on each one individually.

Following training, the method's performance is validated using accuracy as well as four other evaluation metrics: Precision, Recall, F1-score, and Area Under the Receiver Operating Characteristic Curve (ROC AUC) score. The following formulas are used to compute precision, recall, and F1-score:

**Table 7.1:** Network architecture.

| Inp | 1 × 1 × 256 × 3 | Kernel size/number | Padding | Activation | Rate |
|---|---|---|---|---|---|
| BN | 1 × 1 × 256 × 3 | – | – | – | – |
| C1 | 1 × 8 × 256 × 3 | – | – | – | – |
| BN | 1 × 8 × 256 × 3 | (9 × 3)/8 | Same | ReLU | – |
| P1 | 1 × 8 × 128 × 3 | – | – | – | – |
| C2 | 1 × 16 × 128 × 3 | (2 × 1)/8 | Valid | – | – |
| BN | 1 × 16 × 128 × 3 | (3 × 3)/16 | Same | ReLU | – |
| P2 | 1 × 16 × 32 × 3 | – | – | – | – |
| Dr | – | (4 × 1)/16 | Valid | – | – |
| Fl | 1,536 | – | – | – | 0.5 |
| SVM | 1 | – | – | – | – |

BN: batch normalization; C: convolutional layer; P: pooling layer; Dr: dropout; Fl: flattened layer; SVM: support vector machine.

$$\text{Precision} = \frac{\text{TP}}{\text{TP} + \text{FP}} \tag{7.16}$$

$$\text{Recall} = \frac{\text{TP}}{\text{TP} + \text{FN}} \tag{7.17}$$

$$\text{F1} = 2 \times \frac{\text{Precision} \times \text{Recall}}{\text{Precision} + \text{Recall}} \tag{7.18}$$

where TP denotes the number of true positives for the considered class, the true positive for a target class relates to signals from that class that the network correctly categorizes. On the other hand, false positive refers to the number of signals from other classes that were wrongly classified as belonging to the regarded class. The number of signals that do not belong to the considered class and are not labeled by the classifier is referred to as the true negative (TN).

Table 7.2 summarizes the method's outcomes on the training and validation data sets. The technique classified the validation data set with an accuracy of 0.994 on average, suggesting strong performance. Also, a distinct data set was employed in each example to assess the method's accuracy. To this end, 245 frames from each scenario were collected and sent to the networks, and the TP value in percentage was calculated for each of them using Section 2.2. As shown in Figure 7.6, the accuracy varies between 98.4% and 99.88% for different scenarios, and the technique is 99.1% accurate on average, which means that, despite using binary classifiers, the approach can dependably distinguish between all classes.

**Table 7.2:** Evaluation metrics on the training and validation data.

| Net ID | Training | Validation | | | | |
|---|---|---|---|---|---|---|
| | Accuracy | Accuracy | Precision | Recall | F1 score | ROC AUC |
| 1 | 1.000 | 1.000 | 1.000 | 1.000 | 1.000 | 1.000 |
| 2 | 0.999 | 0.973 | 0.969 | 0.977 | 0.973 | 0.973 |
| 3 | 1.000 | 1.000 | 1.000 | 1.000 | 1.000 | 1.000 |
| 4 | 1.000 | 1.000 | 1.000 | 1.000 | 1.000 | 1.000 |
| 5 | 1.000 | 1.000 | 1.000 | 1.000 | 1.000 | 1.000 |
| 6 | 1.000 | 1.000 | 1.000 | 1.000 | 1.000 | 1.000 |
| 7 | 1.000 | 0.996 | 0.996 | 0.996 | 0.996 | 0.996 |
| 8 | 1.000 | 0.980 | 0.969 | 0.992 | 0.981 | 0.980 |
| 9 | 1.000 | 0.984 | 0.977 | 0.992 | 0.984 | 0.984 |
| 10 | 1.000 | 1.000 | 1.000 | 1.000 | 1.000 | 1.000 |
| 11 | 1.000 | 0.996 | 0.992 | 1.000 | 0.996 | 0.996 |
| 12 | 1.000 | 0.996 | 0.992 | 1.000 | 0.996 | 0.996 |
| 13 | 1.000 | 0.990 | 0.981 | 1.000 | 0.990 | 0.990 |
| 14 | 1.000 | 1.000 | 1.000 | 1.000 | 1.000 | 1.000 |
| 15 | 1.000 | 1.000 | 1.000 | 1.000 | 1.000 | 1.000 |
| 16 | 1.000 | 1.000 | 1.000 | 1.000 | 1.000 | 1.000 |
| 17 | 1.000 | 1.000 | 1.000 | 1.000 | 1.000 | 1.000 |
| 18 | 1.000 | 1.000 | 1.000 | 1.000 | 1.000 | 1.000 |
| 19 | 0.994 | 0.922 | 0.943 | 0.898 | 0.920 | 0.922 |
| 20 | 1.000 | 1.000 | 1.000 | 1.000 | 1.000 | 1.000 |
| 21 | 1.000 | 1.000 | 1.000 | 1.000 | 1.000 | 1.000 |
| 22 | 1.000 | 1.000 | 1.000 | 1.000 | 1.000 | 1.000 |
| 23 | 1.000 | 1.000 | 1.000 | 1.000 | 1.000 | 1.000 |
| 24 | 1.000 | 1.000 | 1.000 | 1.000 | 1.000 | 1.000 |
| 25 | 1.000 | 1.000 | 1.000 | 1.000 | 1.000 | 1.000 |
| 26 | 1.000 | 1.000 | 1.000 | 1.000 | 1.000 | 1.000 |
| 27 | 1.000 | 1.000 | 1.000 | 1.000 | 1.000 | 1.000 |
| 28 | 1.000 | 1.000 | 1.000 | 1.000 | 1.000 | 1.000 |
| 29 | 0.992 | 1.000 | 1.000 | 1.000 | 1.000 | 1.000 |
| 30 | 0.994 | 0.996 | 0.992 | 1.000 | 0.996 | 0.996 |

### 7.4.2 Effect of batch size

While all other hyperparameters remain constant, the training procedure is repeated for each of the three batch size values of 8, 16, and 32. Table 7.3 summarizes the average results. Although batch number 8 yields excellent results, the outcomes deteriorate slightly as batch size increases. As a result, changing batch size does not affect learning damage features in this technique.

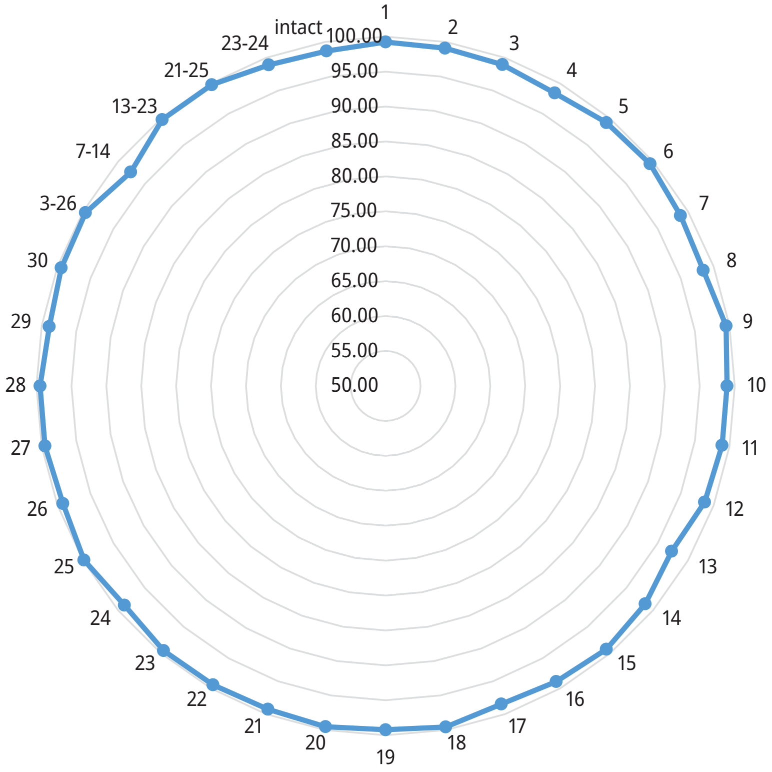

**Figure 7.6:** Accuracy in each scenario (in percentage).

**Table 7.3:** Evaluation metrics for different batch sizes.

| Batch size | Training | Validation | | | | |
|---|---|---|---|---|---|---|
| | Train accuracy | Valid accuracy | Precision | Recall | F1 score | ROC AUC |
| 8 | 0.999 | 0.994 | 0.994 | 0.995 | 0.994 | 0.994 |
| 16 | 1.000 | 0.993 | 0.992 | 0.994 | 0.993 | 0.993 |
| 32 | 0.999 | 0.992 | 0.990 | 0.993 | 0.992 | 0.992 |

### 7.4.3 Signal length

Figure 7.7 indicates that all assessment measures decline marginally when the signal length is cut in half. Even though the minimum validation accuracy was reported to be 0.891 for a single joint, the average remained at 0.989. In general, even when the signal duration is cut in half, the process is highly reliable and accurate.

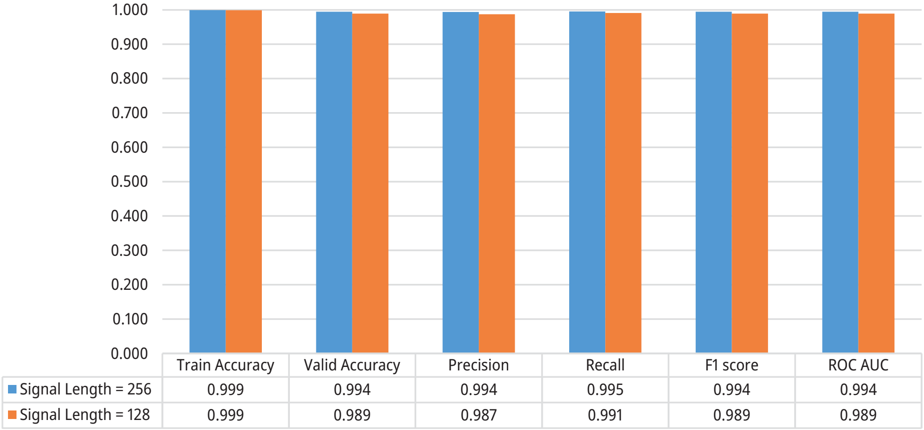

| | Train Accuracy | Valid Accuracy | Precision | Recall | F1 score | ROC AUC |
|---|---|---|---|---|---|---|
| ■ Signal Length = 256 | 0.999 | 0.994 | 0.994 | 0.995 | 0.994 | 0.994 |
| ■ Signal Length = 128 | 0.999 | 0.989 | 0.987 | 0.991 | 0.989 | 0.989 |

**Figure 7.7:** Evaluation metrics for different signal lengths.

### 7.4.4 Sample rate

As previously stated, the preceding parts used 75% of data set A for the training phase. As a result, we wanted to see if we could reduce the quantity of data needed to train the networks by lowering the sample rate. The issue is accomplished by employing a half sample rate and limiting the amount of training data to 50%. As shown in Figure 7.8, downsampling the training data to around 66% of its previous size had no discernible effect on the method's performance. The method proved a resilient algorithm against data scarcity with an accuracy score of 0.989 on the validation data set in this case.

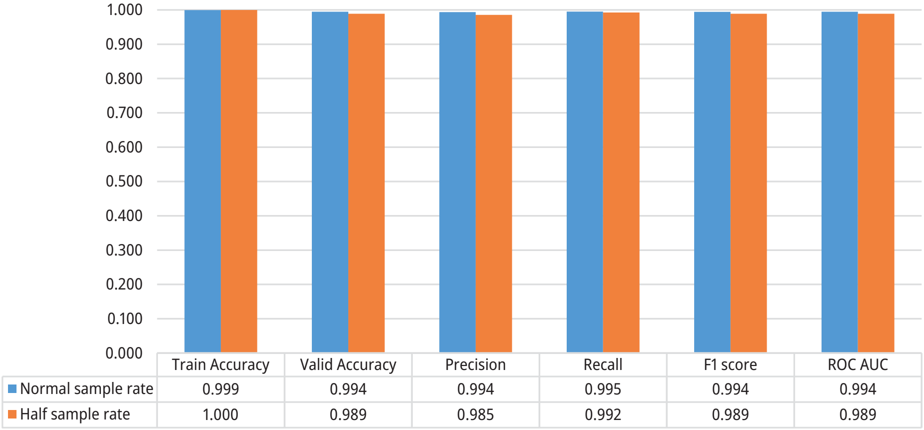

| | Train Accuracy | Valid Accuracy | Precision | Recall | F1 score | ROC AUC |
|---|---|---|---|---|---|---|
| ■ Normal sample rate | 0.999 | 0.994 | 0.994 | 0.995 | 0.994 | 0.994 |
| ■ Half sample rate | 1.000 | 0.989 | 0.985 | 0.992 | 0.989 | 0.989 |

**Figure 7.8:** Effect of sample rate.

### 7.4.5 Robustness against noisy data

Even though the data in this study came from real measurements, where containing noise is inevitable, three different signal-to-noise ratio (SNR) levels of white Gaussian noise (WGN) were added to the original signals to evaluate the method’s capacity to learn under high noise situations. The SNR is computed as follows [26]:

$$\mathrm{SNR_{dB}} = 10 \times \log_{10}\left(\frac{P_{\mathrm{signal}}}{P_{\mathrm{noise}}}\right) \tag{7.19}$$

where $P_{\mathrm{signal}}$ and $P_{\mathrm{noise}}$ represent the average power of the signal and the noise, respectively.

The training approach was repeated with a training data set containing additive WGN with SNRs of 0, 2.5, and 5 dB. Figure 7.9 depicts the original signal, its noisy form,

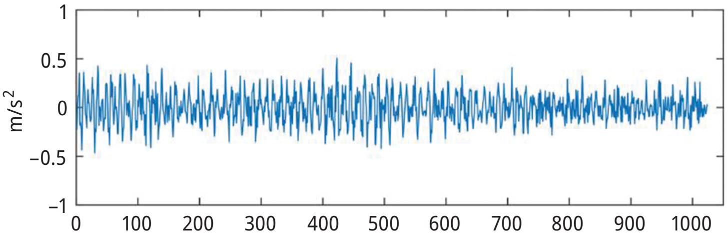

Original signal

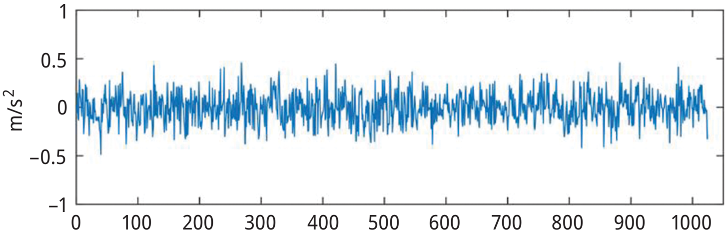

Noise

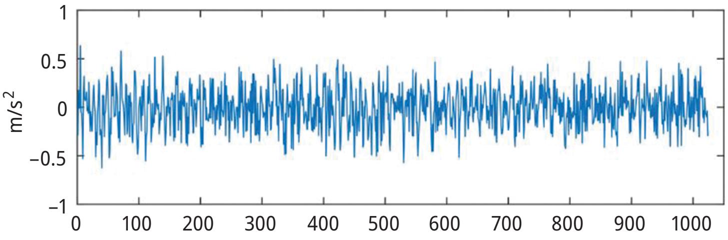

Noisy signal

**Figure 7.9:** Acceleration time-history for a 1 s (1,024 samples) signal of joint 2, additive WGN with SNR = 0 dB, and noisy signal.

and the additive WGN with SNR = 0, indicating that the average power of the signal and the noise are equal. The hyperparameters are all the same as they were in Section 4.1. Following training, the CNNs were validated using the validation data set with the same levels of WGN. These three SNRs were chosen to denote extreme noise conditions.

Figures 7.10 and 7.11 compare the results of the noisy scenarios to the noise-free condition for the training and validation data sets, respectively. Although an SNR of 0 dB indicates a severe noise condition, most networks maintained an accuracy of higher than 90%. Furthermore, as seen in Figure 7.12, the method's accuracy at 5 dB and 2.5 dB SNR levels has decreased marginally compared to noise-free data, while it remains accurate at a high SNR level of 0 dB. In general, the proposed methodology has proven to be a reliable tool for detecting structural degeneration in various environmental circumstances.

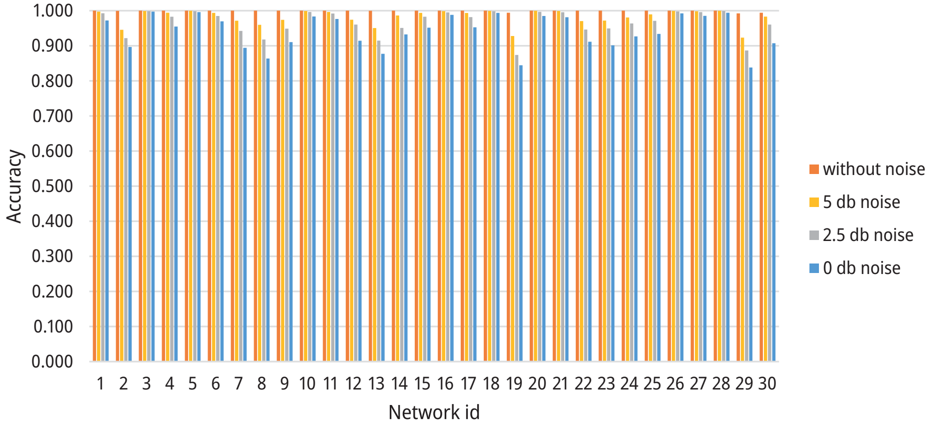

**Figure 7.10:** Networks' accuracy of training data for different SNR levels.

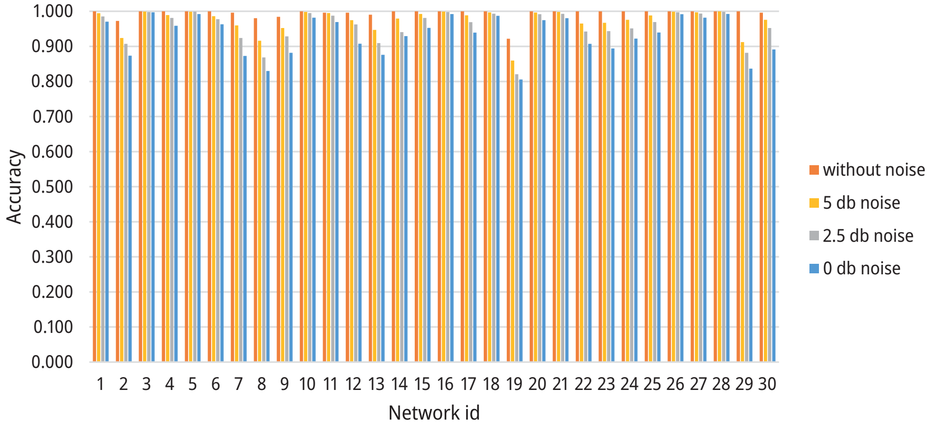

**Figure 7.11:** Networks' accuracy of validation data for different SNR levels.

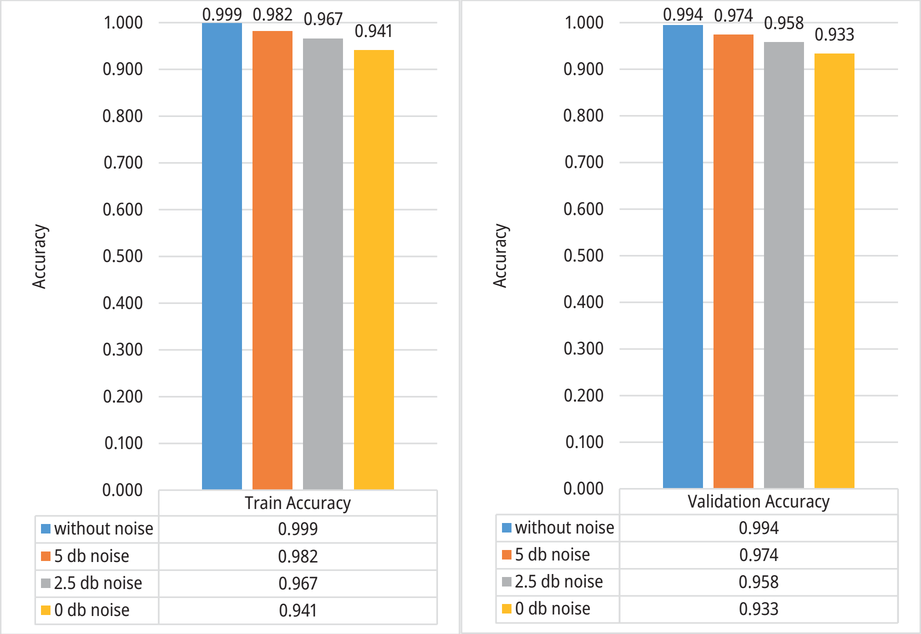

**Figure 7.12:** Average accuracy of (a) training data and (b) validation data for different SNR levels.

### 7.4.6 Speed performance

To calculate the suggested CNN-SVM's speed, 245 frames of length 256 were delivered to each network, and the required time was determined independently using the GPU and CPU. After that, the average required time to process a single frame signal is determined. The findings are based on a mean of 30 runs. The results show that a 256-frame render takes 0.419 ms on GPU and 0.424 ms on CPU. The time required to process a single frame was not significantly different while using the CPU or GPU due to the network's modest architecture. However, the time required to classify a 1-s signal for each CNN-SVM is approximately 1.7 ms, demonstrating that the method is both fast and robust, making it suitable for real-time applications.

## 7.5 Conclusion

- Findings show that the proposed method outperforms others in detecting structural damage in both single and double damage cases.
- Both the training and validation data sets were subjected to white Gaussian noise with three distinct SNR values. The technique was 93% accurate on the validation

data set. As a result, this examination indicates the method's promising performance in terms of robustness in encountering signal noises.
- Even in noisy environments, the algorithm can learn damage features straight from raw acceleration data, with no preprocessing or handcrafted feature extraction required.
- This study aimed to examine how batch size, signal length, and sample rate affected the results. The method's performance is sufficiently resistant to these changes.
- The amount of data necessary for training is lowered by adding signals from two existing accelerometers to the input. It also enables the method to use a two-dimensional architecture, which converges faster and has more learnable parameters than the 1D kind.
- Unlike traditional approaches, this technology is decentralized, with each CNN adhering to a straightforward design. As a result, the suggested technique is computationally quick and low-cost, allowing it to be implemented on various ordinary devices.
- The proposed method's required time to evaluate new data is smaller than for real-time alternatives.

However, this method necessitates data from damaged structures, which is costly and, in some instances, difficult to generate in real-world applications. As a result, future works will consider the feasibility of applying finite element methodologies to generate damaged data and the one-vs-all classification strategy. Given that the proposed method was tested on a data set with joint damages, it should be tested on other damage scenarios as well, such as mass changes and stiffness reduction. As a future study, the authors also considered adding a capacity for anticipating damage severity to the existing system. Another practical limitation is the number of accelerometers that can be included in complex construction. Future studies using fewer accelerometers should be investigated to overcome this issue.

# References

[1] J. Zhang, et al. Structural damage detection based on vibration signal fusion and deep learning. *Journal of Vibration Engineering & Technologies*, 10(4):1205–1220, 2022, DOI: https://doi.org/10.1007/s42417-022-00438-7.

[2] V. R. Gharehbaghi, et al., A critical review on structural health monitoring: definitions, methods, and perspectives. *Archives of Computational Methods in Engineering*, 2021. DOI: https://doi.org/10.1007/s11831-021-09665-9.

[3] V. R. Gharehbaghi, et al. Supervised damage and deterioration detection in building structures using an enhanced autoregressive time-series approach. *Journal of Building Engineering*, 30:101292, 2020, DOI: https://doi.org/10.1016/j.jobe.2020.101292.

[4] V. R. Gharehbaghi, et al. Deterioration and damage identification in building structures using a novel feature selection method. In *Structures*. Elsevier, DOI: https://doi.org/10.1016/j.istruc.2020.11.040.

[5] X. Huang, et al. Surface damage detection for steel wire ropes using deep learning and computer vision techniques. *Measurement*, 161:107843, 2020, DOI: https://doi.org/10.1016/j.measurement.2020.107843.

[6] Y. Dokuz and Z. Tufekci. Mini-batch sample selection strategies for deep learning based speech recognition. *Applied Acoustics*, 171:107573, 2021, DOI: https://doi.org/10.1016/j.apacoust.2020.107573.

[7] S. F. Stefenon, et al. Fault detection in insulators based on ultrasonic signal processing using a hybrid deep learning technique. *IET Science, Measurement & Technology*, 14(10):953–961, 2021, DOI: https://doi.org/10.1049/iet-smt.2020.0083.

[8] C. Modarres, et al. Convolutional neural networks for automated damage recognition and damage type identification. *Structural Control and Health Monitoring*, 25(10):e2230, 2018, DOI: https://doi.org/10.1002/stc.2230.

[9] A. Shihavuddin, et al. Wind turbine surface damage detection by deep learning aided drone inspection analysis. *Energies*, 12(4):676, 2019, DOI: https://doi.org/10.3390/en12040676.

[10] O. Avci, et al. Structural damage detection in real time: Implementation of 1D convolutional neural networks for SHM applications. In *Structural Health Monitoring & Damage Detection, Volume 7*, 49–54. Springer, 2017. DOI: https://doi.org/10.1007/978-3-319-54109-9_6.

[11] Q. Han, et al. CNN-based bolt loosening identification framework for prefabricated large-span spatial structures. *Journal of Civil Structural Health Monitoring*, 2022, DOI: https://doi.org/10.1007/s13349-022-00561-9.

[12] O. Abdeljaber, et al. 1-D CNNs for structural damage detection: Verification on a structural health monitoring benchmark data. *Neurocomputing*, 275:1308–1317, 2018, DOI: https://doi.org/10.1016/j.neucom.2017.09.069.

[13] O. Avci, et al. Convolutional neural networks for real-time and wireless damage detection. In *Dynamics of Civil Structures*. Vol. 2, 129–136. Springer, 2020, DOI: https://doi.org/10.1007/978-3-030-12115-0_17.

[14] S. Ghazvineh, et al., *Application of 2-D Convolutional Neural Networks for Damage Detection in Steel Frame Structures*. arXiv preprint arXiv:2110.15895, 2021 DOI: https://doi.org/10.48550/arXiv.2110.15895.

[15] S. Albawi, T. A. Mohammed, and S. Al-Zawi. *Understanding of a convolutional neural network*. In *2017 International Conference on Engineering and Technology (ICET)*. IEEE, 2017. DOI: https://doi.org/10.1109/ICEngTechnol.2017.8308186.

[16] S. Ioffe, and C. Szegedy. *Batch normalization: Accelerating deep network training by reducing internal covariate shift*. In *International Conference on Machine Learning*. PMLR, 2015. DOI: https://doi.org/10.48550/arXiv.1502.03167.

[17] V. Nair, and G. E. Hinton. Rectified linear units improve restricted Boltzmann machines. In *The International Conference on Machine Learning*, 2010.

[18] X. Glorot, A. Bordes, and Y. Bengio. *Deep sparse rectifier neural networks*. In *Proceedings of the fourteenth international conference on artificial intelligence and statistics*. 2011, JMLR Workshop and Conference Proceedings.

[19] A. Krizhevsky, I. Sutskever, and G. E. Hinton. ImageNet classification with deep convolutional neural networks. *Communications of the ACM*, 60(6):84–90, 2017.

[20] N. Srivastava, et al. Dropout: A simple way to prevent neural networks from overfitting. *The Journal of Machine Learning Research*, 15(1):1929–1958, 2014.

[21] I. Goodfellow, Y. Bengio, and A. Courville. *Deep Learning*. MIT press, 2016.

[22] S. Sharma and S. Sen. One-dimensional convolutional neural network-based damage detection in structural joints. *Journal of Civil Structural Health Monitoring*, 10(5):1057–1072, 2020, DOI: https://doi.org/10.1007/s13349-020-00434-z.

[23] O. Abdeljaber, et al. Dynamic testing of a laboratory stadium structure. In *Geotechnical and Structural Engineering Congress 2016*. 2016, DOI: http://dx.doi.org/10.1061/9780784479742.147.

[24] D. P. Kingma, and J. Ba, *Adam: A method for stochastic optimization*. arXiv preprint arXiv:1412.6980, 2014 DOI: https://doi.org/10.48550/arXiv.1412.6980.

[25] T. Guo, et al. Damage detection in a novel deep-learning framework: A robust method for feature extraction. *Structural Health Monitoring*, 19(2):424–442, 2020, DOI: https://doi.org/10.1177/1475921719846051.

[26] W. Zhang, et al. A deep convolutional neural network with new training methods for bearing fault diagnosis under noisy environment and different working load. *Mechanical Systems and Signal Processing*, 100:439–453, 2018, DOI: https://doi.org/10.1016/j.ymssp.2017.06.022.

Jice Zeng, Zihan Wu, Manuel A. Vega, Michael D. Todd*, Zhen Hu*

# 8 Fast probabilistic damage detection using inverse surrogate models

**Abstract:** Bayesian inference has been widely employed in structural health monitoring (SHM) to evaluate structural integrity by inferring damage indices based on physics-based computational simulations and or field observations; this is a fundamentally inverse problem. To overcome the challenge caused by the computationally intensive physics-based simulations, machine learning (ML) models have been enabled as forward emulators to supplant the conventional physics-based simulations in Bayesian inference. While the forward ML models provide a viable solution to the computational challenge in probabilistic damage detection using Bayesian inference, it requires coordination with Bayesian inference algorithms, followed by evaluation via likelihood functions. For complex stochastic systems, the likelihood functions sometimes are analytically intractable even though the forward model has been replaced with a computationally cheap ML model. This poses challenges to model-based probabilistic damage detection in SHM. This chapter presents two inverse surrogate modeling methods for two scenarios of problems to enable for fast probabilistic damage detection without the need of evaluating the likelihood function. The first method is for problems where a one-to-one mapping exists between the observations and damage indices. A variational Bayesian neural network is developed to directly map observations to damage indices and to account for uncertainty in the observations. The second method adopts the idea of normalizing the flow and is suited to problems with highly nonlinear behavior when there is no clear one-to-one mapping between the observations and the damage indices. A summary and a conditional invertible neutral network (cINN) are employed to extract features for damage detection and to perform the nonlinear mapping between observations and posterior distributions of

---

**Acknowledgment:** The authors acknowledge financial support from the United States Army Corps of Engineers through the US Army Engineer Research and Development Center Research Cooperative Agreement W9132T-22-20014.

---

***Corresponding author: Michael D. Todd,** Department of Structural Engineering, University of California San Diego, La Jolla, CA 92093, USA, e-mail: mdtodd@eng.ucsd.edu

***Corresponding author: Zhen Hu,** Department of Industrial and Manufacturing Systems Engineering, University of Michigan-Dearborn, Dearborn, MI 48128, USA, e-mail: zhennhu@umich.edu

**Jice Zeng,** Department of Industrial and Manufacturing Systems Engineering, University of Michigan-Dearborn, Dearborn, MI 48128, USA

**Zihan Wu,** Department of Structural Engineering, University of California San Diego, La Jolla, CA 92093, USA

**Manuel A. Vega,** Advanced Engineering Analysis Group (W-13), Los Alamos National Laboratory, Los Alamos, NM, USA

https://doi.org/10.1515/9783110791426-008

damage indices. Two engineering application examples, including a miter gate and a concrete building frame, are used to demonstrate the presented inverse surrogate models for probabilistic damage detection in SHM.

# 8.1 Introduction

## 8.1.1 Background of structural damage detection

Structural damage is defined as any deviation (either intentional or unintentional) in material, geometric, and/or connectivity characteristics that cause the structure to be unable to perform its designed function; in the worst cases, damage may threaten structural integrity and serviceability [1]. Common examples of structural damage types include corrosion (change in material), cracking (change in geometry), looseness of bolts (change in connectivity), and broken welds (change in geometry/connectivity). Damage may occur anywhere on a structure, and its expression ranges from the microscale to the global scale (both in spatial extent and in time scales). Although structural damage may not cause a complete failure (e.g., structural collapse), system functionality may not reach to the expected or required quality due to the occurrence of a damage [2]. If a damage remains sustained and undetected, it can incrementally accumulate and propagate over time, and eventually lead to structural failure. For example, damage stems from fatigue or corrosion, which is prone to progressively grow, resulting in failures over a long period, while fire, earthquake or other unexpected events can cause failure in a short time [3].

Figure 8.1(a) illustrates the three common methods for condition assessment and damage detection, namely, visual inspection, nondestructive testing (NDT), and structural health monitoring. Visual inspection is the most common historical (and current) method for structural condition assessment. It is typically executed by a human inspector tasked to observe the structural condition, and evaluate the state based on the inspectors’ experience and some form of rubric or other guidelines [4]. Although visual inspection is easy to implement and applicable to many scales of damage, it is not suitable for complex and large-scale structures, since damage may occur to structural components with restricted accessibility/observability (i.e., internal damage masked by decorative coverings) or difficult to visually detect (i.e., loose bolts) [5]. In addition, visual inspection often provides only qualitative damage assessment in the absence of a well-defined rubric, and the entire process is labor-intensive, cost-consuming, and requires operational interruption. The reliability of inspection results also heavily relies on qualified and highly trained inspectors.

To overcome limitations of visual inspection, NDT techniques have been extensively studied to effectively detect and monitor deterioration in engineering structures. NDT realizes condition assessment and damage detection in a local sense,

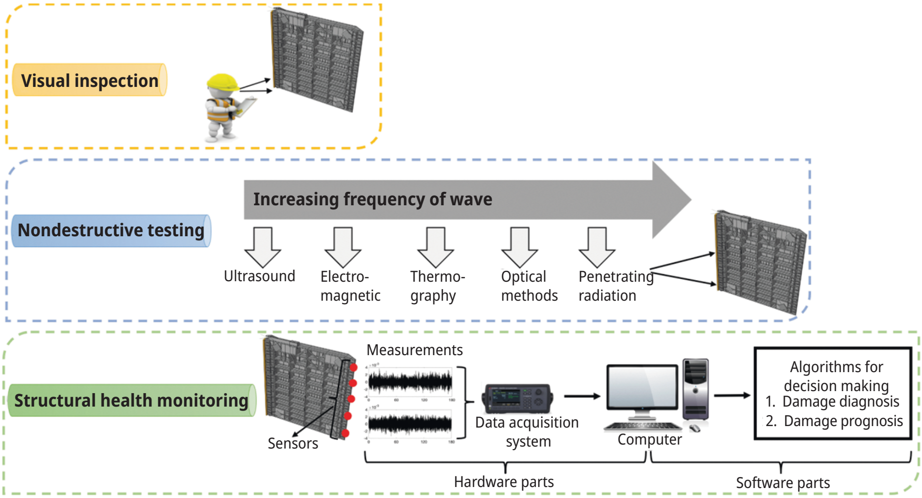

**Figure 8.1(a):** Methods for condition assessment and damage detection; .

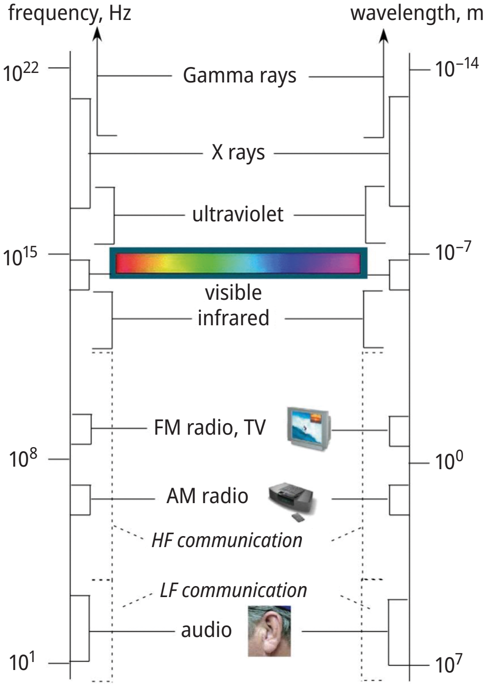

**Figure 8.1(b):** Different frequency/wavelength ranges allow for different NDT interrogation methods.

particularly when prior information concerning possible damage location is available [6]. A considerable number of NDT techniques are well-established and can be categorized based on different ranges of the interrogating parameter wavelength or, inversely, the frequency. Interaction between the interrogating parameter at a certain frequency of the investigated structures enables us to detect structural damage using characteristics of the wave spectrum [7]. Traditional NDT techniques include acoustic emission [8], ultrasound [9], guided (Lamb) waves [10], thermography [11], and laser Doppler vibrometer [12], among others (see Figure 8.1(b)). Although NDT techniques operate in a relatively simple way and can identify local damage due to the localized nature, prior knowledge of the damage type and the location is generally required. The implementation process is also susceptible to human error, and, often most importantly, the system or structure usually must be taken out of service to perform the NDT.

Some of these issues and challenges in visual inspection and NDT have promoted the idea of online, continuous monitoring, without taking the system out of service, now widely known as structural health monitoring (SHM). SHM is a process of in-service health evaluation – continuously tracking the structural status and identifying damage through a reliable and autonomous monitoring system [13]. It enables us to understand the behavior of the structure under diverse operational conditions, take precautions to prevent severe damage, and benefit from repairing and maintenance work. The objective of SHM is to perform a continuous or periodical health monitoring of crucial structures for deciding whether a timely remedial (maintenance, repair, etc.) action is needed or not. The basic principle of SHM techniques is that the sensing system or hardware deployed on the structure of interest and analysis system or software work in alignment to implement the task of monitoring and evaluation. The hardware part encompasses sensors mounted on the structure, such as accelerometers, strain gauges, or others, and data acquisition modules for data collection [14]. Fundamental processing, often known as intelligent feature extraction, must be performed to extract meaningful information, accounting for the current status of structure being evaluated [15]. With the assistance of hardware and software, SHM provides the capability to trace the condition variation of structure over time using measured structural responses from a network of sensors. The information concerning the structural performance on targeted function is continuously updated during the long-term or continuous SHM, which potentially avoids faults or defects to evolve to an unacceptable level. SHM has evolved into a workflow built on statistical pattern recognition, governed by a few fundamental axioms [16].

As such, SHM may be considered an inverse problem where deficiencies of a structure are *inferred* using collected measurements in the field, given a certain known input. A comprehensive monitoring solution combines SHM, which is a *diagnostic* capability, with a *prognostic* capability. Diagnostics identifies the occurrence, localization, classification, and/or quantification of damage, representing the current state of the system. Through prognostics, the information acquired from the diagnostic stage is used to estimate the remaining useful life of a structure or some other such limit state. Therefore, as shown in Figure 8.2, an SHM strategy can be broadly outlined over five levels [13]. The five levels in Figure 8.2 represent the accumulated knowledge regarding the structural damage states. Level 1 aims at confirming the presence of damage in a structure. This is usually achieved by observing the structural properties identified over time, such as modal data (natural frequency and mode shape), strain energy, and stiffness variation. The goal of level 2 is to determine the damage location. The methods involving guided waves and ultrasonics can sometimes achieve both level 1 and 2 together, since wave propagation and wave source location are known [17]. To identify the damage types at level 3, correlation between the data representing some specific damage types and the currently measured data is a prior, effectively requiring supervised learning [18]. For levels 4 and 5, advanced modeling (such as through physics-based finite element analysis (FEA)) is usually needed to achieve damage quantification and prognostics.

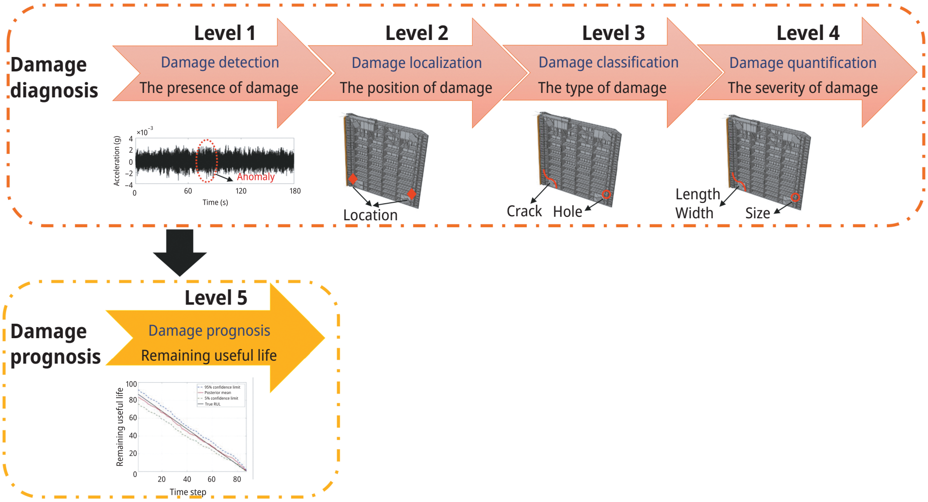

**Figure 8.2:** Five levels of damage detection in SHM.

## 8.1.2 Methods for structural damage detection

Structural damage detection can be generally divided into two groups: data-enabled and physics-enabled methods. The two groups of methods are complementary, as their combination is frequently employed for application to damage detection. It is difficult to conclude that one of them is absolutely superior to the another since they exhibit different performance results, depending on the different contexts and what is available. An exhaustive discussion on the two groups of methods in SHM is available in [19].

Figures 8.3 and 8.4 summarize the characteristics of data-enabled and physics-enabled methods in terms of appropriate application contexts, advantages, and disadvan-

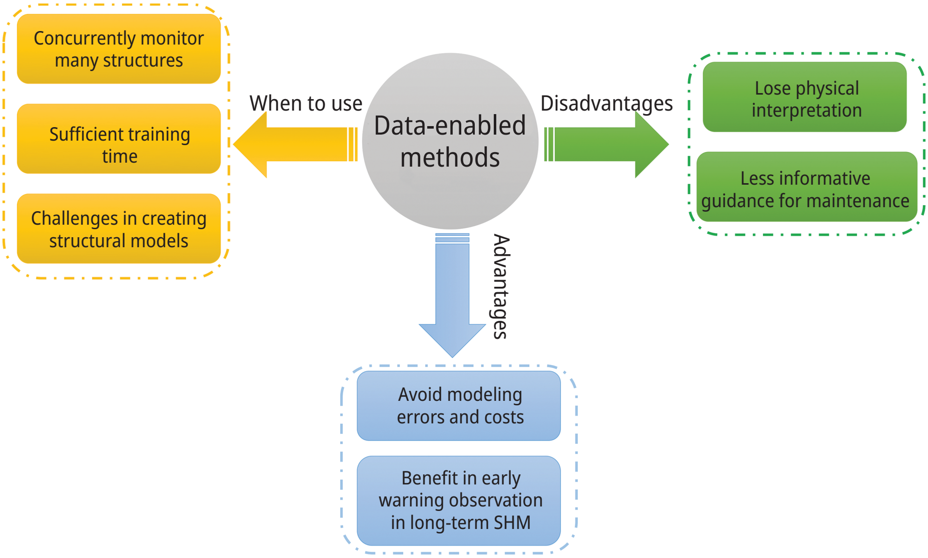

**Figure 8.3:** Data-enabled methods for SHM.

tages. For example, data-enabled methods do not require creating an FE model of a structure, as the implementation is achieved by comparing the current damage condition to previous observations. Therefore, these methods typically use artificial intelligence and pattern recognition methods for damage detection to elicit this "change detection," or anomalous behavior. Specifically, instead of solving an inverse problem that uses the recorded data to infer model parameters, data-enabled methods detect anomalies using unsupervised learning techniques to compare the reference/baseline features recorded in a presumed "healthy" condition, to features from the current period; there is no direct physical interpretation. Data-enabled methods are usually relatively easy to implement, avoid the challenges in physical modeling of complex structures, and have low computational cost demands [20]. Some popular methods include auto-associative Artificial Neural Networks (ANNs) [21], autoregressive models [22], response surface model [23], or any abnormal detectors (e.g., distance measure). The key components in these methods are data processing, dimensionality reduction, feature extraction, and anomaly detection. Because the underlying methodology is unsupervised, one of the challenges in using these methods is distinguishing true damage from falsely detected damage that may be caused by environmental change [24].

On the other hand, physics-enabled methods for damage detection require creating a structural model (e.g., an FE model). With an FE model, structural responses can be predicted at a new damage state, given a related loading condition. Typically, an FE model is initially established based on the design, and measured data from the real structure are used to update the FE model, which will be elaborately introduced in the next section. Compared to pure data anomaly detectors, these methods consider the underly-

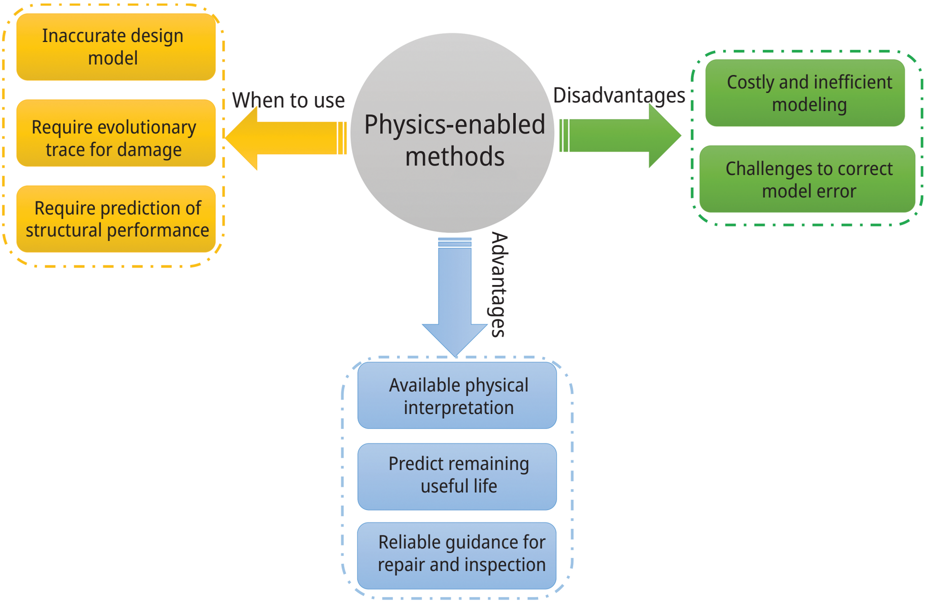

**Figure 8.4:** Physics-enabled methods for SHM.

ing physics, such as material, geometric, boundary, and connectivity properties of the structure. These methods, therefore, can explicitly represent data under various operational conditions and simulate structural behavior, which further explains the possible reasons for variation [25]. FE model has been extensively employed for damage detection of engineering structures in SHM. However, such model-based methods are relatively computationally expensive and time-consuming to generate. Furthermore, modeling errors or bias are inevitably introduced, due to assumptions, simplifications, unknown or missing physics, etc. Correcting such errors would be very challenging and requires sufficient high-quality measurements [26]. In addition, there may be lots of candidate models due to the different modeling strategies, and it may take prohibitive time to compare and select the optimal one.

In summary, structural damage detection in SHM is a quite broad topic. In this chapter, we will only focus on physics-enabled methods for damage detection.

### 8.1.3 Finite element model updating for damage detection

Physics-enabled structural damage detection has been growing since the 1990s as computational modeling capabilities have grown dramatically; with the development and execution of increasingly complex models, it comes with the advantages of physical interpretability and even prediction of future performance (prognostics) [27]. Finite element model updating (FEMU) is a desirable model-based damage detection method to achieve sustainable condition assessment for engineering structures in SHM. FEMU aims to minimize the discrepancy between model predictions and the measured counterparts by progressively adjusting the model parameters or hyperparameters until the model can successfully predict the observed structural condition(s) [28, 29]. As shown in Figure 8.5, FEMU, in general, can be categorized into two main classes: deterministic methods and stochastic methods.

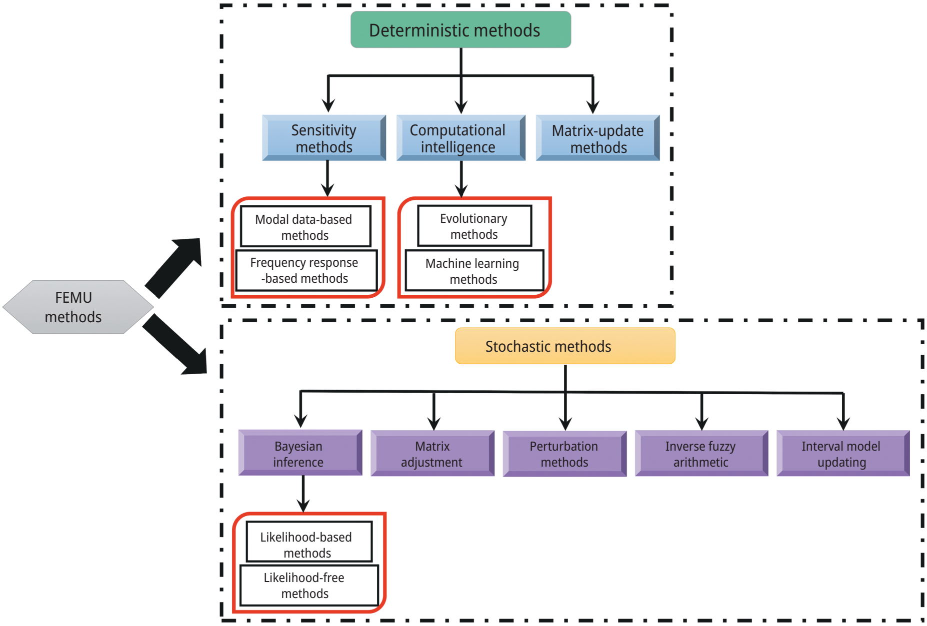

**Figure 8.5:** FEMU methods for damage detection.

Deterministic methods, such as sensitivity methods [30, 31] and evolutionary methods [32, 33], are defined as the optimization of a single FE model to reduce the error between the actual test and the model-derived results. These methods only give a unique solution based on a single calibration of structural parameters. The confidence and reliability in representing a physical structure using the updated parameters are not available. The model's credibility must be quantified through a measure of robustness to uncertainty and prediction accuracy for observations that are not recorded in the field test [34]. On the other hand, stochastic methods provide a way to incorporate structural uncertainties into the prediction process by describing model parameters as a range or distribution functions, considering multiple sets of possible models [35]. Popular stochastic methods include Bayesian inference [36], covariance matrix adjustment [37], perturbation method [38], interval model updating [39], and inverse fuzzy arithmetic [40]. Stochastic methods identify not only the optimal model parameters, but also the associated uncertainty of the parameters. Stochastic methods have been in-depth investigated and widely applied for model updating and structural damage detection. A thorough literature review of stochastic FEMU can be found in [41].

## 8.2 Probabilistic structural damage detection using Bayesian model updating

A wide range of stochastic methods have been developed and successfully applied to various civil infrastructure systems in the last few decades. Among these methods, one of the most widely used is the Bayesian model updating. It has attracted a thriving interest and has been extensively employed for model updating, probabilistic damage detection, and system identification [42–44]. The Bayesian-based structural damage detection starts with a FE model, parameterized by assumed uncertain structural parameters, denoted by $\boldsymbol{\theta}$. In the Bayesian model updating, the measurements collected from the actual structure are used to update the FE model parameters, $\boldsymbol{\theta}$, and the controllable parameters are involved during the updating process. The model parameters refer to random variables related to the FE modeling that need to be calibrated using observations; conversely, the controllable parameters refer to those that are controllable or fully observable in a test or an experiment, such as external excitation (in some cases). Specifically, suppose a FE model $\mathbf{y}_m = G(\boldsymbol{\theta}, \mathbf{f}_{1:m})$ is available, where $\mathbf{y}_m \in \mathbb{R}^{N_Y \times 1}$ denotes the output of the FE model at time step $m$, $N_Y$ is the number of outputs, $\mathbf{f}_{1:m} = [\mathbf{f}_1^T, \mathbf{f}_2^T, \cdots, \mathbf{f}_m^T] \in \mathbb{R}^{(N_u \times m) \times 1}$ denotes the external excitations during the past $m$ time steps, and $N_u$ is the number of excitation variables, the relation between the experimental observations, $\mathbf{y}_{o,m} \in \mathbb{R}^{N_Y \times 1}$, and the model-derived outputs is expressed as follows

$$\begin{aligned} \mathbf{y}_{o,m} &= \mathbf{y}_m + \pi(\mathbf{f}_{1:m}) + \tau_m, \\ &= G(\boldsymbol{\theta}, \mathbf{f}_{1:m}) + \pi(\mathbf{f}_{1:m}) + \tau_m, \end{aligned} \tag{8.1}$$

where $\pi(\mathbf{f}_{1:m})$ is the model bias of a FE model, $\tau_k \sim N(\mathbf{0}, \Sigma)$ is the observation error that is usually simulated as Gaussian noise with zero-mean vector and diagonal covariance matrix whose diagonal elements are the variances, $\sigma_i^2, i = 1, \cdots, N_Y$, of the measurement noise for the $i$-th response.

Considering both excitation and observations, the uncertain model parameters $\boldsymbol{\theta}$ can be estimated or updated using the Bayes' theorem,

$$p_{\boldsymbol{\theta}|\mathbf{y}}(\boldsymbol{\theta}|\mathbf{y}_{o,1:m}, \mathbf{f}_{1:m}) = \frac{p_{\mathbf{y}|\boldsymbol{\theta}}(\mathbf{y}_{o,1:m}|\boldsymbol{\theta}, \mathbf{f}_{1:m}) p_{\boldsymbol{\theta}}(\boldsymbol{\theta})}{\int p_{\mathbf{y}|\boldsymbol{\theta}}(\mathbf{y}_{o,1:m}|\boldsymbol{\theta}, \mathbf{f}_{1:m}) p_{\boldsymbol{\theta}}(\boldsymbol{\theta}) \mathbf{d}\boldsymbol{\theta}} \propto p_{\mathbf{y}|\boldsymbol{\theta}}(\mathbf{y}_{o,1:m}|\boldsymbol{\theta}, \mathbf{f}_{1:m}) p_{\boldsymbol{\theta}}(\boldsymbol{\theta}), \tag{8.2}$$

where $p_{\boldsymbol{\theta}}(\boldsymbol{\theta})$ is a prior distribution of $\boldsymbol{\theta}$, which reflects the existing knowledge and the initial assumptions that are about to be updated by the uncertain model parameters (collectively known as “plausibility.”). Theoretically, one can use any type of $p_{\boldsymbol{\theta}}(\boldsymbol{\theta})$, depending on the specific application and measurement information. In eq. (8.2), the $\mathbf{y}_{o,1:m} = [\mathbf{y}_{o,1}, \cdots, \mathbf{y}_{o,m}] \in \mathbb{R}^{N_Y \times m}$ are the observations from $t_1$ to $t_m$, and $p_{\mathbf{y}|\boldsymbol{\theta}}(\mathbf{y}_{o,1:m}|\boldsymbol{\theta}, \mathbf{f}_{1:m})$ is the likelihood function, given $\boldsymbol{\theta}$ and excitation measurement $\mathbf{f}_{1:m}$. The likelihood function reflects how good is the model, which is characterized by the model parameter $\boldsymbol{\theta}$ and used to describe the true nature of the structural system, successfully reproducing the actual observations. $p_{\boldsymbol{\theta}|\mathbf{y}}(\boldsymbol{\theta}|\mathbf{y}_{o,1:m}, \mathbf{f}_{1:m})$ is the posterior distribution that usually requires solving intractable and high-dimensional integrals. The popular ways to estimate the posterior distribution are Markov Chain Monte Carlo (MCMC) sampling methods, such as metropolis hasting (MH) [45], delayed rejection and adaptive metropolis (DRAM) [46], differential evolutionary adaptive metropolis (DREAM) [47], and sequential Monte Carlo simulation (SMC) [48].

In some situations, input excitation is not measured or otherwise known, such as in a test or an experiment under ambient vibration in which the vibration is triggered by natural/non-artificial force, for example, wind, traffic, or human walking. In these cases, excitation is often assumed to be broadband Gaussian white noise. Equation (8.2) is therefore rewritten as

$$\begin{aligned} p_{\boldsymbol{\theta}|\mathbf{y}}(\boldsymbol{\theta}|\mathbf{y}_{o,1:m}) &= \int p_{\boldsymbol{\theta}|\mathbf{y}}(\boldsymbol{\theta}|\mathbf{y}_{o,1:m}, \mathbf{f}_{1:m}) p_{\mathbf{f}}(\mathbf{f}_{1:k}) \mathbf{d}\mathbf{f}_{1:m}, \\ &\propto \int p_{\mathbf{y}|\boldsymbol{\theta}}(\mathbf{y}_{o,1:m}|\boldsymbol{\theta}, \mathbf{f}_{1:m}) p_{\mathbf{f}}(\mathbf{f}_{1:k}) \mathbf{f}_{1:m} p_{\boldsymbol{\theta}}(\boldsymbol{\theta}), \end{aligned} \tag{8.3}$$

where $p_{\mathbf{f}}(\mathbf{f}_{1:m})$ is the join probability distribution of $\mathbf{f}_{1:m}$.

To solve either eqs. (8.2) or (8.3), various approaches have been developed in either likelihood-based or likelihood-free schemes [49, 50]. A noticeable drawback for both classes of methods is the required high computational effort due to the large number of model runs required to achieve a satisfactory convergence. To tackle the computational burden, numerous surrogate modeling methods have been proposed, which substantially reduce the computational expense, through the form of either order-reduced models [51] or various types of metamodels, such as Gaussian process regression [35, 52], response surface [53, 54], polynomial chaos [55, 56], and artificial neural networks [57, 58]. However, there are still challenges in the application of surrogate modeling to model updating, for the purposes of informing SHM. For example, assumptions and approximations in the surrogate model construction may lead to accuracy loss in surrogate predictions. In addition, many applications are limited in the use of scalar-valued or time-averaged data collected under ambient vibration such as modal data (natural frequencies and mode shapes) identified from the time series data [59]. Multiple surrogate models, corresponding to the relationship between a set of modal data and model parameters, are formulated, which may increase the computational cost [60]. For the situation where the input excitations are not measured, the performance of model updating is strongly correlated to how well the modal data are identified and what modal data will be adopted. A direct use of output-only time-series data has been largely ignored in surrogate model-based model updating and damage detection. Furthermore, using surrogate models may not necessarily realize remarkable speed-ups as the fundamental limitation of needing to run the surrogate model many times may remain.

Motivated by addressing the computational challenges of the current Bayesian inference methods for structural damage detection, this chapter presents two types of inverse surrogate modeling methods, which allows us to efficiently solve eqs. (8.2) or (8.3) without evaluating any likelihood function, and obtain the posterior distribution of damage parameters $\boldsymbol{\theta}$ for any given observations in real time. This enables for real-time SHM using probabilistic damage detection methods.

## 8.3 Inverse surrogate models for fast probabilistic damage detection

In this section, inverse surrogate modeling methods for fast probabilistic damage detection are presented. As shown in Figure 8.6, the presented inverse surrogate modeling methods, in general, consists of two phases, including an offline training phase and an online damage detection phase.

In the offline training phase, $N_t$ training samples of $\boldsymbol{\theta}$ are first generated according to its prior distribution. Denoting the training samples as $\boldsymbol{\theta}_{\text{train}} = [\boldsymbol{\theta}_t^{(1)}, \cdots, \boldsymbol{\theta}_t^{(N_t)}]$ and by accounting for various uncertainty sources, synthetic observation data $\mathbf{y}_{i,1:T}^{\text{syn}}, i = 1, \cdots, N_t$ can be obtained, where $\mathbf{y}_{i,1:T}^{\text{syn}}$ represents the synthetic observation generated using the $i$-th training sample of $\boldsymbol{\theta}$. Next, inverse surrogate models are constructed to map the synthetic observations to posterior distributions of $\boldsymbol{\theta}$ directly. After the training of the inverse surrogate models in the online detection phase, measurements $\mathbf{y}_{o,1:T}$ collected from field test are passed through the trained inverse surrogate models to obtain the posterior samples of $\boldsymbol{\theta}$, without evaluating any likelihood function, which can often be a time-consuming phase of the process.

In this chapter, two types of inverse surrogate models are presented for fast probabilistic damage detection.

- The first type of surrogate model is for problems with an invertible response function $\mathbf{y}_m = G(\boldsymbol{\theta}, \mathbf{f}_{1:m})$. In other words, there is a one-to-one mapping between $\boldsymbol{\theta}$ and $\mathbf{y}_m$, such that an inverse surrogate model can be constructed to obtain posterior samples of $\boldsymbol{\theta}$ directly using $\mathbf{y}_m$.
- The second type of surrogate model is for a more generalized case, where the one-to-one mapping between $\boldsymbol{\theta}$ and $\mathbf{y}_m$ does not exist. A conditional invertible neural network (cINN) is used in conjunction with normalizing the flow to achieve the probabilistic mapping between the observations and the posterior distribution of $\boldsymbol{\theta}$.

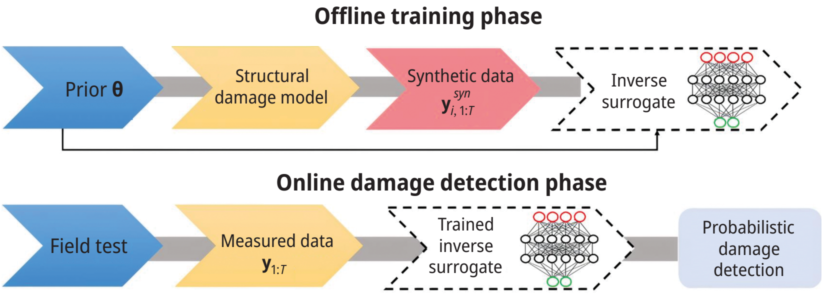

**Figure 8.6:** Flowchart of probabilistic damage detection using inverse surrogates.

In what follows, this chapter presents details of the two types of inverse surrogate models and their application to probabilistic damage detection.

## 8.3.1 Inverse surrogate model for damage detection with invertible models

As mentioned above, when $\mathbf{y}_m = G(\boldsymbol{\theta}, \mathbf{f}_{1:m})$ is invertible, one can directly build a surrogate model to map the observations $\mathbf{y}_{o,1:T}$ to the damage parameters $\boldsymbol{\theta}$. The unmeasured input excitation, however, becomes "noise" in the inverse surrogate model due to the lack of information. The Bayesian method can be employed in the inverse surrogate model to account for this part of uncertainty by quantifying the uncertainty in the damage parameters $\boldsymbol{\theta}$. In this section, the Bayesian neural network is employed to accomplish this task.

### 8.3.1.1 Bayesian neural network (BNN) architecture

ANN as a widely used data-driven method has been proven its great potential for various purposes through SHM applications, especially for highly nonlinear structures with complicated failure models. Traditional ANNs are mostly built to generate point prediction where the prediction accuracy may be strongly affected by the quality and noise level of the training data. As an alternative way to train an ANN over deterministic mathematical models, the Bayesian neural network (BNN) is more robust against training data uncertainties [61] such as uncertainty due to the unmeasured input excitations in the case of inverse surrogate.

As shown in Figure 8.7, a BNN is essentially a neural network with a prior distribution on each network parameter, accounting for its uncertainty (i.e., the weights and biases). The uncertainty in these weights and biases can be propagated into network predictions, which provides insightful reliability-related information in the context SHM problems. The joint posterior distribution of the network parameters, after observing a set of training data ($\mathbf{X}_{\text{tr}}, \mathbf{Y}_{\text{tr}}$), can be expressed as follows:

$$p(\mathbf{w}, \mathbf{b}, \Sigma | \mathbf{Y}_{\text{tr}}, \mathbf{X}_{\text{tr}}) = \frac{p(\mathbf{Y}_{\text{tr}} | \mathbf{w}, \mathbf{b}, \Sigma, \mathbf{X}_{\text{tr}}) p(\mathbf{w}, \mathbf{b}, \Sigma | \mathbf{X}_{\text{tr}})}{p(\mathbf{Y}_{\text{tr}} | \mathbf{X}_{\text{tr}})}, \\ = \frac{p(\mathbf{Y}_{\text{tr}} | \mathbf{w}, \mathbf{b}, \Sigma, \mathbf{X}_{\text{tr}}) p(\mathbf{w}, \mathbf{b}, \Sigma | \mathbf{X}_{\text{tr}})}{\iiint p(\mathbf{Y}_{\text{tr}} | \mathbf{w}, \mathbf{b}, \Sigma, \mathbf{X}_{\text{tr}}) p(\mathbf{w}, \mathbf{b}, \Sigma | \mathbf{X}_{\text{tr}}) d\mathbf{w} d\mathbf{b} d\Sigma}, \tag{8.4}$$

where $\mathbf{w}$, $\mathbf{b}$, and $\Sigma$ represent the weights, biases, and the covariance matrix of the model, respectively. Based on the prior, the posterior predictive distribution, $\mathbf{Y}_{\text{test}}$, after observing a set of new data, $\mathbf{X}_{\text{test}}$, can be calculated as

$$p(\mathbf{Y}_{\text{test}} | \mathbf{X}_{\text{test}}, \mathbf{Y}_{\text{tr}}, \mathbf{X}_{\text{tr}}) = \iiint p(\mathbf{Y}_{\text{test}} | \mathbf{w}, \mathbf{b}, \Sigma, \mathbf{X}_{\text{test}}) p(\mathbf{w}, \mathbf{b}, \Sigma | \mathbf{Y}_{\text{tr}}, \mathbf{X}_{\text{tr}}) d\mathbf{w} d\mathbf{b} d\Sigma. \tag{8.5}$$

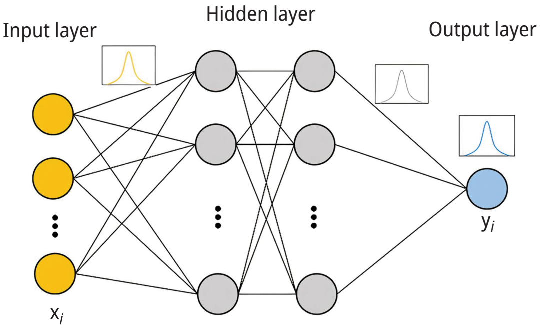

**Figure 8.7:** BNN architecture.

The high-dimensional marginalization term in the denominator of eq. (8.4) is typically intractable. Therefore, variational inference (VI) is employed as an approximation method in the process of training a BNN, which assumes a family of distributions, $Q$ that is simpler than $p(\mathbf{w}, \mathbf{b}, \Sigma | \mathbf{Y}_{\text{tr}}, \mathbf{X}_{\text{tr}})$, and finding the closest member, $q^*(\mathbf{w}, \mathbf{b}, \Sigma)$, in that family that is similar to the true distribution. The similarity between the two distributions can be measured by the Kullback-Leibler (KL) divergence – the choice of the dissimilarity function.

In the rest of the section, the parameter, $\boldsymbol{\omega}$, will be used to represent the parameters $\mathbf{w}$, $\mathbf{b}$, and $\Sigma$ for simplicity. The optimization model in VI is given by [62]

$$q^*(\boldsymbol{\omega}) = \arg\min\{KL(q(\boldsymbol{\omega}) \| p(\boldsymbol{\omega} | \mathbf{Y}_{\text{tr}}, \mathbf{X}_{\text{tr}}))\}. \tag{8.6}$$

The above KL divergence can be expressed using the evidence lower bound (ELBO) as

$$\text{KL}(q(\boldsymbol{\omega}) \| p(\boldsymbol{\omega} | \mathbf{Y}_{\text{tr}}, \mathbf{X}_{\text{tr}})) = \text{ELBO}(q(\boldsymbol{\omega})) + E[\log(p(\mathbf{Y}_{\text{tr}} | \mathbf{X}_{\text{tr}}))], \tag{8.7}$$

where the ELBO is defined as

$$\mathrm{ELBO}(q(\boldsymbol{\omega})) = E_{q(\boldsymbol{\omega})}[\log(p(\mathbf{Y}_{\mathrm{tr}}|\boldsymbol{\omega}, \mathbf{X}_{\mathrm{tr}})p(\boldsymbol{\omega}))] - E_{q(\boldsymbol{\omega})}[\log(q(\boldsymbol{\omega}))]. \tag{8.8}$$

Finally, the closest member from the family of the distributions can be found by maximizing the ELBO as follows:

$$\begin{aligned} q^*(\boldsymbol{\omega}) &= \underset{q(\boldsymbol{\omega})\in Q}{\arg\min}\{\mathrm{KL}(\mathrm{q}(\boldsymbol{\omega})\|\mathrm{p}(\boldsymbol{\omega}|\mathbf{Y}_{\mathrm{tr}}, \mathbf{X}_{\mathrm{tr}}))\}, \\ &= \underset{q(\boldsymbol{\omega})\in Q}{\arg\max}\{\mathrm{ELBO}(\mathrm{q}(\boldsymbol{\omega}))\}. \end{aligned} \tag{8.9}$$

#### 8.3.1.2 Structural damage detection using a BNN as the inverse surrogate model

Civil structures commonly experience several types of failure modes (e.g., cracking, corrosion, and boundary condition changes) during their lifetime. An FE model and surrogate models may thus be used to map the measured structural response to certain types of damage features in an inverse analysis, as discussed in the earlier parts of this chapter. As shown in Figure 8.8, the output data (e.g., strain measurements) and the input data (i.e., the damage, to be defined below) from a high-fidelity FE model become the input data and output data to train a BNN surrogate model. More specifically, the inputs of the inverse surrogate are $\mathbf{y}_{o,1:T}$ and the output is the damage parameter vector $\boldsymbol{\theta}$. Once the

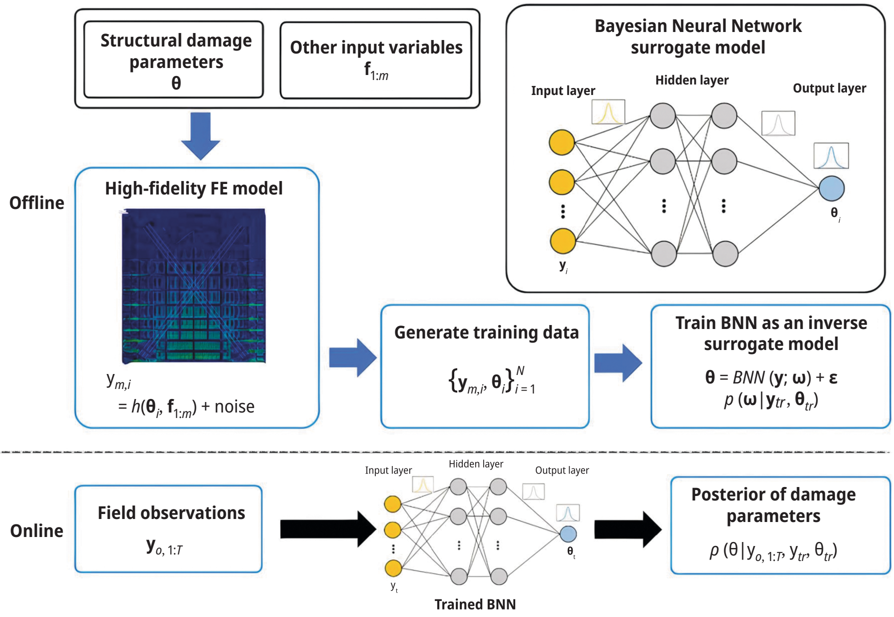

**Figure 8.8:** Damage detection and decision flow using BNN as an inverse surrogate.

BNN surrogate model is trained, the severity of the damage feature can be predicted by the model based on the newly observed strain data. Such probabilistic distribution of the prediction enables the process of fast probabilistic damage detection for risk-informed decision-making.

### 8.3.2 Conditional invertible neural networks for probabilistic damage detection

If $\mathbf{y}_m = G(\boldsymbol{\theta}, \mathbf{f}_{1:m})$ is not invertible, the above-presented BNN will be inapplicable due to the ill-posedness of the inverse problem. This section introduces the second type of inverse surrogate based on the cINN and normalizing flow. In what follows, normalizing flows are first briefly introduced and later, the inverse surrogate is presented in detail.

#### 8.3.2.1 Normalizing flows

Normalizing flows is the mapping between a complex distribution and a known and easy-to-sample probability distribution (e.g., normal distribution). The mapping between the two distributions is invertible and differential. Assume that one has random variables $\boldsymbol{\theta} \in \mathbb{R}^N$, with complex and irregular PDF $p_\theta(\cdot): \mathbb{R}^N \to \mathbb{R}$, and $\mathbf{Z} \in \mathbb{R}^N$ is a multivariate Gaussian distribution, with PDF $p_\mathbf{Z}(\mathbf{z}) \in \mathbb{R}$. Figure 8.9 shows the two types of mapping in normalizing flow, namely generative direction and normalizing direction.

Generative direction uses an invertible function to realize the forward movement where a base distribution is transformed into a target complex distribution. Specifically, $\mathbf{z}$ is first sampled from the base distribution $p_\mathbf{Z}(\mathbf{z})$ and a generator $\boldsymbol{\theta} = r(\mathbf{z})$ is applied, where $\mathbf{r}(\cdot)$ is an invertible function, to obtain samples of $\boldsymbol{\theta}$. On the other hand, normalizing direction makes flow in the opposite direction: from a complex and irregular PDF to a more regular and normal distribution. Let $\mathbf{k}(\cdot) = \mathbf{r}^{-1}(\cdot)$ be the inverse of $\mathbf{r}(\cdot)$ such that $\mathbf{z} = \mathbf{r}^{-1}(\boldsymbol{\theta}) = \mathbf{k}(\boldsymbol{\theta})$, $\mathbf{k}(\cdot)$ maps the complex and irregular distribution of $\boldsymbol{\theta}$ to a multivariate Gaussian distribution [63]. Under this condition and adopting the Jacobian matrix, a PDF can be computed through another PDF as follows [63]:

$$p_{\boldsymbol{\theta}}(\boldsymbol{\theta}) = p_\mathbf{z}(\mathbf{z}) \left| \det\left( \frac{\partial \mathbf{k}(\boldsymbol{\theta})}{\partial \boldsymbol{\theta}} \right) \right| = p_\mathbf{z}(\mathbf{z}) \left| \det\left( \frac{\partial \mathbf{r}(\mathbf{k}(\boldsymbol{\theta}))}{\partial \mathbf{z}} \right) \right|^{-1}, \tag{8.10}$$

where $\frac{\partial \mathbf{k}(\boldsymbol{\theta})}{\partial \boldsymbol{\theta}}$ is the Jacobian of $\mathbf{k}$, and $\frac{\partial \mathbf{r}(\mathbf{k}(\boldsymbol{\theta}))}{\partial \mathbf{z}}$ is the Jacobian of $\mathbf{r}$. Equation (8.10) implies that the expected distribution $p_{\boldsymbol{\theta}}(\boldsymbol{\theta})$ can be estimated by performing a push forward of $p_\mathbf{z}(\mathbf{z})$ through $\mathbf{r}(\cdot)$.

There are several aspects that need to be emphasized in normalizing flows. First, the transformation in a normalizing flow strictly requires an invertibility property. Second, the dimensions of inputs and outputs must be the same. In addition, accord-

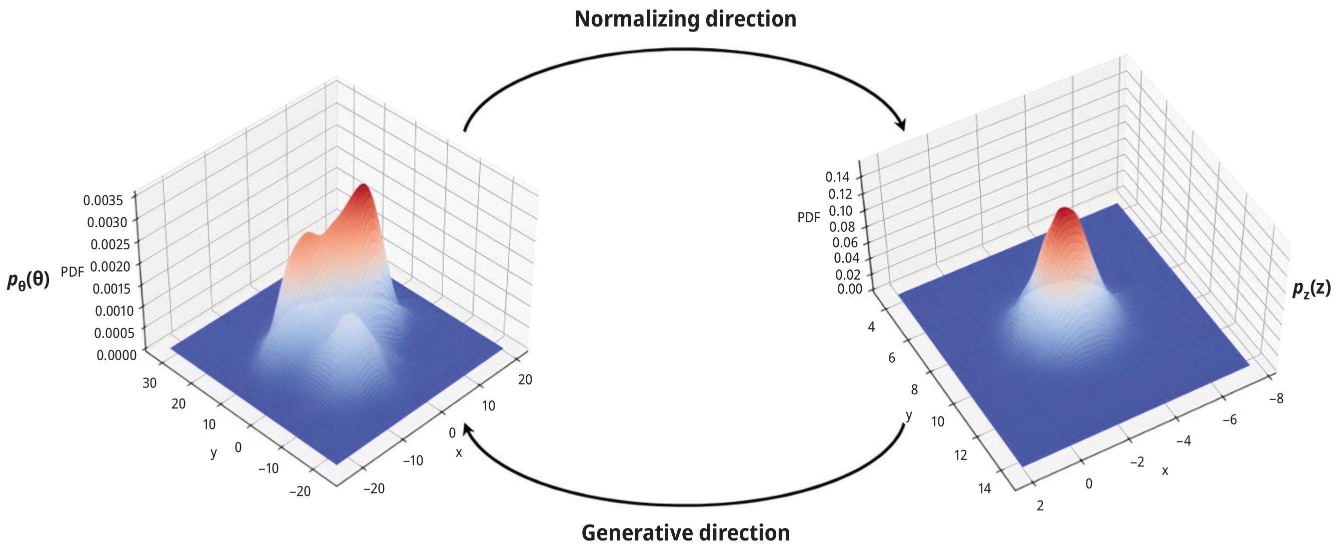

**Figure 8.9:** Illustration of normalizing flow.

ing to eq. (8.10), the computation of the determinant of Jacobian matrix plays a key role in the distribution transformation in a normalizing flow. Therefore, selecting an appropriate flow/transformation structure that has easy-to-compute Jacobian matrix in a normalizing flow is a priority. In particular, $\mathbf{k}(\cdot)$ is constructed, which contains a set of $M$ bijective functions: $\mathbf{k}(\cdot) = \mathbf{k}_1(\cdot) \circ \cdots \circ \mathbf{k}_{M-1}(\cdot) \circ \mathbf{k}_M(\cdot)$ is the composition of functions, and $\mathbf{r}_j(\cdot) = \mathbf{k}_j^{-1}(\cdot)$, $j = 1, \cdots, M$ exists. It can be shown that the resulting $\mathbf{r}(\cdot) = \mathbf{r}_1(\cdot) \circ \cdots \circ \mathbf{r}_{M-1}(\cdot) \circ \mathbf{r}_M(\cdot)$ is also bijective. However, in practice, it is difficult to create the nonlinear and complicated transformation satisfying the abovementioned requirements [64]. Considerable effort has gone in to develop a proper flow structure. Dinh et al. [65] proposed the use of a sequence of invertible bijective functions so that the resulting composition is still invertible and the determinant of the Jacobian becomes a specific form, which makes its calculation computationally efficient. In this chapter, the cINN, with a stack of affine coupling layers (ACL), is used as invertible functions to achieve bijective transformation.

#### 8.3.2.2 Conditional invertible neural network

The architecture of cINN is constructed by stacking multiple conditional affine coupling layers (cACLs). cACL is an extended ACL that was proposed by Dinh et al. [65] and applied to an invertible mapping between inputs and outputs. The difference between ACL and cACL is conditional inputs, for example, observations, are put aside/added to the original ACL building blocks.

Figures 8.10 and 8.11 illustrate the workflow of a cINN architecture for forward transformation and inverse transformation, respectively. For forward transformation, shown in Figure 8.10, each cACL incorporates two scale functions, denoted as $u_1(\cdot)$, $u_2(\cdot)$, and two translation functions, denoted as $v_1(\cdot)$, $v_2(\cdot)$. These four internal functions could be modeled as any arbitrary neural networks trained in the forward path. The layer splits the input and output vector $\boldsymbol{\theta}$ and $\mathbf{z}$ into two halves $\boldsymbol{\theta} = (\boldsymbol{\theta}_1, \boldsymbol{\theta}_2)$ and $\mathbf{z} = (\mathbf{z}_1, \mathbf{z}_2)$, respectively. Taking the observation $\mathbf{y}_o$ as an additional conditioning input, the forward transformation is realized as follows [65]:

$$\mathbf{z}_1 = \boldsymbol{\theta}_1 \odot \exp(u_2(\boldsymbol{\theta}_2, \mathbf{y}_0)) + v_2(\boldsymbol{\theta}_2, \mathbf{y}_0), \tag{8.11}$$

$$\mathbf{z}_2 = \boldsymbol{\theta}_2 \odot \exp(u_1(\mathbf{z}_1, \mathbf{y}_0)) + v_1(\mathbf{z}_1, \mathbf{y}_0), \tag{8.12}$$

where $\odot$ is the element-wise multiplication.

The forward transformation can be easily inverted. With $\mathbf{z} = (\mathbf{z}_1, \mathbf{z}_2)$ inversely passing through the cACL, the inverse transformation based on the workflow in Figure 8.11 is given as [65]

$$\boldsymbol{\theta}_1 = (\mathbf{z}_1 - v_2(\boldsymbol{\theta}_2, \mathbf{y}_0)) \odot \exp(-u_2(\boldsymbol{\theta}_2, \mathbf{y}_0)), \tag{8.13}$$

$$\boldsymbol{\theta}_2 = (\mathbf{z}_2 - v_1(\mathbf{z}_1, \mathbf{y}_0)) \odot \exp(-u_1(\mathbf{z}_1, \mathbf{y}_0)), \tag{8.14}$$

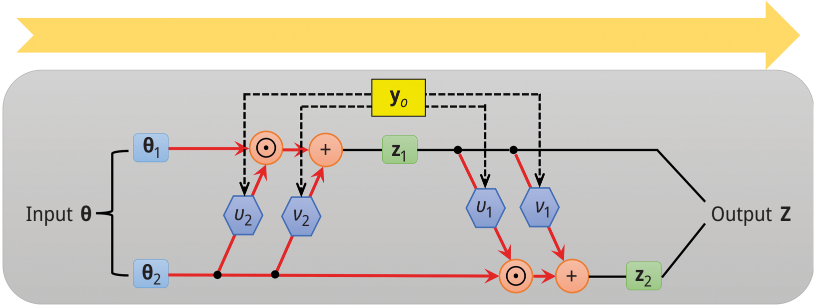

**Figure 8.10:** The forward transformation in cACL.

Equations (8.11)–(8.14) make the determinant of Jacobian in eq. (8.10) easy to evaluate due to the simple mathematical expression of Jacobian in cACL (upper or lower triangle matrix). Then, through the invertible transformation and eq. (8.10), a simple distribution $p_{\mathbf{z}}(\mathbf{z})$, such as the standard Gaussian distribution, may be transformed to a complex distribution $p_{\boldsymbol{\theta}}(\boldsymbol{\theta})$.

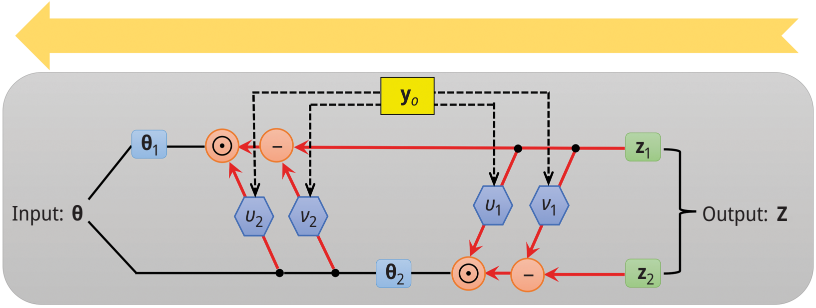

**Figure 8.11:** The inverse transformation in cACL.

Finally, by sequentially stacking multiple cACLs, a neural network is established allowing for a non-linear bijective mapping between a complex distribution $p_{\boldsymbol{\theta}}(\boldsymbol{\theta}|\mathbf{y}_o)$ and a multivariate Gaussian distribution $f_{\mathbf{Z}}(\mathbf{z})$ according to the normalizing flow theory described in Sec. 8.3.2.1. The resulting network is the so-called a cINN [66]. In the entire cINN, all cACL are sequentially connected in such a way that the output of each cACL serves as the input to the next one. Regarding the parameter inference, the starting inputs and ultimate outputs are respectively specified as parameters of interest $\boldsymbol{\theta}$ and the latent variable $\mathbf{z}$. In summary, mappings between $p_{\boldsymbol{\theta}}(\boldsymbol{\theta}|\mathbf{y}_o)$ and a multivariate Gaussian PDF $p_{\mathbf{Z}}(\mathbf{z})$ in the cINN may be realized using an invertible function $\mathbf{z} = \mathbf{k}_{\boldsymbol{\omega}}(\boldsymbol{\theta}; \mathbf{y}_o)$ with hyper-parameters $\boldsymbol{\omega}$ for normalizing direction transformation, and its inverse function $\boldsymbol{\theta} = \mathbf{k}_{\boldsymbol{\omega}}^{-1}(\mathbf{z}; \mathbf{y}_o)$ for generative direction transformation.

### 8.3.2.3 Structural damage detection using cINN and normalizing flows

**(a) Training of cINN as an inverse surrogate for posterior estimation**

Building upon normalizing flow and the cINN described above, the goal is to approximate the posterior distribution $p_{\boldsymbol{\theta}}(\boldsymbol{\theta}|\mathbf{y}_{1:T})$ of $\boldsymbol{\theta}$ for any given observations $\mathbf{y}_{1:T}$ using cINN, where $\mathbf{y}_{1:T} = (\mathbf{y}_1, \mathbf{y}_2, \cdots, \mathbf{y}_T)$ and $\mathbf{y}_i$, $\forall i = 1, \cdots, T$ is the $i$th vector of observations. $p_{\boldsymbol{\theta}}(\boldsymbol{\theta}|\mathbf{y}_{1:T})$ can be expressed in terms of $\mathbf{k}_{\boldsymbol{\omega}}$ in a cINN:

$$\boldsymbol{\theta} \sim p_{\boldsymbol{\theta}}(\boldsymbol{\theta}|\mathbf{y}_{1:T}) \Leftrightarrow \boldsymbol{\theta} = \mathbf{k}_{\omega}^{-1}(\mathbf{z}, \mathbf{y}_{1:T}), \tag{8.15}$$

where $\mathbf{z}$ are latent variables following standard distribution $\mathbf{z} \sim N(\mathbf{z}|\mathbf{0},\Pi)$. The transformation in eq. (8.15) is performed through a cINN.

As a machine learning inverse surrogate, identifying the optimal hyperparameters $\hat{\boldsymbol{\omega}}$ is of paramount importance. The optimal hyperparameters of cINN are identified by minimizing the KL divergence between the target and the approximate posterior-given observations $\mathbf{y}_{1:T}$ as follows [66]:

$$\begin{aligned}
\hat{\boldsymbol{\omega}} &= \arg\min_{\boldsymbol{\omega}} \mathrm{E}_{p_{\mathbf{Y}_{1:T}}(\mathbf{y}_{1:T})}\left[\mathrm{KL}\left[p_{\boldsymbol{\theta}}(\boldsymbol{\theta}|\mathbf{y}_{1:T})\|\tilde{p}_{\boldsymbol{\theta},\boldsymbol{\omega}}(\boldsymbol{\theta}|\mathbf{y}_{1:T})\right]\right],\\
&= \arg\min_{\boldsymbol{\omega}} \mathrm{E}_{p_{\mathbf{Y}}(\mathbf{y}_{1:T})}\left[\mathrm{E}_{p_{\boldsymbol{\theta}|\mathbf{Y}}(\boldsymbol{\theta}|\mathbf{y}_{1:T})}\left[\log\{p_{\boldsymbol{\theta}}(\boldsymbol{\theta}|\mathbf{y}_{1:T})\} - \log\{\tilde{p}_{\boldsymbol{\theta},\boldsymbol{\omega}}(\boldsymbol{\theta}|\mathbf{y}_{1:T})\}\right]\right],\\
&= \arg\max_{\boldsymbol{\omega}} \mathrm{E}_{p_{\mathbf{Y}}(\mathbf{y}_{1:T})}\left[\mathrm{E}_{p_{\boldsymbol{\theta}|\mathbf{Y}}(\boldsymbol{\theta}|\mathbf{y}_{1:T})}\left[\log\{\tilde{p}_{\boldsymbol{\theta},\boldsymbol{\omega}}(\boldsymbol{\theta}|\mathbf{y}_{1:T})\}\right]\right],\\
&= \arg\max_{\boldsymbol{\omega}} \iint p_{\boldsymbol{\theta},\mathbf{Y}}(\mathbf{y}_{1:T}, \boldsymbol{\theta}) \log\{\tilde{p}_{\boldsymbol{\theta},\boldsymbol{\omega}}(\boldsymbol{\theta}|\mathbf{y}_{1:T})\}\mathbf{d}\boldsymbol{\theta}\mathbf{d}\mathbf{y}_{1:T},
\end{aligned} \tag{8.16}$$

where $p_{\mathbf{Y}_{1:T}}(\mathbf{y}_{1:T})$ is the PDF of $\mathbf{y}_{1:T}$, $\mathrm{E}[\cdot]$ is expectation operator, $\tilde{p}_{\boldsymbol{\theta},\boldsymbol{\omega}}(\boldsymbol{\theta}|\mathbf{y}_{1:T})$ is the estimated posterior of $\boldsymbol{\theta}$ for a given $\boldsymbol{\omega}$ of the cINN, and $\mathrm{KL}[\cdot]$ is the KL divergence operator.

According to the fundamental theory of normalizing flow presented in Section 8.3.2.1:

$$\tilde{p}_{\boldsymbol{\theta},\boldsymbol{\omega}}(\boldsymbol{\theta}|\mathbf{y}_{1:T}) = p_{\mathbf{z}}(\mathbf{z} = \mathbf{k}_{\boldsymbol{\omega}}(\boldsymbol{\theta};\, \mathbf{y}_{1:T}))\left|\det\left(\frac{\partial \mathbf{k}_{\boldsymbol{\omega}}(\boldsymbol{\theta};\, \mathbf{y}_{1:T})}{\partial \boldsymbol{\theta}}\right)\right|. \tag{8.17}$$

Hence the optimization model in eq. (8.16) can be rewritten as

$$\hat{\boldsymbol{\omega}} = \arg\max_{\boldsymbol{\omega}} \iint p_{\boldsymbol{\theta},\mathbf{Y}}(\mathbf{y}_{1:T}, \boldsymbol{\theta})\left\{\log\{\tilde{p}_{\boldsymbol{\theta},\boldsymbol{\omega}}(\boldsymbol{\theta}|\mathbf{y}_{1:T})\} + \log\left|\det\left(\frac{\partial \mathbf{k}_{\boldsymbol{\omega}}(\boldsymbol{\theta};\, \mathbf{y}_{1:T})}{\partial \boldsymbol{\theta}}\right)\right|\right\}\mathbf{d}\boldsymbol{\theta}\mathbf{d}\mathbf{y}_{1:T}. \tag{8.18}$$

Assume that there are $N_{MCS}$ sets of synthetic data generated from a forward model as illustrated in Figure 8.6. Equation (8.18) can be approximated using these samples as [66]

$$\hat{\boldsymbol{\omega}} = \arg\max_{\boldsymbol{\omega}} \left\{ \frac{1}{N_{MCS}} \sum_{i=1}^{N_{MCS}} \left( \log p\left(\mathbf{k}_{\boldsymbol{\omega}}(\boldsymbol{\theta}^{(i)}; \mathbf{y}_{1:T}^{(i)})\right) + \log \left| \det\left( \left.\frac{\partial \mathbf{k}_{\boldsymbol{\omega}}(\boldsymbol{\theta}; \mathbf{y}_{1:T})}{\partial \boldsymbol{\theta}}\right|_{\boldsymbol{\theta}^{(i)}, \mathbf{y}_{1:T}^{(i)}} \right) \right| \right) \right\}, \tag{8.19}$$

where $N_{MCS}$ is the number of MCS samples, $\boldsymbol{\theta}^{(i)}$ is the $i$th MCS sample of $\boldsymbol{\theta}$, and $\mathbf{y}_{1:T}^{(i)}|\boldsymbol{\theta}^{(i)}$ is the synthetic observation generated using a forward model with inputs of $\boldsymbol{\theta}^{(i)}$.

Taking the negative of eq. (8.19) and recalling the latent variables $\mathbf{z}$ are defined as a standard Gaussian distribution so that $p_{\mathbf{z}}(\mathbf{z} = \mathbf{k}_{\boldsymbol{\omega}}(\boldsymbol{\theta}; \mathbf{y}_{1:T})) = \frac{1}{\sqrt{2\pi}} \exp\left\{ -\frac{1}{2} [\mathbf{k}_{\boldsymbol{\omega}}(\boldsymbol{\theta}; \mathbf{y}_{1:T})]^2 \right\}$, the optimization model for training cINN is rewritten as

$$\hat{\boldsymbol{\omega}} = \arg\min_{\boldsymbol{\omega}} J(\boldsymbol{\omega}), \tag{8.20}$$

with

$$J(\boldsymbol{\omega}) = \frac{1}{N_{MCS}} \sum_{i=1}^{N_{MCS}} \left( \frac{1}{2} \left[ \mathbf{k}_{\boldsymbol{\omega}}(\boldsymbol{\theta}^{(i)}; \mathbf{y}_{1:T}^{(i)}) \right]^2 - \log \left| \det\left( \left.\frac{\partial \mathbf{k}_{\boldsymbol{\omega}}(\boldsymbol{\theta}; \mathbf{y}_{1:T})}{\partial \boldsymbol{\theta}}\right|_{\boldsymbol{\theta}^{(i)}, \mathbf{y}_{1:T}^{(i)}} \right) \right| \right), \tag{8.21}$$

where $J(\boldsymbol{\omega})$ is treated as a loss function for the posterior estimate, which can be solved by any stochastic gradient descent methods.

### (b) Structural damage detection using cINN

Since monitoring data in SHM are usually in the format of time series, images, or video, an additional neural network can be used in conjunction with the cINN for damage detection. Such a framework has been proposed by Radev et al. [67] and is named as BayesFlow. This additional neural network is essentially a preprocessing step for the simulated or measured data, prior to the cINN, for damage detection. In BayesFlow, this neural network is called a summary network. Through the addition of a summary network, measured raw data (i.e., $\mathbf{y}_{1:T}$) is summarized or filtered to a fixed-size and low-dimensional length, which will be used as inputs to cINN for damage detection using the Bayesian model updating method. The summary network allows to automatically learn the maximally informative statistics directly from the measured data rather than the traditional handcrafted features. The choice of the summary network depends on the properties of the measured data. For example. a bidirectional long short-term memory (LSTM) [68], as a summary network, is well tailored to time-series data, as LSTM network typically enables to naturally manipulate the sequential measurement with long-memory and nonlinear features. Another preference of summary network may be a 1D fully connected convolutional neural network (CNN), which has been adopted to learn summary statistics of temporal responses for Bayesian inference [69].

After accounting for the summary network, the flowchart of probabilistic damage detection using inverse surrogates given in Figure 8.6 is revised as shown in Figure 8.12.

Mathematically, a summary network can be expressed as

$$\tilde{\mathbf{y}} = \lambda_{\boldsymbol{\gamma}}(\mathbf{y}_{1:T}), \tag{8.22}$$

where $\lambda_{\boldsymbol{\gamma}}(\cdot)$ is the summary network with parameter $\boldsymbol{\gamma}$, and $\tilde{\mathbf{y}}$ is the summarized feature from the network that will be used as $\mathbf{y}_0$ in the inference network (i.e., cINN).

To ensure the performance of damage detection, the cINN and summary network need to be trained together. The hyperparameters $\boldsymbol{\omega}$ and $\boldsymbol{\gamma}$ of the two neural networks (i.e., cINN and summary network) are estimated by minimizing the expected KL divergence, similar to eq. (8.16). The optimization model given in eq. (8.20) can be revised accordingly as follows [67]:

$$\hat{\boldsymbol{\gamma}}, \hat{\boldsymbol{\omega}} = \underset{\boldsymbol{\gamma},\boldsymbol{\omega}}{\arg\min}\, J(\boldsymbol{\gamma},\boldsymbol{\omega}), \tag{8.23}$$

where

$$J(\boldsymbol{\gamma},\boldsymbol{\omega}) = \frac{1}{N_{MCS}}\sum_{i=1}^{N_{MCS}}\left(\frac{1}{2}\left[\mathbf{k}_{\boldsymbol{\omega}}\left(\boldsymbol{\theta}^{(i)};\lambda_{\boldsymbol{\gamma}}\left(\mathbf{y}_{1:T}^{(i)}|\boldsymbol{\theta}^{(i)}\right)\right)\right]^2 - \log\left|\det\left(\frac{\partial \mathbf{k}_{\boldsymbol{\omega}}\left(\boldsymbol{\theta};\lambda_{\boldsymbol{\gamma}}\left(\mathbf{y}_{1:T}^{(i)}|\boldsymbol{\theta}^{(i)}\right)\right)}{\partial\boldsymbol{\theta}}\bigg|_{\boldsymbol{\theta}^{(i)},\mathbf{y}_{1:T}^{(i)}}\right)\right|\right). \tag{8.24}$$

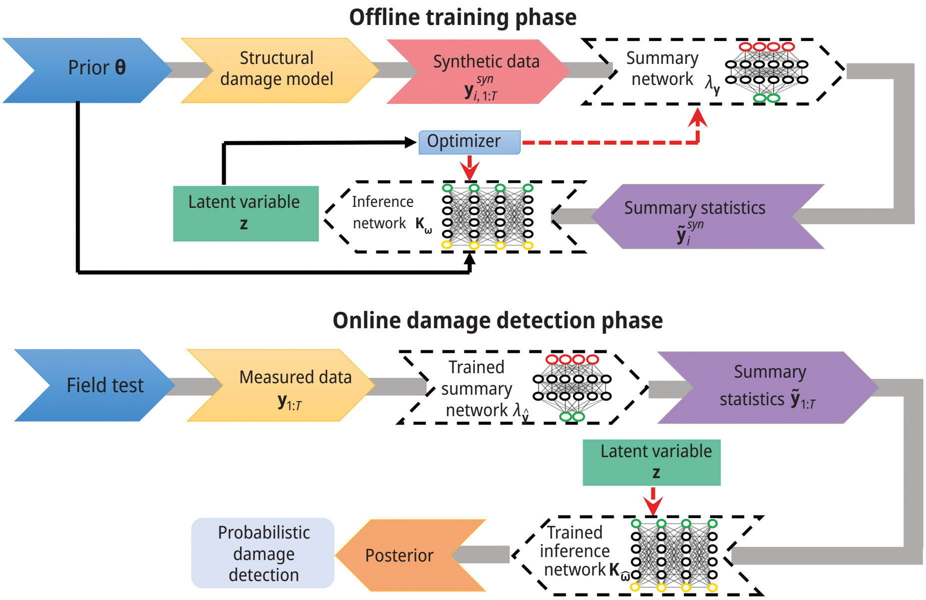

**Figure 8.12:** Probabilistic damage detection using a summary network and an cINN.

After the estimation of the parameters, $\hat{\boldsymbol{\gamma}}, \hat{\boldsymbol{\omega}}$, the posterior distribution $p_{\boldsymbol{\theta}}(\boldsymbol{\theta}|\mathbf{y}_{1:T})$ may be efficiently approximated for a given $\mathbf{y}_{1:T}$ using the inverse surrogate.

The above presented inverse surrogate process, including variational BNN and cINN, can achieve the amortized inference. Although a relatively expensive computational cost is needed during the training, it may be executed offline. After the training, the trained networks can efficiently estimate the posterior of the damage parameters for any given new observed data within a few seconds. Next, two case studies will be used to demonstrate the presented inverse surrogates in this chapter.

# 8.4 Case studies

## 8.4.1 Case study 1: damage detection of a miter gate

### 8.4.1.1 Modeling of miter gate failure

Miter gates play an important role in inland waterway systems by helping cargo ships navigate different water elevations [70]. The aging of these steel structures is manifested by multiple forms of damage. Among them, the most concerned damage is the quoin block damage, leading to the contact loss between the quoin block and the lock wall, as shown in Figure 8.13. A “gap” is referred to as the severity of such a contact loss.

**Figure 8.13:** Quoin block damage (gap).

An FE model for a miter gate was constructed using Abaqus 2020 as shown in Figure 8.14. The model has been previously validated with field data to provide accurate physics, which is employed in this paper to predict the strain responses of the gate [71, 72]. As indicated in Figure 8.14, the “gap length” (i.e., quoin block contact loss) is modeled by not fixing the full length of the contacting boundary conditions along a certain length.

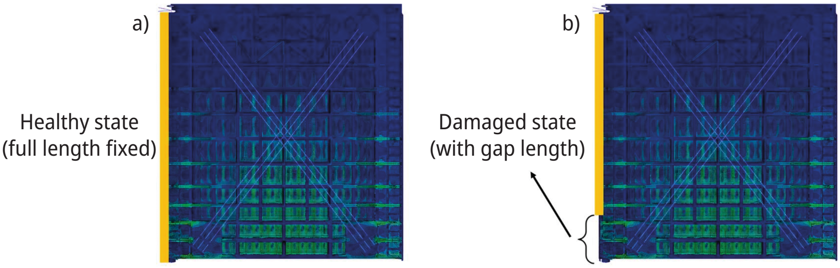

**Figure 8.14:** Quoin block damage (gap length) simulation using the FE model.

### 8.4.1.2 BNN surrogate modeling and damage detection

The BNN surrogate model used in this section contains two layers, with 50 neurons in its hidden layer, to learn the mapping between the strain measurement and the gap length. For training and testing data, 3,000 data points were obtained using the ABAQUS FE model by varying the value of the damage parameter (i.e., gap) for training and testing purposes. Among the 3,000 data points, 2,000 of them are used for training and the remaining are for testing. During training, synthetic measurements are used as input, and the gap length is used as output by following the procedure described in Section 8.3.1.

After the training of the BNN as an inverse surrogate model, it is employed to directly map strain measurements to probabilistic damage parameter (i.e., gap length). Figure 8.15 shows the sensor readings from 4 randomly selected sensors deployed on the miter gate. The sensor readings are obtained by adding noise to the synthetic sensor measurements.

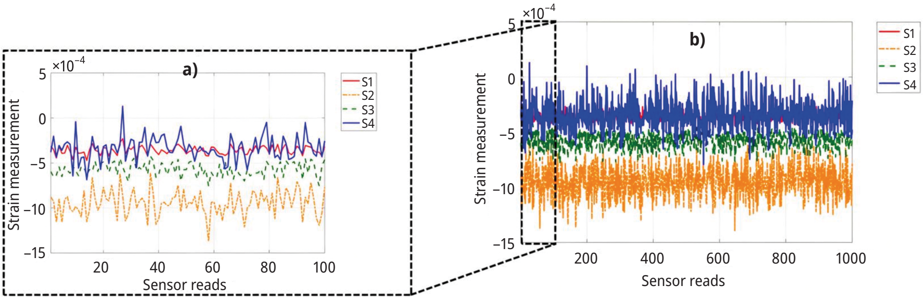

**Figure 8.15:** An example of sensor reads from four randomly selected strain gauges: (a) first 100 reads and (b) first 1,000 reads.

Figure 8.16 shows the predicted posterior distribution of the gap length over 1,000 time steps. As shown in Figure 8.16(b), the mean prediction and the 95% confidence intervals suggest that the BNN model can accurately predict the damage state (i.e., the gap length) with high confidence for given strain measurements.

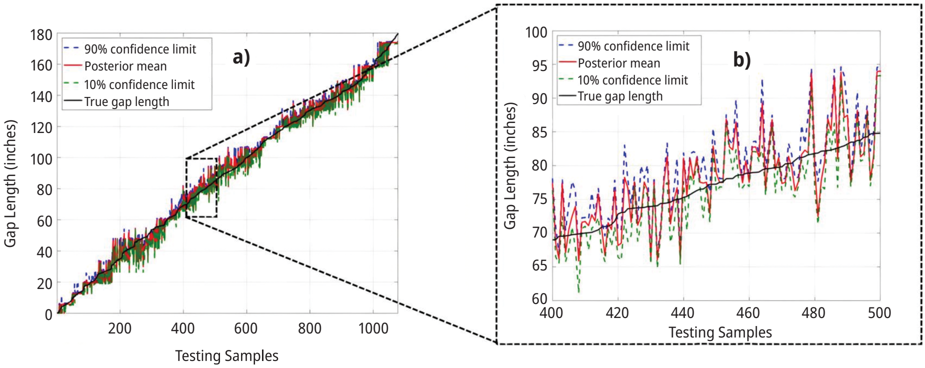

**Figure 8.16:** Damage detection results: (a) posterior distribution of the gap length over 1,078 time steps and (b) posterior distribution of gap length using the selected 100 time steps.

Figure 8.17 depicts the comparison of the posterior distributions obtained from BNN and the true gap length for four different time instants. As shown in this figure, the mean of the posterior distribution is very close to the true gap length. This demonstrates the effectiveness of using BNN as an inverse surrogate model for fast probabilistic damage detection.

## 8.4.2 Case study 2: a concrete building frame

### 8.4.2.1 Modeling of damage in a concrete building frame

A concrete building frame, a full-scale test structure in Structural Engineering and Materials Laboratory on Georgia Tech Campus [64, 73], is used to verify the capability of cINN (i.e., the second type of inverse surrogate model described in Sec. 8.3.2) for damage detection. Four identical frame components, denoted as #1 ~ #4 in Figure 8.18. (a), and another two frames at the outermost and innermost for collapse prevention are assembled to form the entire building frame. Due to the separated distribution among all frames and a clear space between every two components, each frame component can be modeled and analyzed independently. In this case study, structural damage detection for the frame component #1 is implemented to demonstrate the capability of the presented inverse surrogate. Figure 8.18 (a) shows the front, elevation, and side view of frame #1.

Figure 8.18 (b) shows the FE model of frame #1 in which 2,302 DOFs are considered, and a diagonal mass matrix is designed with zero element in the rotational direction [74]. In the concrete building, a total of six stiffness parameters, representing the change in elastic modulus, are selected to be updated, denoted as $\theta_1 \sim \theta_6$, as shown in Figure 8.18 (b), where $\theta_1 \sim \theta_4$, respectively, are assigned to reflect the change between the nominal and the actual elastic modulus of the longitudinal beam members ($x$ direc-

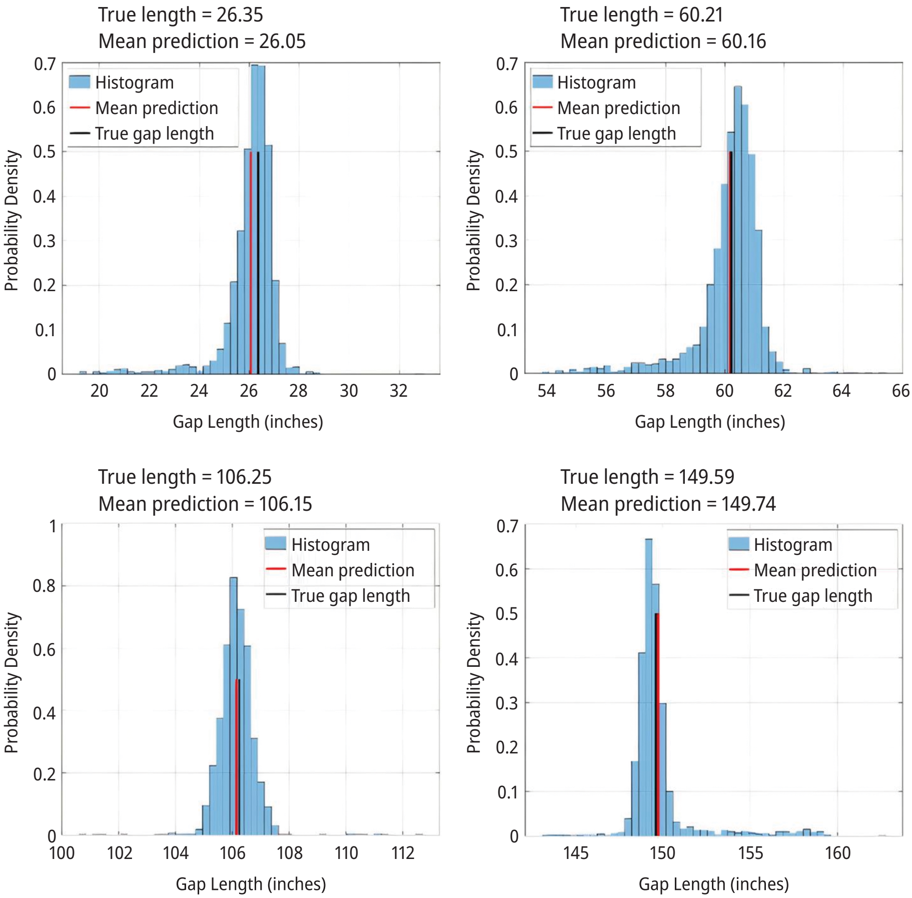

**Figure 8.17:** Comparison of posterior distribution history and the true gap length for four different cases.

tion) at the first and second floors. Similarly, $\theta_5 \sim \theta_6$, respectively, are assigned to reflect changes in the elastic modulus for both the slab and the lateral beam members (y direction) at the first and second slabs. In addition, suppose that a vibration test is performed under ambient vibration so that the input excitation is not known but is modeled as Gaussian white noise with power spectral density of 3 $\mathrm{N}/\sqrt{\mathrm{Hz}}$. Figure 8.18 (b) shows the deployment of accelerometers at the two slabs; only vibration responses on the vertical and longitudinal directions ($z$ and $x$ directions) are measured. Since the number of sensors is limited and the measured data are always incomplete in practice, only acceleration data at 26 DOFs are measured. Regarding data configuration, 4-min acceleration responses are measured with a sampling frequency of 100 Hz. To mimic the measurement noise, the Gaussian white noise of 5% root-mean-square (RMS) noise-signal-ratio (NSR) is added to all measured data. Figure 8.19 shows the example of two measured acceleration responses.

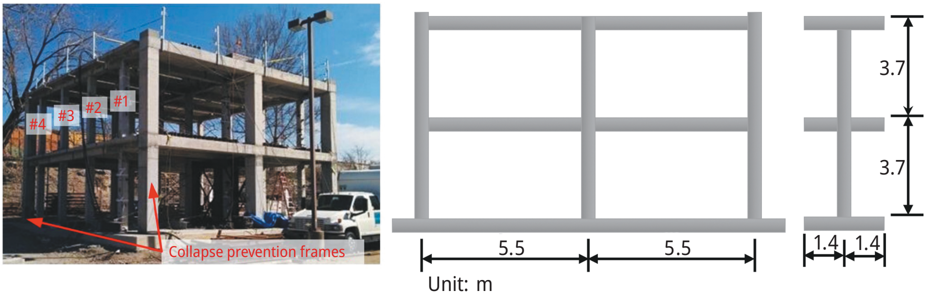

(a) View of the structure

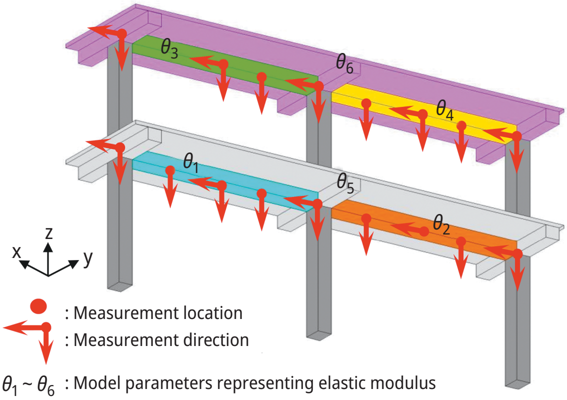

(b) Model of frame #1

**Figure 8.18:** Concrete building frame.

#### 8.4.2.2 Structural damage detection using cINN as an inverse surrogate

A total of 800 sets of training samples with respect to six stiffness parameters are generated from uniform distribution $U \sim (-0.3, 0.3)$, using Latin hypercube sampling. Based on the samples, 800 sets of acceleration responses are generated using the FE model. An extra 100 sets of data are generated for model validation. The summary network and cINN described in Section 3.2 are jointly trained. Ten independent cACLs are stacked to build the architecture of cINN. Forty epochs with 200 iterations each are adopted to train the neural networks using the simulated acceleration data. After the training and validation of the summary network and cINN, damage detection can be performed. In this example, one damage scenario with multiple damage locations is intentionally created, as listed in Table 8.1. Suppose the initial FE model is in an intact state. The negative sign in Table 8.1 denotes stiffness reduction. For instance, $\theta_1 = \frac{E_1^d - E_1^{ud}}{E_1^{ud}} = -10\%$ represents stiffness reduction of 10% in the elastic modulus of the longitudinal beam members at the first floor, where $E_1^d$ and $E_1^{ud}$, respectively, are the damaged and undamaged elastic modulus.

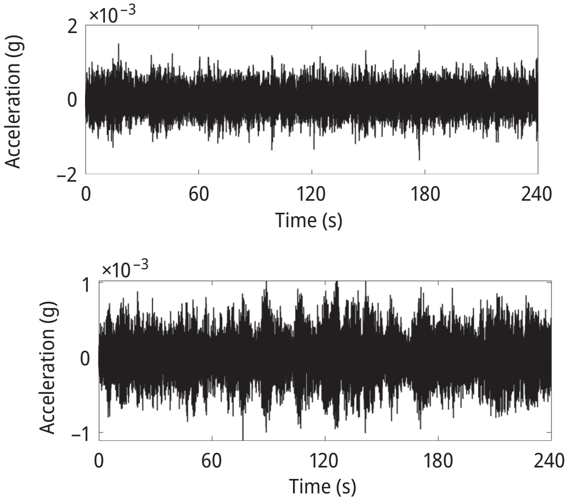

**Figure 8.19:** An example of measured acceleration for 4 min.

**Table 8.1:** Damage location and severity of concrete building.

| Damage scenario | Damage location (damage severity) |
|---|---|
| 1 | $\theta_1$ (−10%), $\theta_3$ (−20%), $\theta_4$ (−10%), $\theta_5$ (−20%) |

Ten sets of vibration responses at 26 DOFs under damaged condition are measured with 4-min duration. The performance of inverse surrogate on damage detection is also compared with an advanced sampling-based method called, DREAM [47]. When applying DREAM for damage detection, acceleration data have to be converted into frequency-domain data, such as modal data, for example, natural frequencies and mode shapes, due to the assumption of ambient vibration and unmeasured excitation. Herein, the first eight modes, identified from the same measured accelerations in the damaged condition, are used in DREAM. A total of 20,000 samples are generated to estimate the posteriors.

Figure 8.20 shows the results of damage detection by BayesFlow (i.e., the inverse surrogate with a summary network and a cINN) and DREAM. The inverse surrogate (i.e., BayesFlow) shows outstanding performance in detecting structural damage across different datasets, while the number of data sets significantly affects the performance of DREAM. For example, in the case of one data set, it is seen in Figure 8.20(a) that the posterior estimates from DREAM show inferior accuracy compared to BayesFlow, such as maxima far away from the true values (e.g., $\theta_1 \sim \theta_2$) and having very flat shapes (e.g.,

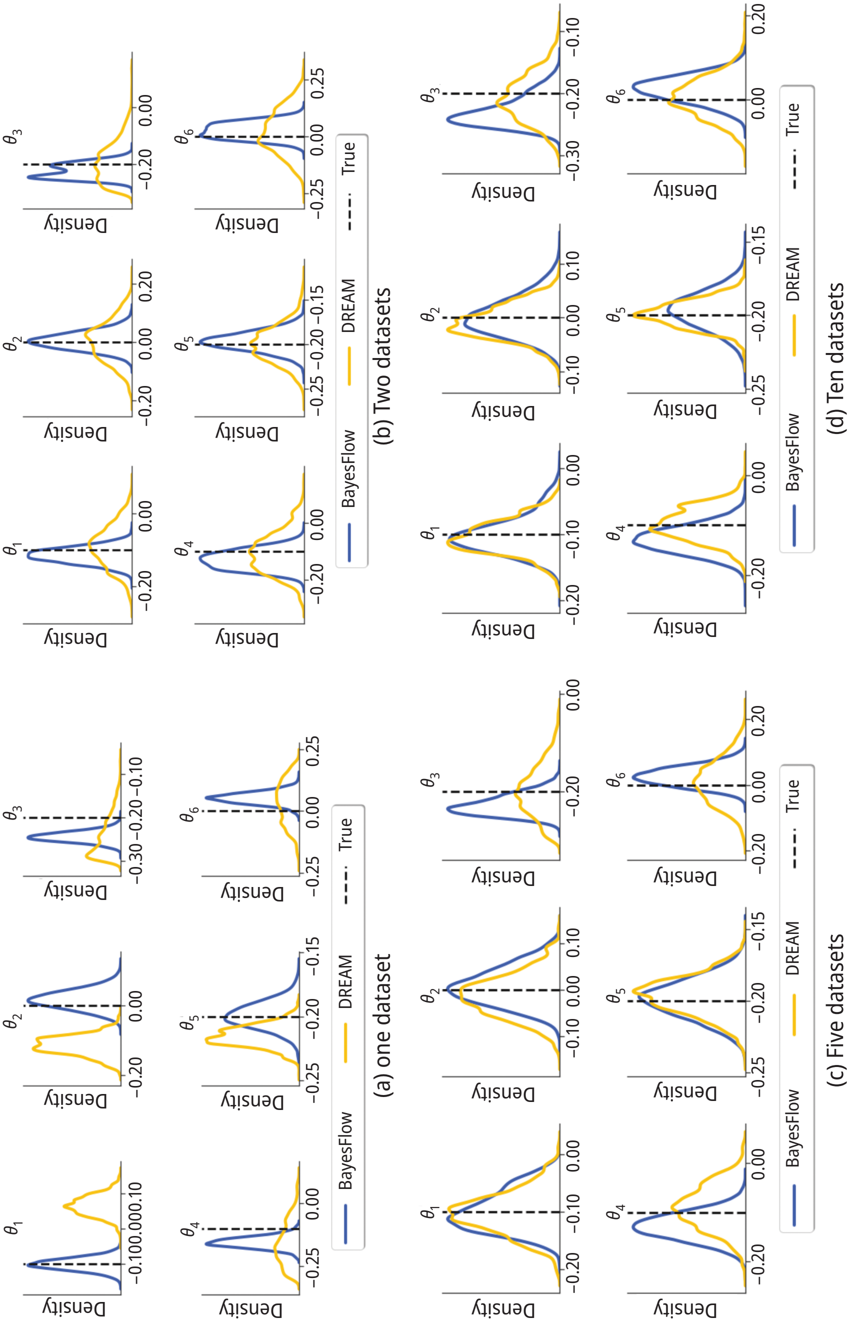

(a) one dataset

(b) Two datasets

(c) Five datasets

(d) Ten datasets

**Figure 8.20:** Posterior distributions from inverse surrogate (i.e., BayesFlow) and DREAM for different numbers of datasets.

$\theta_1, \theta_2, \theta_6$). In one given dataset, DREAM gives complete false damage state estimation, while the inverse surrogate (i.e., BayesFlow) still accurately estimates the posteriors for all parameters. With the amount of data increasing in Figures 8.20(b)–(d), the accuracy of damage detection using DREAM tends to be increased noticeably. However, all posterior densities from DREAM in Figure 8.20(b) distribute over a relatively wider region, but the posterior shapes from the inverse surrogate (i.e., BayesFlow) have smaller dispersion. With more data available, the approximate posteriors from the two methods become similar, as illustrated in Figure 8.20 (c) and (d).

Figures 8.21–8.24 show the results of the identified damage severity and the associated uncertainties. As seen in Figure 8.21, where only single data set is available, BayesFlow identifies stiffness reduction with good accuracy while DREAM falsely detects the damage severity in terms of $\theta_2$. In addition, although the stiffness reduction for $\theta_3 \sim \theta_5$ identified by two methods is similar, the associated uncertainties from DREAM are much larger than that from BayesFlow, indicating less reliability using DREAM.

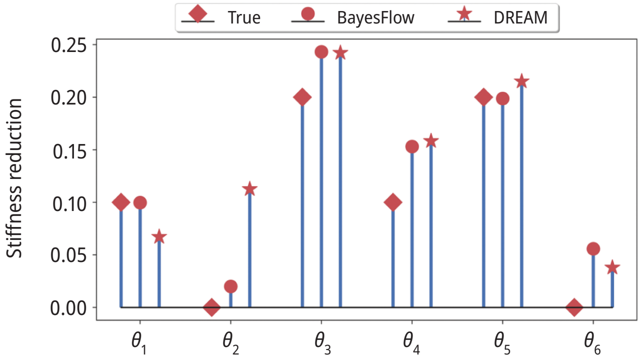

(a) Damage severity

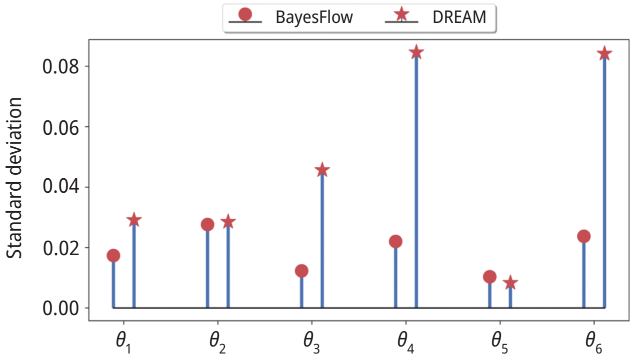

(b) Damage uncertainty

**Figure 8.21:** Damage identification by one datasets on concrete building.

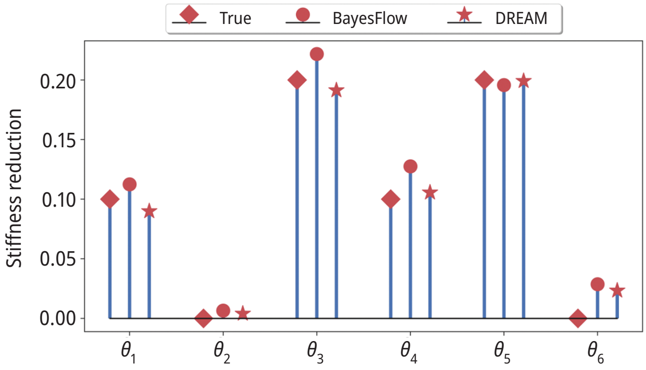

(a) Damage severity

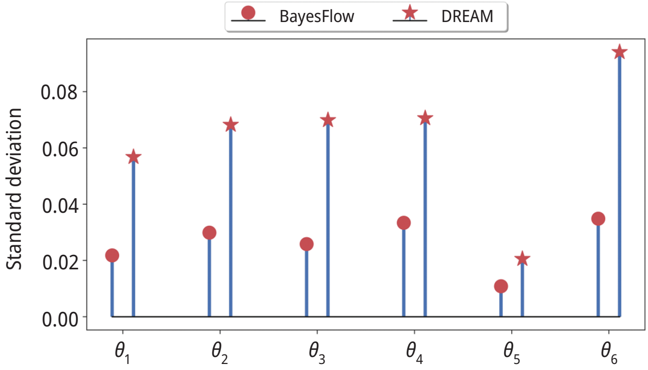

(b) Damage uncertainty

**Figure 8.22:** Damage identification by two datasets on concrete building.

As shown in Figures 8.22–8.24, with the number of datasets increasing, the damage severity identified by BayesFlow and DREAM get closer to the ground truth. However, the identified damage uncertainties, characterized by the standard deviation using BayesFlow, are significantly lower than those from DREAM. It probably can be explained that the use of modal data in DREAM inevitably induces errors, which may result in additional uncertainty on parameter estimation. The results again confirm that the inverse surrogate model (i.e., BayesFlow) performs better than DREAM on probabilistic damage detection in two aspects: (1) Inverse surrogate has a stable and robust performance on damage detection, given different data information; (2) Inverse surrogate identifies damage severity with low uncertainty, indicating reliability on damage detection.

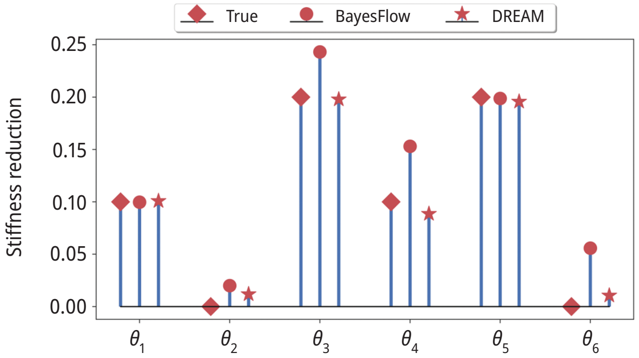

(a) Damage severity

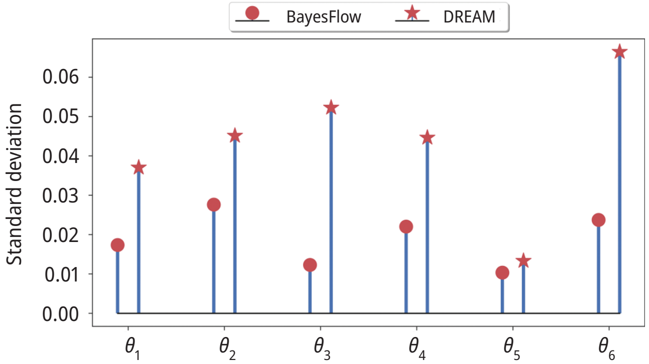

(b) Damage uncertainty

**Figure 8.23:** Damage identification by five datasets on concrete building.

Table 8.2 summaries the computational cost using the inverse surrogate and DREAM for damage detection, given ten datasets. It is noted that the inverse surrogate (i.e., BayesFlow) takes around 25 h for training. After training, it takes 7 s to perform damage detection on ten datasets. On the contrary, DREAM takes about 3.2 h to complete the task of damage detection.

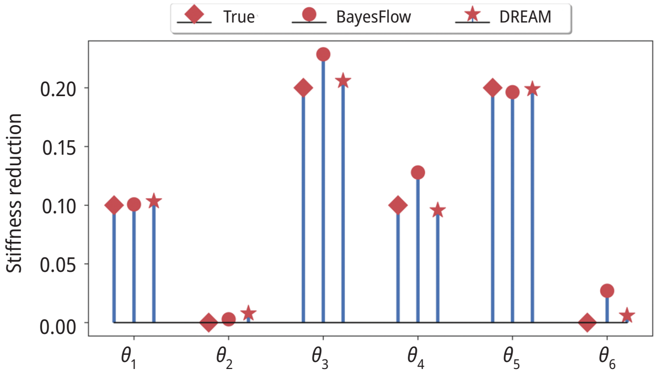

(a) Damage severity

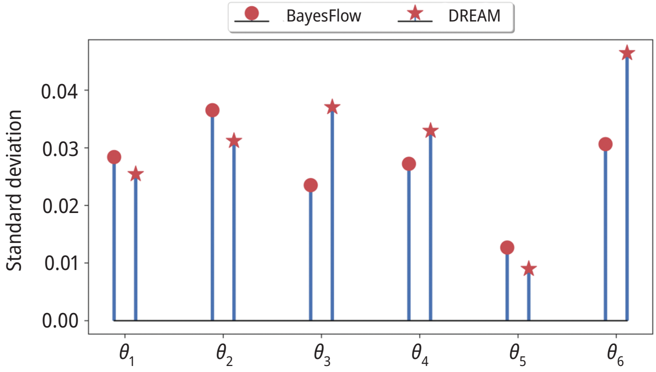

(b) Damage uncertainty

**Figure 8.24:** Damage identification by ten datasets on concrete building.

**Table 8.2:** Comparison of computational cost between inverse surrogate and DREAM.

| **Inverse surrogate** | | **DREAM** |
|---|---|---|
| **Training (h)** | **Inference (s)** | **Inference (h)** |
| 25 | **7** | 3.2 |

## 8.5 Conclusion

This chapter presents two types of inverse surrogate modeling methods for fast probabilistic damage detection. The first type of inverse surrogate is based on the Bayesian neural network and is for the problem with invertible response function. The other type of inverse surrogate is for problems with more generalized nonlinear response functions.

The presented inverse surrogate modeling methods can bypass the high computational effort required by the conventional Bayesian model updating-based SHM. They consist of an offline training phase and an online damage detection phase. In the offline training phase, synthetic damage data and observation data are collected from high-fidelity simulation models for the training of the inverse surrogates. After the training of the surrogates, the surrogate models can be used in the online phase to efficiently predict the posterior distribution of the damage parameters without computing complicated likelihood functions.

Damage detection in a miter gate and in a concrete building frame are used to demonstrate the capability of the presented inverse surrogate modeling methods. Results show that although inverse surrogate takes a long time in training, the training can be carried out offline. Damage detection can be conducted in real time, given measurement data after the training. It indicates that inverse surrogate is a feasible and promising tool for model updating and probabilistic structural damage detection.

## References

[1] C. R. Farrar, and K. Worden. An introduction to structural health monitoring. *Philosophical Transactions of the Royal Society A: Mathematical, Physical and Engineering Sciences*, 365(1851):303–315, 2007.

[2] K. He, and W. Zhu. *Structural damage detection using changes in natural frequencies: Theory and applications*. In *Journal of Physics: Conference Series*. IOP Publishing, 2011.

[3] A.-M. Yan, G. Kerschen, and P. De Boe et al. Structural damage diagnosis under varying environmental conditions – Part I: A linear analysis. *Mechanical Systems and Signal Processing*, 19(4):847–864, 2005.

[4] D. Agdas, J. A. Rice, and J. R. Martinez et al. Comparison of visual inspection and structural-health monitoring as bridge condition assessment methods. *Journal of Performance of Constructed Facilities*, 30(3):04015049, 2016.

[5] C.-Z. Dong, and F. N. Catbas. A review of computer vision–based structural health monitoring at local and global levels. *Structural Health Monitoring*, 20(2):692–743, 2021.

[6] S. K. Dwivedi, M. Vishwakarma, and A. Soni. Advances and researches on non destructive testing: A review. *Materials Today: Proceedings*, 5(2):3690–3698, 2018.

[7] M. R. Jolly, A. Prabhakar, and B. Sturzu et al. Review of non-destructive testing (NDT) techniques and their applicability to thick walled composites. *Procedia CIRP*, 38: 129–136, 2015.

[8] C. C. Ciang, J.-R. Lee, and H.-J. Bang. Structural health monitoring for a wind turbine system: A review of damage detection methods. *Measurement Science and Technology*, 19(12):122001, 2008.

[9] M. Ettouney, and S. Alampalli. *Infrastructure Health in Civil Engineering*. CRC press, Boca Raton, FL, 2012.

[10] X. Niu, H. Chen, and H. R. Marques *Piezoelectric transducer array optimization through simulation techniques for guided wave testing of cylindrical structures*. In *The 8th ECCOMAS Thematic Conference on Smart Structures and Materials (SMART 2017)*. 2017.

[11] V. Munoz, B. Valès, and M. Perrin, et al. Damage detection in CFRP by coupling acoustic emission and infrared thermography. *Composites Part B: Engineering*, 85: 68–75, 2016.

[12] D. M. Siringoringo, and Y. Fujino. Experimental study of laser Doppler vibrometer and ambient vibration for vibration-based damage detection. *Engineering Structures*, 28(13):1803–1815, 2006.

[13] H.-P. Chen. *Structural Health Monitoring of Large Civil Engineering Structures*. John Wiley & Sons, 2018.

[14] R. P. Bandara, T. H. Chan, and D. P. Thambiratnam. Frequency response function based damage identification using principal component analysis and pattern recognition technique. *Engineering Structures*, 66: 116–128, 2014.

[15] F. N. Catbas, H. B. Gokce, and M. Gul. Nonparametric analysis of structural health monitoring data for identification and localization of changes: Concept, lab, and real-life studies. *Structural Health Monitoring*, 11(5):613–626, 2012.

[16] K. Worden, C. R. Farrar, and G. Manson et al. The fundamental axioms of structural health monitoring. *Proceedings of the Royal Society A: Mathematical, Physical and Engineering Sciences*, 463(2082):1639–1664, 2007.

[17] F. A. Masurkar, and N. P. Yelve. Optimizing location of damage within an enclosed area defined by an algorithm based on the Lamb wave response data. *Applied Acoustics*, 120: 98–110, 2017.

[18] H. Maeda, Y. Sekimoto, and T. Seto et al. Road damage detection and classification using deep neural networks with smartphone images. *Computer-Aided Civil and Infrastructure Engineering*, 33(12):1127–1141, 2018.

[19] C. R. Farrar, and N. A. Lieven. Damage prognosis: The future of structural health monitoring. *Philosophical Transactions of the Royal Society A: Mathematical, Physical and Engineering Sciences*, 365(1851):623–632, 2007.

[20] C. R. Farrar, and K. Worden. *Structural Health Monitoring: A Machine Learning Perspective*. John Wiley & Sons, 2012.

[21] O. I. Abiodun, A. Jantan, and A. E. Omolara et al. State-of-the-art in artificial neural network applications: A survey. *Heliyon*, 4(11):e00938, 2018.

[22] J. M. Haslbeck, L. F. Bringmann, and L. J. Waldorp. A tutorial on estimating time-varying vector autoregressive models. *Multivariate Behavioral Research*, 56(1):120–149, 2021.

[23] Y. Lian, and M.-S. Liou. Multiobjective optimization using coupled response surface model and evolutionary algorithm. *American Institute of Aeronautics and Astronautics Journal*, 43(6):1316–1325, 2005.

[24] M. Azimi, A. D. Eslamlou, and G. Pekcan. Data-driven structural health monitoring and damage detection through deep learning: State-of-the-art review. *Sensors*, 20(10):2778, 2020.

[25] P. Aryan, A. Kotousov, and C. T. Ng et al. A model-based method for damage detection with guided waves. *Structural Control and Health Monitoring*, 24(3):e1884, 2017.

[26] V. Venkatasubramanian, R. Rengaswamy, and K. Yin et al. A review of process fault detection and diagnosis: Part I: Quantitative model-based methods. *Computers & Chemical Engineering*, 27(3):293–311, 2003.

[27] M. I. Friswell and J. E. Mottershead. *Finite Element Model Updating in Structural Dynamics*. Kluwer Academic Publishers, Dordrecht; Boston, 1995.

[28] M. Song, S. Yousefianmoghadam, and M.-E. Mohammadi et al. An application of finite element model updating for damage assessment of a two-story reinforced concrete building and comparison with lidar. *Structural Health Monitoring*, 17(5):1129–1150, 2018.

[29] B. A. Zárate, and J. M. Caicedo. Finite element model updating: Multiple alternatives. *Engineering Structures*, 30(12):3724–3730, 2008.

[30] T. Zhu, W. Tian, and S. Weng et al. Sensitivity-based finite element model updating using dynamic condensation approach. *International Journal of Structural Stability and Dynamics*, 18(08):1840004, 2018.

[31] M. Rezaiee-Pajand, A. Entezami, and H. Sarmadi. A sensitivity-based finite element model updating based on unconstrained optimization problem and regularized solution methods. *Structural Control and Health Monitoring*, 27(5):2020.

[32] M. Abdel-Basset, L. Abdel-Fatah, and A. K. Sangaiah. Metaheuristic algorithms: A comprehensive review. *Computational Intelligence for Multimedia Big Data on the Cloud with Engineering Applications*, 185–231, 2018.

[33] F. A. Hashim, K. Hussain, E. H. Houssein, et al. Archimedes optimization algorithm: A new metaheuristic algorithm for solving optimization problems. *Applied Intelligence*, 51(3):1531–1551, 2021.

[34] C. Mares, J. Mottershead, and M. Friswell. Stochastic model updating: Part 1 – Theory and simulated example. *Mechanical Systems and Signal Processing*, 20(7):1674–1695, 2006.

[35] H.-P. Wan, and W.-X. Ren. Stochastic model updating utilizing Bayesian approach and Gaussian process model. *Mechanical Systems and Signal Processing*, 70–71: 245–268, 2016.

[36] J. L. Beck, and L. S. Katafygiotis. Updating models and their uncertainties. I: Bayesian statistical framework. *Journal of Engineering Mechanics*, 124(4):455–461, 1998.

[37] Y. Govers, and M. Link. Stochastic model updating – Covariance matrix adjustment from uncertain experimental modal data. *Mechanical Systems and Signal Processing*, 24(3):696–706, 2010.

[38] H. H. Khodaparast, J. E. Mottershead, and M. I. Friswell. Perturbation methods for the estimation of parameter variability in stochastic model updating. *Mechanical Systems and Signal Processing*, 22(8):1751–1773, 2008.

[39] H. H. Khodaparast, J. E. Mottershead, and K. J. Badcock. Interval model updating with irreducible uncertainty using the Kriging predictor. *Mechanical Systems and Signal Processing*, 25(4):1204–1226, 2011.

[40] T. Haag, J. Herrmann, and M. Hanss. Identification procedure for epistemic uncertainties using inverse fuzzy arithmetic. *Mechanical Systems and Signal Processing*, 24(7):2021–2034, 2010.

[41] E. Simoen, G. De Roeck, and G. Lombaert. Dealing with uncertainty in model updating for damage assessment: A review. *Mechanical Systems and Signal Processing*, 56–57: 123–149, 2015.

[42] J. Zeng, and Y. H. Kim. Identification of structural stiffness and mass using Bayesian model updating approach with known added mass: numerical investigation. *International Journal of Structural Stability and Dynamics*, 20(11):2020.

[43] P. Ni, J. Li, and H. Hao et al. Probabilistic model updating via variational Bayesian inference and adaptive Gaussian process modeling. *Computer Methods in Applied Mechanics and Engineering*, 383: 113915, 2021.

[44] F.-L. Zhang, S.-K. Au, and Y.-C. Ni. Two-stage Bayesian system identification using Gaussian discrepancy model. *Structural Health Monitoring*, 20(2):580–595, 2021.

[45] S. Chib, and I. Jeliazkov. Marginal likelihood from the Metropolis–Hastings output. *Journal of the American Statistical Association*, 96(453):270–281, 2001.

[46] H. Haario, M. Laine, and A. Mira et al. DRAM: Efficient adaptive MCMC. *Statistics and Computing*, 16(4):339–354, 2006.

[47] J. A. Vrugt. Markov chain Monte Carlo simulation using the DREAM software package: Theory, concepts, and MATLAB implementation. *Environmental Modelling & Software*, 75: 273–316, 2016.

[48] J. S. Liu, and R. Chen. Sequential Monte Carlo methods for dynamic systems. *Journal of the American Statistical Association*, 93(443):1032–1044, 1998.

[49] A. Thelen, X. Zhang, and O. Fink et al. A Comprehensive Review of Digital Twin–Part 2: Roles of Uncertainty Quantification and Optimization, a Battery Digital Twin, and Perspectives. *arXiv preprint arXiv:2208.12904*, 2022.

[50] A. Thelen, X. Zhang, and O. Fink et al. A Comprehensive Review of Digital Twin–Part 1: Modeling and Twinning Enabling Technologies. *arXiv preprint arXiv:2208.14197*, 2022.

[51] C. I. Van Damme, M. S. Allen, and J. J. Hollkamp. Updating geometrically nonlinear reduced-order models using nonlinear modes and harmonic balance. *AIAAJ*, 58(8):3553–3568, 2020.

[52] C. E. Rasmussen. Gaussian processes in machine learning. In *Summer School on Machine Learning*. Springer, 2003.

[53] P. Moser, and B. Moaveni. Environmental effects on the identified natural frequencies of the dowling hall footbridge. *Mechanical Systems and Signal Processing*, 25(7):2336–2357, 2011.

[54] K. Worden, and E. Cross. On switching response surface models, with applications to the structural health monitoring of bridges. *Mechanical Systems and Signal Processing*, 98: 139–156, 2018.

[55] P. Ni, Y. Xia, and J. Li et al. Using polynomial chaos expansion for uncertainty and sensitivity analysis of bridge structures. *Mechanical Systems and Signal Processing*, 119: 293–311, 2019.

[56] S. Adhikari, and H. H. Khodaparast. A spectral approach for fuzzy uncertainty propagation in finite element analysis. *Fuzzy Sets and Systems*, 243: 1–24, 2014.

[57] H. Sung, S. Chang, and M. Cho. Reduction method based structural model updating method via neural networks. *AIAA Scitech 2020 Forum*, 2020.

[58] Y. Lu, and Z. Tu. A two-level neural network approach for dynamic FE model updating including damping. *Journal of Sound and Vibration*, 275(3–5):931–952, 2004.

[59] S. Trehan, K. T. Carlberg, and L. J. Durlofsky. Error modeling for surrogates of dynamical systems using machine learning. *International Journal for Numerical Methods in Engineering*, 112(12):1801–1827, 2017.

[60] H.-P. Wan, and W.-X. Ren. A residual-based Gaussian process model framework for finite element model updating. *Computers & Structures*, 156: 149–159, 2015.

[61] A. Bate, M. Lindquist, and I. R. Edwards et al. A Bayesian neural network method for adverse drug reaction signal generation. *European Journal of Clinical Pharmacology*, 54(4):315–321, 1998.

[62] A. Graves. Practical variational inference for neural networks. *Advances in Neural Information Processing Systems*, 24, 2011.

[63] I. Kobyzev, S. J. Prince, and M. A. Brubaker. Normalizing flows: An introduction and review of current methods. *IEEE Transactions on Pattern Analysis and Machine Intelligence*, 43(11):3964–3979, 2020.

[64] J. Zeng, M. D. Todd, and Z. Hu. Probabilistic damage detection using a new likelihood-free Bayesian inference method. *Journal of Civil Structural Health Monitoring*, 1–23, 2022.

[65] L. Dinh, J. Sohl-Dickstein, and S. Bengio. Density estimation using real nvp. *arXiv preprint arXiv:1605.08803*, 2016.

[66] L. Ardizzone, C. Lüth, J. Kruse, et al., Guided image generation with conditional invertible neural networks. *arXiv preprint arXiv:1907.02392*, 2019.

[67] S. T. Radev, U. K. Mertens, and A. Voss, et al. BayesFlow: Learning complex stochastic models with invertible neural networks. *IEEE Transactions on Neural Networks and Learning Systems*, 2020.

[68] A. Graves, and J. Schmidhuber. Framewise phoneme classification with bidirectional LSTM and other neural network architectures. *Neural Networks*, 18(5–6):602–610, 2005.

[69] M. Akesson, P. Singh, and F. Wrede, et al. Convolutional neural networks as summary statistics for approximate Bayesian computation. *IEEE/ACM Transactions on Computational Biology and Bioinformatics*, 2021.

[70] M. A. Vega, Z. Hu, and T. B. Fillmore, et al. A novel framework for integration of abstracted inspection data and structural health monitoring for damage prognosis of miter gates. *Reliability Engineering & System Safety*, 211: 107561, 2021.

[71] B. A. Eick, Z. R. Treece, B. F. Spencer Jr, et al. Automated damage detection in miter gates of navigation locks. *Structural Control and Health Monitoring*, 25(1):e2053, 2018.

[72] V. Hoskere, B. Eick, and B. F. Spencer Jr, et al. Deep Bayesian neural networks for damage quantification in miter gates of navigation locks. *Structural Health Monitoring*, 19(5):1391–1420, 2020.

[73] X. Dong, X. Liu, and T. Wright et al. Validation of wireless sensing technology densely instrumented on a full-scale concrete frame structure. In *Transforming the Future of Infrastructure through Smarter Information: Proceedings of the International Conference on Smart Infrastructure and ConstructionConstruction, 27–29 June 2016*. ICE Publishing, 2016.

[74] X. Dong, and Y. Wang. Formulation and optimization algorithm comparison for the FE model updating of large-scale models. 2018.

Saurabh Gupta, Syam Nair

# 9 Remote sensing techniques for post-disaster infrastructure health monitoring

**Abstract:** Natural disasters can be predicted but cannot be controlled. Earthquakes, tsunamis, and cyclones are among humankind's most catastrophic natural disasters. Disasters not only affect human life but also damage the infrastructure. Estimating infrastructure damages play a critical role in finding out the area and the amount of work that needs to be reconstructed. One of the major problems is to analyse accurate damages in buildings rapidly. Accurate destruction analysis helps engineers and planners provide a plan for rehabilitation in the affected area. This chapter discusses the different remote sensing techniques used in building damage detection. The study reviews damages due to different natural hazards and outlines the general framework for building damage detection. In this chapter, we also propose a novel approach with a framework for disaster damage monitoring using various data sources.

## 9.1 Introduction

The first important task after natural disaster was to immediately assess the damages. This data supports various organisations to respond quickly, which may reduce the number of casualties. For the same, [1] have developed a real-time damage assessment system to estimate building damage within 15 min after an earthquake occurs using satellite data. Real-time damage assessment and detection system is the primary source during the period of initial disaster response. The planning and assessment help in short-term and long-term recovery. Sometimes, damage detection and estimation are not so accurate and show variation from ground reality; this uncertainty is due to the different data collection and interpretation techniques. Thus, the study of various data collection techniques and data interpretation techniques is necessary.

In this chapter, a literature analysis is presented for the various remote sensing techniques, and presented as a framework. In addition, this article also discusses the different methods for data interpretation. In the chapter's last section, we propose a novel tribrid approach for post-disaster damage assessment using unmanned aerial vehicle (UAV) and satellite data.

---

**Saurabh Gupta**, **Syam Nair,** Indian Institute of Technology Kanpur, India

https://doi.org/10.1515/9783110791426-009

## 9.2 Literature survey

The use of remote sensing for building damage detection is not novel. In the last two decades, many researchers used various remote sensing techniques to estimate building damage. Satellites have different types of visual and non-visual wavelength bands, such as SAR, high-resolution imagery, multi-spectral, and hyper-spectral, which show the capability of observing the Earth to collect various valuable information. On the other hand, data can also be collected from manual aerial vehicle (MAV) and UAV using high-resolution cameras and light detection and ranging (LiDAR). The literature from the last two decades is discussed in Table 9.1.

**Table 9.1:** Summary of remote sensing methodologies used in building damage detection.

| S. no. | Author | Disaster | Year | Methodology |
|---|---|---|---|---|
| 1 | [2] | Izmit, earthquake, Turkey | 1999 | Post-earthquake aerial images were collected and further processed using image enhancement and edge detection. Polygons are created over different buildings using a watershed segmentation method and the damage is then assessed. |
| 2 | [3] | Beichuan earthquake, China | 2006 | Aerial images are captured using camera-mounted UAV. DSM (digital surface model) is created for pre-disaster and post-disaster data and they are compared to check the damage in buildings. The data is segmented, shape- and texture-based are extracted and compared for pre and post-disaster events to estimate building damage. |
| 3 | [4] | Haiti earthquake | 2010 | Both LiDAR data and images were captured using an aerial survey. DEM (digital elevation model) and DSM were obtained from LiDAR data. The image data is then georeferenced and orthorectified with LiDAR data. Image segmentation and classification are carried out using eCongition software. The result was then evaluated with the help of ArcGIS software having an accuracy between 70 and 79%. |

**Table 9.1** (continued)

| S. no. | Author | Disaster | Year | Methodology |
|---|---|---|---|---|
| 4 | [5] | BAM earthquake, Iran | 2004 | Pre and post-event image data are collected and merged with the old vector map. The image is then georeferenced to create a building polygon map. The image is then classified and labelled, and geometric features are extracted to determine damage to the building. Sensitivity analysis is performed using ANFIS. The overall accuracy was 76.36%, with a kappa coefficient of 0.63. |
| 5 | [6] | Chastel landslide | 2012 | The methodology is based on combining SAR data with LiDAR point cloud data. The point cloud data comprises GPS (global positioning system) and topographical data. |
| 6 | [7] | Yushu earthquake | 2010 | Satellite high-resolution images are used along with the building polygon. The building is analysed for roof edge and interior, improving the accuracy. Buildings are colour coded based on the damage. The overall accuracy is 84.10%. |
| 7 | [8] | Indonesia, 2016; Nepal, 2015; Italy, 2009; Haiti, 2010; Nepal, 2015; Taiwan, 2016. | 2010–2016 | Satellite data, airborne data, UAV datasets were collected and analysed. The model is then trained and tested using CNN (convolution neural network). |
| 8 | [9] | Hurricane Sandy, USA | 2012 | UAV-mounted camera is used along with machine learning. |
| 9 | [10] | Haiti earthquake | 2010 | Comparison between pre- and post-earthquake satellite data using CNN. |
| 10 | [11] | Van City earthquake | 2011 | Aerial cameras are used to capture images and a comparison is made between pre- and post-earthquake DSM models, based on geometric properties such as area, and the perimeter is then extracted. |
| 11 | [12] | Nagapattinam, Tsunami, India | 2004 | Using image analysis, pre- and post-Tsunami are compared using high-resolution imagery satellite data. |
| 12 | [1] | Kumamoto earthquake | 2016 | Fixed-wing UAV is used to capture images, and two machine learning methods – bag-of-visual-words model and a CNN model – were used for determining damages in four different levels, based on the damage. |

In Table 9.1, the literature discusses various remote sensing techniques. Interpretation technics show promising result, with an accuracy between 80 and 90%. From the table, we can conclude that the various methods follow a common approach. The framework for the same is illustrated in the flow chart in Figure 9.1.

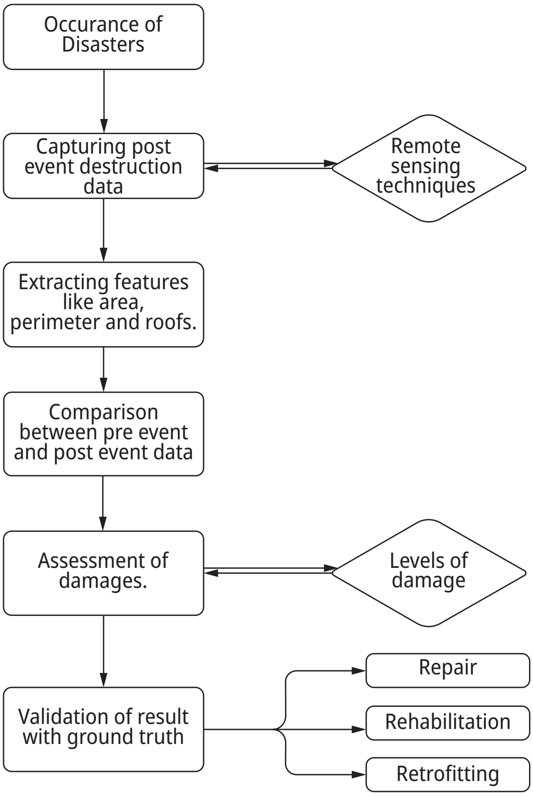

**Figure 9.1:** Basic framework for building damage detection.

As explained in the flow chart, as soon as a disaster occurs, we need to decide the remote sensing technique that will be appropriate and accurate in that situation. The choice depends on the funds, availability, and expertise [13]. Once the technique is finalised, data is captured and further processed. Features such as polygon, area, perimeter, and roofs are extracted. These features are then compared with the pre-event data. This gives an estimate of the damages that can be evaluated with the ground reality which helps to determine the accuracy of the developed methodology. The output provides a guideline to the administration about the structure that requires repair, rehabilitation, or retrofitting.

**Table 9.2:** Remote sensing techniques and interpretation techniques for building damage assessment.

| Adopted remote sensing techniques | Adopted data interpretation methods |
|---|---|
| – Satellite imagery | – Image processing |
| – LiDAR | – Machine learning (ML) |
| – High-resolution camera with MAV | – Deep learning (DL) |
| – Camera with UAV | – Computer vision |
| | – Surface models (DEM, DSM) |
| | – Bundled software |

SAR data is mainly used in satellite imagery, besides radar. Remote sensing is used for weather and it can also collect data for urban mapping. Its sensitivity is enough to capture the heights of the building in pre and post-event data. The resolution can be up to 1 m for the latest generation of VHR space-borne SAR sensors like TerraSAR-X and COSMO-SkyMed, which are useful for urban area analysis at the building level.

Some forms of damage (e.g. pancake collapses) cannot be identified from 2D photos, but can be detected using airborne LiDAR system rapid and by comprehensive capture of exact height data. There is little study on utilising actual pre-event and post-event LiDAR data for building damage identification because LiDAR is still a relatively new technology, and many areas do not have LiDAR coverage. MAV has the benefit of capturing data of a very large area with a single scan, and can take lot more time and resources than UAV, while UAV is readily available and requires less flight planning. For a disaster like a cyclone or hurricane, a UAV is more suitable than MAV to collect data. UAVs are also cost-effective for data collection.

Similarly, many data interpretation techniques are discussed in Table 9.2. Image processing is the oldest method and the backbone for all other processes. Machine learning and deep learning are based on learning algorithms, and researchers use supervised learning to train the classifiers and test them on actual data.

Numerous preliminary tests have been carried out by scientists all around the world to learn more about identifying earthquake-induced structural damage. The spatial resolution of the data in Table 9.3 is less than 10 metres, making it suitable for locating earthquake damage to buildings. Optical images can be processed to extract a variety of different types of data, including grayscale, spectra, texture, shape, morphological features, and so on [14, 15], while a digital elevation model (DEM) or stereoscopic measurement can be used to obtain height and volume data [16–18].

**Table 9.3:** Remote sensing satellite with the spatial resolution.

| Satellite/platform | Spatial resolution | Satellite/platform | Spatial resolution |
|---|---|---|---|
| Worldview-3 | 0.3 m | TerraSAR-X | 1 m |
| GeoEye-1 | 0.41 m | Spot 6 | 1.5 m |
| Worldview-2 | 0.46 m | Formosat-2 | 2 m |
| QuickBird | 0.6 m | IRS-P5 (Cartosat-1) | 2.5 m |
| Worldview-1 | 0.5 m | ALOS | 4 m |
| Pleiades-1 | 0.5 m | RapidEye | 5 m |
| EROS-B | 0.7 m | Spot 5 | 5 m |
| IKONOS | 1 m | Spot 4 | 10 |
| KOMPSAT-2 | 1 m | | |

## 9.3 Structural damage evaluation criteria

In Table 9.4, we see the various degrees of damage that may happen to buildings. If the extent of the damage is variable, so must be the measures taken in response. Heavy damage to a building necessitates a quick evaluation, does not call for more identification precision (since the damages are substantial), and cannot be inspected up-close without putting inspectors at risk. As a result, contactless instruments may be the most suitable option. On the other side, bridge tests may be conducted on structures with moderate damage. However, a higher degree of precision is needed in these cases. Rapid testing strategies, based on vibration, may be the most suited option here. It is often advised that high-accuracy procedures and long-term monitoring systems be established in the event of lightly damaged structures, even when no major damage is obvious. The different levels of marking structures while processing data is shown in Figure 9.2.

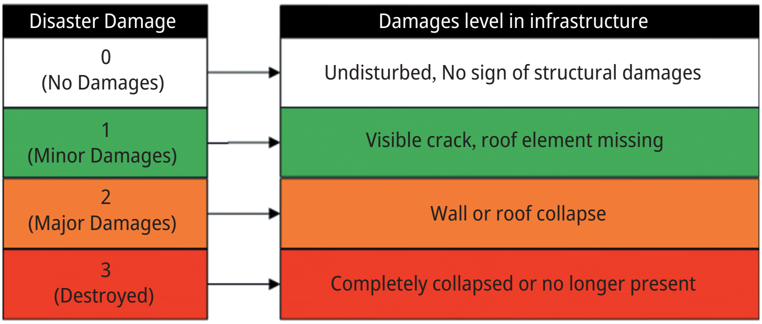

| Disaster Damage | Damages level in infrastructure |
|---|---|
| 0<br>(No Damages) | Undisturbed, No sign of structural damages |
| 1<br>(Minor Damages) | Visible crack, roof element missing |
| 2<br>(Major Damages) | Wall or roof collapse |
| 3<br>(Destroyed) | Completely collapsed or no longer present |

**Figure 9.2:** Different damage level markers for data processing.

**Table 9.4:** A summary of damage level of infrastructures.

| Damage level | Description | Implications |
|---|---|---|
| Heavy damage | – Displacement and compressive component shear failure<br>– Distinct residual motion, connection settling<br>– Foundation scour and vertical offset<br>– Massive spalling and cracking in the concrete<br>– Accepting the arrival of the bulk of reinforcements<br>– Superstructure has been severely damaged or unsettled<br>– Substantial and irreversible bending | – Importance is placed heavily on evaluating performance.<br>– Signs indicate that the area is closed off and no one can enter.<br>– It could be necessary to replace it, either partially or entirely. |
| Moderate damage | – Compression parts have moderate cracking and spalling<br>– Major spalling and cracking of shear keys, and bent blots and keeper bars without unseating<br>– Moderate decrease in cover concrete mass Moderate<br>– Approaching moderation<br>– Foundation scour or medial settling | – Evaluation is on the low-to-medium priority list.<br>– Access is denied or severely limited.<br>– There is a test for the bridge, and it is essential that repairs be made right away to prevent further degradation. |
| Light damage | – The foundation has several small cracks and spalls.<br>– Hinge spalling and little fractures.<br>– Modest cracking in the compressive parts.<br>– Jamming from debris (can be cleaned).<br>– Distortion does not seem to be permanent.<br>– Cover concrete with fine fissures. | – Undervalued emphasis on evaluation.<br>– Free and easy availability.<br>– Needs only cosmetic work, however permanent monitoring may be necessary. |

## 9.4 Infrastructure damage detection by comparing pre-disaster data with post-disaster data

One common technique for assessing structural damage caused by an earthquake is change detection, with pre-and post-event remote sensing data. Methods for change detection, such as improved image analysis and a comparison of classification results, can be used to determine the changes in a structure over time. Improving photos uses mathematical processes such as subtraction of bands, rationing, and image regression to merge several images taken at various times.

### 9.4.1 Satellite imagery

It is common practise to utilise high-resolution satellite photos to survey a vast region and assess damage to buildings and other infrastructure. The primary benefit of this approach is that it aids authorities, hazard rescue teams, and relief workers in assessing the extent of the damage to structures, and making plans for rescue/emergency operations and organizing relief activities. Satellite image assessment techniques use time-lapse comparisons to evaluate the extent of physical damage to buildings and landscapes [19]. Some operations have identified damaged structures by comparing photographs taken before and after a disaster [20–22]. The field, in this respect, has utilised several methods. Satellite photos taken in the aftermath of the Oklahoma City tornado were studied by Myint et al. [21], utilising component analysis, image recognition, and object-oriented classification to identify the damaged buildings. Results were found to be more exact with the object-oriented categorisation. The majority of analytic methods, however, still rely on the time-consuming and resource-intensive human labour of a team of professionals scanning thousands of photos [23]. Therefore, various object-classification-based automatic assessment techniques have been suggested [24–26]. These techniques include the minimal distance classifier, the decision tree algorithm, and the support vector machine. Automated aerial imaging damage detection methods were compared by Ye et al. [27]. In order to train and evaluate the image classification algorithms, feature sets were first extracted from the photos. The findings suggest that combining feature sets with several categorisation techniques might achieve the most significant results. One key drawback of satellite imagery-based methods is that it is necessary to have photos from both before and after a threat occurs.

### 9.4.2 Unmanned aerial vehicles (UAVs)

Increasingly, high-resolution photos are captured quickly using unmanned aerial vehicles (UAVs). UAVs have their uses and benefits while requiring an on-site operation. This platform allows for a more thorough inspection and, as a result, a more precise damage assessment by taking a huge number of photographs and videos. UAVs are more practical, inexpensive, and simple to operate than satellites because of the recent developments in sensing, low-cost cameras, and autonomous navigation. Because of these benefits, UAVs are increasingly being used to evaluate severely damaged buildings where access is restricted. Three phases make up the UAV-driven damage assessment [28]. (2) Visual data analytics: extracting information characteristics from pictures and comparing with a priori information to discover deviations from the norm. (1) Image acquisition: gathering photographs or videos of damaged structures or places. Third, data visualisation tools allow for quick assessment of the present damaged state of structures. Several research projects have been carried out utilising this method, demonstrating the great potential of this framework for use in damage assessment. Hallermann and Morgenthal [29] showed how this system might be used in practice to detect the movement of a massive retaining wall. Separate footage from UAVs captured the wall in its calibration (original) and converted (distorted) states. In order to detect alterations to the wall, the collected images underwent photogrammetric analysis and were converted into a 3D point cloud, which was then compared and displayed using an appropriate software. As the findings show, this method may diagnose bridge deformation (including deck distortion, tower tilt, and piling settlement) effectively and quickly. Notably, like satellite imagery-based approaches, this technique calculates the displacement by comparing the "calibration-transformed" state of the wall. Most of these techniques, however, share the difficulty of post-hazard procedures' lack of previous knowledge since they detect flaws by comparing the differences between a healthy and damaged building. Fernandez et al. [30] employed object-based image analysis (OBIA) to evaluate extensive damage to building roofs, concrete facades, and brick facades using a damaged image to address this issue. Objects relevant to the damage were extracted from UAV photos using an image segmentation method in OBIA. It is possible to identify broken components more precisely when used with the aforementioned items.

Results showed that OBIA-processed oblique pictures are helpful in locating critical damage in buildings. However, there is a dearth of studies investigating the use of this technique for the damage assessment of essential assets like bridges.

Although UAVs have a lot of potential for quick damage assessment, following natural disasters, they still have several issues to work out before they can be used efficiently. A few of the most important ones are (1) data collection from unseen sections of the structures; (2) feature description and configuration information standards; and (3) auto-pilot, path planning, and navigation algorithms [31]. There have been several attempts to create self-navigational pathways using simultaneous localisation and mapping methods. Fernandez Galarreta et al. [30] highlighted the benefits of using GPS waypoints with pre-existing maps when navigating a vehicle. However, natural disasters can result in quick modifications to structures and the surroundings, which are not taken into consideration. This might result in navigational challenges and safety concerns that were not anticipated. In order to overcome this shortcoming, Michael et al. [32] used a 3D map of the post-hazard buildings, made up of 3D point clouds, created by rotating a laser scanner and a 2D occupancy grid map. But there has not been enough research done on the second and third obstacles thus far. PLD can be used as a priori knowledge about a building's geometry and other physical and functional properties.

### 9.4.3 Machine learning

Uncertainty increases significantly when extensive data from several sources are combined to improve catastrophe preparedness and response. Due to the sheer volume of integrated data, manual interpretation and analysis are no longer sufficient; instead, advanced automatic analysis methods are necessary to ensure the process runs smoothly and effectively. Since its introduction in disaster management two decades ago, machine learning has become one of the most effective methods for filtering out irrelevant data and speeding up the analysis in disaster situations, which aids in rapid prediction analysis and determining the best response strategies.

Automatically categorising tweets on disaster relief efforts using text classification of social media data speeds up the process of locating relevant tweets. "[33]" Artificial Intelligence for Disaster Response (AIDR) was created by 34 to categorise user-generated content during catastrophes into predetermined groups of data (such as "needs," "damage," etc.). To do this, it continually gathers data from Twitter, analyses it (through machine learning classification algorithms), and makes use of human input [via crowdsourcing) in real time. During the 2013 Pakistan Earthquake, AIDR was put to test to determine whether or not tweets were instructive. To quickly evaluate massive amounts of aerial data for time-sensitive disaster response, Bejiga et al. [35] suggested a hybrid crowdsourcing and real-time machine learning system based on AIDR. Features of interest in aerial photographs were annotated with the help of crowd (such as damaged shelters and roads blocked by debris]. These manually annotated characteristics were used to teach a supervised machine learning system how to identify them in previously viewed photos.

Dynamic decision-making is enhanced and human contact is decreased when damage detection techniques are used. It can be time-consuming, error-prone, and expensive to conduct a damage assessment based only on visual interpretation of satellite/aerial pictures and films. Additionally, in areas where the death toll is higher, supplementary data like UAV products, LiDAR, or GIS databases are typically unavailable [36]. While traditional statistical methods assume a normal distribution of the data, machine learning algorithms continuously adjust to new conditions and improve over time [37]. When compared to more conventional approaches to categorization and change detection, the accuracy of machine learning algorithms is often higher. Non-linear datasets [38] can be used, as can learning with little training data [39], and challenging classification issues can be solved. The usefulness of Artificial Neural Networks and Random Forests in identifying building damages, induced by the 2010 Haiti earthquake, was studied by [40] using high spatial resolution data gathered using WorldView-1 and Quickbird 2.

One of the more recent advances in machine learning that has potential in disaster management is new learning. Using a convolutional neural network, Cha et al. [41] suggested a method for detecting fractures in concrete without the usual calculation of a defect feature, which is affected by noise in the data. Traditional edge detection approaches (canny and Sobel) fail to offer significant fracture information; however, the suggested methodology successfully categorised the detected cracks into diverse characteristics such as bright light spots, shadows, and extremely thin cracks. In order to extract data from YouTube videos depicting natural disasters such floods, fires, mudslides, tornadoes, and lightning, Pouyanfar and Chen [42] suggested an ensemble deep learning architecture. Shots are taken from videos by border recognition and key-frame selection, and features are subsequently extracted using deep learning reference models for each shot. The characteristics were fed into well-known classifiers like Decision Trees and Support Vector Machines to do the classification.

Machine Learning, historical and Big Data analytics, and real-time catastrophe monitoring are just some of the ways in which predictive damage assessment technologies are helping to refine their damage predicting models. Modelling connections between computed seismic parameters and potential earthquake occurrences was the focus of a 2017 study by Asim et al., who examined four machine learning techniques: a pattern recognition neural network, a recurrent neural network, a random forest, and a linear programming boost ensemble classifier. The ability to adapt to ever-changing crisis conditions is another benefit of automating such procedures.

## 9.5 Proposed tribrid approach using satellite and UAV data

Optical and radar satellite data are widely recognised as having great potential for use in crisis management settings. Loss assessments, following natural catastrophes, have been the subject of several research in recent years [2, 5]. Previous decades' low spatial resolution datasets prevented reliable loss assessment because damaged structures were too tiny to fit within individual pixels. Inadequate financial judgments are made in relation to the reconstruction of infrastructures due to wrong evaluation. Contrarily, aerial imaging, particularly UAV-based monitoring, has proven useful in the construction of new buildings and other infrastructure [1, 9]. While satellite-based and aerial-based assessments are looked at individually in the literature, combining the two is still a mostly uncharted territory when it comes to disaster recovery management. It is for this reason that frameworks for financial choices necessitate integrated modelling techniques. Even if there are flaws and unknowns in the comprehensive damage assessment, the situation can be modelled with the help of the suggested Disaster Damage Rating (DDR) model. The modelling requires the overlay of many data sets, such as those captured by hyperspectral satellites, high-resolution UAVs, and data collected from the field. The generation of orthophoto pictures using UAV allows for the superimposition of the data set in a common coordinate system after which the damage can be assessed in 3D, and the missing pieces may be reconstructed in 4D using UAV data. In addition to a more precise assessment, the model will also assign a score on the Damage

Scale (DS). A machine learning framework [8] will be constructed based on the DS to determine the appropriate infrastructure treatments. The completed FDF can serve as a repository for relevant financial facts for use in making future choices.

### Innovation/novelty

- UAV data and satellite data are underutilised in the infrastructure management field.
- The novel tribrid approach, which involves UAV and satellite data, followed by verification with field data, gives a correlation with global data.
- The proposed research uses machine learning algorithms, extending it to damage detection applications, which will automate the process and eliminate human errors.
- The research focuses on damage monitoring and provides a framework for decision-making at each stage to formulate financial strategies.
- The study develops a rating model for monitoring, which is used as a key parameter in the financial decision framework in later stages.

Satellite and UAV data complement each other when it comes to incorporating temporal and spatial features. Nanosatellites (such as Planet labs) placed in the low orbits of the Earth provide high-resolution spatial data (1–10 m) that can be used for macro analysis, but due to lower data quality, does not satisfy all applications. A micro-UAV shifts the remote sensing (RS) paradigm by allowing end users to control acquisition features [43]. The RS UAV's strengths are its ultra-spatial resolution (centimetric to millimetric) and acquisition flexibility. The proposed solution for the problem is (Flowchart 1) to incorporate field data and UAV data into global data, which gives the comfort to micro-level analysis. There are two segments in the proposed solution, (i) Model Calibration, which involves "data comparison" and "Multiscale Explanation"; which provide parameters for Model calibration to analyse a model quantitatively and qualitatively. The calibration parameters thus obtained can be used as input for the next process of "Data Fusion" (refer to flowchart 1 in Figure 9.3) (ii) The second portion give an overview of the data fusion process, which is persuaded by analysing pixel and features in both the data when superimposed together. Using a decision matrix, the conditional assessment of the infrastructure is performed. The testing data is then verified with the ground truth obtained by field data. Each infrastructure is then marked with a rating scale, which is proposed as "Disaster Damage Rating" for the proposed solution. Optimisation algorithm(s) can be used in the last portion of the research to initialise the framework for treatment allotment, and the data is used by continuous model learning. The research outcomes provide a synergy between the UAV and satellite data to overcome the current limitations [44]. The research provides a combined workflow that must be facilitated and adapted to automated and accurate monitoring.

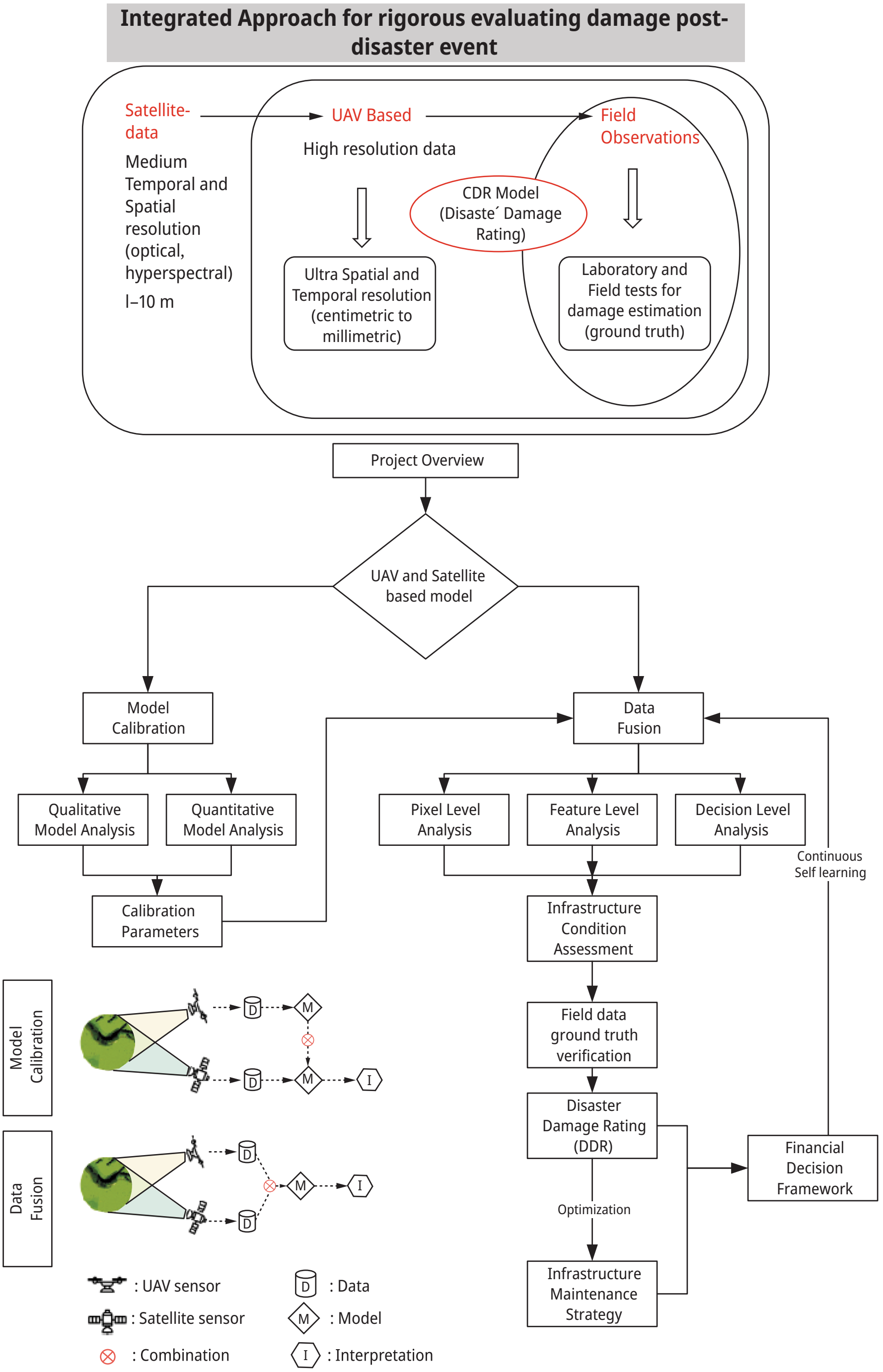

**Figure 9.3:** Proposed tribrid approach for infrastructural damage assessment for post-disaster scenarios.

Considering a post-disaster scenario, the research methodology is divided into 4 subcategories as described in Flowchart 2 (Figure 9.4): (i) data acquisition, which involves data collection from various open source databases such as MODIS, Terra, UNOSAT, and paid satellite data services such as Planet lab. Data needs to be extracted for a given latitude and longitude using python programming. Secondly, UAV data can be collected from the site itself (if possible) or obtained from respective agencies, along with the extrinsic and intrinsic properties of the camera used by the UAV. By collecting the data, a database is created for (ii) pre-processing, which involves Atmospheric Correction and Radiometric Calibration, Pan Sharpening, and Co-registered Reflectance Imagery for satellite data. Similarly, for UAV data, tie points and markers are marked to perform alignment correction, followed by the generation of orthophoto generation for quick mapping and point cloud generation (converting raster data to vector data). The DSM and DEM models are created for analysis using vector point cloud data. The processed satellite and UAV data are then passed through various (iii) feature extraction processes. For feature extraction, various data processing (DP) domain is proposed (photometric, geometric, hybrid, and transformational approaches); the best-performing approach is chosen, and the data is then passed through different DP filters as described in Flowchart 4. The desired feature is then extracted using segmentation and classification. The condition of the structure member is then assessed and validated with field data. A machine learning CNN/ANN-based defect prediction model is used to decide each structure's maintenance priority. (iv) An optimisation algorithm is used to find the trade off between the required resources and the short- and long-term strategy, to finalise the resource allocation approach, which leads to the final financial decision framework.

## 9.6 Conclusion

In-depth research on building damage detection methods has shown that these techniques were developed, considering the specifics of the data they were meant to analyse, with practically every natural catastrophe affecting the same geographic region. Therefore, testing all these procedures with a single or small sample of experimental data makes it difficult to compare their relative merits quantitatively. Still, the aforementioned review may be utilised to make some broad generalisations regarding the current trends and the results of most investigations. Infrastructure damage detection increasingly uses various remote sensing techniques and the associated GIS (Geographic Information System) data. A resolution of 10 to 0.3 m is obtained using a wide variety of optical, SAR, LiDAR, raster, and vector data types, as well as airborne and space-based remote sensors. Due to their many advantages, different data types may be used in several contexts.

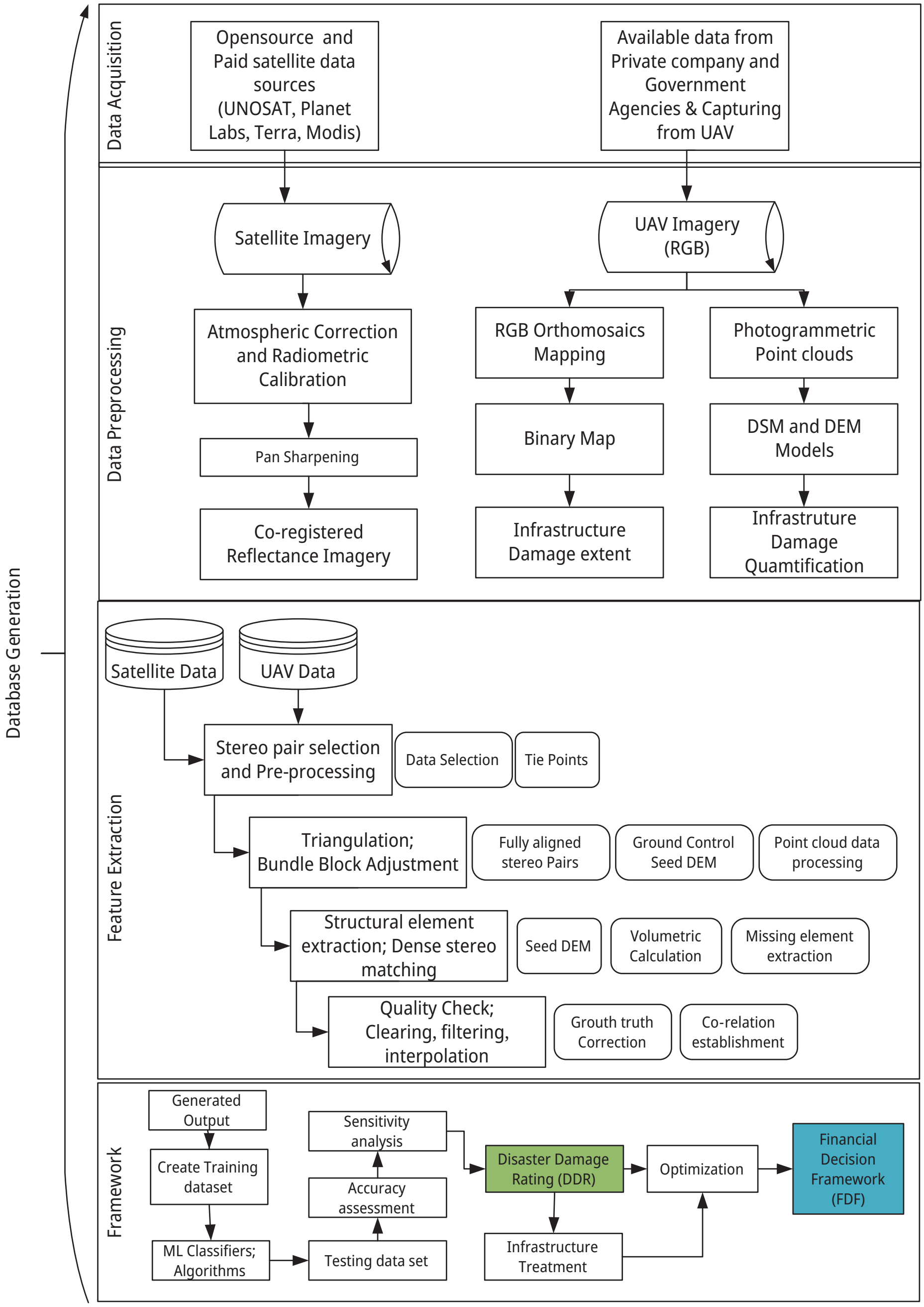

**Figure 9.4:** Proposed methodology for infrastructural damage assessment for post-disaster scenarios.

# References

[1] S. Naito, H. Tomozawa, Y. Mori, H. Fujiwara, and G. Shoji. Building-damage detection method based on machine learning utilising aerial photographs of the Kumamoto earthquake. *Earthquake Spectra*, 1–22, 2020. https://doi.org/10.1177/8755293019901309.

[2] M. Turker, and E. Sumer. Building-based damage detection due to earthquake using the watershed segmentation of the post-event aerial images. *International Journal of Remote Sensing*, 29 (11):3073–3089, 2008. DOI: 10.1080/01431160701442096.

[3] H. Sui, et al. A novel 3D building damage detection method using multiple overlapping UAV images. *International Archives of the Photogrammetry, Remote Sensing and Spatial Information Sciences – ISPRS Archives*, 40(7):173–179, 2014. DOI: 10.5194/isprsarchives-XL-7-173-2014.

[4] T. T. H. Pham, et al. Towards a rapid automatic detection of building damage using remote sensing for disaster management: The 2010 Haiti earthquake. *Disaster Prevention and Management: An International Journal*, 23(1):53–66, 2014. DOI: 10.1108/DPM-12-2012-0148.

[5] M. Janalipour, and A. Mohammadzadeh. Building damage detection using object-based image analysis and ANFIS from high-resolution image (Case Study: BAM Earthquake, Iran). *IEEE Journal of Selected Topics in Applied Earth Observations and Remote Sensing*, IEEE, 9(5):1937–1945, 2016, DOI: 10.1109/JSTARS.2015.2458582.

[6] A. Anghel, et al. Combining space borne SAR images with 3D point clouds for infrastructure monitoring applications. *ISPRS Journal of Photogrammetry and Remote Sensing*, International Society for Photogrammetry and Remote Sensing, Inc. (ISPRS), 111:45–61, 2016, DOI: 10.1016/j.isprsjprs.2015.11.008.

[7] X. Ye, et al. Building-based damage detection from postquake image using multiple-feature analysis. *IEEE Geoscience and Remote Sensing Letters*, IEEE, 14(4);499–503, 2017, DOI: 10.1109/LGRS.2017.2651050.

[8] F. Nex, D. Duarte, F. G. Tonolo, and N. Kerle. Structural building damage detection with deep learning: Assessment of a state-of-the-art CNN in operational conditions. *Remote Sensing*, 11(23), 2019, https://doi.org/10.3390/rs11232765.

[9] Y. Li, W. Hu, H. Dong, and X. Zhang. Building damage detection from post-event aerial imagery using single shot multibox detector. *Applied Sciences (Switzerland)*, 9(6), 2019, https://doi.org/10.3390/app9061128.

[10] J. Z. Xu et al. Building damage detection in satellite imagery using convolutional neural networks, In *33rd Conference on Neural Information Processing Systems (NeurIPS 2019)*, Vancouver, Canada, (NeurIPS), 2019. Available at: http://arxiv.org/abs/1910.06444.

[11] M. Erdogan, and A. Yilmaz. Detection of building damage caused by Van Earthquake using image and digital surface model (DSM) difference. *International Journal of Remote Sensing*, Taylor & Francis, 40(10):3772–3786, 2019, DOI: 10.1080/01431161.2018.1552816.

[12] G. S. Merlin and G. W. Jiji. Building damage detection of the 2004 Nagapattinam, India, Tsunami using the texture and spectral features from IKONOS images. *Journal of the Indian Society of Remote Sensing. Springer India*, 47(1):13–24, 2019. DOI: 10.1007/s12524-018-0858-z.

[13] L. Dong, and J. Shan. A comprehensive review of earthquake-induced building damage detection with remote sensing techniques. *ISPRS Journal of Photogrammetry and Remote Sensing*, International Society for Photogrammetry and Remote Sensing, Inc. (ISPRS), 84:85–99, 2013. DOI: 10.1016/j.isprsjprs.2013.06.011.

[14] P. Gamba and F. Casciati. GIS and image understanding for near-real-time earthquake damage assessment. *Photogrammetric Engineering and Remote Sensing* 64:987–994, 1998.

[15] H. D. Guo, L. L. Lu, J. W. Ma, M. Pesaresi, and F. Y. Yuan. An improved automatic detection method for earthquake-collapsed buildings from ADS40 image. *Chinese Science Bulletin*, 54(18):3303–3307, 2009.

[16] M. Rezaeian and A. Gruen. Automatic classification of collapsed buildings using object and image space features. *Springer: Geomatics Solutions for Disaster Management*, 135–148, 2007.

[17] X. Tong, Z. Hong, S. Liu, X. Zhang, H. Xie, Z. Li, S. Yang, W. Wang, and F. Bao. Building-damage detection using pre- and post-seismic high-resolution satellite stereo imagery: A case study of the May 2008 Wenchuan earthquake. *ISPRS Journal of Photogrammetry and Remote Sensing*, 68:13–17, 2012.

[18] M. Turker, and B. Cetinkaya. Automatic detection of earthquake-damaged buildings using DEMs created from pre- and post-earthquake stereo aerial photographs. *International Journal of Remote Sensing*, 26(4):823–832, 2005.

[19] A. Singh. Review article digital change detection techniques using remotely-sensed data. *International Journal of Remote Sensing*, 10:989–1003, 1989.

[20] D. Brunner, G. Lemoine, and L. Bruzzone. Earthquake damage assessment of buildings using VHR optical and SAR imagery. *IEEE Transactions on Geoscience and Remote Sensing*, 48(5):2403–2420, 2010.

[21] S. W. Myint, M. Yuan, R. S. Cerveny, and C. P. Giri. Comparison of remote sensing image processing techniques to identify tornado damage areas from Landsat TM data. *Sensors*, 8:1128–1156, 2008.

[22] S. Radhika, Y. Tamura, and M. Matsui Texture-wavelet analysis for automating wind damage detection from aerial imageries. In *Proceedings of the 2013 3rd IEEE International Advance Computing Conference (IACC)*, 1246–1250. Ghaziabad, India, 22–23 February 2013.

[23] E. Sagara. Hurricane Sandy's Destruction: Aerial Assessment Shows Nearly 72K Buildings Damaged in NJ. The Star Ledger. 18 November 2012. Available online: https://www.nj.com/news/2012/11/hurricane_sandys_destruction_a.html (accessed on 20 November 2019).

[24] T. Balz, and M. Liao. Building-damage detection using post-seismic high-resolution SAR satellite data. *International Journal of Remote Sensing*, 31:3369–3391, 2010.

[25] S. Radhika, Y. Tamura, and M. Matsui. Use of post-storm images for automated tornado-borne debris path identification using texture-wavelet analysis. *Journal of Wind Engineering and Industrial Aerodynamics*, 107:202–213, 2012.

[26] F. Yamazaki, T. T. Vu, and M. Matsuoka. Context-based detection of post-hazard damaged buildings in urban areas from satellite images. In *Urban Remote Sensing Joint Event*. 1–5, IEEE, Piscataway, NJ, USA, 2007.

[27] S. Ye, S. H. H. Nourzad, A. Pradhan, I. Bartoli, and A. Kontsos Automated Detection of Damaged Areas after Hurricane Sandy using Aerial Color Images. In *Proceedings of the Computing in Civil and Building Engineering*, Orlando, FL, USA, 23–25 June 2014.

[28] Y. Ham, K. K. Han, J. J. Lin, and M. Golparvar-Fard. Visual monitoring of civil infrastructure systems via camera-equipped Unmanned Aerial Vehicles (UAVs): A review of related works. *Visualization in Engineering*, 4:1, 2016.

[29] N. Hallermann, and G. Morgenthal. Visual inspection strategies for large bridges using Unmanned Aerial Vehicles (UAV). In *Proceedings of the 7th IABMAS, International Conference on Bridge Maintenance, Safety and Management*, 661–667. Shanghai, China 7–11 July 2014.

[30] J. Fernandez Galarreta, N. Kerle, and M. Gerke. UAV-based urban structural damage assessment using object-based image analysis and semantic reasoning. *Natural Hazards and Earth System Sciences*, 15:1087–1101, 2015.

[31] K. Han, J. Lin, and M. Golparvar-Fard. A formalism for utilisation of autonomous vision-based systems and integrated project models for construction progress monitoring. In *Proceedings of the 2015 Conference on Autonomous and Robotic Construction of Infrastructure*, Ames, IA, USA, 2–3 June 2015.

[32] N. Michael, S. Shen, K. Mohta, V. Kumar, K. Nagatani, Y. Okada, S. Kiribayashi, et al. Collaborative mapping of an earthquake damaged building via ground and aerial robots. In *Field and service robotics: results of the 8th international conference*, pp. 33–47. Springer Berlin Heidelberg, 2014.

[33] M. Imran, C. Castillo, J. Lucas, P. Meier, and S. Vieweg. AIDR: Artificial intelligence for disaster response. In *Proceedings of the 23rd international conference on world wide web*, pp. 159–162. 2014.

[34] J. Chae, D. Thom, Y. Jang, S. Kim, T. Ertl, and D. S. Ebert. Public behavior response analysis in disaster events utilising visual analytics of microblog data. *Computer Graphics*, 38:51–60, 2014.

[35] M. B. Bejiga, A. Zeggada, A. Nouffidj, and F. Melgani. A convolutional neural network approach for assisting avalanche search and rescue operations with UAV imagery. *Remote Sensing*, 9:100, 2017.

[36] M. E. Kahn. The death toll from natural disasters: The role of income, geography, and institutions. *Review of Economics and Statistics*, 87:271–284, 2005.

[37] D. Goldberg, and J. Holland. Genetic algorithms and machine learning. *Machine Learning*, 3:95–99, 1988.

[38] J. Benediktsson, P. H. Swain, and O. K. Ersoy. Neural network approaches versus statistical methods in classification of multisource remote sensing data. *IEEE Transactions on Geoscience and Remote Sensing*, 28:540–552, 1990.

[39] Y. Shao, and R. S. Lunetta. Comparison of support vector machine, neural network, and CART algorithm for the land-cover classification using limited data points. *ISPRS Journal of Photogrammetry and Remote Sensing*, 70:78–87, 2012.

[40] A. J. Cooner, Y. Shao, and J. B. Campbell. Detection of urban damage using remote sensing and machine learning algorithms: Revisiting the 2010 Haiti earthquake. *Remote Sensing*, 8:868, 2016.

[41] Y.-J. Cha, W. Choi, and O. Büyüköztürk. Deep learning-based crack damage detection using convolutional neural networks. *Computer-Aided Civil and Infrastructure Engineering*, 32(5):361–378, 2017.

[42] Pouyanfar, S., and S.-C. Chen. Automatic video event detection for imbalance data using enhanced ensemble deep learning. *International Journal of Semantic Computing*, 11(01): 85–109, 2017.

[43] S. Srivastava, S. Gupta, O. Dikshit, and S. Nair. A review of UAV regulations and policies in India. In *Lecture Notes in Civil Engineering*, vol. 51, 315–325. Springer, 2020. https://doi.org/10.1007/978-3-030-37393-1_27.

[44] T. Zwegliński. Using drones in disaster aerial needs reconnaissance and damage assessment-Three-dimensional modelling and orthophoto map study. *Sustainability (Switzerland)*, 12(15):1–20, 2020. DOI: https://doi.org/10.3390/su12156080.

Cemre Kılınç, Süleyman İpek, Esra Mete Güneyisi*, Erhan Güneyisi

# 10 Recent developments in the building information modeling-based programs used for structural and architectural purposes

**Abstract:** Nowadays, building activities are expanding quickly, and the requirements in the design and construction sectors are developing. Devoted to these requirements, programs based on building information modeling (BIM) are employed to create digital representations of the physical and functional characteristics of spaces and to manage project processes. BIM-based programs enable the creation of computational and parametric designs while also enabling the simultaneous fabrication of the project. Thanks to these programs, the project management process keeps moving forward quickly while the construction process is not negatively impacted by the design-related modification. However, since they can allow interdisciplinary work and cooperation, BIM-based programs are regarded beneficial. Diverse professional groups are simultaneously active in the design projection stages, encouraging the use of a common language and working as a community, ensuring a coordinated effort. It can be stated that BIM-based programs were not immediately introduced into the building sector with all these beneficial aspects and underwent a development and change process like how all computer-based programs go through in their development phase. This chapter covers the latest scholarly developments in the BIM-based programs used for structural and architectural purposes.

## 10.1 Introduction

A correct definition of building information modeling (BIM) has been given by the British Standards Institute as “BIM is a process where data about a building is generated and managed throughout the course of its entire life.” In this regard, BIM can be considered a system where each building element is represented by a 3D component at its center, and formed as a package in which the processes and technologies are integrated. Building information modeling (BIM) is a technology that allows the crea-

---

***Corresponding author: Esra Mete Güneyisi,** Department of Civil Engineering, Gaziantep University, 27310 Gaziantep, Turkey, e-mail: eguneyisi@gantep.edu.tr
**Cemre Kılınç, Süleyman İpek**, Department of Architecture, Bingöl University, 12000 Bingöl, Turkey
**Erhan Güneyisi,** Department of Civil Engineering, Harran University, 63300 Şanlıurfa, Turkey

https://doi.org/10.1515/9783110791426-010

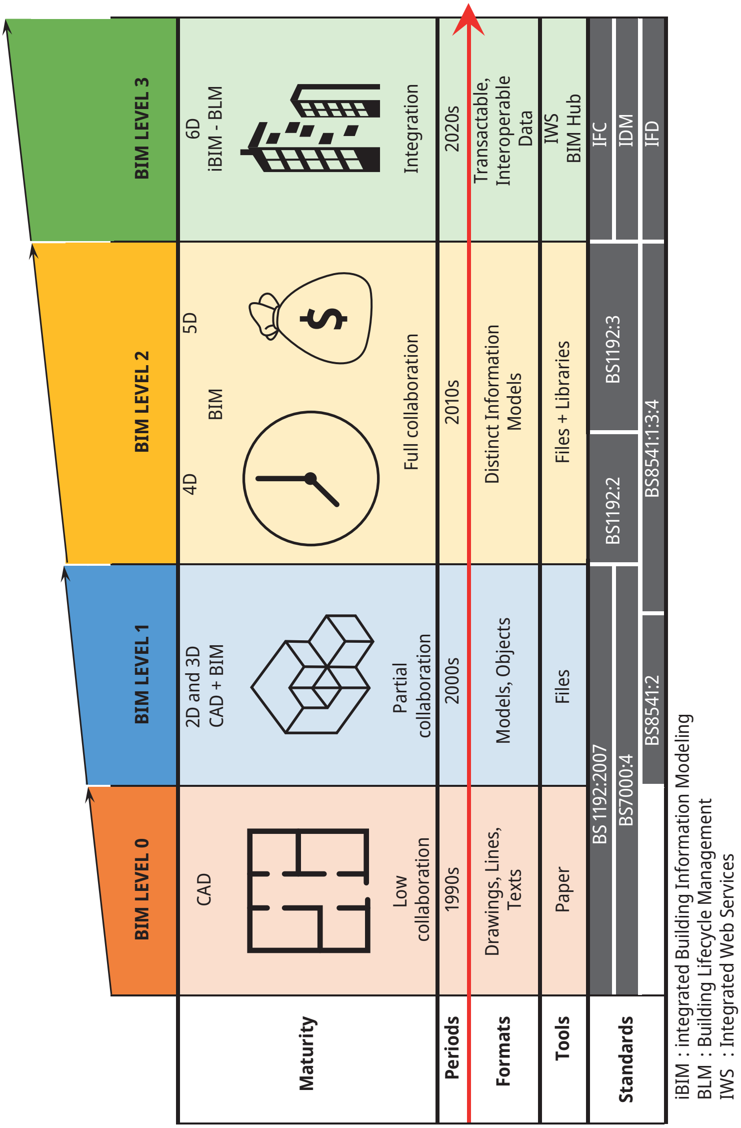

**Figure 10.1:** BIM levels depicting the maturity levels (inspired from the BIM levels presented by [17–20]).

tion, storage, management, and modification of three-dimensional (3D) parametric and object-based project productions in the architectural, engineering, and construction (AEC) sectors [1]. BIM technology can also be expressed as creating a digital twin of a structure prior to its construction [2]. While BIM technology has been used by a few companies till a short time ago, it has now begun to become a common tool in the AEC sector [3].

The ability of the BIM-based software to continuously advance the analytical process throughout the design phase is by far its greatest benefit. The BIM software that has a multiple-layered running feature can be revised in the modeling stage of the structure and of the building while the analysis stage continues. The project management stage may readily include the new possibilities that may arise during the design phase, and the project can go forward in a planned manner without suffering any harm [4–7]. This allows for the simultaneous solution of several issues with a small margin of error. On the other hand, BIM-based programs offer concurrent incorporation of several professional groups into a project by presenting parametric design principles. Being a revisable infrastructure, BIM has additional benefits for the collaboration of disciplines throughout the project design [8]. This scenario makes the project simple to manage and reduces coordination problems between the many professional groups [9, 10]. As a result, the project creation stages progress steadily [11, 12].

Currently, BIM-based software has begun to replace conventional design approaches due to technological advancements [13]. BIM technology has gotten ahead of traditional delivery methods that are thought of as two-dimensional (2D) by having numerical information storage with regard to all project data, and offering access opportunities at any time. Especially during the project stage, a more efficient control compared to the traditional stage is provided since the digital designs have countless numerical data that constitute the BIM, and can be updated with changes [14, 15]. BIM technology, which is based on a design tool at a file level, involved period, and the amount of collaboration, can be handled at four different maturity levels as indicated in Figure 10.1 and as described below [16, 17]:

- The first level, often known as Level 0, is the one that addresses a project's fundamental components. It covers the use of paper-based CAD drawing techniques, which are typically seen as the stage prior to BIM. Further, it is an outdated level, where cooperation is almost nonexistent and is slowly being abandoned by occupation specialists today.
- The second level, or Level 1, is arguably the most popular BIM level, combining 2D documentation with 3D CAD concepts. It is regarded as a system where CAD files and BIM work together in a basic database that is developed for sharing purposes. While there is more cooperation at this level compared to the previous level, it is still done under the contractor's control and in an electronic environment using common data sharing methods.
- The third level, Level 2, focuses on collaboration across disciplines. Although different professional groups work on separate models, they always use the same

standard file format for recording and sharing. This is highly useful since it enables simultaneous disciplinary control over a project.
- Level 3, also known as Open BIM, is a result-oriented level where the parties involved in all processes of the project can access the model produced through a common central system, and much more comprehensive and deep cooperation is offered. Since all parties can simultaneously access the entire information during the building process, the risk is reduced.

As stated earlier, BIM-based programs, as a digital representation of a structure, have the capability of simultaneously incorporating several professional practices. These practices are conducive to many actors participating in a project. While each individual in any professional practice works alone in the traditional method of project production, BIM technology has succeeded to meet all professional practices on a common ground so as to be integrated, if required. In this direction, considering in the view of different professional practices:

(i) in architectural practice, BIM technology offers a method of parametric design to the users. This feature provides advantages to architects by constituting the forms such as organic and fractal, excepting linear design forms, on the realistic ground. At the same time, BIM gives architects a significant advantage in terms of visualization. In contrast to the traditional approaches, BIM-based programs allow the production and visualization tasks of the project to be performed simultaneously. For example, it is possible to create a section, a façade, and a 3D model all at once when an architectural design is drawn. Thanks to these programs, render presentations that are a significant piece of visualization of an architectural project can be rapidly generated. In this particular, it can be stated that when the BIM-based programs are taken into consideration in the architectural context, they provide a work package that includes design, visualization, parametric modeling, clash detection, building performance analysis, data management, object library, and collaboration tools.

(ii) on the other hand, BIM technology has begun to be favored in construction practice as a result of project management programs that offer prospects for time saving during the construction phase, estimating potential issues at the construction site caused by the assembly. Integration of architectural design and structural features during the project preparation stage might save time. Considering the intensity of structural elements in a project model, these elements may clash much more in the case of traditional 2D methods; however, thanks to the BIM-based programs, detection of such cases becomes easy, and project planning and project management progress much more properly. Additionally, the stage where every detail is manually managed on paper has been converted into standard software as a paperless system, making it simple to control the workflow on the construction site [21]. This coordinated work provides minimized error margin for manufacturing and quantity takeoff cost calculations. Similar to the architectural context, when the BIM-based programs are taken into consideration in the structural context, it can be said that it provides a work package involving building performance analysis, data management, planning, on-site software, and collaboration.

When it is evaluated in general, the following can be delivered simultaneously through the BIM-based programs, as also presented schematically in Figure 10.2 [3]:

- The whole process of the project, from the idea stage to the stage, when the building is built and delivered, can be planned [*Programming phase*],
- By transferring to the computer, every aspect of the project that is intended to be produced, from the first idea to the smallest detail, can be identically designed [*Design phase*],
- The components can be modeled prior to the construction process, and the site coordination can be organized prior to the building process [*Preconstruction phase*]
- The entire model may be built in accordance with the real conditions, and any modifications can be implemented simultaneously and immediately during manufacturing on-site [*Construction phase*],
- By moving through a second phase, when the building's operations and maintenance were handled after construction is complete, management and sustainability can both be supplied [*Operations and Maintenance phase*],
- The service life of the building can be foreseen, and recycling of the building by separating out the components can be monitored, and as a consequence, it can be provided that when the building completed its service life, it is no longer a rubble waste [*Demolition phase*].

It is believed that to comprehend the direction that BIM-based programs are going, which is considered to be more involved in architectural and engineering applications in the near future, it is required to look at the historical development process by reading from the past to the present.

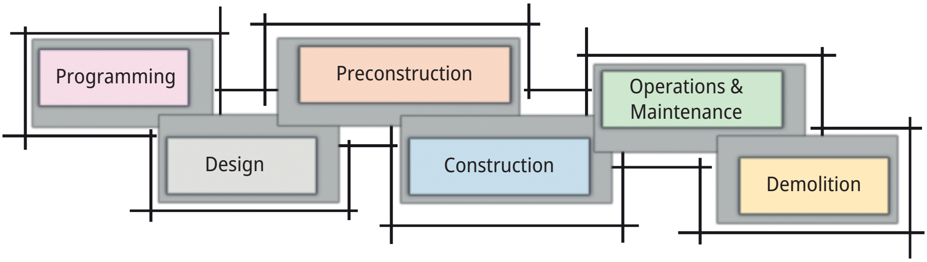

**Figure 10.2:** Visual representation of BIM's stages adapted from the study of Azhar et al. [3].

## 10.2 Historical development of BIM

Although BIM-based programs are becoming more popular today, they have a long history that dates back to the 1960s. The foundation of BIM technology, employed in the AEC sectors, is 2D computer-aided drafting (CAD) programs, also known as computer-aided design tools. The start of this technology to the AEC methodology began with putting the Sketchpad program providing 2D drawing potential on the market in the year 1963. This program gives the opportunity to digitally illustrate projects that are created on paper. The number of such 2D programs has gradually increased, following the meeting of manual drawing with technology. But due to the increase in the size of the projects, indirectly built structures, and with increase in their functions as a result of the development of technology, these programs began to be insufficient [22]. In 1977, Charles Eastman advocated that 2D programs fell short and then started to evolve Graphical Language for Interactive Design [23]. Research institutes for the creation of workspace-presenting programs with parametric databases were established in the 1980s; these studies served as the foundation for the creation of BIM-based technology. It was considered that CAD software, together with the newly generated software types, did not provide parametric solutions software types with databases that contain descriptions of a model's whole geometry [24] and this situation led to the gradual widespread use of the BIM technology.

The program, with the name Archicad, was released to the market in 1984 by a firm called Graphisoft. In addition to being a tool that uses Eastman's developed graphical language, Archicad serves as the basis for all BIM-based systems developed after it [25]. On the other hand, the RUCAPS software system developed in 1986 is a program that first takes into consideration the temporal phasing concept of the building period of a structure. The program was employed in the stepwise construction of Terminal 3 of Heathrow Airport [2]. The Center for Integrated Facility Engineering's establishment in 1988 is recognized as the turning point for BIM technology. The center developed a considerable resource for the purpose of advancing the development of four-dimensional (4D) building modeling [26]. The Building Design Advisor developed in 1993 was used to model a building and simulate its context. The program consists of a medium where the graphic analysis and simulation, from the conceptual first stages of a building to the features of the whole building components, were integrated. In addition to this, the program offers a basic optimization option with producing solutions for a building model in the direction of alternative conditions [27]. The CATIA program, whose inception dates back to 1977, has had a remarkable evaluation through time as a 3D program designed by the airplane manufacturing company, Dassault System. The program and the substructure it offers were used in the Guggenheim Museum, constructed in Bilbao, Spain in 1997, and has come to the forefront of architectural and structural projects by making quite complex forms real [28].

CAD software has begun to lag behind BIM-based programs since the early 2000s as a result of the advancement of parametric modeling and technological development, and BIM-based programs have begun to be integrated into the applications of AEC projects [3]. Revit software, which is based on using object-oriented programming, was launched in the market for the construction industry in 2000. In 2002, the software was purchased by a company named Autodesk and it evolved according to the company's politics. Revit created a revolutionary effect by modeling all components of a building with the parametric language it uses, and integrating the fourth dimension, time, into the structure [6, 26]. Revit gained popularity as a program, where an interdisciplinary link was offered by creating the versions, as being integrated into the architectural substructure, prepared for civil and mechanical engineers in recent years by Autodesk. The collaboration made possible by BIM technology enabled the creation of larger and more intricate building projects. The integration of different professional practices drew the attention of big construction companies and promoted them to use BIM technology in their projects. The FormIt-named software developed by Autodesk in 2012 with a motto of "every project starts with a sketch" became a software of BIM, providing usage on mobile devices. This software, where the modeling incorporates fingers with a digital pencil, has become a leaping point for the BIM world [29]. Numerous BIM-based tools have been developed and released in the years after the year 2000. The aforementioned types of software have become the pioneer of recent programs and contributed to their developments. From the past to the present, it is anticipated that BIM technology has left its mark in the construction industry and in production sectors in terms of providing the programs used by the different disciplines to come to the same ground and make rapid progress.

## 10.3 Categorization of BIM-based technology

BIM, a collaborative digital building process, is a technology with steadily rising users that has been evolving and expanding quickly in recent years. According to the tenth annual BIM report published by the National Building Specification (NBS), a UK-based business, only 13% of the design and other construction professionals were using BIM programs in 2010, while that number had increased to 73% as of 2020. Again, per the same report, while the rate of people who have never heard of BIM technology was 43% in 2010, this rate decreased to 1% in 2020 [30]. Based on these findings, it can be concluded that the usage of BIM technology is spreading throughout the professions of designers, manufacturers, architects, engineers, and contractors [31]. According to the Allied Market Research's report on the BIM in Construction Market, as of 2019, this technology's market value was €4.5 billion. Again, according to this report, it is estimated that this market will grow by about 15.2% annually and reach a value of €13.7 billion by 2027 [32]. From this information, it can be deduced that new software will be added to the BIM technology industry, which currently has already a large selection of software. Finding the right program to employ from all of these options may be quite challenging.

BIM users are not required to utilize or have knowledge about every software in this context, but they are expected to have a conceptual understanding of the applications of BIM-based software across a variety of disciplines, as well as a working knowledge of the current software [33]. Categorizing BIM technology under the subheadings of design, construction, and operation/maintenance phases as presented in Figure 10.3 will make it very easy for the user to both learn and follow the developments in this context. As can be seen from the given figure, BIM-based programs can be categorized under the subheadings of parametric modeling, object library, design, collaboration, visualization, and conflict detection in the design phase category; on-site and planning software, data visualization and management, collaboration, and 4D&5D concepts in the construction category; parametric modeling, building performance analysis, and data management and visualization in the operation/maintenance phase category. Here, it should be noted that parametric modeling is a common subheading in the design and operation/maintenance phases, data management and visualization are a common subheading in both the operation/maintenance and construction phases, and collaboration is a common subheading in the design and construction phases. In this regard, further information on these subcategories and the software that is frequently employed in them is provided Figure 10.3.

### 10.3.1 Parametric modeling [in design and operations/ maintenance phases]

The term “parametric” means the one related to numerical or other measurable factor or factors, constituting one of the clusters that define a system or determine the operation conditions, or expressed by them. When it is used for design purposes, nevertheless, it represents the ability to apply the dimension modification to its form when the value of a dimension pertaining to geometry is altered [34**]**. When it is taken into consideration in this context, parametric modeling in BIM technology is a joint technology service that is included in both the design phase and the operations/ maintenance categories, as can be seen in Figure 10.3. But it should be noted that the thing intended to be expressed by the parametric modeling notion given under the design phase category differs from the thing intended to be expressed in the notion given under the operations/maintenance category. While the concept of parametric modeling in the design phase takes its name from the project variables that are being changed during the design and simulation phases of the project [35], the parametric modeling concept in operations/maintenance phases frequently takes its name from the human, environmental, technical, and financial variables that occur during the digital transformation of the real estate assets [36]. Thereby, the parametric modeling in the design phase helps to model and optimize the feasibility of the project and offer adherence to the submission guidelines [35]. On the other hand, the parametric modeling provided under the issue of operations and maintenance enables the creation of digital records for use in operation, service, and maintenance once the building is handed over [36]. In both cases, more visible and more flexible projects with a higher analysis depth are presented to clients by parametric modeling.

The information and data are associated via algorithms on a digital platform and the whole system is updated in the case of any change. As a consequence, human errors are eliminated or minimized and crucially, the time spent for updating the designs is decreased. Parametric modeling tools, composed of a series of mathematical equations and algorithms, must be predicated on data from a real project or must be verified using data from a real project in order to be valid. It can be tested by mathematical models, of which indeterminacy cases were previously described and proved, and its previous experiences can be easily embodied. Besides, since they have less prejudgment than the human thinking processes, it is much easier to design that are gradually becoming complex, with fewer sources and within a shorter time [35]. In this context, parametric modeling can be generally defined as a modeling approach of creating a product platform conforming to past-based design strategies and offering design automation [37]. Programs with the commercial names of *Catia*, *SolidWorks*, *AutoDesk Fusion 360*, *Hypar*, *SpaceMaker*, and *Dynamo* are frequently used in the parametric modeling of the design phase, whereas those with the commercial names of *MainManager*, *ArchiBus*, *Active 3D*, *Ecodomus*, *Ajour*, *Dalux*, *Spinal*, and *PlanIt* are generally employed in the parametric modeling of the operations/maintenance phase.

## 10.3.2 Object libraries [in design phase]

By positioning the objects, the model produced in any design tool gains significance. Objects not only bring a model design to a better level but also make it technically understandable. The designed objects can be of any size and type. A model designed in an architectural sense takes on significance with the objects in it. The architectural design expresses itself better and becomes meaningful by detailed modeling of a chair in the kitchen, an armchair in the living room, a bed in the bedroom, a floor lamp on the dresser, or a soap dish in the bathroom. These models' textures and materials, in addition to their well-thought-out model, form them with all the necessary technical aspects, giving them their realistic appearance. Object libraries provide a distinct discipline inside the BIM technology by assigning realistic textures and materials to the designed models.

It is not necessary to prepare objects just in modeling programs. Object libraries can operate independent of the designed application, thanks to the infrastructure provided by BIM. As the programs may be associated with a BIM infrastructure with a common denominator, the location and extension of the file may no longer matter. Any equipment that has been meticulously designed may move from one platform to another. Since the models of the designed objects are already available, this condition offers accessibility, and speeds up the project manufacturing process. All these possibilities become an advantage for program users [26]. Commercial programs like *MagiCAD*, *Avail*, *Bimobject*, *BimCo*, and *Unifi* are favored for creating an object library during the design stage.

### 10.3.3 Design [in design phase]

Any BIM-based program offers the user a wide range of design possibilities. Each step of the design is drawn separately and sequentially when using a standard 2D application for design. Every sketch, therefore, has a large margin for error. On the other hand, each stage is drawn simultaneously while creating a model in a BIM-based program. The program issues a warning if an error occurs at any point. In this way, faults from all other stages are fixed along with the drawing. Unlike a CAD-based system, which expresses the design in lines, BIM-based designs use real elements to represent the actual building components. Besides, with the BIM-based system, forms like organic, amorphous, and fractals that can be challenging to represent in any 2D application can be designed on a realistic foundation. However, the diversity of programs that BIM provides makes it a favored technology, and makes parametric drawings easier [23]. The integration of both time (4D) and cost (5D) concepts in design is made possible by BIM technology, which goes beyond merely creating boundary-definite spaces [16]. Thus, the boundaries of a building conceptualized in the BIM technology can be integrated into the model, as well as its materials, with both their qualities and cost. In the design phase, *Revit*, *Tekla Structures*, *Allplan*, *ArchiCAD*, *Autodesk Civil 3D*, *Novapoint*, *Bentley*, and *BricsCAD* commercial programs are generally used to design a model.

### 10.3.4 Collaboration [in design and construction phases]

Collaboration and working in a real collaborative workplace, backed by digital technology, are two very different things. Operational tools that enable full participation of all participants in the construction process are now integrated into the technology, resulting in greater overall productivity. Building Information Modeling and Management, an integrated management system that enables time, cost, and quality control, in addition to 3D visualization, gives the chance to more effectively address this shortcoming in the architectural, engineering, construction owner, and operator sector. Design and construction activities in the architectural, engineering, construction owner, and operator sector include several interconnected firms working together to offer customized solutions to owners [38]. While this association is mostly managed on paper in the conventional working environment, BIM has left this practice behind. BIM-based programs enable multidisciplinary collaboration by enabling the transmission of drawings through an integrated software so that the design team and the construction team may collaborate on the same foundation [39]. In project-based construction, each partner has his/her own specialties, work schedules, and obligations, in addition to his/her own culture, values, and interests. The resulting BIM-enabled projects are therefore carried out through a significant network of various professional specialists [40]. The ultimate objective herein is to ensure that all project participants and stakeholders comprehend the expected outcome as well as their specific responsibilities and roles. The key tools required for the success of the project include the BIM Execution Plan and the Common Data Environment, a document shared in a common digital environment that should clearly include roles, responsibilities, processes, and specific outcomes, and supported by initial and ongoing mandatory training [41]. The effectiveness, degree, and relevance of collaboration in such initiatives also determine BIM technology's sales value [42]. However, in recent years, there have been some developments that have influenced the way joint work and collaboration, including the organization of construction projects and the roles of different participants, most notably the trend toward greater openness among project participants [43] and the proliferation of BIM [44]. Additionally, the existence of several distinct organizations and professional groups, in addition to the physical distance between them, might make it difficult to maintain a cooperative relationship [45]. In this context, while collaboration in the design phase is usually done with commercial programs such as *Isetia*, *Aconex*, *Autodesk Bim 360*, *Bim Track*, *Imerso*, and *Bimsync*, collaboration in the construction phase is usually done with commercial programs such as *Interaxo*, *Revizto*, *Bim Collab*, *Thinkproject*, and *Trimble Connect*.

### 10.3.5 Visualization [in design phase]

The term "Visualization" can be defined in the most traditional sense as transferring a building in a 3D model. One of the most prominent aspects of BIM-based programs is visualization. There are visualization tools that are not BIM-based as well, but BIM-based programs offer a lot of opportunities to users in this regard. A model may be expressed and rendered in 3D with success, effectiveness, and high quality using visualization software other than the BIM-based ones. However, BIM-based programs extend the concept of visualization by integrating the existing environmental analysis and sustainability analyses into the 3D model. Namely, the designed model is not independent of its context but can be represented along with the entire built environment in which it is located. The realistically designed environment helps to evaluate the model in terms of physical criteria such as the location and height of the model, its closeness to neighboring buildings, if any, and the approach of vehicle/pedestrian pathways. Furthermore, other environmental aspects such as solar orientation, climate information, energy demand estimation, and the building's need for natural light can be added to these criteria in order to provide a real basis for the model. Besides, an accurate integration of the desired material, texture, and color into the model is another element that lends realism to a model, and BIM does this successfully. With the cooperation of BIM-based platforms, models are created and then rendered on common platforms by assigning materials-textures-colors, providing very realistic productions.

In addition, in terms of effectively conveying the shape of a model, BIM-based programs have become highly preferred. BIM technology may also be used to model projects with tough parametric design decisions and set them on a realistic foundation for construction [46]. With technological advancements, BIM has begun to be combined with virtual reality applications. Through add-ons to the programs, projects can be experienced while they are still in the design phase, which is advantageous not only for clients but also for sector personnel and contractors. The integration of BIM with augmented reality applications provides a great advantage to the sector's employees in field studies and helps in the adoption of technology [47]. All these make BIM-based programs more advantageous than other 3D modeling programs. Commercial programs named *Vrex*, *Isetia*, *Insite VR*, *Kubity*, *Fuzor*, *Lumion*, *Kubity*, *Fuzor*, and *Lumion* are frequently used for visualization during the design phase.

### 10.3.6 Clash detection [in design phase]

BIM-based programs offer the ability to describe clashes between any two elements, of which there are several kinds available during the architectural design stage. Additionally, the programs determine if one element interacts with another one or not, as well as how an element integrates with another when it does. In conventional design techniques, these clashes can be seen as long as attention is paid on paper. If the model is being constructed, there may be significant losses in terms of labor, time, and money. However, in BIM-based technology, these clashes are detected by the programs at the design stage, and thereby, the program warns due to clashes in the model. Programs whose commercial names are *Navisworks*, *Isetia*, and *Solibri* are generally used for clash detection during the design phase.

### 10.3.7 Data management and visualization [in construction and operations/maintenance phases]

Data management and visualization are two important common subheadings that can be categorized under both the construction and operations/maintenance phases. Understanding the significance of data, meaning facts and figures put together for reference or analysis is crucial in order to know what data management and visualization represent. At this point, it can be said that data is important because it enables people, organizations, and companies to make better decisions, solve problems more easily, evaluate performance quickly and easily, improve processes, and comprehend clients or consumers better [48]. That is why companies, institutions, or organizations, small or large, profit or non-profit, private or public, are undergoing a digital transformation where they are applying ones and zeros as best they can. Today, with the data gathered on the basis of these ones and zeros, everything from people's behavior to habits, needs, and consumption is modeled through mathematical expressions and algorithms, and predictions are made about what will happen tomorrow, what will be needed, and how people will behave. In this context, due to the similar needs in BIM-based technology, continuous data collection and both visualization and management of these data are important. As a matter of fact, all BIM-based programs that have been developed, are being developed, and will be developed are based on the use of this data. Therefore, the management and visualization of data are important both for the operation and use of the programs. Compiling and organizing the gathered data into groups or classes is the initial step in data management. Then, while presenting this classified data, visualization tools such as pie charts, bar charts, histograms, area charts, scatter plots, timelines, Gantt charts, heat maps, highlight tables, and bullet graphs are used to analyze and understand the data. In this context, three main groups were defined for the collected data: unstructured, semi-structured and structured [49, 50].

As the name suggests, the unstructured data type is data that has no established format. It may include a mix of text, video, email, and image files, but it can only be useful when properly organized, processed, and analyzed. Data of this kind has no specific format or order, does not follow any rules or semantics, has no easily recognizable structure, cannot be stored in a spreadsheet-like format (i.e., based on rows and columns), and cannot be directly used or understood by a program. Unstructured data is estimated to account for 80% of the world's official data [51, 52].

A semi-structured type is a data type that may be handled via metadata tagging, which will enable us to capture useful information. With this type of data, it is difficult to determine the meaning of the data and even more difficult to store the data in rows and columns, as in a standard database; so it is not always possible to automate data analysis, even if metadata is available. Data of this type may not have identical properties within the same group, are grouped with similar entities, do not fit into a data model but contain tags and metadata, and cannot be kept in a spreadsheet-like format, that is, based on rows and columns [51, 52].

The third type of data is structured data, which is a systematic database that can be used right away by companies for processing and analysis. It consists of information transformed and formatted into a well-defined data model. Such data is translated into fields with pre-built layouts that may be read and retrieved by a related database. This method of storing information is the ideal of the three types, and although the relational model minimizes data redundancy, it still requires caution because structured data is more interdependent and, therefore, sometimes, less flexible. The most important characteristics of this type of data are that it conforms to a data model, similar entities are grouped, the characteristics within the same group are the same, the data is contained in fixed fields within a record, and the definition and meaning of the data are clearly known [51, 52].

What is actually targeted by data management and visualization can be better expressed by the DIKW hierarchy, a four-tiered pyramid of data, information, knowledge, and wisdom. The DIKW hierarchy is a hierarchy of relationships that describes how raw data can be transformed into information, then knowledge, and then wisdom, with each layer adding specific attributes over and above the previous one [51]. In this hierarchy of relationships, data is the most basic level; information adds context; knowledge determines how to use it; wisdom determines when and why to use it [53]. Thus, as you move up the pyramid, data without any specific meaning is transformed into knowledge, and then wisdom, by applying structure, organization, classification, and categorization [51]. As a result, we can think of data management and visualization as a way to “approach” and eventually “solve” problems in the BIM-based technology. Programs whose commercial names are *Isetia*, *ProjectWise*, *ViewPoint*, and *BIMEye* are frequently used in the data management of the construction, whereas those having commercial names of *Areo*, *Tableau*, *Domo*, *Isetia*, and *Data Studio* are generally employed in the data visualization of the construction. On the other hand, commercially named programs such as *Opidis*, *Isetia*, *dRofu*s, *GliderBIM*, and *Verify3D* are broadly used programs in the data management of operations/maintenance.

### 10.3.8 On-site and planning software [in construction phase]

The construction of the structure, which is designed and detailed, is a process that requires systematic and controlled work. This stage, which is at least as important as the design stage on the road, from design to construction, is a stage that requires serious cooperation, organization, responsibility, planning, and safety measures. Although it seems to take place entirely on the field, it is carried out with serious office support in the background. In this construction process, where both time and cost are taken into account, many technical teams work together, and the productions are carried out according to a certain timetable and succession relationship. The organization of the construction site, the follow-up of the production and schedule, the coordination between the teams, the planning of the process, and taking the necessary security measures are vital for the healthy and trouble-free construction of a project in this process, where any disruption can both delay the construction and pose serious financial and security problems. The main objective of this process is to complete the construction without any safety problems, without any loss of time and/or additional costs, and with smooth and targeted quality production.

In this context, BIM technology offers a wide range of programs related to the process described above, helping to ensure that the project is completed to the desired specifications, on schedule, on time, at the projected cost, and with zero safety problems. BIM technology makes planning more efficient, reduces the risk of schedule overruns, identifies troublesome processes and enables early corrective measures, provides insight into current and future resource utilization for accurate forecasts and decisions, solves potential work package backlogs by leveling or modifying them, enables the ability to create and collaborate on manufacturing or process-related checklists from anywhere with real-time access, facilitates collaboration with subcontractors, enables easy security measures and notification of protocols in this context, and saves time while reducing risk [54, 55]. In addition, teams are categorized and notified through BIM-based programs so that there is no complication, and progress or setbacks are continuously reported, enabling instant monitoring of changes and costs. It facilitates work follow-up by providing systematic and immediate notification of the work done and to be done. It is possible to involve both the contractor and the clients. In addition to all these, by enabling surveillance and tracking of financial mobility from a single point, possible losses are prevented [56]. With all these benefits, BIM technology makes a significant contribution to the safe completion of the construction, both within the planned timeframe and at the targeted quality and cost. Commercially named *StreamBIM*, *CoConstruct*, *CheckD*, *Dalux*, *PlanGrid*, *Isetia*, and *Fonn* programs are frequently used as on-site software during the construction, whereas those named *Powerproject*, *Primavera*, *Tilos*, *Office Project*, and *Isetia* are generally employed as planning programs during the construction.

### 10.3.9 4D and 5D concepts [in construction phase]

The most remarkable features offered by BIM-based technology are 4D and 5D concepts. In its basic sense, 4D is the inclusion of a temporal component in a 3D model. The project process is time management and involves all stakeholders such as employers, contractors, and technical staff in the AEC sector. When effective management of time, one of the most critical issues in the sector, is provided, a more efficient process is ensured in terms of the project's production budget as well, thereby, better site organization is accomplished by designing and incorporating project deadlines into the BIM infrastructures. In addition, project timeframes are used to analyze design modifications and/or revisions to prevent misunderstanding during planning. In the event of problems, disruptions, and changes, field crews can more rapidly ascertain in what stage and how much of the project's progress would be impacted. As a result, stakeholders attain the least amount of job losses and the greatest possible profits. There are three primary steps in the integration of 4D into projects: modeling, planning, and assembly. All three stages should involve the time component, and they should be flexible enough to be revised and updated as needed [57].

The 5D concept, on the other hand, is a variation of the 3D concept in which the concept of time, along with the notion of cost, is included. 5D, which can also be expressed as a cost estimating feature, can be integrated into BIM models and defined as the process of calculating the new project budget in the case of any design change. Although 5D is often thought of as the stage that comes after the planning of 4D, it can actually ensure precise cost planning from the project's pre-conceptual stage. Costs can thus be analyzed comparatively as a cost estimate before the start of the project's field phase and as a cost after completion [58]. By the completion of the model phase and the start of field studies, this plan can be updated as the project progresses, and a new cost plan can be prepared [59]. In the sector, 4D and 5D software integrated into BIM-enabled projects has been increasing day by day, and time and cost have become one of the most crucial components of the AEC industry. Programs with brand names like *Powerproject*, *Cost*, *BuilderTrend*, *Synchro*, *Isetia*, *CostOS*, *Simio*, *iTWO*, *VicoOffice*, and *Assemble* are widely used in this BIM feature with a wide range of programs.

### 10.3.10 Building performance analysis [in operations/ maintenance phase]

Building performance analysis enables simultaneous testing of the design decisions within the context of the physical environmental conditions of a building as a quantitative, measurable factor. The prediction of how a building will respond to environmental and sustainability factors in the pre-construction phase is tested through analysis. Design decisions may be revised and updated, in line with the analysis of the simulations created. Building performance analysis can be performed at any conceptual or advanced stage of design. A variety of features are decided in the design of a building, such as

- its form and typology,
- its façade elements and the occupancy-void ratio on the façade,
- the properties of the building material employed,
- the location of the building,
- its surroundings and construction status, and
- the local climatic conditions

These factors directly exert an influence on the outcomes of the building performance analysis. Daylight, sun/shade, solar radiation, climate, wind, and energy analyses are among the building performance analysis methods frequently used in the BIM technology. With the analyses performed, it is possible to ensure that the proposed space will have the optimum thermal comfort, air quality comfort, and visual comfort characteristics, once it is constructed. In addition, the building designed in terms of the designated environmentally friendly materials can be made efficient, healthy, recyclable, and long-lasting in terms of energy recovery. The sustainability of a structure after construction depends on all of these features [60, 61]. During the operations and maintenance phase, programs commercially named *Green Building Studio, OneClick*, *StaadPro*, *Scia*, *Sefaira*, *Equa*, *Ies*, and *Cype* are generally used for building performance analysis.

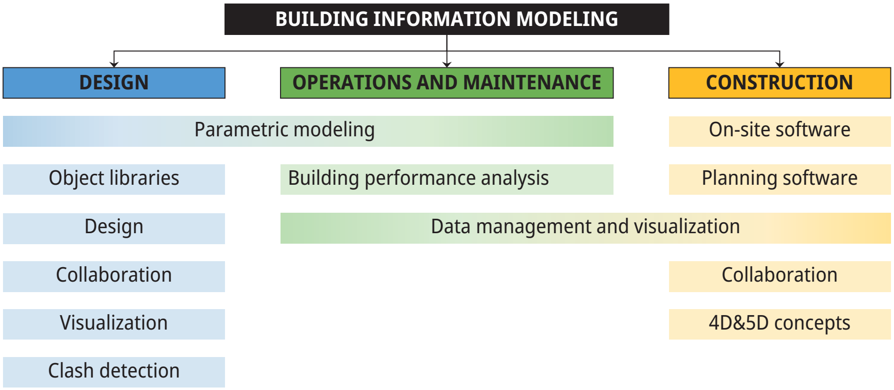

**Figure 10.3:** Categorization of BIM-based technology.

## 10.4 Stats about BIM-based technology

The paradigm shifts that the design and construction sector underwent as a result of their encounter with computers have brought them to the current-day stage. This industry, which has transitioned quickly from 2D to 3D, has brought BIM-based programs to the fore and increased their usage. From the perspective of different disciplines, BIM is now employed in the field of architecture at a rate of 60%, and it is predicted that this percentage will increase to 89% by 2024. On the other hand, it is estimated that BIM-based technology, currently used at a rate of 46% in civil engineering applications, will reach a rate of 72% in 2024, while that, employed at a rate of 51% in other engineering fields, is expected to reach 80% usability in 2024 [62].

BIM has a high market value, in addition to the services it offers to the AEC. As was previously stated, the market value of BIM was 4.5 billion € in 2019 and is anticipated to increase to 13.7 billion € by 2027. The industry needs to exhibit an annual growth rate of around 15.2% from 2020 to 2027 in order to reach this figure [31]. In this growth, it is thought that the pandemic that started in 2020 has been a driving force in making digitalization mandatory. However, the fact that some countries from Europe to Asia require BIM, in line with certain rules, has a great role in the spread of this sector. Norway, Denmark, Sweden, Netherlands, Poland, Russia, Germany, France, England, Italy, and Spain in Europe; USA, Mexico, Brazil, Chile, and Argentina in the Americas; Japan, Malaysia, and Thailand in the Asian continent; Nigeria, Ethiopia, and Tanzania in Africa; Australia and New Zealand in the Australian continent are among these countries.

Another aspect that raises interest in the use of BIM programs is the object libraries generated by them. Companies may more easily contact object creators directly, thanks to BIM as a sector. Through the agency of the partnerships established, the updating of the object designs, in accordance with the request of the companies, has been effective in the transformation of the BIM technology into a preferred brand. In this direction, sales on the BIMobject platform have surged by 51%, notably throughout the course of the 2019–2020 year [63].

Interest in BIM-based programs has risen as a result of the AEC industry adopting a collaborative working system. In this context, 73% of the companies in the AEC sector state that the collaborative working model offered by the BIM technology is more sensitive, fast, and reliable [31].

Moreover, the global interest in the construction industry and its products leads it to becoming more widespread and increasing its value. By 2060, 230 billion square meters of additional construction space are anticipated to be built, according to the United Nations Department of Economic and Social Affairs. Such an amount of production leads the AEC sector to BIM programs that produce advantageous and efficient solutions in terms of time-saving [64].

In this direction, the advancements described in the usage of BIM technology in the AEC industry provide a numerical evaluation and give ideas about the future orientation of BIM.

## 10.5 Conclusions

Given the information and explanations provided above, it can be concluded that BIM technology is on its way to becoming an indispensable component of the AEC industry, and that the industry will soon be completely integrated into this technology. With its many benefits, BIM technology, which is involved in all stages of a project, from design to operation, is used by more and more designers, architects, manufacturers, engineers, and contractors. This makes BIM to have an increasing market share in the sector.

Categorizing BIM technology under the subheadings of design, construction, and operation/maintenance will make it easier to comprehend the technology. Users can benefit from BIM in a variety of ways, including design and modeling, visualization, wide and realistic object libraries, and clash detection throughout the design process. On the other hand, during the construction phase, BIM-based technology assists the user on the basis of managing and visualizing data, providing software on-site and in planning, constituting collaboration, and offering 4D/5D concepts, while in the operations/maintenance phase, users receive services from BIM in the areas of parametric modeling, building performance analysis, and data management and visualization.

BIM technology, which is becoming more popular in the AEC industry by the day, motivates many developers to create new software due to its characteristics. As a result, a variety of BIM-based program pools are created. It is not possible for users or other interested parties to have complete knowledge of all programs. Each program has unique benefits and drawbacks. Therefore, BIM either adapts the existing programs to user or client demands or creates new programs in response to their needs, by providing user-oriented services. Consequently, it would be a more effective and rational solution to contact the developer companies after determining why the user needs BIM, with the aid of the categorization described above.

# References

[1] R. Vanlandea, C. Nicolle, and C. Cruz. IFC and building lifecycle management. *Automation in Construction*, 18(1), 70–78, 2008. https://doi.org/10.1016/j.autcon.2008.05.001.

[2] C. Eastman, P. Teicholz, R. Sacks, and K. Liston. *BIM Handbook*. John Wiley & Sons, New Jersey Hoboken, 2011.

[3] S. Azhar. Building information modeling (BIM): Now and beyond. *Australasian Journal of Construction Economics and Building*, 12(4), 15–28, 2012. https://doi.org/10.5130/AJCEB.v12i4.3032.

[4] Y. Diao, S. Kato, and K. Hiyama. Development of an optimal design aid system based on building information modeling. *Building Simulation*, 4:315–320, 2011. https://doi.org/10.1007/s12273-011-0054-3.

[5] M. O. Fadeyi. The role of building information modeling (BIM) in delivering the sustainable building value. *International Journal of Sustainable Built Environment*, 6(2), 711–722, 2017. https://doi.org/10.1016/j.ijsbe.2017.08.003.

[6] A. H. Oti, W. Tizani, H. Abanda, A. Jalyzada, and J. H. Tah. Structural sustainability appraisal in BIM. *Automation in Construction*, 69:44–58, 2016. https://doi.org/10.1016/j.autcon.2016.05.019.

[7] G. Karaoğlu. Mimari Tasarımda BIM. 2020. MSc Dissertation. Eskişehir Technical Univeriste, Institute of Graduate Education, Eskişehir, Turkiye. [In Turkish]

[8] T. Mousiadis, and S. Mengana. Parametric BIM: Energy Performance Analysis Using Dynamo for Revit. 2016. MSc Dissertation. Stockholm: KTH Royal Institute of Technology.

[9] P. Baynum, R. R. A. Issa, and O. Svetlana. Building information modeling in support of sustainable design and construction. *Journal of Construction Engineering*, 139(1), 25–34, 2013. https://doi.org/10.1061/(ASCE)CO.1943-7862.0000560.

[10] S. Habibi. The promise of BIM for improving building performance. *Energy and Buildings*, 153:525–548, 2017. https://doi.org/10.1016/j.enbuild.2017.08.009.

[11] M. Kassem, and B. Succar. Macro BIM adoption: Comparative market analysis. *Automation in Construction*, 81:286–299, 2017. https://doi.org/10.1016/j.autcon.2017.04.005.

[12] V. Fernandez-Mora, I. J. Navarro, and V. Yepes. Integration of the structural project into the BIM paradigm: A literature review. *Journal of Building Engineering*, 53:104318, 2022. https://doi.org/10.1016/j.jobe.2022.104318.

[13] S. T. Hossain, and K. Amor Bin Zaman. Introducing BIM in outcome based curriculum in undergraduate program of architecture: Based on students perception and lecture-lab combination. *Social Sciences & Humanities Open*, 2022.

[14] A. Porwal, and K. N. Hewageb. Building information modeling (BIM) partnering framework for public construction projects. *Automation in Construction*, 204–214, 2013.

[15] M. Turan, and A. Ö. Yavuz. Kavramsal tasarımda yapı bilgi modellemesi ile tasarım süreci üzerine düşünmek. *International Journal of 3D Printing Techologies and Digital Industry*, 6(1):40–53, 2022. https://doi.org/10.46519/ij3dptdi.1015389 [In Turkish].

[16] J. Oceans. Why is BIM design relevant in the modern architecture? BIM design software and process. 2021. Retrieved on 17/11/2022, from https://revizto.com/en/bim-design/

[17] United BIM. BIM Maturity Levels Explained- Level 0, Level 1, Level 2, Level 3. 2016. Retrieved on 26/11/2022, from https://www.united-bim.com/bim-maturity-levels-explained-level-0-1-2-3/

[18] LetsBuild. What is Building Information Modeling? 2019. Retrieved on 28/11/2022, from https://www.letsbuild.com/blog/bim-maturity-levels

[19] BibLus. BIM maturity Levels: from stage 0 to stage 3. 2019. Retrieved on 28/11/2022, from https://biblus.accasoftware.com/en/bim-maturity-levels-from-stage-0-to-stage-3/

[20] Civil Engineer. How to Basic – BIM Level's and 2-6D's. 2022. Retrieved on 28/11/2022, from https://civilengineering.engineer/howtobimsimple/

[21] Autodesk. BIM for structural engineering. 2022. Retrieved on 03/11/2022, from https://www.autodesk.com/industry/aec/bim/structural-engineering.

[22] M. Mathews. BIM collaboration in student architectural technologist learning. *Journal of Engineering, Design and Technology*, 11(2), 190–206, 2013. https://doi.org/10.1108/JEDT-10-2011-0067.

[23] M. İnceoğlu, and B. İnan. Bilgisayar destekli tasarımın gelişimi: Yeni bir mimari metodoloji olarak YBM. *GSI Journals Serie C: Advancements in Information Sciences and Technologies*, 3(1):47–65, 2020. https://dergipark.org.tr/tr/pub/aist/issue/52639/661853. [In Turkish].

[24] M. Wierzbicki, C. De Silva, and D. Krug. BIM – History and trends. In *CONVR2011 International Conference on Construction Applications of Virtual Reality*, 141–150. Weimar, 2011.

[25] B. Martens, and H. Peter. 2007. ArchiCAD: best practice: the Virtual Building revealed. Retrieved from https://books.google.com.tr/books?id=4oUeAQAAIAAJ

[26] M. S. Bergin. A brief history of BIM. 2012. Retrieved on 07/11/2022, from https://www.archdaily.com/302490/a-brief-history-of-bim

[27] K. Papamichael, J. LaPorta, and H. Chauvet. Building Design Advisor: Automated integration of multiple simulation tools. *Automation in Construction*, 6:341–352, 1997. https://doi.org/10.1016/S0926-5805(97)00043-5.

[28] G. Karaoğlu, and M. İnceoğlu. Bilbao etkisi üzerinden bina bilgi modellemesini okumak. *Journal of Architecture and Life*, 779–791, 2021. https://doi.org/10.26835/my.866374.

[29] Autodesk. Every project starts with a sketch. 2022. Retrieved on 08/11/2022, from https://formit.autodesk.com/

[30] NBS. NBS' 10th National BIM Report. 2020. Retrieved on 25/11/2022, from https://www.thenbs.com/knowledge/national-bim-report-2020

[31] S. Chase. The statistics proving BIM means business. 2021. Retrieved on 25/11/2022, from https://business.bimobject.com/en/blog/statistics-proving-bim-means-business/

[32] T. Pednekar, and O. Sumant. *BIM in Construction Market: Global Opportunity Analysis and Industry Forecast, 2020-2027*. Allied Market Research, 2021.

[33] S. Lucas. BIM software to use in 2022. 2020. Retrieved on 25/11/2022, from https://blog1.bricksapp.io/blog/en/bim-software-2021-ultimate-list/

[34] DesignTech. Parametric Modelling. 2022. Retrieved on 20/11/2022, from https://www.designtechsys.com/articles/parametric-modelling

[35] Galorath. What is parametric modeling? 2022. Retrieved on 20/11/2022, from https://galorath.com/what-is-parametric-modeling/

[36] Ajour System. Digital operation and maintenance. n.d. Retrieved on 20/11/2022, from https://ajoursystem.com/en/ajourfm/

[37] K.-H. Chang. Chapter 3 – solid modeling. e-design. *Computer-Aided Engineering Design*, 125–167, 2015. https://doi.org/10.1016/B978-0-12-382038-9.00003-X.

[38] Y. Liu, S. V. Nederveen, and M. Hertogh. Understanding effects of BIM on collaborative design and construction: An empirical study in China. *International Journal of Project Management*, 35(4), 686–698, 2017. https://doi.org/10.1016/j.ijproman.2016.06.007.

[39] V. Singh, N. Gu, and X. Wang. A theoretical framework of a BIM-based multi-disciplinary collaboration platform. *Automation in Construction*, 20:134–144, 2011. https://doi.org/10.1016/j.autcon.2010.09.011.

[40] A. Grilo, A. Zutshi, R. Jardim-Goncalves, and A. Steiger-Garcao. Construction collaborative networks: The case study of a building information modelling-based office building project. *International Journal of Computer Integrated Manufacturing*, 26:152–165, 2013. https://doi.org/10.1080/0951192X.2012.681918.

[41] Building in Cloud. BIM collaboration is the key to success. 2022. Retrieved on 28/11/2022, from https://www.buildingincloud.net/en/operation/bim-collaboration-is-the-key-to-success-learn-how-bim-helps-achieve-improved-project-outcomes/

[42] D. Cao, H. Li, G. Wang, and T. Huang. Identifying and contextualising the motivations for BIM implementation in construction projects: An empirical study in China. *International Journal of Project Management*, 35(4), 658–669, 2017. https://doi.org/10.1016/j.ijproman.2016.02.002.

[43] M. Hertogh, and E. Westerveld. Playing with Complexity. Management and organisation of large infrastructure projects. Rotterdam: Erasmus University Rotterdam. 2010. Retrieved on 28/11/2022, from https://repub.eur.nl/pub/18456

[44] D. Bryde, M. Broquetas, and J. M. Volm. The project benefits of building information modelling (BIM). *International Journal of Project Management*, 31(7), 971–980, 2013. https://doi.org/10.1016/j.ijproman.2012.12.001.

[45] R. Volk, J. Stengel, and F. Schultmann. Building information modeling (BIM) for existing buildings – Literature review and future needs. *Automation in Construction*, 38:109–127, 2014. https://doi.org/10.1016/j.autcon.2013.10.023.

[46] P. Ivson, A. Moreira, F. Queiroz, W. Santos, and W. Celes. A systematic review of visualization in building information modeling. *IEEE Transactions on Visualization and Computer Graphics*, 26(10), 3109–3127, 2020. https://doi.org/10.1109/TVCG.2019.2907583.

[47] S. C. Chai, M. Klufallah, S. Kuppusamy, and A. A. Yusof. BIM integration in augmented reality model. *International Journal of Technology*, 10(6), 611–619, 2019. https://doi.org/10.14716/ijtech.v10i7.3278.

[48] Grow. Why is data important for your business? 2022. Retrieved on 27/11/2022, from https://www.grow.com/blog/data-important-business

[49] A. C. Anadiotis, O. Balalau, C. Conceição, H. Galhardas, M. Y. Haddad, I. Manolescu, T. Merabti, and J. You. Graph integration of structured, semistructured and unstructured data for data journalism. *Information Systems*, 104:101846, 2022. https://doi.org/10.1016/j.is.2021.101846.

[50] P. Ambika. Chapter thirteen – machine learning and deep learning algorithms on the industrial internet of things (IIoT). *Advances in Computers*, 117(1), 321–338, 2020. https://doi.org/10.1016/bs.adcom.2019.10.007.

[51] E. Pellegrino, M. A. Bottiglieri, G. Crump, L. C. Pieper, and D. Touil. *Managing and Visualizing Your BIM Data: Understand the Fundamentals of Computer Science for Data Visualization Using Autodesk Dynamo, Revit, and Microsoft Power BI*. Packt Publishing, 2021.

[52] A. Tondak. Structured, Semi Structured and Unstructured Data. 2022). Retrieved on 27/11/2022, from https://k21academy.com/microsoft-azure/dp-900/structured-data-vs-unstructured-data-vs-semi-structured-data/

[53] G. Jifa. Data, information, knowledge, wisdom and meta-synthesis of wisdom-comment on wisdom global and wisdom cities. *Procedia Computer Science*, 17:713–719, 2013. https://doi.org/10.1016/j.procs.2013.05.092.

[54] CoConstruct. Features. 2022. Retrieved on 28/11/2022, from https://www.coconstruct.com/how-it-works

[55] Primavera. Construction engineering. 2022. Retrieved on 28/11/2022, from https://www.oracle.com/tr/industries/construction-engineering/primavera-p6/

[56] Dalux. Dalux field. 2022. Retrieved on 28/11/2022, from https://www.dalux.com/dalux-field

[57] Bim Teknoloji. 4D BIM Modelleme nedir? 2020. Retrieved on 26/11/2022, from https://www.bimteknoloji.com/fikir/4d-bim-modelleme-nedir/ [In Turkish]

[58] S. Hamil. What is BIM? 2021. Retrieved 11 26, 2022, from NBC for Specifiers: https://www.thenbs.com/knowledge/bim-dimensions-3d-4d-5d-6d-bim-explained

[59] Hitech. What Does 5D BIM Mean for Cost Managers? 2016. Retrieved on 26/11/2022, from https://www.hitechbimservices.com/blog/what-does-5d-bim-mean-for-cost-managers.php

[60] S. Ofluoğlu. BIM ve performatif mimari tasarım. Autodesk Yapı Tasarım Atölyesi 5. 2015. İstanbul. Retrieved on 28/11/2022, from https://www.slideshare.net/sofluoglu/bim-ve-bina-performans-analizi [In Turkish]

[61] R. Jin, B. Zhong, L. Ma, A. Hashemi, and L. Ding. Integrating BIM with building performance analysis in project life-cycle. *Automation in Construction*, 106:102861, 2019. https://doi.org/10.1016/j.autcon.2019.102861.

[62] Autodesk. BIM acceleration by sector. 2022. Retrieved on 24/11/2022, from https://www.autodesk.com/industry/aec/bim

[63] bimobject. 2022 global guide to BIM mandates | Resource | BIM. 2022. Retrieved on 24/11/2022, from https://business.bimobject.com/en/resources/a-manufacturer-s-guide-to-global-bim-mandates-and-initiatives/#form

[64] BM Environment Programme. As buildings and construction sector grows, time running out to cut energy use and meet Paris climate goals. 2017. Retrieved on 24/11/2022, from https://www.unep.org/news-and-stories/press-release/buildings-and-construction-sector-grows-time-running-out-cut-energy

Liam Bousfield, Serik Tokbolat*, Peter Demian

# 11 Evaluating the current state of digitalisation of the UK construction industry

**Abstract:** Due to the significant role of the construction industry in terms of the impact on economies and the environment, digitalisation of this sphere deserves special attention. This study aims to evaluate the state of digitalisation of the UK construction industry from the perspective of construction professionals. A critical review of existing literature is conducted to identify and evaluate the (1) barriers to adoption and implementation of digital practices, (2) the gap in adoption between small and medium enterprises and large-sized companies, (3) currently available, and (4) future technologies. The findings of the literature review were further investigated by adopting the mixed method approach, combining qualitative and quantitative research methods to develop a comprehensive understanding of the digitalisation phenomena in the context of the UK construction industry. In total, 81 questionnaire responses were returned and 5 interviews were conducted to gauge the opinions of construction professionals. The results reveal how there have been minimal advancements, in line with prior predictions, and how there is still considerable room for improvement to digitalise the industry. The study is an up-to-date snap shot of the current reality in the field of construction digitalisation in the UK and therefore provides the actual picture of the current state of affairs that could be useful for the industry as a whole.

## 11.1 Introduction

The benefits of moving to a digitalised construction industry are numerous. With the main aim of improving data efficiency and its communication, implementation of a digitalised strategy can facilitate further developments during various construction stages, such as advances in testing and surveying methods [1]. The concept of a digital industry was first acknowledged in the 1970s with the implementation of the "digital revolution", also known as industry 3.0 [2]. Industry 3.0, which involved the use of

---

***Corresponding author: Serik Tokbolat,** School of Architecture, Design and the Built Environment, Nottingham Trent University, UK; Faculty of Engineering, University of Nottingham, UK, e-mail: stokbolat@gmail.com
**Liam Bousfield,** School of Architecture, Design and the Built Environment, Nottingham Trent University, Murphy International Ltd., UK
**Peter Demian,** School of Architecture, Building and Civil Engineering, Loughborough University, UK

https://doi.org/10.1515/9783110791426-011

electronics and information technology to advance the automation processes, introduced the world to the potential benefits that digital technologies can provide, and laid the foundation for industry 4.0. The fourth industrial revolution, which advanced the automation, monitoring, and analysis of supply chains processes through integration of smart technologies, epitomises the importance of digital technologies across all industries, including the construction sector [3]. Industry 4.0 has triggered numerous changes across the industry and at the same time also created many opportunities to develop it further, with its focus for efficiency of project delivery being at the forefront [4]. Industry 4.0 was introduced to enrich the various construction processes with the use of digital information technologies. The implementation of industry 4.0 encouraged the development and further adoption of digital technologies and skills that can be observed today as well as provided insight into the cyber-physical systems available to the industry [4].

With the implementation of industry 4.0, the UK government has recognised the benefits that a digitalised industry can provide. As a result, various government schemes have come to fruition to supplement the adoption, namely the Construction Strategy 2016–2020 [5], Digital Built Britain Scheme [6], and Construction 2025 [7]. The Construction 2025 strategy outlines a forecasted £200bn per annum market for digital technologies by 2030 [8], which would lead to an increase in productivity of 15% if digital technologies are universally adopted [9]. According to the NBS construction technology report (2019), the infusion of digital technologies throughout the industry will be a massive contributor to combating the current sustainability issues the industry faces. In addition, the government launched the Centre for Digital Built Britain to lead the digital transformation of the built environment in the UK. The centre ran the National Digital Twin programme (NDTp) along with the Department for Business, Energy, and Industrial Strategy. The programme works with future users and early adopters in order to develop an Information Management Framework to connect digital twins [10].

There has been a need for the UK construction industry to become more digitalised, especially considering the recent events such as the fire at the Grenfell Tower and more recently with the COVID-19 pandemic, thus highlighting the importance of having an effective handover for technical information [11]. In fact, due to the pandemic, the UK construction industry has seen a rapid infusion of digital technologies into various elements of the workplace. In a survey conducted by the National Bureau of Statistics (NBS), due to COVID-19, 98% of respondents claimed they had seen a variety of changes to company processes operationally through the implementation of digital technologies [11]. This is further evidenced through an increased investment in the digital technology market, whilst the UK was suffering a major economic crisis as a result of the pandemic [12].

The aim of this research is to critically analyse the current state of digitalisation of the UK construction industry. The specific objectives of this study aimed at defining the current barriers preventing the adoption of digital technologies within the UK construction industry. The study also attempted to evaluate whether there is a difference in digital technologies adoption between the large-sized companies and SMEs in the UK construction industry. This analysis was supported by the investigation of the current digital technologies used in the UK construction industry and a discussion of the potential digital technologies the UK construction industry should adopt in the future.

## 11.2 Literature review

### 11.2.1 Current barriers to adoption

Whilst the idea of a digitalised construction industry is not a new concept, the perceived benefits of adoption are limited and often disregarded due to the barriers that the industry currently faces. According to the government's Construction 2025 scheme (2013), two-third of all construction companies are not partaking in any innovative schemes. There could be many reasons for this; however, as seen in the McKinsey Survey (2019), 84% of the respondents stated that digital transformation fell short of what was expected, thus resulting in a lack of scheme adoption. The main barrier to adoption of digitalisation by the industry at present is the lack of an effective digital strategy. If there is not a consistent strategy across all areas of the business, the adoption of the technologies will not be effective [13]. The lack of a digital strategy is one of the largest barriers for digitalisation of an industry in the beginning stages due to businesses not being able to competently grasp their strategic influences [14].

In addition to the lack of digital strategy, an insufficient innovation culture is a major barrier to adoption in the UK market. According to [15], digital transformation can only occur if there are both digital and cultural amendments to a business model. In the UK industry, people often overlook the importance of culture in a business and how it coincides with digital change. Digital change is a process that needs influence from all members of the business. There needs to be an enhanced focus on a companywide innovative business model to be able to combine both aspects, facilitating the formation of a digitally integrated industry. This concept is further explored by [16] and his "cultural and management barriers" states that a lack of top management commitment will adversely influence those further down the hierarchy. Similarly, [14] outlines how uncertainty of managers and employees, coupled with insufficient capabilities within the team and a lack of willingness to take the risks associated with a digital shift, are key barriers associated with company culture.

Further supporting the above, the start-up costs of implementing digital technologies across the organisation are a major reason for lack of execution. The Construction 2025 government scheme [8] outlines how the financial risk associated with innovation is one of the reasons why innovation rarely occurs throughout the industry, with the financial impacts of Research and Development [R&D] being a deterrent. This is further supported by [16] with the "economic and finance barriers" element of his analysis stating that high investment, lack of R&D resources, and Return on Investment [ROI] are significant barriers. This element also intertwines with the “lack of pertinent competencies” barrier outlined by [14].

To further explain the above barriers, the [17] outlined how third parties can also have an adverse influence on digital adoption through the following elements. First, “Fragmentation,” which outlines how the current projects undertaken in the construction industry are disjointed amongst supply chains. The key to achieving a successful digital shift is through consistent alterations, which need to be made across the different elements of the construction process [17]. Second, “Lack of replication” – as a lot of the construction projects in the UK are bespoke to client needs and delivered in various ways, it is difficult to generalise how approaches should be taken and hence a full-scale transformation will be required for each project. This is consistent with the “Technical technology barriers” outlined by 16, where it is argued that there is a lack of scalability and standardisation. Figure 11.1 below shows both the internal and external barriers outlined above.

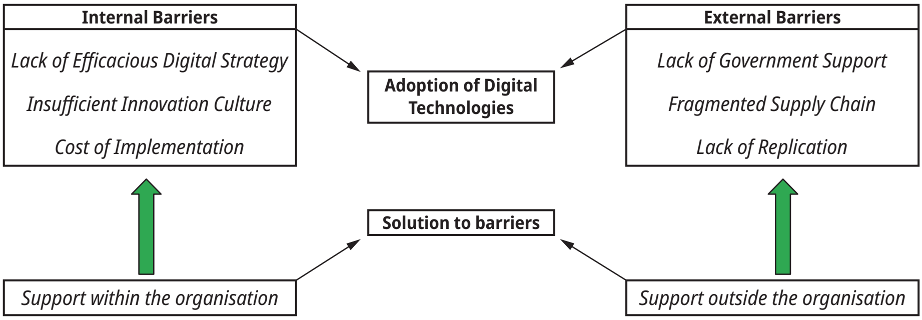

**Figure 11.1:** Barriers to adoption.

## 11.2.2 SMEs vs large organisations

SME adoption of digital technologies will play an integral part to achieving a digitalised construction industry. First, the BIM report (2020) outlines how there is still a divide between large-sized organisations and SMEs – this being evidenced through 80% of large-sized organisations utilising Building Information Modelling (BIM), compared with only 62% of small-medium enterprises. In a report produced by [18], it can be seen that large companies are almost three times more likely to adopt digital technologies, such as BIM, when compared with SMEs. Consequently, the 2015 report revealed just over 50% of SMEs were ready for the digital shift compared with nearly 90% of large companies [18]. This is further evidenced in the [17], where a comparison was drawn between SMEs and large-sized companies, evidencing that 34% of large-sized companies had over five years experience with BIM compared with only 16% of SMEs [18].

Supplementary to industry 4.0, the UK government has encouraged SMEs to employ a digital strategy, in line with large-sized companies, in an attempt to bridge the gap [19]. This is explored by [20], claiming that the start-up cost of BIM level one was extremely detrimental to SMEs, and many SME have not fully recovered. As a result, with the government pushing for similar investment into BIM level two, they have created a lag between the two business dimensions. If the UK government wants to successfully digitalise the industry, there needs to be a focus on the training of staff in SMEs to be able to competently utilise the technologies [21].

It is said that companies in the earlier years of BIM adoption, usually small-medium enterprises, show a negative Return on Investment (ROI) or only break even on their BIM investments, compared to large-sized organisations that usually show a positive ROI [22]. This is due to the start-up costs of implementing the technologies, which have had an adverse effect on cash flow for small-medium enterprises compared with large-sized businesses [18]. As outlined earlier, the difference in adoption between large-sized companies and SMEs has had a detrimental effect on SMEs. The use of BIM level two was made a legal requirement on all projects worth at least £5 m in 2016 [23]. It was determined that the adoption of BIM level two in SMEs was posterior to large-sized companies, and as result of the lack of adoption, work winning by SMEs was extremely difficult [20]. This is further supported by the Federation of Master Builders (2016), who state that 40% of SMEs fail to win 90% of the public projects they submit a bid for, and over half of all SMEs state they have seen a reduced success in bidding for works in the last five years.

## 11.2.3 Current digital technologies used in the UK construction industry

### 11.2.3.1 Building information modelling (BIM)

The notion of a digitalised construction industry was initially brought to light through the implementation of BIM. In a study conducted by Accenture (2014), the UK construction industry was highlighted as the sector with the lowest adoption and implementation of digital technologies, with 75% of construction employees in the UK not having advanced technologies incorporated in their business. It was claimed that the construction industry had a slow adoption and integration due to various reasons, such as minimal understanding of BIM benefits.

As previously highlighted, April 2016 saw the UK government introduce BIM level two as a mandatory element for all public sector works [24]. Since the enforcement of this mandate, there has been an increase of 8% in BIM usage across employees, this is the biggest increase in a three-year period [25]. The UK is currently advocating the use and benefits of BIM, providing both standards and descriptions of best use, with many other countries using the UK model as a template for implementation [26]. This is a direct result of BIM contributing to a saving of £855 m on UK construction schemes in 2016 [26].

The mandate was implemented due to the increasing need for public infrastructure and spending as well as combating the current adversarial environmental effects the industry is having. There is an enhanced focus on a reduction in the amount of fossil fuels used and due to this requirement, in line with the BIM level two mandate, the government implemented a scheme called “spend carefully, build more and to a sustainable quality standard” [27].

BIM, as a process and a standard, will contribute to the UK government’s aim for the construction industry to be net zero carbon by 2050. BIM aids in the utilisation of energy and resources used on site, and often acts as a guide to developing sustainable projections of a project [26]. The year 2020 marked 10 years of BIM usage. The 2016 projections saw BIM being implemented in 97% of all projects [26]. Alas, with a variance of 26%, it demonstrates how the industry is not digitalising at a rate that was projected.

It is important to note that BIM has seen many successes since implementation. In a report conducted by [18], 59% of respondents from the UK construction industry stated they reported a positive return on investment for BIM, with over 25% of respondents claiming the implementation of BIM had a very high positive return on investment. Finally, with a new generation of industry individuals coming through from the “millennials” and “generation Z” age groups, the use of digital technologies is the norm for these individuals from a young age. From a survey conducted by NBS, it states that 80% of employees aged under 40 have adopted BIM in their projects, compared with 60% for those 55 or over [28]. The cultural aspect and attitudes towards digital adoption differ between the age groups.

#### 11.2.3.2 Drones and unmanned aerial vehicles (UAVs)

There has been limited research into the application of drones and UAVs in the UK construction industry; however, as a result of the UK government passing the “modern transport bill” in 2019, the use of drones/UAVs in construction has grown significantly. UAVs and drones have seen a substantial growth in recent times due to the affordability [29] and accuracy [30] of the technology. This means applications of these technologies is becoming the norm and they have many uses such as health and safety of sites, surveying of construction sites, and progress tracking [31–33].

Design errors can cause significant amount of disputes in the UK construction industry. Drones can be used to counteract this issue by capturing real-time, accurate data from site and reporting it to generate more accurate models that are continuously updated. Benefits offered by drones to the industry are significant, as shown through a 61% increase in the accuracy of information being produced [34].

As the UK construction industry strengthens its digital capabilities, the use of drones and UAVs are becoming more applicable to multiple stages of construction [35]. Traditionally, drones were only employed in the preliminary stages of construction; however, this has now changed. In recent times, drones are utilised in the full life cycle of the project [36]. According to [36], drones provide up to date, real-scale images, which allow for more accurate modelling. Drones are more recently being used in internal 3D mapping of structures, where traditionally their uses were focused on external aerial mapping. As shown in a study by [37], the 3D mapping capabilities of drones provide a wide range of accurate imagery, which would otherwise be difficult.

As applications of drones and UAVs move away from traditional uses and into other phases of the construction life cycle, it is important to evaluate the effectiveness and accuracy of the imagery produced by the drones and UAVs [38]. It was discovered that the accuracy between the imagery produced by a drone and a 3D model were far better than those produced using other technologies, with the degree of error being less than 4 cm. The information provided by the aerial images is then converted into 3D models through the process of 3D reconstruction [35]. Drones and UAVs can capture these points remotely and offer a wider range of information when compared with other methods [33].

## 11.2.4 Future digital technologies for the UK construction industry

### 11.2.4.1 Blockchain technology

The idea of using blockchain technology in the construction industry is a relatively new concept even though it has been widely explored in other industries. Blockchain is an electronic source of record keeping that is securely kept, authenticated, and maintained by the various parties through a decentralised network [39]. Blockchain saves the information in blocks and adds it to a chain at scheduled intervals, which forms a chain of information that is extremely difficult to corrupt [40]. Blockchain is comprised of various elements that make it applicable to the construction industry. First, the decentralised element – this means there is no “middleman” involved with moneys or contracts, such as bank transfer or the use of a lawyer [41]. This has various monetary benefits as the associated costs that the banks and lawyers charge in order to complete the transaction can be avoided [42].

This element is applied through blockchain’s electronic document management. As the data is decentralised, it can be automatically updated across all systems and offers a comprehensive information management software for the whole project life cycle [43]. All the information is stored in a decentralised information base where validation is needed from all participants in the chain. This allows all participants in the chain to receive the same information without any room for error or discrepancy [40]. However, it has been found that blockchain technology is not always suitable for storage of all data [44].

As many construction projects produce mass amounts of data and need all data stored, blockchain may not be suitable as only limited data can be stored [44]. Blockchain technology also has applications in construction contract management. “Blockchain 2.0” outlines the usage of smart contracts. The use of a blockchain smart contract can potentially disregard the need for a main contractor, with smart contracts being set up between all the relevant third parties directly [40]. This is conducted through an “autonomous” element. With the technology being autonomous, once the programme is launched, the contract and the entity that initiated do not need to be in further contact [45]. This element allows for the use of algorithms that will automatically trigger the “execution, verification, and enforcement” of the smart contract [40]. The BIM, UAV, and Blockchain technologies were selected as examples from a wide range of technologies due to their relative popularity and recognition. Further research should consider a wider range of technologies.

To conclude, historically the industry has faced payment disputes in construction projects with issues such as non-payment or late payment often occurring [46]. Through the implementation of smart contracts, blockchain technology can act as a solution to these payment disputes. This will influence the way future contracts are set up and can avoid litigation [47]. The use of blockchain and smart contract will remove the risk of litigation occurring as the payments will be automated [48].

## 11.3 Methodology

This study has considered data collected from the scientific literature and primary data sources. A potential risk of relying on published literature is that there is no control over the quality of the information provided. In order to control this risk, an evaluation of the reliability of the information had been conducted prior to inclusion in this study. When carrying out primary research, a survey approach has been adopted using a questionnaire. The questions were based on a Likert scale to measure the relative impact from strongly disagree (1) to strongly agree (5), multiple choice questions, and closed questions. The Likert scale questions were used as they are universally adopted as a comprehensive way of collecting data, which is easy to understand and analyse the results. This data was gathered through various professionals in the UK construction industry. The advantage of using these professionals is that they are directly involved in the delivery of a construction project from start to finish. Moreover, semi-structured direct interviews have been carried out. The interview questions were semi-structured to allow the professionals to further expand their views of the questions, previously limited in the questionnaire. Obtaining both qualitative and quantitative data has facilitated a reliable evaluation of the current state of digitalisation within the UK construction industry.

The research for this study has included both the use of qualitative data collection and quantitative data collection. According to Hurmerinta-Peltomaki and [49], the use of a mixed methodology approach increases the validity and accuracy of the results. Furthermore, the use of a mixed method approach offers the benefits of both qualitative and quantitative data collection to be utilised effectively [50].

The research questions were structured to clearly establish relationships between different job roles, sectors, and viewpoint on the state of digitalisation within the UK construction industry. An understanding of the company size, sector, job role, age group, and perception on adoption is imperative to either proving or disproving the findings from the literature review. Upon conducting the research for this study, it was identified that similar questions have been asked regarding this topic, namely in a study conducted by [51]. This study conducted research into the state of digitalisation of the South African construction industry and there were limited similarities in studies currently conducted in the UK.

### 11.3.1 Survey

Even though the questionnaires offer an “even international coverage,” when compared to other methods, there are still some limitations associated with the data collection method [52]. According to [53], one of the main issues surrounding the use of questionnaires is the potential for dishonesty in answers. This can often be as a result of “social desirability bias”. This matter has been managed through the questionnaire being anonymous. With the questionnaire being anonymous, the need for social approval of answers is removed. Furthermore, with the questionnaire being closed, it is claimed to be difficult to grasp the emotions of the participant. This is also discussed by [53], who states without these elements, essential data may be missed. In order to counteract this issue, a mixed methodology approach has been used with semi-structured interviews that allow participants to further expand their viewpoints.

### 11.3.2 Semi-structured interviews

The interview questions were split into five main sections. The first section was intended to identify the type of respondent who would be undertaking the interview, outlining their depth of experience and the skeleton knowledge surrounding a digital focus in the construction industry. The next four sections were split, based on the four objectives. The second section surrounded a discussion around the potential barriers to adoption and the key elements that need to be addressed to combat these barriers. From the literature review and the questionnaire responses, it was clear there was a gap in adoption between large-sized companies and small-medium enterprises. With the questionnaire only outlining whether there was a clear gap, it was important to identify why the participants felt this was the case. In addition to this, identification and expansion on ways to reduce this gap was included. Section three of the interview surrounded the current digital technologies in the industry. This was helpful to evaluate the reliability of the literature reviewed and identify whether the two digital technologies discussed in the literature review were being used within the industry. The final element of the interview discussed future technologies. The future technology discussed in the literature review was “blockchain technology”. This topic was discussed as it was a niche element of construction, which is yet to be fully adopted. With there being limited research on the topic, it was important to identify whether the individuals interviewed were aware of the applications and whether they believed it was integral to the further development of the industry.

Whilst interviews have many benefits, there are also factors of limitation. When conducting the interviews, there is always an element of uncertainty. There is the potential risk that the interviewee may misunderstand the question [54] and, in some instances, respond incorrectly. To ensure this does not occur in the interview, the interview questions were semi-structured, but without ambiguity. They were well-defined and concise, with a clear path of the topics that the interviewee shall discuss. Furthermore, there was potential for the ”interview effect,” which could affect the results provided by the interviewee [55]. In order to minimise this issue, the interviews were conducted over Microsoft Teams due to the coronavirus pandemic, and the camera was always switched off.

## 11.3.3 Research sample

The research sample used for this study included construction individuals who are currently in the industry from various sectors, age groups, job roles, and company sizes. The aim of this sample was to cover a broad range of construction professionals. The sample selected for this study was identified initially using social media, particularly LinkedIn. LinkedIn is an extremely useful tool due to there currently being over 722 million users on the platform [56].

The study reached out to 652 connections on LinkedIn, with 91.56% of connections involved in the construction industry. With 597 individuals within the network from various construction roles, experiences and company size, the network was deemed to be representative of the industry. The post on LinkedIn had 712 views. With a total of 81 responses from the sample, there was a 11.38% response rate. According to both [57] and [58], a response rate of 10–15% is standard for an external survey, thus showing the response rate for the questionnaire aligns with expectations of the methodology. There was a 100% response rate on the semi-structured element of the research. The research sample for the interviews consisted of five interviews, three of these from small-medium-sized enterprises and two from large-sized companies.

### 11.3.4 Method of analysis

The questionnaire has been selected due to its scalability and comparability benefits as well as its ability to cover a vast range of participants. This questionnaire was structured and closed to allow for clear comparisons to be drawn using quantitative data. The analysis techniques utilised were based on the use of Mean Item Score, which was used to score the level of digitalisation within the different elements, and additional statistical measures and value manipulation measures were used to further express the viewpoints of the sample.

The interviews were semi-structured and open. The interviews were thematically analysed, identifying similarities and differences between the responses. In addition, there was an analysis done on the consistency in response between the different company sizes and their viewpoints on the industry in relation to digital technologies. A mixed-method approach was used to compare the three types of data collected – two primary research methods, the questionnaire and the interview, and the secondary data collection through the existing literature.

## 11.4 Results

The questionnaire was issued with the intention of identifying a larger sample size of the UK construction industry. There were 81 responses in total, with 14 responses from the Small-Medium Business group, 9 from the Small-Medium Enterprise, 2 from a medium-sized company, and 56 from the large-sized company group. The interview sample consisted of five interviewees – two of these being from a large-sized company, and the other three being from small-medium enterprises. All five participants fell in the “Generation X” sample group, with all participants having a similar level of site experience in order to draw clear comparisons between company size and viewpoints.

### 11.4.1 Barriers to adoption

The literature review revealed that the four main barriers to adoption are “lack of government initiative”, “cost implications”, “lack of digital culture”, and a “lack of a digital strategy” as shown in the table 11.1. From the respondents, 67.90% state that they believe a lack of a digital culture is the main barrier to adoption; this being the most nominated response. This is closely followed by cost implications, with 61.70% of respondents selecting this barrier. It was interesting to see that there was over a 20% gap between selection of “lack of digital culture” and “lack of a digital strategy”. The literature review revealed how these two elements interlink and one cannot be achieved without the other.

**Table 11.1:** Barriers to adoption.

| Barrier | Responses | % |
|---|---|---|
| Lack of digital culture | 55 | 67.9% |
| Cost implications | 50 | 61.7% |
| Lack of digital strategy | 38 | 46.9% |
| Lack of government initiatives | 31 | 38.3% |
| Other | 13 | 15.6% |

The barrier that was most prevalent from the interview discussion was a “lack of digital culture”, highlighted by 80% of the interviewees. This was explored by [59] and [16] stating how people often overlook the importance of culture in a business and how it is essential to successfully digitalise. It was a surprise that only one of the respondents highlighted “lack of a digital strategy” as a barrier. The literature review revealed that this was one of the main barriers to adoption, stating “lack of a digital strategy is one of the largest barriers for digitalisation of an industry” [14].

In order to identify the difficulty to adopt digital technologies, the below question was proposed to get a consensus of their opinions as shown in Figure 11.2. By using the mean item score method of analysis, an overall score of 3.19 was calculated. This shows that from all the responses, on average, the respondents believe it is moderately difficult to adopt digital technologies in the industry. This is a relatively consistent view across company sizes, with the mean item scores ranging between 3.09 and 3.66.

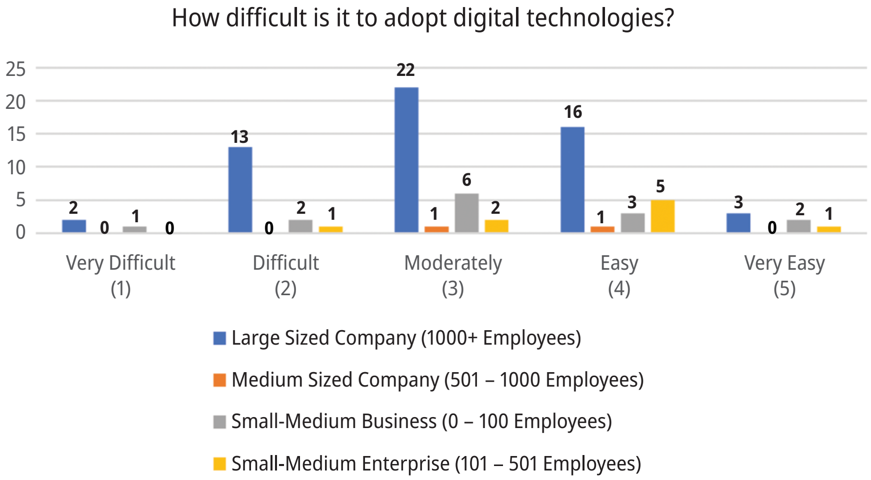

**Figure 11.2:** Difficulty to adopt by company size.

The results from this section do not necessarily compare with the findings in the literature review. The literature review revealed that there was a clear gap between large-sized companies and small-medium enterprises in terms of adoption and the ease associated with adoption. Even though only 33.93% of large-sized companies claimed that it was either difficult or very difficult to adopt the technologies compared with 66.67% of SMEs, there is only a variance of 0.57 between their mean item scores.

### 11.4.2 Large-sized company vs SME

From the results below as shown Figure 11.3, most of the respondents believe that there is a clear gap between the two groups, with just under 94% claiming so.

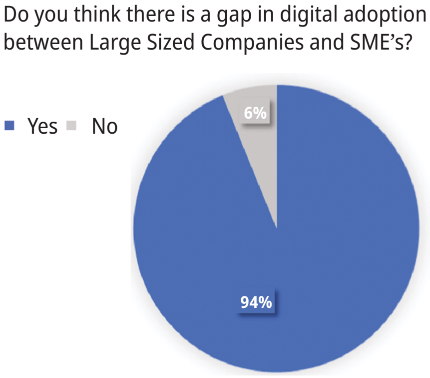

**Figure 11.3:** Gap in adoption.

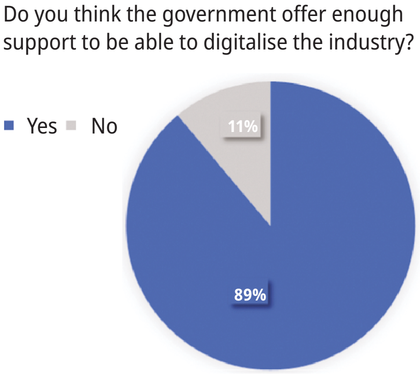

**Figure 11.4:** Government support.

From the interview responses, 100% of the large-sized company sample group stated that there was a gap in adoption between large-sized companies and SMEs, when compared with only 66.67% of the SME sample group. It was fascinating to identify why one of the SME sample interviewees claimed that there was no gap, stating "they both utilise similar technologies". The literature review revealed that one of the key reasons for the gap between the two company sizes is due to lack of government support, this being highlighted in both the questionnaire and the interviews. Referring to Figure 11.4, it is clear that most respondents believe that the government does not offer enough support to be able to digitalise the industry, with 89.90% stating this viewpoint.

Moreover, the literature review predicted that the SME group would have a high percentage of respondents claiming that the government does not offer enough support. The literature review revealed that a lack of government support has meant work winning for SMEs has become far more difficult. This is supported by 100% of the respondents from the SME sample group; they stated that the government does not provide a substantial amount of support to be able to digitalise. From the interviews, “lack of resources” and “lack of funding” were highlighted by 80% of the respondents, supporting the literature evidence [21]. The literature review revealed that the implementation of the BIM level two mandate has created a gap between the two company sizes. This was explored by one of the interviewees, stating “there is a gap, and it is because the government made BIM level 2 mandatory in 2016”. By using the mean item score method of analysis, an overall score of 4.28 was calculated. This shows that from all the responses, on average, the respondents are in between – being likely and very likely to support the adoption of digital technologies in their business as shown in Figure 11.5 below.

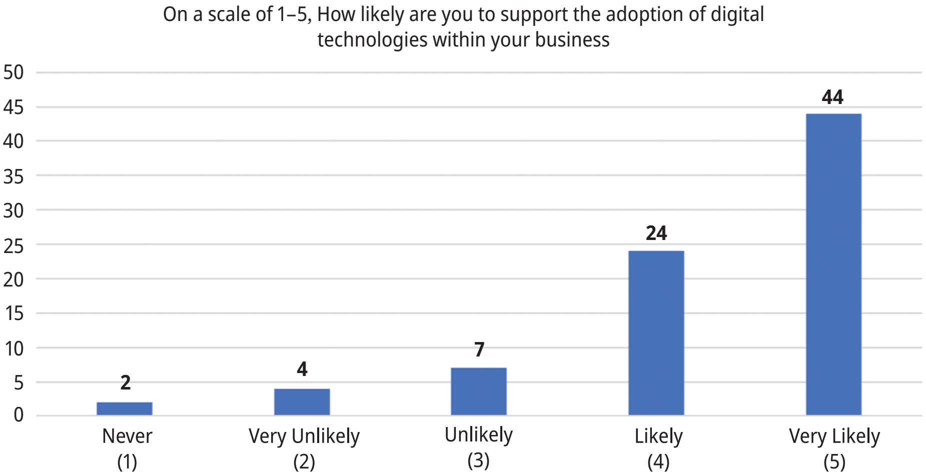

**Figure 11.5:** Likely to support adoption.

It was interesting to see that the mean item score for the large-sized company was 4.48 compared to the mean item score of 3.22 for small-medium enterprises. The results from the study are the same as the findings in the literature review. The literature review revealed that a positive culture towards adoption of innovative solutions was more prevalent in large-sized companies when compared to small-medium-sized enterprises. As outlined previously, almost 93% of the respondents of the large-sized company group state they are likely or very likely to support the adoption of digital technologies. This is more than double the result found from the small-medium enterprise sample group. The results found in the questionnaire once again reiterate that there is a clear gap and acts as a viable validation of the findings revealed in the literature review.

## 11.4.3 Current technologies

### 11.4.3.1 Building information modelling

From the literature review, BIM was highlighted as the "backbone of digital transformation of the construction industry" and one of the key digital technologies contributing to the growing digital revolution.

The questionnaire results as shown in Figure 11.6 revealed that, overall, 74.07% of the respondents are either, aware, or very aware of building information modelling. By using the mean item score method of analysis, a score of 3.98 was calculated. This result evidences how the respondents are only aware of BIM. This is not consistent with findings from the literature review. The literature review stated that as of 2020, over 70% of the industry personnel are using building information modelling in their projects. If this was the case, it would be expected that there would be a mean item score between 4 and 5 as a high level of usage would coincide with a high level of awareness. From the interview results, 100% of the interviewees were aware of BIM as a technology, with all currently using it in their projects bar one. In terms of current applications, the majority of the interviewees were aware of all the applications outlined in the literature review. There were two elements of BIM that were highlighted by the sample group that was not identified in the literature review; these being "applications in clash detection "and "virtual testing".

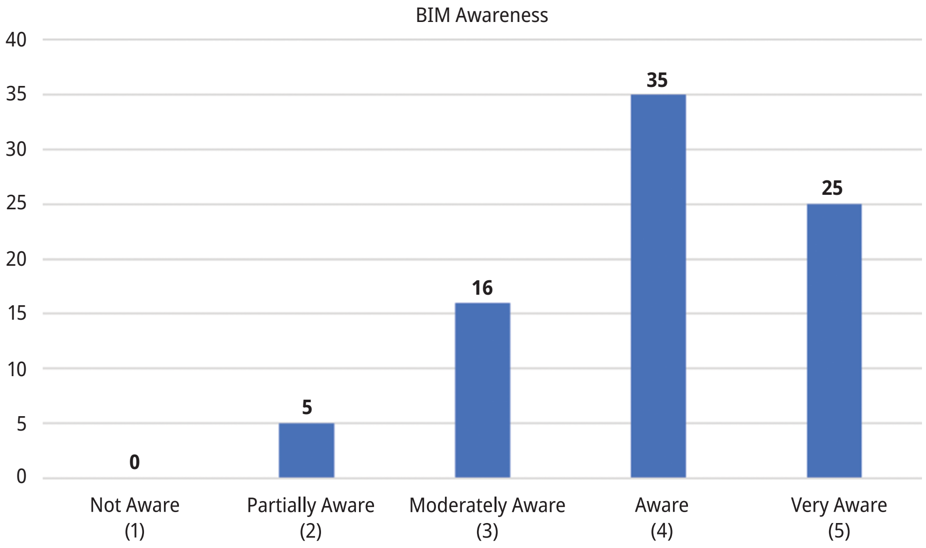

**Figure 11.6:** BIM awareness.

### 11.4.3.2 Drones/UAVs

The literature review revealed that the use of drones/UAVs is one of the most adopted current digital technologies in the UK construction industry. As shown in Figure 11.7, just over half of the respondents state that they are either aware or very aware of drones/UAVs, with 51.85% stating this.

By using the mean item score method of analysis, a score of 3.19 was calculated. This shows that from all the responses, on average, the respondents are only moderately aware of drones/UAVs uses. This is not consistent with the findings from the literature review as the review highlighted many uses and current applications within the industry. The interviews revealed that 100% of the interviewees are aware of drones/UAVs; however, only 40% currently use them in their projects, with both interviewees being from the large company sample group. The interviews revealed that the most commonly occurring applications were for media, handovers, and topographical surveys. These were also highlighted as key elements for application in the literature review. As expected, there were more identified applications from the large-sized company sample group, compared with small-medium-sized, and this coincides with the findings from the literature review. There was a clear split in opinion between the two company sizes, with the small-medium-sized enterprise personnel stating, “it is expensive and very few small companies have this ability” and the large-sized company group stating that “Drones are the way forward”.

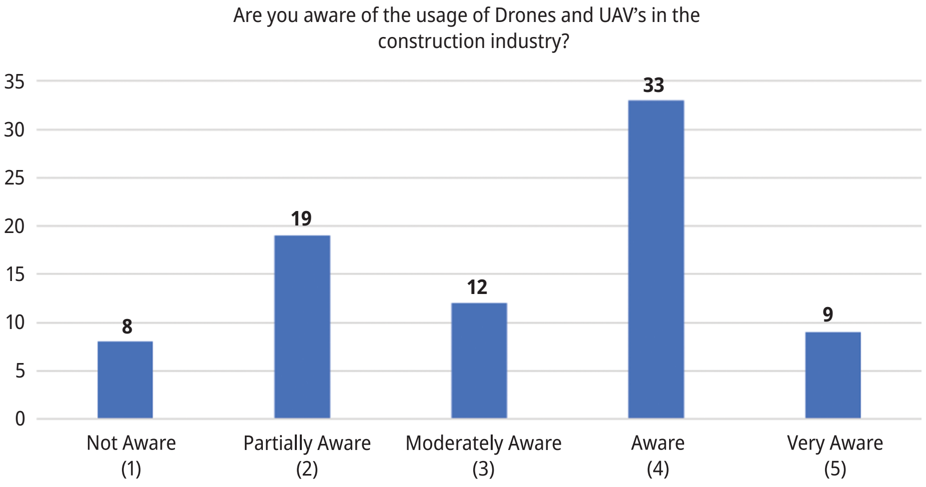

**Figure 11.7:** Drones/UAV awareness.

## 11.4.4 Future technology

### 11.4.4.1 Blockchain technology

Blockchain technology was the future technology explored in the literature review. Figure 11.8 below outlines the respondents’ current level of awareness of blockchain technology. The results clearly evidence that 65.40% of the participants were not aware of blockchain technology, with only 28 respondents stating they are aware of blockchain technology.

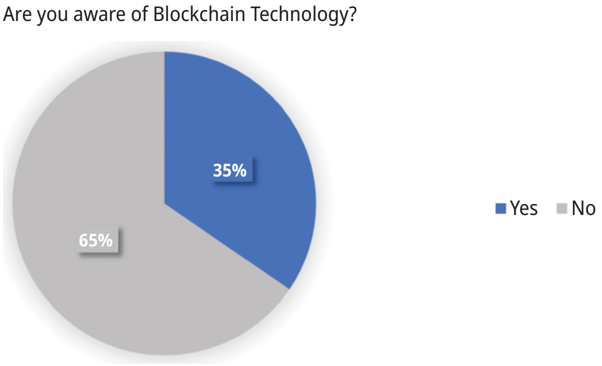

**Figure 11.8:** Awareness of blockchain.

Furthermore, it was important to identify whether there was a clear gap between the awareness by company size. Prior to conducting the research, it was alleged that there would be a clear gap in awareness between these two company sizes. However, that is not the case, as both the sample groups have a larger proportion of respondents claiming they are not aware of the technology, with 62.50% of the large-sized company group stating they were not aware of the technology, compared to 66.67% in the SME group. The results from the interviews regarding this topic are aligned with what was expected prior to undertaking the interviews. As expected, 100% of the interviewees from the large-sized company sample group were aware of blockchain technology and 100% of those in the SME sample were not aware. This coincides with the differing cultural viewpoints revealed between the two in the previous analysis and the literature review.

## 11.5 Discussion

When addressing the objective of identifying and evaluating barriers to adoption of construction digitalisation, it was clear to see that the barriers identified in the literature review were consistent with what was found in both primary data collection results. From what can be seen, with the earliest literature used in this section of the study being from 2004, the same barriers have remained constant for a period of nearly 17 years. The findings have also highlighted where additional measures need to be implemented in order to facilitate a successful digital shift, thus supporting the conclusions drawn from previous researchers.

The study findings have also identified that there is a clear gap in adoption of digital practices and technologies between large-sized companies and SMEs. Both the literature reviewed and the primary data results come to the same conclusion. It was interesting to identify the adverse effects the government has caused on this gap, with both the literature review and primary data stating that they have “increased the gap” between the two. The findings from this section support previously published conclusions from academics, thus reinforcing its validity.

When discussing BIM as a part of current digital technologies used in the UK construction industry, the primary data results were consistent with the findings from the literature review for the most part, apart from levels of awareness from the primary data, compared with the stated levels of uses in the literature review. This aspect was quite thought-provoking as it was believed, due to the multiple applications and current uses of BIM within the industry, that the findings from both would be consistent. However, both sections concluded that BIM was the digital technology that was utilised the most within the UK construction industry.

Drones/UAV usage was highlighted as the second most adopted digital technology within the industry. Unfortunately, some of the findings from the primary data results were not consistent with this theory and the literature review findings, with the interviewees showing a more positive attitude towards this technology. According to the literature review, the use of drones in construction has grown significantly as a result of the modern transport bill. However, the questionnaire results did not evidence this with a relatively low level of adoption being found. This is contrasted by the findings of the interviews, with one interviewee stating, “Drones are the way forward”.

Discussion surrounding blockchain technology centred around the point if it is a future technology the industry should adopt. As there was limited research into this technology due to the recent awareness of its beneficial elements, with the earliest literature used being from late 2015, it was difficult to draw confident conclusions about its conceptual element vs application element. The literature review revealed the various applications where blockchain technology can be used within the industry, stating how implementation will help tackle industry’s old issues such as poor productivity and payment disputes. The data collected from the questionnaire exposed how little the current industry knows about blockchain technology and the benefits it can provide for the industry. This is however contrasted by the interviews, with two of the interviewees discussing all of the benefits that blockchain can provide for the industry.

## 11.6 Conclusions

The aim of this study was to evaluate the state of digitalisation of the UK construction industry. After collating all the information, it is clear to see that the industry is only moderately advanced in terms of digitalisation. To further substantiate this point, the first objective discusses the barriers to adoption. This objective revealed a number of barriers that have been constant and affected the digital uptake in the industry for a number of years. If the industry is to be able to successfully integrate digital technologies, the barriers need to be addressed and this needs to be from a "top-down" approach, with additional support needed both internally and externally to a business. Furthermore, the main issue currently is the emerging gap between large-sized companies and SMEs. As the literature review revealed, SMEs account for 99% of the construction industry. There will not be a substantial growth in the impact that digitalisation can have within the industry without the gap between the two company sizes being addressed, a key theme being the lack of government support, once again putting emphasis on the "top-down" approach. Discussion surrounding BIM and drones/UAVs revealed that the current industry is not as technologically advanced as the literature review revealed, with BIM awareness differing from claimed usage and awareness as also the current knowledge of the uses within the industry for drones/UAVs. The final element surrounded the implementation of a new digital technology within the industry, blockchain technology. The literature review revealed the mass amounts of commercial applications where blockchain can be used within the industry and how it can interlink with current technologies such as BIM to improve its current uses. If the industry is to continue to digitalise at an advanced rate, the adoption of these future technologies is imperative.

## Reference

[1] J. Miguel. Overview | Digitalisation In The Construction Industry. 2019. [online] Build Up. Available at: https://www.buildup.eu/en/news/overview-digitalisation-construction-industry [Accessed 21 January 2021].

[2] S. Pandit. What Is The Main Difference Between Industry 3.0 And Industry 4.0? – Quora. 2020. [online] Quora.com. Available at: https://www.quora.com/What-is-the-main-difference-between-Industry-3-0-and-Industry-4-0 [Accessed 21 January 2021].

[3] M. Santoshi. n.d. Industry 4.0: Its Impact On The Construction Sector. [online] The Constructor. Available at: https://theconstructor.org/digital-tools/industrial-revolution-construction/87300/ [Accessed 21 January 2021].

[4] M. Ellis. Industry 4.0 And The Future Of Construction. 2018. [online] REBIM®. Available at: https://rebim.io/industry4-0-and-the-future-of-construction/ [Accessed 21 January 2021].

[5] R. Garvey. Government Construction Strategy 2016-20 – Constructing Excellence. 2020. [online] Constructingexcellence.org.uk. Available at: https://constructingexcellence.org.uk/government-construction-strategy-2016-20/ [Accessed 22 January 2021].

[6] R. McPartland, and J. Sharman. What Is Digital Built Britain?. 2017. [online] NBS. Available at: https://www.thenbs.com/knowledge/what-is-digital-built-britain [Accessed 22 January 2021].

[7] R. Klein. Construction 2025: Making It Happen. 2013. [online] Building. Available at: https://www.building.co.uk/comment/construction-2025-making-it-happen/5058873.article [Accessed 22 January 2021].

[8] HM Government, H. Construction 2025. 2013. [online]. Available at: https://assets.publishing.service.gov.uk/government/uploads/system/uploads/attachment_data/file/210099/bis-13-955-construction-2025-industrial-strategy.pdf.

[9] N. Ainscough, R. Jackson, G. Tate, A. Kell, and S. Hamill. NBS Construction Technology Report 2019. 2019. [online] NBS. Available at: https://www.thenbs.com/knowledge/nbs-construction-technology-report-2019 [Accessed 22 January 2021].

[10] CDBB. National Digital Twin Programme. 2022. [online]. Available at https://www.cdbb.cam.ac.uk/what-we-do/national-digital-twin-programme

[11] NBS, and K. Barker. Report: Construction manufacturers and COVID-19, future impact. 2020. [online] Thenbs.com. Available at: https://manufacturers.thenbs.com/resources/knowledge/construction-manufacturers-and-covid-19.

[12] Digital Adoption. Digitalization, Transformation, And Agility: The New Normal. 2020. [online] Available at: https://www.digital-adoption.com/digitalization-transformation/ [Accessed 22 January 2021].

[13] G. Kane. Strategy, not Technology, Drives Digital Transformation. 2015. [online] MIT Sloan Management Review. Available at: https://sloanreview.mit.edu/projects/strategy-drives-digital-transformation/

[14] K. Vey, T. Fandel-Meyer, J. S. Zipp, and C. Schneider. Learning & development in times of digital transformation: Facilitating a culture of change and innovation. *International Journal of Advanced Corporate Learning (IJAC), [online]*, 10(1):22–32, 2017.

[15] A. Lundberg The Digital Transformation – Potential And Barriers. 2018. [online] Diva-portal.org. Available at: https://www.diva-portal.org/smash/get/diva2:1242131/FULLTEXT01.pdf [Accessed 25 January 2021].

[16] G. Mills. 2020. [online] Getitright.uk.com. Available at: https://getitright.uk.com/live/files/reports/8-giri-ucl-barriers-adoption-future-digital-engineering-technology-1-452.pdf [Accessed 25 January 2021].

[17] J. Koeleman. Decoding digital transformation in construction | McKinsey. 2019. [online] www.mckinsey.com. Available at: https://www.mckinsey.com/business-functions/operations/our-insights/decoding-digital-transformation-in-construction

[18] McGraw Hill Construction. SmartMarket Report The Business Value of BIM for Construction in Major Global Markets: How Contractors Around the World Are Driving Innovation With Building Information Modeling. 2020. [online]. Available at: https://www.icn-solutions.nl/pdf/bim_construction.pdf.

[19] N. Muna, and N. Sued. Barriers of Supply Chain Digitalization from the Perspective of Malaysian SMEs. 2008. [online] Available at: https://jtmt.utem.edu.my/jtmt/article/view/5953/3992.

[20] K. A. Awwad, A. Shibani, and M. Ghostin. Exploring the critical success factors influencing BIM level 2 implementation in the UK construction industry: The case of SMEs. *International Journal of Construction Management*, 1–8, 2020.

[21] L. Arendt. Barriers to ICT adoption in SMEs: How to bridge the digital divide? *Journal of Systems and Information Technology*, 10(2):93–108, 2008.

[22] McKinsey & Company. The case for digital reinvention. 2017. [online] McKinsey & Company. Available at: https://www.mckinsey.com/business-functions/mckinsey-digital/our-insights/the-case-for-digital-reinvention.

[23] Designing Buildings. BIM level 2. 2021. [online] Designingbuildings.co.uk. Available at: https://www.designingbuildings.co.uk/wiki/BIM_level_2.

[24] HM Government. Reporting to HM Treasury and Cabinet Office Government Construction. 2016. [online]. Available at: https://assets.publishing.service.gov.uk/government/uploads/system/uploads/attachment_data/file/510354/Government_Construction_Strategy_2016-20.pdf.

[25] H. Cherkaoui. UK follows through on BIM level 2 mandate. 2017. [online] LetsBuild. Available at: https://www.letsbuild.com/blog/uk-government-follows-bim-level-2-mandate.

[26] NBS. National BIM Report 2016. 2016. [online] NBS. Available at: https://www.thenbs.com/knowledge/national-bim-report-2016.

[27] R. Waterhouse, A. Matthews, and M. Bew. National BIM Report 2016. 2016. [online] NBS. Available at: https://www.thenbs.com/knowledge/national-bim-report-2016

[28] A. Boutle, J. Ford, S. Davidson, D. Sinclair, D. Bain, and M. Turpin. NBS' 10th National BIM Report. 2020. [online] NBS. Available at: https://www.thenbs.com/knowledge/national-bim-report-2020.

[29] J. G. Martinez, M. Gheisari, and L. F. Alarcón. UAV integration in current construction safety planning and monitoring processes: case study of a high-rise building construction project in chile. *Journal of Management in Engineering*, 36(3):05020005, 2020.

[30] W. W. Greenwood, J. P. Lynch, and D. Zekkos. Applications of UAVs in Civil Infrastructure. *Journal of Infrastructure Systems*, 25(2):04019002, 2019.

[31] S. Bang, H. Kim, and H. Kim. UAV-based automatic generation of high-resolution panorama at a construction site with a focus on preprocessing for image stitching. *Automation in Construction [online]*, 84:70–80, 2017.

[32] P. Gonçalves, J. Sobral, and L. A. Ferreira. Unmanned aerial vehicle safety assessment modelling through petri Nets. *Reliability Engineering & System Safety*, 167:383–393, 2017.

[33] R. Horgan. How drones are changing construction. 2020. [online] New Civil Engineer. Available at: https://www.newcivilengineer.com/opinion/how-drones-are-changing-construction-25-10-2020/.

[34] Autodesk. Drones Technology for AEC Industry-A boon! | Search | Autodesk Knowledge Network. 2019. [online] knowledge.autodesk.com. Available at: https://knowledge.autodesk.com/search-result/caas/simplecontent/content/drones-technology-for-aec-industry-boon.html [Accessed 19 Mar. 2021].

[35] N. Anwar, F. Najam, and M. A. Izhar. Construction Monitoring and Reporting using Drones and Unmanned Aerial Vehicles (UAVs). 2018. [online] Available at: https://www.researchgate.net/publication/326264559_Construction_Monitoring_and_Reporting_using_Drones_and_Unmanned_Aerial_Vehicles_UAVs.

[36] S. Goessens, C. Mueller, and P. Latteur. Feasibility study for drone-based masonry construction of real-scale structures. *Automation in Construction*, 94:458–480, 2018.

[37] J. S. Álvares, D. B. Costa, and R. R. S. De Melo. Exploratory study of using unmanned aerial system imagery for construction site 3D mapping. *Construction Innovation*, 18(3):301–320, 2018.

[38] A. S. Ahmad Shazali, and K. N. Tahar. Virtual 3D model of Canseleri building via close-range photogrammetry implementation. *International Journal of Building Pathology and Adaptation*, 38 (1):217–227, 2019.

[39] IBM. What is blockchain?. 2019. [online] Ibm.com. Available at: https://www.ibm.com/blockchain/what-is-blockchain [Accessed 9 Feb. 2021].

[40] K. M. San, C. F. Choy, and W. P. Fung. The potentials and impacts of blockchain technology in construction industry: A literature review. In *IOP Conference Series: Materials Science and Engineering, [online] 495*, 012005. 2019.

[41] A. Koutsogiannis, and N. Berntsen. Blockchain and construction: the how, why and when | BIM+. 2019. [online] www.bimplus.co.uk. Available at: https://www.bimplus.co.uk/people/blockchain-and-construction-how-why-and-when/ [Accessed 9 Feb. 2021].

[42] D. Hughes. The Impact of Blockchain Technology on the Construction Industry. 2019. [online] Medium. Available at: https://medium.com/@hangadave/the-impact-of-blockchain-technology-on-the-construction-industry-85ab78c4aba6 [Accessed 9 Feb. 2021].

[43] Ž. Turk, and R. Klinc. Potentials of blockchain technology for construction management. *Procedia Engineering*online, 196:638–645, 2017.

[44] Q. Lu, and X. Xu. Adaptable blockchain-based systems: A case study for product traceability. *IEEE Software*, 34(6):21–27, 2017.

[45] M. Swan. Blockchain: Blueprint for a New Economy. 2015. [online] Google Books. "O'Reilly Media, Inc." Available at: https://www.google.co.uk/books/edition/Blockchain/RHJmBgAAQBAJ?hl=en&gbpv=1&dq=inauthor:%22Melanie+Swan%22&printsec=frontcover [Accessed 9 Feb. 2021].

[46] Handle. Why Are Payment Issues Persistent in the Construction Industry? | Handle. 2019. [online] Handle Available at: https://www.handle.com/construction-payment-issues/ [Accessed 9 Feb. 2021].

[47] J. J. Sikorski, J. Haughton, and M. Kraft. Blockchain technology in the chemical industry: Machine-to-machine electricity market. *Applied Energy, [online]*, 195:234–246, 2017.

[48] J. Wang, P. Wu, X. Wang, and W. Shou. The outlook of blockchain technology for construction engineering management. *Frontiers of Engineering Management*, 4(1):67, 2017.

[49] L. Hurmerinta-Peltomäki, and N. Nummela. Mixed methods in international business research: A value-added perspective. *Management International Review, [online]*, 46(4):439–459, 2006.

[50] J. C. Greene, V. J. Caracelli, and W. F. Graham. Toward a conceptual framework for mixed-method evaluation designs. *Educational Evaluation and Policy Analysis*, 11(3):225, 1989.

[51] D. Aghimien, C. Aigbavboa, and A. Oke. (PDF) Digitalisation For Effective Construction Project Delivery In South Africa. 2018. [online] ResearchGate. Available at: https://www.researchgate.net/publication/326271662_Digitalisation_for_Effective_Construction_Project_Delivery_in_South_Africa [Accessed 25 January 2021].

[52] Account Learning. Advantages and Disadvantages of Questionnaires. 2021. [online] accountlearning.com. Available at: https://accountlearning.com/advantages-and-disadvantages-of-questionnaires/#:~:text=Questionnaires%20suffer%20from%20the%20following%20limitations:%201%20Its [Accessed 2 Mar. 2021].

[53] S. Debois. 10 Advantages and Disadvantages of Questionnaires – Survey Anyplace. 2019. [online] Survey Anyplace. Available at: https://surveyanyplace.com/questionnaire-pros-and-cons/ [Accessed 2 Mar. 2021].

[54] Sociology Group. Advantages and Disadvantages of Interview in Research. 2019. [online] Sociology Group. Available at: https://www.sociologygroup.com/advantages-disadvantages-interview-research/.

[55] S. Mcleod. Structured and Unstructured Interviews | Simply Psychology. 2014. [online] Simplypsychology.org. Available at: https://www.simplypsychology.org/interviews.html [Accessed 2 Mar. 2021].

[56] M. Iqbal. LinkedIn Usage and Revenue Statistics (2018). 2019. [online] Business of Apps. Available at: https://www.businessofapps.com/data/linkedin-statistics/ [Accessed 19 Feb. 2021].

[57] SurveyTown. Calculate Number of Respondents for Statistic Significance. 2016. [online] SurveyTown. Available at: https://surveytown.com/number-of-respondents-needed/ [Accessed 19 Feb. 2021]

[58] PeoplePulse. Survey Response Rates. [online] PeoplePulseTM – Online Survey Software | Australian Survey Software. 2021. Available at: https://peoplepulse.com/resources/useful-articles/survey-response-rates/ [Accessed 19 Feb. 2021].

[59] J. Loonam, S. Eaves, V. Kumar, and G. C. Parry. Towards digital transformation: Lessons learned from traditional organisations. 2017.

# Index

https://doi.org/10.1515/9783110791426-012